# THOR-ODIN DOME: CONSTRAINTS ON PALEOCENE-EOCENE ANATEXIS AND DEFORMATION, LEUCOGRANITE GENERATION AND THE TECTONIC EVOLUTION OF THE SOUTHERN OMINECA BELT, CANADIAN CORDILLERA

by

Alana Maxine Hinchey, B.Sc.H., M.Sc.

A thesis submitted to the Faculty of Graduate Studies and Research

in partial fulfillment of the requirements for the degree of

Doctor of Philosophy, Department of Earth Sciences

Ottawa-Carleton Geoscience Centre and

Department of Earth Sciences

Carleton University

Ottawa, Ontario

May, 2005

# ABSTRACT

Thor-Odin dome is one of two structural culminations of the Monashee complex, located in the southeastern Omineca belt of the Canadian Cordillera. The dome comprises a supracrustal cover sequence and >1.8 Ga North American basement rocks that experienced polydeformation, high-grade metamorphism and anatexis during the Late Cretaceous - Eocene stage of the Cordilleran orogen. Pervasive Paleocene - Eocene deformation transposed and overprinted Precambrian relationships and structures.

Basement ortho- and paragneiss contain ubiquitous stromatic leucosome as well as discrete phenocrystic and pegmatitic vein-type leucosome, which are all interpreted to have formed as a result of *in situ* melting in the Paleocene-Eocene. The stromatic leucosome is infolded with the country rock ($F_2$) and contains a weak foliation. The phenocrystic and pegmatitic vein-type leucosome crosscut the stromatic leucosome, as well as the transposition foliation ($S_2$). SHRIMP $^{206}Pb/^{238}U$ zircon ages range from ca. 56 to 52 Ma, interpreted as the timing of leucosome crystallization. Evidence for *in situ* anatexis includes: igneous textures, field relations, major and trace element chemistry, Nd isotope chemistry and zircon morphology. The onset of anatexis, at ca. 56 Ma, was a result of regional prograde metamorphism and was, at least in part, coincident with the formation of the penetrative ($S_2$) transposition foliation and large recumbent ($F_2$) tight to isoclinal folds. Pervasive anatexis continued during $F_3$ and $F_4$ folding.

The timing of metamorphism in Thor-Odin basement gneiss was constrained by U-Pb SHRIMP analyses of monazite from cordierite-gedrite rocks and interlayered quartzite. Monazite grains have $^{206}Pb/^{238}U$ ages ranging from ca. 56 to 52 Ma. Monazite grew and/or were recrystallized during high-grade metamorphism and anatexis. Intergration of events with published geothermobarometry results indicate that peak metamorphism of 8-10 kbar and 800 °C in the basement gneiss culminated by ca. 56 Ma with the onset of anatexis, and the rocks underwent subsequent isothermal decompression, to < 5 kbar, which ended ca. 52 Ma.

Anatexis in the basement gneiss of Thor-Odin was synchronous with the emplacement at higher structural levels of the 62-52 Ma peraluminous, S-type Ladybird leucogranite suite. Leucosome from Thor-Odin dome and the leucogranites have similar major and trace element chemistry, classifying as peraluminous, S-type granites. In addition, they have overlapping isotopic signatures with $\varepsilon Nd_{(55\ Ma)}$ values of -5.0 to –17.2 for the leucogranites and –9.5 to –23.6 for the leucosome samples. These correlations suggest that at least part of the Ladybird suite likely formed via mid-crustal melting of North American basement rocks dominated by rocks of sedimentary origin.

In the Paleocene, Thor-Odin dome was deeper (up to 6 km) and hotter than adjacent rocks of the Frenchman Cap dome, the northern culmination of the Monashee Complex, indicating that there may be two different structural panels within the complex that were juxtaposed, likely by $F_2$ folding, late in the Paleogene tectonic evolution. A tectonic model for evolution of Thor-Odin dome invokes a ductile shear zone(s) to explain the diachronous timing of the end of deformation, metamorphism and anatexis in the structurally overlying Middle Crustal Zone and in Thor-Odin dome.

# ACKNOWLEDGEMENTS

Many people supported me in countless ways throughout the course of my Ph.D. It would be next to impossible to thank all those who contributed in a variety of different ways to the completion of this thesis. I am truly thankful.

I would like to extend my sincerest thanks to Sharon Carr, who proposed this project and introduced me to the Monashee Mountains. This project was made possible by a research grant from the National Science and Engineering Research Council (NSERC) to Sharon Carr, which supported all aspects of the project including field support and laboratory procedures. I would like to acknowledge OGS scholarships as well as scholarships and travel grants from Carleton University. Sharon is thanked for providing an excellent learning environment as well as superb guidance, input and critical reviews of this thesis. I benefited greatly from discussions in and out of the field with Paul McNeill, Paul Williams, Phil Simony, Richard Brown, and Stefan Kruse. Paul McNeill is especially thanked for proving a digital map of Thor-Odin dome and for always being willing to discuss the various questions that arose through our studies.

Thanks to Nicole Rayner from the SHRIMP lab at the GSC, who helped me with the U-Pb data collection and reduction. Brian Cousens and John Blenkinsop are thanked for access to analytical facilities and for their guiding hands while I learned how to run the TIMS. I received technical support from many people including Peter Jones, Mike Jackson, Pat Hunt, Ron Hartree and Lewis Ling. Their assistance in sample analyses or sample preparation is greatly appreciated.

Fellow graduate students and friends provided excellent intellectual support, scientific discussion and a social haven. Specifically, thanks to Jen Owen for much needed breaks and to Fionnula Devine for being a inspiring office companion.

I would like to sincerely thank my family; their love and support has helped guide me through this adventure. The Alaskan fishing trips every summer, were a much loved break, so thank you Mom and Dad. I would also like to thank Morgan and Barbara Hinchey for their support and love across the miles.

Finally, I would like to thank my husband, John, for all his support, love, kindness, patience and helpful discussions throughout this process. Completing our Ph.D.s has definitely brought us closer together, and I look forward to the future adventures in our lives.

# ORIGINAL CONTRIBUTIONS

This research focuses on further understanding the evolution of the southern Omineca belt through a multi-disciplinary investigation into the geology, geochronology, geochemistry and structure of Thor-Odin dome, Monashee Complex. Research involved five months of fieldwork in the summers of 2002 and 2003, during which time I carried out lithological and structural mapping as well as sampling at a scale of 1:10 000 and 1:5 000. Mapping was done in parts of the following 1:20 000 BC TRIM sheets (North American Datum 1983; UTM zone 11): 82L.060, 82L.050, 82L.040, and 82K.031. These data were compiled with previous results to produce geological maps and a cross section for the southern Canadian Cordillera. Samples were collected for U-Pb geochronology, major and trace element geochemistry, isotopic geochemistry and petrographic studies.

For the geochronologic component of this study, I carried out U-Pb Sensitive High Resolution Ion Microprobe (SHRIMP) analyses on zircon and monazite from six samples. Three samples were of variably deformed anatectic leucosome and were analyzed to constrain the timing of deformation and anatexis. Two samples of cordierite-gedrite rock and one samples of an interlayered quartzite were analyzed to constrain the timing of metamorphism. I performed all stages of sample preparation including crushing, grinding, mineral separation and grain selection, under the supervision of Sharon Carr. Prior to and after SHRIMP analysis, zircon and monazite grains were imaged by backscattered electron (BSE) and cathodoluminescence (CL) at the GSC and at Carleton University. Monazite crystals were imaged by Dr. Mike Jercinovic at the University of Massachusetts using X-ray elemental mapping for yttrium, thorium, uranium and calcium. The CL, BSE and X-ray elemental images were utilized to select analytical sites on the grains. The U/Pb zircon and monazite analyses using the SHRIMP at the Geological Survey of Canada (GSC) in Ottawa were completed under the guidance of Richard Stern, Bill Davis and Nicole Rayner.

An investigation of the geochemical character of selected rocks from the study area was carried out to characterize the peraluminous Ladybird granite suite, basement leucosome and selected basement rocks. These studies evaluated the anatectic nature of the leucosome, the link between peraluminous granites and basement leucosome, and the evolution of the cordierite-gedrite basement rocks. I completed all aspects of sample preparation. I carried out major and some trace element X-ray Fluorescence (XRF) analyses at the University of Ottawa under the supervision of Ron Hartree. Rare earth element and some trace element analyses were obtained by Inductively Coupled Plasma-Mass Spectrometry (ICP-MS) on contract from Geoscience Laboratories and ACME. Whole-rock Rb-Sr and Sm-Nd analyses were carried out at Carleton University under the supervision of Brian Cousens and John Blenkinsop.

The data produced in this study required significant revision of previous models proposed for the tectonic evolution of the region, specifically the extent of ductile basement involved in the Cordilleran orogeny. I formulated a tectonic model in which basement is highly strained and melted in the final stages of the Cordilleran orogenesis.

# METHOD OF PRESENTATION

This thesis is presented as five papers (Chapters 1, 2, 3, 4, and 5), each with a different focus to highlight themes and topics of this research. This format is intended to facilitate the publication of this research; however, it introduces some unavoidable redundancies. My intent when submitting these chapters to scientific journals is to be first author on all papers in co-authorship with Sharon Carr, Paul McNeill and Nicole Rayner on Chapter 1, with Sharon Carr on Chapter 2 and Chapter 3; and, with Sharon Carr and Nicole Rayner on Chapter 4. Chapter 5 is a tectonic synthesis paper co-authored with Sharon Carr. Chapter 6 is a summary of the conclusions from this thesis.

# TABLE OF CONTENTS

CHAPTER 2

**The S-type Ladybird leucogranite suite of southeastern British Columbia: geochemical and isotopic evidence for a genetic link with migmatite formation in North American basement gneiss of the Monashee complex**



CHAPTER 3

**Cordierite-gedrite basement rocks and associated garnet amphibolites of Thor-Odin dome, Monashee complex: protolith composition and implications for the petrogenesis of North American basement rocks**

# LIST OF FIGURES AND MAPS

## FIGURES

## MAPS

# LIST OF TABLES

# LIST OF APPENDICES

# CHAPTER 1

## Paleocene-Eocene high-grade metamorphism, anatexis and deformation in Thor-Odin dome, Monashee complex, southeastern British Columbia


### Abstract

Thor-Odin dome of the Monashee complex, in the southeastern Canadian Cordillera, comprises >1.8 Ga migmatitic basement gneiss with infolds of unconformably overlying supracrustal rocks of the cover sequence, and is part of the deepest exposed structural level in the Omineca belt. Ortho- and paragneiss of the basement contain ubiquitous stromatic leucosome as well as discrete phenocrystic and pegmatitic vein-type leucosome, which are all interpreted to have formed as a result of *in situ* melting in the Paleocene-Eocene. The stromatic leucosome is infolded with the country rock ($F_2$), contains a weakly developed foliation, and has a biotite rich melanosome. The phenocrystic and pegmatitic vein-type leucosome crosscut the stromatic leucosome as well as the transposition foliation ($S_2$). Leucosome contains igneous textures such as euhedral phenocrysts of plagioclase and potassium feldspar with primary albite and carlsbad twins twinning, cumulate textures, and myrmekitic intergrowths of plagioclase and quartz; there is no evidence of alteration of minerals. The major and trace element chemistry of all leucosome types is typical of melts generated by partial melting of the continental crust. The sharply faceted crystal shapes, internal fine-scale oscillatory zoning, and low Th/U ratios of zircon from the leucosome support an igneous source and are typical of zircon that grew in a partial melting environment. The basement gneisses reached peak P-T conditions that are consistent with those required for partial melting in the host gneisses. SHRIMP $^{206}Pb/^{238}U$ ages from zircon range from ca. 56 to 52 Ma and are interpreted to represent a protracted crystallization event of the leucosome. Zircon commonly contains discrete cores that have sharp contacts with the surrounding younger zircon. The $^{207}Pb/^{206}Pb$ ages from cores range from ca. 2.6 to 1.8 Ga. The cores are

interpreted as detrital grains inherited from the host paragneiss. Basement paragneisses are Paleoproterozoic and the basement complex is interpreted as a subsurface continuation of the Canadian Shield. Anatexis was ongoing by ca. 56 Ma, as a result of regional prograde metamorphism, and was coincident, at least in part, with the formation of the penetrative $S_2$ transposition foliation and large recumbent $F_2$ tight to isoclinal folds. Anatexis continued during $F_3$ and $F_4$ folding. Decompression melting continued to ca. 52 Ma and was concomitant with the $D_5$ extensional deformation. Thor-Odin dome, located in the hinterland of the southeastern Canadian Cordillera, experienced high-grade metamorphism, anatexis, penetrative deformation and large scale folding in the Paleocene to Eocene (ca. 56 to 52 Ma).

## 1.1. Introduction

The formation of migmatites has been attributed to several processes, including: a) injection of externally derived magma (Sederholm, 1934; Weber and Barbey, 1986; Barbey et al., 1990); b) partial melting (anatexis) with or without segregation (Mehnert, 1968; Johannes et al., 1995), c) metamorphic differentiation (Robin, 1979; Ashworth and McLellan, 1985); and d) metasomatism (Misch, 1968; Olsen, 1984; 1985). Metamorphic differentiation at subsolidus conditions and partial melting, with or without segregation of initial melts, are widely recognized as the main processes of migmatite formation (Chavagnac et al., 1999). It is commonly believed that the leucosome portions of most migmatites were once components of a partial melt (Johannes et al., 2003).

The Monashee complex in southeastern British Columbia consists of high-grade migmatitic Paleoproterozoic basement rocks and an overlying Paleoproterozoic to Paleozoic cover sequence from part of the deepest exposed structural level in the southern Canadian Cordillera (Fig. 1-1). In this paper, we address the formation of migmatites in the basement rocks of Thor-Odin dome, Monashee complex, to answer several questions: a) did the leucosome form by partial melting (anatexis) of the host gneiss?; b) what is the timing of migmatization?; c) was there more than one migmatite forming event?; and, d) can folded and crosscutting leucosome be used to constrain the timing of deformation? As the Monashee complex contains an important record of the thermal history and deformation style operative during the Late Cretaceous to Eocene construction of the Cordilleran orogen, a study of the migmatites will ideally elucidate the effects of Cordilleran deformation on these rocks.

A combination of field, petrography, geochemistry and geochronology studies were used to demonstrate the anatectic origin of the leucosome, and date the timing of leucosome formation and the structural development of the area. Zircons from three types of leucosome with clear geological relationships from the Thor-Odin dome basement rocks at the Saturday Glacier area were dated using U-Pb SHRIMP (Sensitive High

Resolution Ion Microprobe) methods in order to: a) constrain the age(s) of migmatite formation and thereby constrain the timing of deformation, specifically folding and transposition events; b) test whether there were episodic (several million years) or protracted (Jurassic to Tertiary) periods of melt formation; and, c) evaluate the potential and extent of decompression melting.

## 1.2. Regional geology

The Canadian Cordillera formed as a result of the Paleozoic to Paleogene accretion of fragments of allochthonous and parautochthonous oceanic sequences, continental slivers, volcanic arcs and sedimentary sequences to the western edge of ancestral North America (Monger, 1989). Mesozoic – Paleogene crustal thickening occurred during collision with accreted terranes and westward underthrusting of the North American plate (Fig. 1-1; Monger et al., 1982; Monger, 1989; Gabrielse and Campbell, 1991). By the Middle Jurassic, accreted terranes had begun overriding the pericratonic terranes and Proterozoic and Paleozoic to early Mesozoic platformal sedimentary sequences that had accumulated on the paleomargin of North America (Monger et al., 1982). By the mid-Cretaceous, a 50-60 km thick crustal welt and a foreland basin had formed and during the Cretaceous the Rocky Mountain fold and thrust belt (Foreland belt) formed (Price and Mountjoy, 1970; Coney and Harms, 1984; Brown et al., 1986; Price, 1986). Crustal thickening and burial of the North American sedimentary sequence and overriding terranes resulted in metamorphism and deformation of rocks in the hinterland of the Rocky Mountain fold and thrust belt, termed the Omineca belt (Fig. 1-1; Reesor, 1970; Brown and Read, 1983 and references therein). In the Early Tertiary, southern British Columbia underwent a change from a transpressional to transtensional regime, attributed to changes in far field stresses related to the obliquity of the down-going Kula plate (Lonsdale, 1988; Andronicos et al., 2003). This resulted in Eocene regional extension, and the exhumation of some of the high-grade rocks of the southern Omineca belt via an array of generally north-south striking, brittle and ductile normal faults, which are linked to synchronous

strike-slip fault systems that span the western Cordillera (Ewing, 1981; Tempelman-Kluit and Parkinson, 1986; Brown and Journeay, 1987; Parrish et al., 1988; Struik, 1993; Johnson and Brown 1996 and references therein). In the southern Omineca belt, the lower plates of regional extensional fault systems expose high-grade rocks with relatively young deformation and cooling histories in a Cordilleran metamorphic core complex (Armstrong, 1972; Coney, 1980; Parrish et al., 1988).

The southern Omineca belt is characterized by metamorphic and plutonic rocks and contains structural culminations and belts of high-grade rocks. The Shuswap complex (Fig. 1-1) is defined as a composite metamorphic core complex, bounded on the eastern and western margins by generally north-striking, outward-dipping Eocene normal faults. It is bounded by the 58-50 Ma Columbia River fault (CR) to the east and the 56-45 Ma Okanagan Valley-Eagle River fault system (OV-ER) to the west (Okulitch, 1984; Brown and Journeay, 1987; Parrish et al., 1988; Parkinson, 1992; Bardoux, 1993; Johnson, 1994). The hanging wall rocks of both the CR and the OV-ER faults record older peak metamorphism and cooling (ca. 175 to 135 Ma) and are generally at lower grade than the footwall rocks (Parrish, 1995; Johnson and Brown, 1996). Both the Monashee complex, a basement-cored gneiss complex, and the structurally overlying metasedimentary rocks are contained within the Shuswap complex (Fig 1-1).

The Monashee complex contains two domal culminations, the Thor-Odin and Frenchmen Cap domes, that comprise Paleoproterozoic basement of North American cratonic affinity (Fig. 1-1; Armstrong et al., 1991) complexly infolded with unconformably overlaying Paleoproterozoic to Paleozoic platformal metasedimentary gneisses of the cover sequence (Wheeler, 1965; Reesor and Moore, 1971; Brown, 1980; Crowley, 1997). The dominantly metasedimentary rocks that structurally overlie and surround the Monashee complex have been interpreted as an allochthonous composite thrust sheet termed the Selkirk allochthon (Read and Brown, 1981). The Selkirk allochthon was interpreted to have been transported over the Monashee complex along

the Monashee décollement (MD), a northeast-directed discrete 1-2 km ductile shear zone interpreted as a thrust fault (Fig. 1-1; Brown et al., 1986; Journeay, 1986; Brown et al, 1992; McNicoll and Brown, 1995 and references therein). The MD was correlated with the basal thrust beneath the Rocky Mountain Foreland belt on the basis of balanced cross-sections (Brown et al., 1986) and LITHOPROBE seismic reflection profiles (Cook et al., 1992), thus correlating middle crustal strain in the hinterland with a system of discrete upper crustal faults in the foreland.

Recently authors have questioned the existence of the Monashee décollement (Williams, 1999; Johnston et al., 2000; Spark, 2001; Kuiper, 2003). They have suggested that in Thor-Odin dome in the southern part of the Monashee complex, the MD is not a narrow shear zone of 1-2 km thick as interpreted by Brown et al. (1992). Rather, it is suggested that the rocks show a foreland directed penetrative folding and transposition style of deformation throughout a 4-5 km thickness of crystalline rocks and that there is no structural or lithological break between the Monashee complex and overlying rocks (Williams, 1999; Johnston et al., 2000; Spark, 2001; Kuiper, 2003), leading to the interpretation that the MD does not exist. Recent definitions have defined the MD simply as the boundary between the allochthonous rocks of the Selkirk allochthon and the relatively more autochthonous rocks of the Monashee complex; and that at the latitude of Frenchman cap dome, the lower parts of the Selkirk allochthon structurally above the Monashee complex were deeply buried and mobilized through much of the Cretaceous epoch (Brown and Gibson, in press). For the purpose of this paper, it seems prudent to acknowledge the existence of the MD for Frenchman Cap dome, and to accept the more liberal definition of Brown and Gibson (in press) as the base of the zone of penetrative strain as young as Eocene said to be related to compressional orogenesis. In light of these contentions that the MD is not a discrete structure or does not exist, the transition needs to be reevaluated and implications for models of the tectonic development of the entire region may need to be revised.

Periods of metamorphism, deformation and plutonism occurred within a 120 million year interval in the southern Omineca belt and events have been documented at ca. 175-160, ca. 140, 100-90, 75-60 and 60-55 Ma (Digel et al., 1998; Sevigny et al., 1989, 1990; Scammell, 1993; Parrish, 1995; Vanderhaeghe et al., 1999; Gibson, 2003; Crowley et al., 2003; Reid, 2003; Carr and Simony, in review). Parrish (1995) synthesized known timing of deformation in the southern Omineca belt and suggested that there was a preservation of progressively younger strain and deformation with deeper structural levels, implying progressive incorporation of deeper and more inboard rocks through time. However, recent studies have shown that the relationships between structural level, deformation, and metamorphism are more complicated than this interpretation, and in order to understand the construction of the Omineca belt it is necessary to document these relationships at all structural levels. Metamorphic belts may overprint and crosscut older events. For example, the Cretaceous Cariboo – Monashee – Selkirk metamorphic high transects Middle Jurassic regional metamorphism, while in other locations younger or successions of younger, events may reactivate, overprint and/or partially overlap with older events in a concordant fashion (Digel et al., 1998; Gibson, 2003; Crowley et al., 2003; Reid, 2003; Carr and Simony, in review).

The Monashee complex is of interest as it contains the deepest exposed structural level in the Omineca belt, and hence studies are designed to address the timing of deformation and metamorphism. The rocks of the upper structural levels of Frenchman Cap dome experienced high-grade metamorphism from ca. 80 to 50 Ma; however, a boundary delimiting the base of Eocene Cordilleran deformation has been located at deep structural levels below which Precambrian relationships > 1.8 Ga are preserved (Parrish, 1995; Gibson et al., 1999; Crowley and Parrish, 1999). In contrast, this study confirms that rocks throughout Thor-Odin dome experienced high-grade metamorphism and anatexis during the Paleocene to Eocene (Vanderhaeghe et al., 1999; Norlander et al. 2003; Kuiper, 2003; this study). The panel of rocks that structurally overlies Thor-

Odin dome and in map view surrounds the dome on the southern and western sides is referred to herein as the Middle Crustal Zone (after Carr 1991). It is characterized by Late Cretaceous to Eocene ductile strain, plutonism, and thermal quenching (Carr, 1991). The Middle Crustal Zone rocks were thought to have been carried in the hanging wall of the MD, although this relationship is under reexamination. The boundary between Thor-Odin dome and Middle Crustal Zone rocks occurs on the southwest corner of the dome at Cariboo Alp and has been interpreted as the continuation of the MD (Coleman, 1990; McNicoll and Brown, 1995). Relevant to this study are the rocks of Cariboo Alp, which were deformed and metamorphosed prior to 58 Ma (Coleman, 1990; Carr, 1992), and, Middle Crustal Zone rocks west of the dome at Joss Mountain that were deformed and metamorphosed prior to ca. 70 Ma (Fig. 1-1). The structures at Cariboo Alp were cut by a 58 Ma pegmatite which thereby constrains the timing of the last movement on the MD at this location (Carr, 1991).

Compressional deformation and metamorphism in the Shuswap complex finished slightly before or during extension in the Eocene (Parrish et al., 1988; Carr, 1995). In order to understand the tectonic evolution it has become important to try to document the timing of deformation and metamorphic history at different structural levels within the Omineca belt; this forms the basis of this study of Thor-Odin dome. Although there are some timing constraints on syn- and post-tectonic events, the absolute dating of the timing of the onset of high-grade metamorphism remains elusive (c.f. Foster et al., 2004).

## 1.3. Geology of the Thor-Odin dome

### *1.3.1. Lithology*

The basement rocks of Thor-Odin dome are composed of heterogeneous migmatitic para- and orthogneiss (Fig. 1-2). Basement orthogneiss are dominated by migmatitic, hornblende-biotite-quartzo feldspathic gneiss with a lesser volume of quartz monzonite gneiss. Basement paragneiss comprise: a) heterogeneous migmatitic garnet-sillimanite-

quartzo feldspathic gneiss that are locally rich in cordierite; b) migmatitic cordierite-biotite-quartzo feldspathic gneiss; and c) minor calc-silicates, marbles, and quartzites, and are associated with cordierite-gedrite rocks and amphibolites (Reesor and Moore, 1971; Duncan, 1984). Though lithologically distinct, the basement ortho- and paragneiss are often interlayered at the scale of a few meters, due in large part to transposition by folding, and contacts are further complicated by the abundance of leucosome. Initial U/Pb geochronology studies of zircons from basement orthogneiss yielded crystallization ages of 1934 ± 6 and 1874 ± 21 Ma (Parkinson, 1992). Deposition of the basement paragneiss in Thor-Odin dome likely began by 2.2 Ga, based on a detrital zircon study of a basement paragneiss (Parkinson, 1992), and continued to 1.8 Ga, based on the youngest detrital grains from basement paragneiss (Vanderhaeghe et al., 1999; Kuiper, 2003; this study). The focus of this paper is on basement paragneiss from the Saturday Glacier area in the central part of the Thor-Odin dome (Fig. 1-2 and 3).

The cover rocks comprise a heterogeneous assemblage of metasedimentary rocks that includes quartzites, pelitic schists, marbles, calc-silicates and amphibolites. There have been limited geochronological studies on the cover sequence. A preliminary geochronology detrital zircon study on the basal quartzite of the cover gneiss yielded a similar range of Paleoproterozoic ages as the basement paragneiss, with ages as young as 1825 ± 5 Ma (Kuiper; 2003). There are no constraints on an upper age limit for the cover sequence and the youngest depositional age in Thor-Odin dome is uncertain.

### *1.3.2. Precambrian geological history*

The basement orthogneiss are interpreted to have intruded into the basement paragneiss during the Paleoproterozoic (Parkinson, 1992). Although the homogenous orthogneiss generally have concordant contacts with basement paragneiss, Parkinson (1992) reported local contacts which are intrusive. Exposures of the contact between basement gneisses and the cover sequence show parallelism with gneissosity and penetrative foliation (Spark, 2001). The basal quartzite in contact with basement

gneiss led to the interpretation of a Paleoproterozoic unconformity at the base of the quartzite (Duncan 1982; Parkinson, 1992), although this contact is likely a result of transposition by strain. The details of Precambrian metamorphic and deformation events have been pervasively overprinted by Mesozoic – Eocene Cordilleran deformation and metamorphism. This is in contrast to Frenchman Cap dome which preserves Precambrian metamorphism and deformation at deep structural levels (Crowley and Parrish, 1999).

*1.3.3. Cretaceous – Eocene Cordilleran metamorphic history*

Basement and cover rocks in Thor-Odin dome experienced upper amphibolite to lower granulite facies conditions in the Paleogene at ca. 56 Ma (Hinchey, this study and Chapter 4), and may have reached high grade conditions as early as 75 Ma, on the basis of the age of zircons in leucosome from migmatitic paragneiss at Three Valley gap on the north flank of Thor Odin dome (Parish, 1995; Kuiper, 2003). Throughout the dome, the mineral assemblages are relatively uniform with stable sillimanite-potassium feldspar-melt (Reesor and Moore, 1971). Kyanite and cordierite occur in aluminous basement gneiss, and orthopyroxene occurs in granitic and aluminum-poor basement gneiss (Reesor and Moore, 1971). The rocks of Thor-Odin dome are approximately enclosed within the sillimanite-K feldspar isograd, and rocks of the surrounding Selkirk allochthon are at lower grade with sillimanite-almandine-muscovite assemblages (Reesor and Moore, 1971). U-Pb geochronology studies indicate that metamorphism and penetrative deformation of the Thor-Odin dome basement rocks was ongoing during the Paleogene (Vanderhaeghe et al., 1999; Johnston et al., 2000) at ca. 56 to 52 Ma (this study) based on the ages of anatectic migmatites and metamorphic monazites (Hinchey, Chapter 4).

There is an apparent larger volume of leucosome present in the basement gneiss compared with the cover sequence (Reesor and Moore, 1970; Parkinson, 1992; Norlander et al., 2001). Parkinson (1992), and McNeill and Williams (2003) have therefore argued that migmatization likely predated deposition of the cover sequence. Alternatively, this difference in amount of leucosome may be: a) a result of compositional differences

controlling melt generation, as the cover sequence contains abundant calc-silicate gneiss, quartzites and amphibolites; b) a result of the cover sequence being volumetrically minor relative to basement gneiss (Fig. 1-2 and 1-5); and/or c) that peak P-T conditions attained in the cover sequence may be slightly lower than in the structurally deeper basement gneisses, and thus these rocks may not have experienced pervasive anatexis. Even a small change in peak P-T conditions could change the decompression path and thus the melt reactions that are crossed (see Fig. 1-14). Any of these factors may have controlled the localization of leucosome to certain lithological horizons.

On the northwestern margin of Thor-Odin dome, basement rocks experienced temperatures of ca. 725 °C (Johnston, 1997). Pressure-temperature studies in structurally deeper rocks of the Bearpaw Lake region, in the southwestern part of the dome, indicate that the basement rocks underwent isothermal decompression from the kyanite-potassium feldspar zone ($P > 8$ to 10 kbar) into the sillimanite-cordierite zone ($P < 5$ kbar) at $T \sim 750$ °C, with a maximum temperature of ~ 800 °C (Norlander et al., 2002). The rocks of the Saturday Glacier area of this study are lithologically similar to those of the study of Norlander et al. (2002), are less than 0.5 km structurally deeper and are less than 4 km away (Fig. 1-2 and 1-5). In addition, both areas contain the same peak metamorphic mineral assemblages preserving potassium feldspar-sillimanite-melt in basement paragneiss. Based on complex symplectic textures preserved in basement cordierite-gedrite rocks and amphibolite boudins, Norlander et al. (2002) concluded that the peak regional metamorphic episode occurred in the Tertiary as these textures would not have survived a subsequent metamorphic event. This argument, coupled with the ages of zircon crystallization in leucosome from Thor-Odin dome (Vanderhaeghe et al., 1999; this study) and zircon in leucogranites from structurally higher levels (Carr, 1992; Vanderhaeghe et al., 1999), is consistent with the interpretation that metamorphism coincided with the onset of partial melting. Reaction textures indicate that leucocratic melt interacted with minerals growing in the boudins during decompression (Norlander

et al., 2002), indicating coeval anatexis and decompression. Cooling of Thor-Odin dome occurred in two stages synchronous with the regional extension. The core of dome was affected by rapid cooling from ~700 °C to ~300 °C at ca. 55 to 52 Ma, which was followed by a second cooling event from ~350 °C to ~150 °C at ca. 47-45 Ma based on zircon and monazite U-Pb ages, Ar thermochronology, zircon and apatite fission track ages (Parkinson, 1991; Lorencak et al., 2001; Vanderhaeghe et al., 2003; this study).

At least three styles of leucosome have been documented in Thor-Odin dome. One is folded and concordant with foliation, and two types crosscut the foliation, leading to the initial suggestion of three possible migmatization events (Spark, 2001; McNeill and Williams, 2002). Crosscutting leucosome veins in the basement ortho- and paragneiss have yielded ages of ca. 56 Ma (Vanderhaeghe et al., 1999) and ca. 54 to 52 Ma (this study). This age falls in the range of the ca. 58-55 Ma pegmatitic dykes that crosscut rocks of: a) the cover sequence in Thor-Odin and deformed 62 Ma pegmatite on the southern flank of the dome at Cariboo Alp in rocks structurally above the Monashee complex (Carr, 1992); and, b) the intercalated basement and cover rocks on the northeastern flank at Blanket Mountain (Johnston et al., 2000). These ages are a few million years older than those reported by Kuiper (2003) including: a) zircon lower intercept ages and monazite ages of ca. 52 Ma from a crosscutting aplitic dyke at Blanket Mountain area, and b) a zircon age from a crosscutting aplitic dyke (leucosome) from the core of the dome, near Frigg Glacier, of 48 Ma with a large error of 11 Ma. Kuiper (2003) interpreted these young ages to reflect a hydrothermal event rather than a magmatic crystallization event, largely on the basis of hydrogen and oxygen isotopic studies. However, in light of SHRIMP and geochemical data, we question this interpretation. These ages are reinterpreted as representing the last stages of a protracted metamorphic and anatectic event (see discussion below). There are two other leucosome and pegmatite dating locales in the region. At Joss Mountain, to the northwest and structurally higher than the basement rocks, a 73 Ma pegmatite was deformed by $F_3$ (Johnston et al., 2000)

and structures are crosscut by a 70 Ma post tectonic pegmatite (Kuiper, 2003), thus bracketing the age of the final stages of penetrative deformation at this location. At Three Valley Gap, leucosome formation was ca. 73 Ma (Kuiper, 2003). Figure 1-4 shows a simplified tectonostratigraphic column through Thor-Odin dome, showing the relative structural relations of previously dated rocks in the area and in this study.

*1.3.4. Structural evolution of Thor-Odin dome*

Basement and cover gneiss are characterized by at least four folding events and the map-pattern distribution of basement and cover controlled by large-scale fold interference patterns (Fig. 1-2). These superposed folds produced interference patterns at all scales and all structural levels, and have been interpreted as the principal cause of doming and crustal thickening in the dome (Read, 1980; Duncan, 1982). Figure 1-5 highlights the complex fold interference patterns observed across the dome; however, the cross section is oblique to the profile plane of the fold thereby skewing fold forms. The dominant foliation dips to the west on the western margin of the dome and to the east on the eastern margin, and it wraps around the southern end producing outward dips (Reesor and Moore, 1971). $F_1$ folds are preserved at outcrop scale, and represent either: a) relict Precambrian deformation; or, b) formation during progressive $D_{1-2}$ thickening and tectonic burial. Kilometre-scale, northeast verging, isoclinal $F_2$ fold nappes infold the cover sequence with the underlying basement gneisses (Reesor and Moore, 1971; Read, 1979, 1980; McNeill and Williams, 2004). The $S_2$ transposition foliation is the dominant planar fabric throughout the 4-5 km thick exposed section of Thor-Odin dome and is defined by domainal schistosity, compositional banding and gneissic foliation. $F_3$ folds overprinted earlier folds and commonly lack a well-developed axial planar foliation (Johnston, 1997). $F_4$ folds are open, upright folds that overprint earlier generations of folds. The Pingston fold (Fig. 1-2) is an isoclinal $F_2$ fold that spans the length (~8 km) of the eastern margin of the dome, and it is outlined on the map by the basal quartzite unit (Reesor and Moore, 1971; Spark and Williams, 1996) and its map pattern is controlled

by the superposition of $F_2$ through $F_4$ folds (Fig. 1-5). The entire domal culmination represents a large $F_2$-$F_4$ interference structure containing reoriented and transposed $F_2$ nappes (Fig. 1-5).

The MD has been interpreted to mark the western and southern boundary of Thor-Odin dome from the overlying Selkirk Allochthon. In the Cariboo Alp region, it is interpreted as an imbricated, crustal-scale, compressional shear zone (McNicoll and Brown, 1995). Final thrust movement on the MD occurred in the latest Paleocene and stopped moving by ca. 58 Ma (Carr, 1992). $D_5$ reactivation of foliation and local development of shear bands marked the onset of extension when the rocks were still hot and behaving ductilely (Brown, 1980; Read and Brown, 1981; Journeay, 1986; Carr, 1992; Brown et al. 1992; Johnston et al., 2000; McNeill and Williams; 2003). $D_5$ was progressive, as the rocks cooled, to $D_6$ brittle, extensional faulting. $D_5$ and $D_6$ deformation includes the ductile-brittle CR and OV-ER faults and their reactivation. Widespread intrusion of Eocene pegmatites and generally north-south trending lamprophyre dykes occurred in the Monashee complex during extension (Lane, 1984; Johnson, 1994; Adams et al., 2005). Brittle faulting was preserved in Thor-Odin dome as large steeply dipping north-northwest-striking faults, such as the Three Valley normal fault (Johnson, 1994; Johnston, 1997) and Victor Creek fault (Read, 1980; Kruse and Williams, 2004).

## 1.4. Leucosome at Saturday Glacier

### *1.4.1. Field characteristics and petrography*

Leucosome occurs pervasively throughout the basement and cover gneisses in Thor-Odin dome (Reesor and Moore, 1970; Spark, 2001; McNeill and Williams, 2003). The Saturday Glacier area is located on the western flank of the dome and mapping encompasses approximately a one square kilometre area (Fig. 1-2 and 1-3) on the overturned limb of an northeasterly-verging, steeply dipping $F_2$ isocline (Fig. 1-5). This area is a structurally deep exposure of basement migmatitic paragneiss, and contains

15-50 % volume leucosome. The excellent exposure on recently deglaciated slopes and the extensive variety of leucosome make this area ideal to study leucosome formation. Lithological units can be traced along strike for at least 5 km to the southeast. The dominant lithologies are the compositionally heterogeneous garnet-sillimanite-quartzo feldspathic paragneiss, interlayered at the scale of tens of meters with a homogenous cordierite-biotite-quartzo feldspathic paragneiss with accessory millimeter-scale garnets and sillimanite (less than 1%). This package of pelitic gneiss strikes southeast and dip steeply at ~80° to the west. The garnet-sillimanite-quartzo feldspathic paragneiss contains 15-20% leucosome, whereas the cordierite-biotite-quartzo feldspathic paragneiss contains 35-50% leucosome, and is interpreted to largely represent mesosome or restite (Fig. 1-6). The gneisses are part of a package of metasedimentary gneiss that includes minor quartzites, calc-silicate gneisses, garnet-gedrite-cordierite rocks, and garnet amphibolites. Various styles of leucosome structures are identified within the cordierite-biotite-quartzo feldspathic gneiss, and the relative timing of folds and leucosome formation are apparent. As this study aims to constrain the age of structures within the paragneiss of Thor-Odin dome, field relations constraining the relative timing of structures and leucosome are critical. Migmatite terminology and definitions are from Ashworth (1985), modified from Mehnert (1968). There are three main styles of leucosome: folded stromatic leucosome, phenocrystic and pegmatitic leucosome.

#### 1.4.1.1. Folded stromatic leucosome

The dominant type of leucosome is stromatic (layered) and forms part of a stockwork of interconnected veinlets ranging from 2 mm to 25 cm in thickness, exhibiting a well developed 0.2-0.5 cm wide melanosome on their margin. The folded stromatic leucosome parallels the main transposition foliation ($S_2$), which dips steeply westwards at 82°, and contains a foliation defined by the alignment of biotite grains (Fig. 1-6a). The leucosome is tight to isoclinally folded at the centimeter scale (Fig. 1-7a). Folds defined by leucosome have the same plunge and vergence as $F_2$ folds in the area, and are thus

interpreted as $F_2$ folds. The melt is interpreted to have formed within the foliation, and was mobilized along foliation surfaces feeding into veinlets and veins. Leucosome modal mineralogy is plagioclase ($An_{34}$, 25%), potassium feldspar (perthitic orthoclase, 30%), quartz (42%) and biotite (3%), with accessory phases of apatite, ilmenite and rutile (Fig. 1-7a). The quartz, plagioclase and potassium feldspar grains primarily occur as subhedral to anhedral crystals and commonly contain abundant inclusions of smaller biotite grains and iron-titanium oxides. Quartz has undulose extinction, and plagioclase has flame lamellae. Zircon occurs primarily as inclusions in feldspar and quartz. The melanosome is dominantly composed of coarse-grained biotite.

On the basis of the structural relationships, the leucosome associated with this style of migmatite is interpreted to have formed during $F_2$ folding and represents the oldest leucosome in the outcrop. This type of leucosome occurs throughout the basement gneisses in Thor-Odin dome (Reesor and Moore, 1976; Spark, 2001); however, since leucosome production and deformation may be diachronous at different structural levels then age relationships may vary with structural depth. Nevertheless, the folded stromatic leucosome is considered to be typical of the oldest leucosome type in Thor-Odin dome and certainly within the immediate area of Saturday Glacier.

#### 1.4.1.2. Phenocrystic vein leucosome

The second type of migmatite is of vein (phlebitic) structure and contains leucosome that is coarse grained and granitic in composition. This leucosome is referred to herein as the phenocrystic vein type due to the presence of phenocrysts of potassium feldspar, plagioclase and biotite. It is not folded, does not contain a foliation, and crosscuts both the main transposition foliation and the folded stromatic leucosome (Fig. 1-6b). The planar phenocrystic vein leucosome is exposed for 150 m along a strike of 174° and a dip of 88°. Leucosome thickness varies from 8 to 15 cm, while the melanosome thickness is variable along the length of the leucosome, ranging from 0.1 to 0.4 cm. The melanosome parallels the leucosome and is dominated by aggregates of coarse biotite crystals. The

phenocrystic type of leucosome has a bimodal grain size distribution; the equigranular groundmass is dominated by 0.5-1 cm quartz, plagioclase, potassium feldspar and biotite crystals and surrounds large, 1.5-2 cm, phenocrysts of potassium feldspar, plagioclase and biotite. The modal mineralogy of the leucosome is plagioclase ($An_{32}$, 18%), potassium feldspar (perthitic orthoclase; 30%), quartz (35%) and biotite (15%), with minor muscovite (2%) and accessory phases of ilmenite, rutile and zircon. The quartz, plagioclase, and potassium feldspar grains occur primarily as euhedral to subhedral to crystals. Myrmekitic intergrowths of plagioclase and quartz are common, as are primary igneous albite and carlsbad twins in plagioclase and potassium feldspar (Fig. 1-7b). On the basis of its crosscutting relationship with transposition foliation and specifically the folded stromatic leucosome, the phenocrystic vein leucosome is interpreted to be younger than the folded stromatic leucosome and $F_2$ folding.

1.4.1.3. Pegmatitic vein type

The third type of migmatite observed in outcrop is the pegmatitic vein type. The associated leucosome is pegmatitic, granitic leucosome. This leucosome type trends 232°/84° for 25 meters, is undeformed, and crosscuts both stromatic and phenocrystic leucosome types in this outcrop, as well as the main transposition foliation (Fig. 1-6c). The leucosome does not have an associated melanosome, and occurs as veins that range in thickness from 10 to 15 cm. In hand sample, the leucosome contains 0.5-2 cm intergrowths of potassium feldspar, plagioclase, quartz, and biotite. In thin section, large crystals of potassium feldspar surround euhedral to subhedral grains of quartz, plagioclase, and biotite (Fig. 1-7c). The modal mineralogy comprises plagioclase ($An_{14}$, 10%), quartz (38%), potassium feldspar (perthitic orthoclase; 45%), biotite (5%), and muscovite (2%) with accessory phases of ilmenite and rutile. In thin section, abundant primary igneous textures are preserved, including euhedral grains, and primary albite and carlsbad twinning in plagioclase and potassium feldspar. There is no evidence of any deformation features or microstructures.

On the basis of its relationship with structures, specifically its crosscutting relationship with the folded stromatic and phenocrystic leucosome, the pegmatitic vein leucosome is interpreted to represent the youngest generation of leucosome. The lack of chilled margins associated with this leucosome indicates that the host rocks were still hot during formation. Leucosome production would have ended by the time the dome experienced brittle ($D_6$) deformation, and; therefore, this type of leucosome must have formed pre-$D_6$.

*1.4.2. Whole rock major and trace element geochemistry*

Major element, recalculated to an anhydrous total of 100%, and trace element compositions of 13 samples from all three types of leucosome were analyzed. Sample description and locations are listed in Table 1-1. Representative compositions are presented in Table 1-2 and analytical details are given in Appendix A.1. As there are no distinguishable compositional differences between the leucosome types, all the leucosome samples are treated as one group.

The leucosome samples show little variation in most major element compositions. $SiO_2$ contents range from 71 to 76 wt.% and $Al_2O_3$ ranges from 12 to 15 wt.%. Figure 1-8 shows the CIPW normative proportions of quartz, orthoclase, and albite for the leucosome samples. In this diagram, the orthoclase contents might be slightly overestimated due to mica content of the samples. However, this is a useful petrogenetic tool for estimating the conditions of melt formation in leucogranite compositions with > 90% felsic components (Inger and Harris; 1993). All the samples satisfy this condition. Leucosome samples trend away from the minimum melt composition characteristic of water-saturated phase relations suggesting that they formed via water-undersaturated melting reactions characteristic of dehydration melting (Johannes and Holts, 1990). The CIPW normative proportions (Table 1-2) show that the leucosome samples have a granitic compositions *sensu stricto*, and that all the samples are peraluminous (molar A/CNK >1).

The trace element composition of these rocks exhibit large ranges in the low field strength elements (as defined by Saunders et al., 1980), of Ba (16-2147 ppm) and Sr (14-383 ppm). Most trace element concentrations exhibit a slight decrease in concentration with increasing $SiO_2$ content. The chondrite-normalized rare earth element (REE) patterns of the leucosome samples are fractionated with $La_{(N)}/Yb_{(N)}$ ranging between 1.5 and 50 times chondrite (Fig. 1-9a). In general, the higher $SiO_2$ compositions exhibit less fractionation. The samples show a range in Eu from a slightly positive to strongly negative anomaly. On an extended trace element primitive-mantle normalized spider diagram, the rocks exhibit large enrichments in Ce, Rb, Ba, light REEs, Sr and Zr relative to primitive mantle (Fig. 1-9b), and there are also pronounced negative Nb-Ta and Ti anomalies.

The leucosome REE and extended trace element patterns show similar trends and concentrations of elements when compared to the bulk continental crust and average granite composition (Fig. 1-9). Comparing the leucosome with the host gneiss, both have similar trends and concentrations of elements. Minor differences in the trace element concentrations between the host basement gneiss and the leucosome samples likely reflect fractionation of elements and preferential melt migration of the LFSE relative to the HFSE and REE during partial melting (Sawyer, 1998). The overall trend of decreasing trace element concentrations with increasing silica contents likely reflects the depletion of trace elements in the host gneisses as partial melting continued. The overall geochemical signature, outlined above, is consistent with magmas that formed via partial melting of the continental crust.

### *1.4.3. U-Pb geochronology*

Zircon from a sample of each of the three leucosome types were imaged by backscattered electron (BSE) and cathodoluminescence (CL) on the Electron Microprobe, prior to U-Pb isotopic analysis using the SHRIMP. Data are presented in Table 1-3 and Figure 1-10, and errors are reported as $1\sigma$ in the table. In Figure 1-11, a weighted mean

diagram, errors are reported as 2σ. Analytical procedures are described in Appendix A.1. The $^{206}Pb/^{238}U$ ages are reported for zircon younger than 800 Ma, since the low abundance of $^{207}Pb$ in young zircon leads to very large uncertainties in the $^{207}Pb/^{235}U$ and $^{207}Pb/^{206}Pb$ ages of young grains. $^{207}Pb/^{206}Pb$ ages are reported for zircon older than 800 Ma. Each analyzed sample is described in detail below.

Some features are consistent in the CL and BSE images of zircons from all the samples (Fig. 1-10). Most zircon grains have domains with fine-scale oscillatory zoning that are free of inclusions, have well formed crystal faces, and contain cores (see Fig. 1-10a, grain 38, 41, 28). The inclusion free, fine-scale oscillatory zoned grains and parts of grains, excluding the cores, are typical morphology of magmatic zircon (Corfu et al., 2003) and are interpreted to have grown in contact with melt related to the crystallization of the leucosome, and are referred to as igneous or magmatic zircon. Many of the zircons contain a prominent oscillatory zoned core that is surrounded by a sugary textured zone filled with inclusions dominantly comprising iron titanium oxides (see Fig. 1-10a, grain 38, 41, 28). Where this zone is present, it is commonly rimmed by a 2-10 μm layer that appears bright in CL and dark in BSE, interpreted to result from depletion in the REE and U. This zone is interpreted to represent an alteration or resorption front, attributed to magmatic processes associated with the crystallization of the leucosome, and the cores are interpreted as relict grains inherited from the host paragneiss. The relict cores show variation in internal structures, dominated by oscillatory zoning, although some cores show sector zoning or are homogeneous without visible zoning.

#### 1.4.3.1. Folded stromatic leucosome (AH-02-26)

The zircon population in sample AH-02-26 is dominated by euhedral to subhedral grains, varying from 100 to 250 μm in length. Prominent turbid, sugary textured cores are visible in most grains microscopically. Grain shapes vary but are dominated by tetragonal prisms modified by pyramids, with aspect ratios of 3:1. A total of seventeen grains from this sample, varying in shape and internal structure, were analyzed (Table 1-3).

Representative grains are shown in Figure 1-10a. The magmatic zircons have a weighted mean $^{206}Pb/^{238}U$ age of 55.5 ± 0.6 Ma (2σ error, n=13) with a mean-square of weighted deviates (MSWD) of 1.5. The Th/U ratios for the grains vary from 0.0029 to 0.0079 (Table 1-3). The CL images show that most zircons contain a prominent oscillatory zoned relict core that is surrounded by a zone that has a sugary texture and contains inclusions (Fig. 1-10a). The cores have variable $^{207}Pb/^{206}Pb$ ages from 2307 ± 15 (1σ) to 1856 ± 12 (1σ; Table 1-3), and have Th/U ratios varying from 0.21 to 0.40.

1.4.3.2. Phenocrystic vein leucosome (AH-02-27)

The zircon population in sample AH-02-27 is dominated by euhedral to subhedral, equant grains. Cores are apparent in CL and BSE images. Representative grains are shown in Figure 1-10b. Eight zircon grains from this sample, varying in shape and internal structure, were analyzed (Table 1-3). The magmatic zircon have a weighted mean $^{206}Pb/^{238}U$ age of 54.2 ± 0.8 Ma (2σ error, n=4, MSWD = 4.5; Table 1-3). The Th/U ratios for these grains vary from 0.018 to 0.02. The cores show a range of internal structures in CL images, including oscillatory zoning and complex sector zoning (Fig. 1-10b). The limited amount of magmatic zircon growth observed on some cores is believed to be a result of either: a) the amount of time the inherited core was in contact with the melt; and/or b) the zirconium saturation of the melt, and thus able to grow new zircon, the implications of which are discussed in the section on the origin of leucosome. The $^{207}Pb/^{206}Pb$ ages for the cores vary from 2564 ± 6 (1σ) to the youngest age of 1862 ± 12 (1σ; Table 1-3). The Th/U ratios for the cores vary from 0.03 to 0.87.

1.4.3.3. Pegmatitic vein leucosome (AH-02-29)

The sample AH-02-29 contains a significantly less abundant zircon yield in relation to the other geochronology samples. Most grains are equant and subhedral to anhedral in shape. Under plane-polarized light some grains are clear and colourless, while others contain abundant inclusions and are turbid in appearance. In BSE and CL, some grains

are homogenous with no apparent cores or rims, some have fine-scale oscillatory zoning, and others have a patchy appearance (Fig. 1-10c). Crystals with cores are less prevalent relative to the other samples. Eleven grains from this sample were analyzed and results show that most grains are Precambrian zircons inherited from the host gneiss. Only two grains have Eocene ages (Fig. 1-10c). One is a homogenous crystal with a $^{206}Pb/^{238}U$ age of 52.5 ± 1 (1σ error; Fig. 1-10c grain 2); the SHRIMP analysis is located in the center of the crystal. The second grain has a $^{206}Pb/^{238}U$ age of 54.7 ± 4 Ma (1σ error; Fig. 1-10c, grain 33; Table 1-3). The inherited grains (n= 9) have $^{207}Pb/^{206}Pb$ ages ranging from 2280 ± 12 Ma to 1869 ± 26 Ma (1σ; Table 1-3), with Th/U ratios varying from 0.43 to 1.11. The Eocene ages are interpreted as the crystallization age of the leucosome. All leucosome types contain xenocrysts; however, zircons from the structurally youngest leucosome have the lowest proportion of Eocene ages representing crystallization of the leucosome. This is consistent with other studies of the structurally youngest leucosome, which contain a large detrital population (Oliver et al., 1999). This may reflect either: a) rapid deformation-induced melt extraction from the protolith which would inhibit zircon dissolution from the host rocks and consequently limit growth of new zircon; b) rapid cooling of the rock which would limit the amount of time for new zircon growth; and/or c) the chemistry of the last stages of the melt, which due to small melt volumes may result in rapid Zr saturation inhibiting further dissolution of host-rock zircon (Watson, 1996; Oliver et al., 1999).

#### 1.4.3.4. Interpretation of the geochronology data

The Paleocene-Eocene ages are interpreted as the crystallization age of the leucosome. Statistically, the young ages, that is those that range from ca. 56 to 52 Ma, from all three leucosome samples reflect one age population. When taken as a group, all of the magmatic zircon have a weighted mean $^{206}Pb/^{238}U$ age of 55.1 ± 0.6 Ma (2 σ error, n = 19, MSWD = 1.9 (Fig. 1-11; Table 1-3). It is clear from the young ages and the cross-cutting relationships that leucosome formation and crystallization was an ongoing,

complex process, which occurred over the course of a few million years. Although the stromatic leucosome is likely slightly older than the others, the difference in age is too small to be accurately determined with the number of analysis in hand. Further analysis would be needed to statistically separate the slightly younger zircon population from that of the other samples. This is further complicated by the limited amount of magmatic zircon growth in the cross-cutting pegmatitic leucosome, and the fact that younger leucosome may entrain zircon crystals from slightly older leucosome. For these reasons, the crystallization age of all of the leucosome is interpreted as being ongoing from ca. 56 to 52 Ma. This argument is supported by the apparent lack of fine-scale oscillatory zoned, inclusion free zircon growth, in the BSE and CL images of zircon from the adjacent host paragneiss and surrounding gneiss (Fig. 1-12). Therefore we are confident that the young ages are in fact related to growth of zircon in contact with melt during the crystallization of the respective leucosome types. This interpretation of the timing of crystallization is also supported by previous geochronological studies of the Monashee complex where most authors interpret the young zircon as magmatic in origin based on morphology of the zircon (Vanderhaeghe et al., 1998; Vanderhaeghe et al., 1999; Crowley et al., 2001; Norlander et al., 2002).

## 1.5. Discussion

### *1.5.1. Origin of the leucosome*

There are a number of lines of evidence in support of an igneous nature and anatectic origin for the leucosome in the Saturday Glacier area. The thin-section petrological evidence for an igneous source for leucosome includes the following: euhedral grains, primary twinning in plagioclase and potassium feldspar, abundant phenocrysts, cumulate textures, myrmekitic intergrowths of plagioclase and quartz, a lack of microstructures, and a lack of alteration. The well developed crystal faces on plagioclase, potassium feldspar, and quartz supports the formation of leucosome from a melt and not solid state

processes (Vernon and Collins, 1988). This petrology supports the conclusion that the leucosome was components of a melt and either reflects injection of externally derived magmas or partial melting of the host gneiss.

If the leucosome represented an injection of foreign magma along foliation planes, there would be no expected structural, geochemical or isotopic relationship between the leucosome and the country rocks. The fact that leucosome is both infolded with and crosscuts the host gneiss supports a relationship between deformation and anatexis. In addition, the leucosome is constrained to specific lithological layers which are more pelitic, consistent with an anatectic source (Fig. 1-3). In addition, the major and trace element chemistry is typical of peraluminous, S-type granites (Fig. 1-9), consistent with partial melting of the host paragneiss. The Sr and Nd isotopic composition of the leucosome and host gneiss signatures overlap. The Sr and Nd isotopic composition of the leucosome and host gneiss overlap consistent with the production of leucosome by melting of gneiss in the region (Hinchey and Carr, 2003). In addition, the biotite-rich layer along the edges of the stromatic leucosome (i.e. the melanosome), would not have formed if the melt was externally derived and had been injected (Chavagnac et al., 1999). This evidence supports the formation of leucosome by partial melting of the host gneiss.

Additional field evidence also supports *in situ* melting. Field relationships show leucosome occurs parallel to the foliation and in interconnected veinlets and veins (Fig. 1-6). The melt is interpreted to have formed parallel to the foliation and in low strain areas, was mobilized along foliation surfaces and fed into veinlets and veins. The formation of stromatic leucosome was synchronous with $F_2$ folding throughout the basement rocks of Thor-Odin dome (Reesor and Moore, 1975; Parkinson, 1991; Spark, 2001; McNeill and Williams, 2003). In addition, the consistent amount of melanosome relative to leucosome, and the coarser grain size of the leucosome are consistent with leucosome formation by *in situ* partial melting (Oliver et al., 1999). The collection site of the leucosome as small veins that tend to pinch and swell along strike indicates that host gneisses were likely at

peak P-T conditions, supporting *in situ* partial melting.

The production of melt via dehydration reactions is supported by petrology and P-T conditions. The peak P-T conditions for the basement paragneiss in the southwest part of Thor-Odin dome were 8-10 kbar and 800 °C (Norlander et al., 2002). These P-T conditions were high enough to initiate melting of the basement gneisses in Thor-Odin dome (Fig. 1-14). The rocks of Saturday Glacier are characterized by the metamorphic assemblage of sillimanite + potassium feldspar + melt (Reesor and Moore, 1971), and they underwent near isothermal decompression and dehydration melting (Fig. 1-14; Norlander et al., 2002; this study). Melt may have been produced by several melt generating reactions as shown on Fig. 1-14 and including: Ms + Pl + Qtz = Bt + Kfs + Sil + melt; Bt + Ab + Sil + Qtz = Grt + Kfs + melt; and Bt + Sil = Grt + Crd + melt (Spear et al., 1999; Norlander et al., 2002). The presence of cordierite, millimeter-scale garnets and minor sillimanite, less than 1%, in the host gneiss support the involvement of these minerals in the melt-producing reactions. The P-T conditions are consistent with field, petrographic and geochemical evidence supporting an interpretation of *in situ* anatexis.

The zircon morphology also supports an anatectic, igneous origin for the leucosome. The external morphology with sharp facets and internal fine-scale oscillatory zoning of the crystals all support an igneous source for the zircons. The young zircon has Th/U ratios between 0.0018 and 0.0079, typical for zircon grown in a partial melting environment (Cornell et al. 1999), further supporting a magmatic source. Considering all the evidence stated above, there is sufficient reason to conclude that the leucosome is anatectic in origin and that the leucosome formed from ca. 56 Ma to 52 Ma. The onset of anatexis occurred at, or near, thermal peak metamorphic conditions and melting continued during isothermal decompression.

### *1.5.2. Implications of anatectic origin of leucosome*

The interpretation of ca. 56 to 52 Ma zircon crystallization as magmatic in origin and being related to anatexis is in disagreement with Kuiper's (2003) interpretation

suggesting that the ca. 56 Ma U-Pb ages of zircons reflected hydrothermal growth of zircon in a meteoric fluid. Kuiper's (2003) arguments were based in large part on whole rock oxygen and hydrogen isotope studies and a reinterpretation of disturbed hornblende $^{40}Ar/^{39}Ar$ data of Spark (2001) which range from ca. 118 to 51 Ma. Kuiper (2003) observed that samples with Ar plateau and near-plateau dates younger than 75 - 70 Ma experienced the most whole-rock $O^{18}$ and hornblende D depletions. This led to the conclusion that the older 75 - 70 Ma less depleted dates represented cooling ages and that the Eocene-Paleocene monazite and zircon ages likely reflect growth in a meteoric fluid (Kuiper, 2003). It should be noted that problems can arise when using whole rock isotopic studies to evaluate possible hydrothermal zircon growth (Poitrasson et al., 2002). Ideally oxygen and hydrogen isotopes should be measured on the zircon grains in order to ascertain whether the isotopic signature of a bulk rock or a particular mineral analysis is related to zircon crystallization or overgrowth (Poitrasson et al., 2002). In addition, the extensive brittle faulting in Thor-Odin associated with extension ($D_6$) may have allowed local access of fluids that disturbed the Ar and O systematics.

If extensive meteoric fluids had interacted with the rocks after crystallization of the migmatites between 1800 and 56 Ma as Kuiper (2003) has suggested, then likely the rare earth element patterns should show an enrichment of heavy rare earth elements (HREE) relative to light rare earth elements (LREE), and a negative Ce anomaly, as Ce oxidizes in water and changes from $Ce^{+3}$ to $Ce^{+4}$ (Rollinson, 1993). Carbonate rich fluids are generally required to dissolve metamict zircon (Sinha et al., 1992). If meteoric fluids in Thor-Odin dome were carbonate-rich, then the overall chemical signature would likely be depleted in the REE, and the trace element patterns would reflect a slight depletion in typically immobile elements such as Zr, REE, Y, Hf, Nb, and Ta, and a depletion in typically mobile elements such as K, Rb, Sr and Ba. None of these features is observed in the major and trace element chemistry of the leucosome (Fig. 1-8 and 1-9). The trace element patterns are typical of unaltered granitic rocks (Fig. 1-9). In addition, leucosome

contains twinned and zoned plagioclase and potassium feldspar, myrmekite intergrowth, and euhedral grains of quartz, plagioclase and potassium feldspar, all indicating limited secondary fluid alteration of these rocks (Fig. 1-7).

The well-preserved, faceted morphology of the zircons with fine-scale oscillatory zoning indicates that the grains have not been extensively altered by secondary fluids and/or previous melting events (see Corfu et al., 2003). The zircon cores do not retain any systematic zircon growth ages that may reflect an earlier igneous or anatectic event (Fig. 1-13). There is no geochronological evidence that the alterations such as the turbid, sugary textured zone rich in inclusions and the irregular shape of the cores cannot be explained by processes associated with the abrasion during deposition and diagenesis, Precambrian metamorphism and/or alteration during the ca. 56 Ma anatectic event. There is little evidence for a pre-1.8 Ga migmatization event in this area. These lines of evidence do not support Kuiper's (2003) interpretation that the leucosome production in Thor-Odin dome was dominantly an Early Paleoproterozoic event and that Paleogene zircon growth and/or ages reflects a young meteoric fluid event.

Kuiper's (2003) geochronological data from leucosome are re-evaluated in light of these arguments. Most of the data are from U-Pb TIMS analyses, and fall on a discordia chord with a Precambrian upper intercept and a Paleogene lower intercept. In our reinterpretation the lower intercept is taken to represent the zircon crystallization age. Data sets from leucosome that are affected by this reinterpretation are the following. Samples from basement orthogneiss to the north of this study area, near Blanket Mountain, from a pegmatite (leucosome) in a boudin neck on the limb of an $F_1/F_2$ fold (sample RB-1-93) and a crosscutting aplitic vein (leucosome; sample S298-177), likely have crystallization ages of 51.8 ± 0.7 Ma and 52.7 ± 0.6 Ma, respectively (data from Kuiper, 2003). The sample of crosscutting aplitic (leucosome) dyke (sample S298-213) from the deepest structural levels in the dome (Frigg Glacier area), east of the study area, is 48 ± 11 Ma (data from Kuiper, 2003). All data are consistent with an interpretation of

Paleocene-Eocene metamorphism in rocks of Thor-Odin dome culminating in a ca. 56 Ma protracted anatectic event that lasted to ca. 52 Ma.

*1.5.3. Significance of Paleoproterozoic detrital zircons*

The xenocrystic zircon cores in the leucosome samples range in age from 2564 ± 6 Ma to 1856 ± 12 Ma (Fig. 1-13). The cores are interpreted as relict detrital grains inherited from the host gneiss. The range in ages and high Th/U ratios indicate that the host gneiss is likely of sedimentary provenance. Zircons from the paragneiss were likely incorporated into the leucosome and provided a nucleation site for Paleocene-Eocene magmatic zircon growth during anatexis. The cores do not preserve any systematic overgrowths or ages that may reflect an earlier migmatization event and therefore there is no evidence for a Precambrian anatectic event in this area.

The ages of the inherited cores overlap with those of detrital grains in basement paragneiss from other studies. A sample from the southeast flank of Thor-Odin dome has U-Pb zircon ages that range from ca. 2160 to 1960 Ma and has a Nd model age of 2.3 Ga (Parkinson, 1991). Inherited cores in leucosome samples from the southern flank of Thor-Odin dome and structurally higher than the present study (Vanderhaeghe et al., 1999), have discordant $^{207}Pb/^{206}Pb$ ages as young as 1.6 Ga and concordant ages as young as 1815 Ma. The youngest Precambrian age from this study is a ca. 1860 Ma crystal that does not contain an older core. The basement paragneiss are Paleoproterozoic in age and deposition continued until at least 1.8 Ga. Basement rocks are interpreted to be age equivalents with those of the Canadian Shield and this is consistent with the interpretation that Thor-Odin dome is an exposure of North American basement rocks (Armstrong et al., 1991).

*1.5.4. Timing of deformation and anatexis in Thor-Odin dome*

The relative timing of crystallization of the various leucosome types with respect to structures allows the placement of timing constraints on the deformational history

of Thor-Odin dome. Since the ca. 56 Ma sample of folded stromatic leucosome is interpreted to have been folded by $F_2$, then $F_2$ must have been forming by ca. 56 Ma. Although we have no direct constraints on the timing of the onset of metamorphism in Thor-Odin dome, it is likely that it did not reach high-grade conditions until late in the Cordilleran orogeny, likely during the late Cretaceous.

The pegmatitic vein leucosome with zircon as young as ca. 52 Ma crosscuts all rock units, folding, and other leucosome types. This ca. 52 Ma is interpreted to mark the latest stages of decompression melting, and was synchronous with the exhumation and denudation of the dome, via extension and erosion. Decompression melting likely involved the reaction Bt + Sil = Grt + Crd + L and this reaction is supported by the presence of garnet and cordierite in the host gneiss of the leucosome. $F_3$ and $F_4$ folds are not preserved in the immediate area; however, the 52 Ma leucosome is interpreted to post-date this deformation and predate $D_6$, brittle extension. This is based on the following arguments: a) isobaric decompression melting was followed by isothermal cooling in a short time span; the dome cooled to < 300 °C by ca. 48 Ma (Fig. 1-14; Vanderhaeghe et al., 2003). b) Compression tectonics had likely ended by ca. 55 Ma, based on the timing constraints on the onset of decompression (Vanderhaeghe et al., 1999; Norlander et al., 2002; this study; Fig. 1-14). c) Ductile deformation likely ended shortly after 52 Ma. This interpretation is consistent with monazite ages as young as ca. 52 Ma (Hinchey, Chapter 4), ca. 50 Ma zircon fission track ages indicating cooling below 350°C (Lorencak et al., 2001), and ca. 52 Ma monazite with $^{40}Ar/^{39}Ar$ data showing cooling to 300°C by ca. 48 Ma (Vanderhaeghe et al., 2003).

The different types of leucosome have been interpreted to reflect up to three different anatectic events (Spark, 2001). However, this study shows that leucosome formed during a continuum and limits the timing of leucosome formation to one main melting event in the Paleocene to Eocene. This timing correlates with the U-Pb SHRIMP leucosome ages of 55.9 ± 3.1 Ma and 56.4 ± 1.4 Ma from Vanderhaeghe et al. (1999) in structurally

higher basement gneiss 4 km to the south of the current study area. In addition, these ages also agree within error with Kuiper's (2003) U-Pb TIMS lower intercept age of 48 ± 11 Ma for a crosscutting leucosome from 4.5 km structurally deeper in the basement gneiss (Fig. 1-5). The documented occurrence of folded and cross-cutting leucosome throughout the basement gneiss of Thor-Odin dome (Reesor and Moore, 1971; Spark, 2001; McNeill and Williams, 2003) and the consistent ca. 56 Ma age of said leucosome indicates that this melting event was significant throughout the entire dome.

This study has established that at least part of the transposition foliation ($S_2$), large-scale isoclinal folds that infold cover and basement rocks, as well as $F_3$ and $F_4$ folding occurred from ca. 56-52 Ma. Folding was coincident with anatexis and leucosome formation. In Thor-Odin dome, $F_2$ folding is interpreted to be syn-peak metamorphism and $F_3$ folds are syn- to post-peak metamorphism (Spark, 2001). Prograde metamorphism culminated in the onset of anatexis by ca. 56 Ma. Anatexis continued during isothermal decompression, which lasted until ca. 52 Ma.

## 1.6. Summary of conclusions

1) Basement paragneisses are Paleoproterozoic representing part of the Canadian Shield, have detrital zircon grains that range in age from ca. 2.6 to 1.8 Ga, and were likely deposited to at least ca. 1.8 Ga. Part of the basement paragneiss sequence were intruded by plutonic rocks at ca. 1.9 Ga, which are now termed basement orthogneisses. After ca. 1.8 Ga, the Monashee cover sequence was subsequently deposited onto the basement rocks of Thor-Odin dome. At present there is no control on the age span of deposition of the cover rocks from Thor-Odin dome.
2) Any evidence of Precambrian metamorphic or deformation history has been strongly overprinted by pervasive penetrative Paleogene Cordilleran metamorphism and deformation events.
3) Thor-Odin dome experienced four generations of folding, upper amphibolite to

lower granulite facies metamorphism and anatexis culminating in the core at ca. 56 Ma.

4) Three types of leucosome are preserved in the Saturday Glacier area: folded stromatic, phenocrystic vein and pegmatitic vein type. Leucosome are igneous and formed via *in situ* anatexis based on field relationships, petrography, major and trace element chemistry, peak P-T conditions, and zircon morphology.
5) Anatexis was the culmination of regional metamorphism at ca. 56 Ma. This was likely the first time the basement rocks experienced such high-grade metamorphism and melting.
6) Structures at Saturday Glacier were synchronous with anatexis based on crosscutting relationships between folding and ca. 56 Ma leucosome. At least part of $S_2$ transposition foliation and large-scale $F_2$ isoclines that infold basement and cover, as well as $F_3$ and $F_4$ folds, formed from ca. 56 Ma to as late as ca. 52 Ma.
7) The final stage of deformation and metamorphism in the Thor-Odin dome relative to adjacent overlying rocks of the Middle Crustal Zone is diachronous, with Late Cretaceous-Paleocene deformation and metamorphism at lower levels in the dome outlasting that of higher structural levels. Deformation and metamorphism in Thor-Odin dome represent part of the youngest, ca. 56 Ma, a high-temperature compressional story accompanied by anatexis
8) Isothermal decompression began by ca. 55 Ma and decompression melting continued to ca. 52 Ma and was synchronous with the exhumation and denudation of the dome, via extension and erosion
9) In Thor-Odin dome, high-grade metamorphism, anatexis, penetrative deformation and large scale folding are Paleocene - Eocene in age.

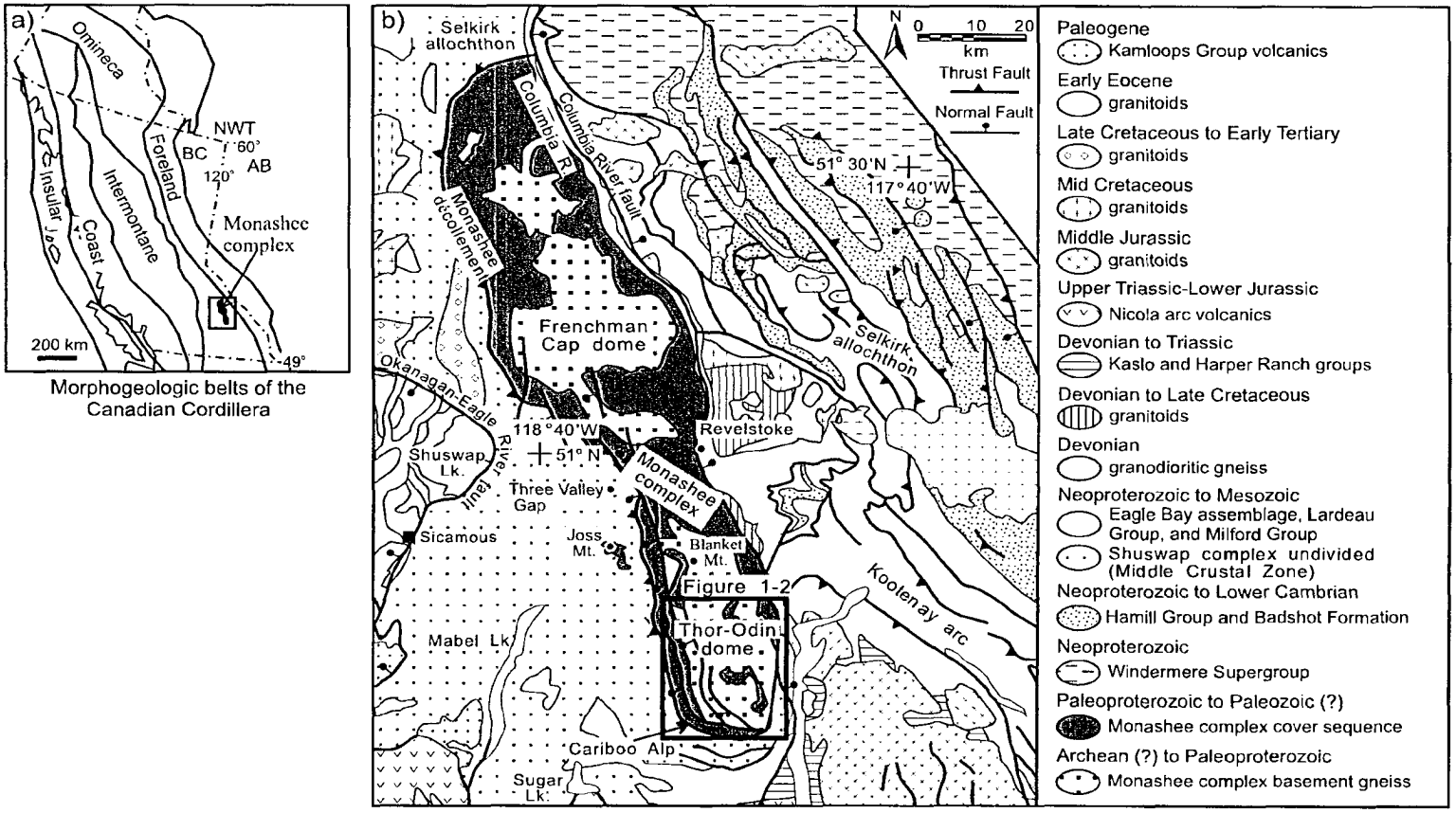


**Figure. 1-1.** (a) Map highlights the five morphological belts of the Cordillera from Wheeler and McFeely (1991). (b) Tectonic assemblage map of southeastern Omineca belt, British Columbia (modified after Scammell and Brown, 1990; Wheeler and McFeely, 1991; Gibson, et al., 1999), outlining the lithological units of the Monashee complex and surrounding area. The box in southern Thor-Odin dome delineates Figure 1-2.

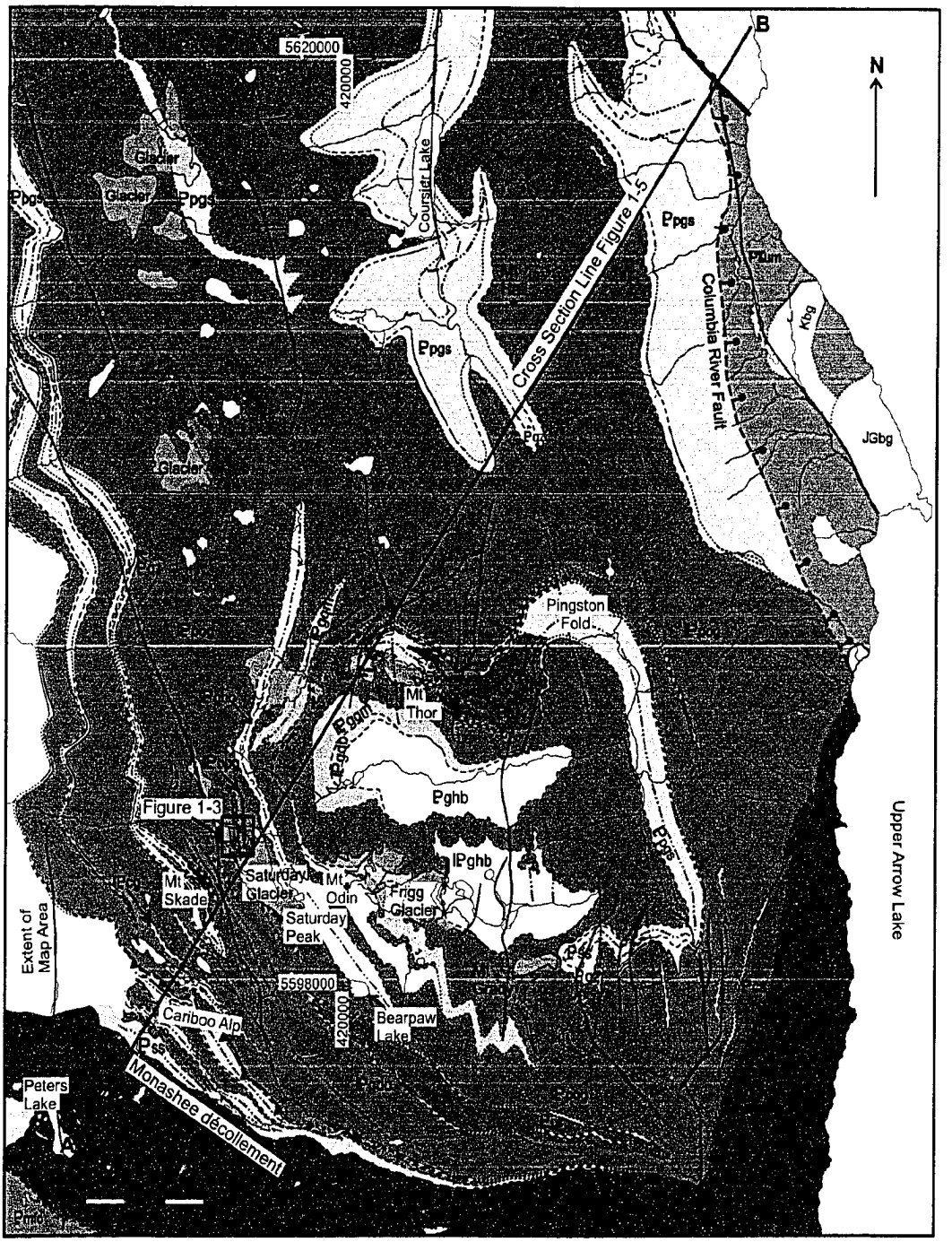


**Figure. 1-2.** Geological map of the Thor-Odin dome, Monashee complex (modified after Reesor and Moore, 1971; Coleman, 1990; Carr, 1992; McNeill and Williams, 2003; Kruse et al., 2004; Unpublished maps of P.D. McNeill, S. Kruse and P.F. Williams, 2004). A box in the southwest part of Thor-Odin dome delineates Figure 1-3 and a cross section line is shown for Figure 1-5. Monashee décollement is drawn based on mapping and interpretation of McNicoll and Brown (1995) at Cariboo Alp.

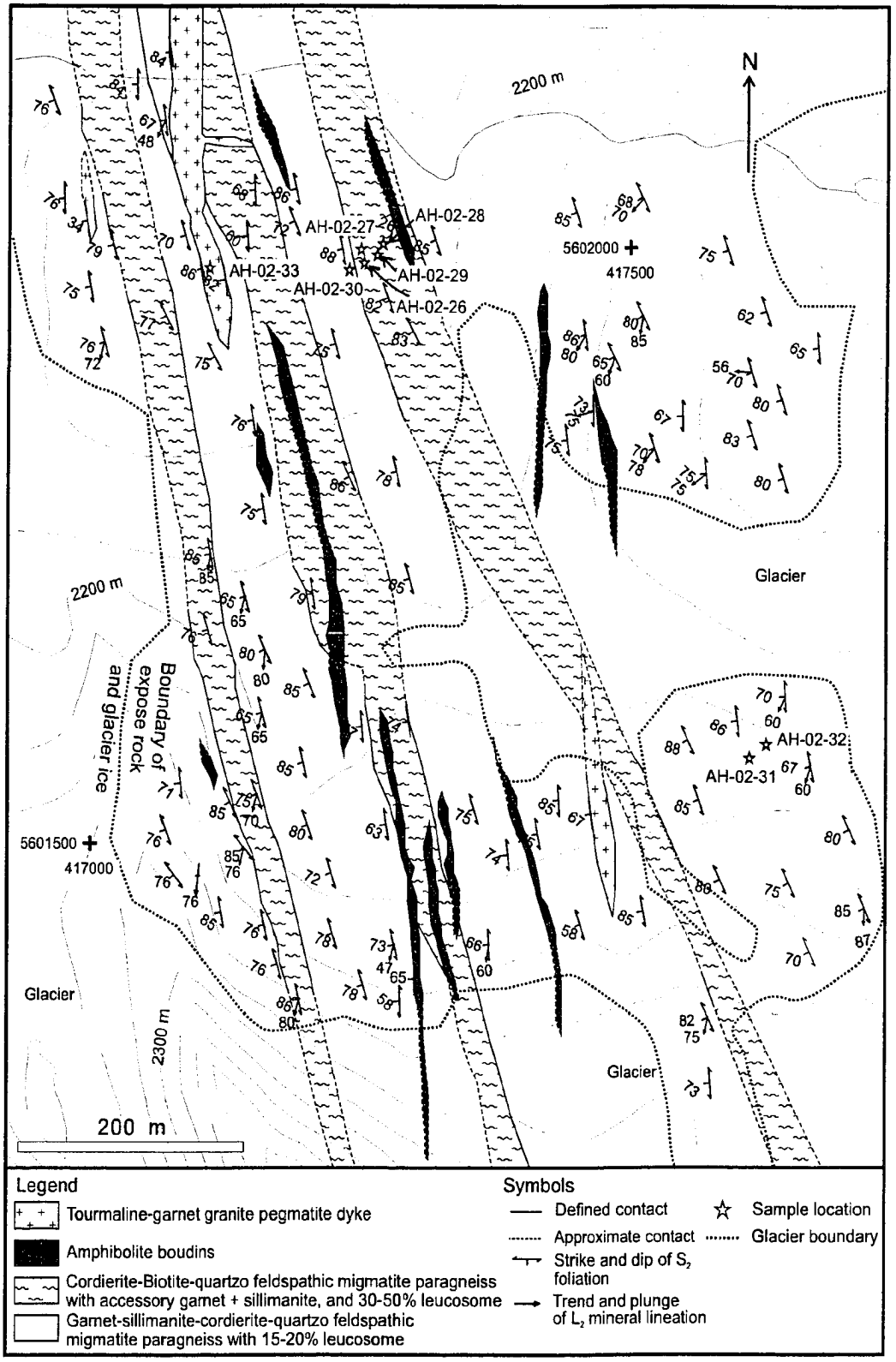


**Figure. 1-3.** Geological map of the Saturday Glacier area, Thor-Odin dome (mapping by A.M. Hinchey). The field area is located on the steeply west dipping limb of a tight east verging $F_2$ fold (see Fig. 1-5).

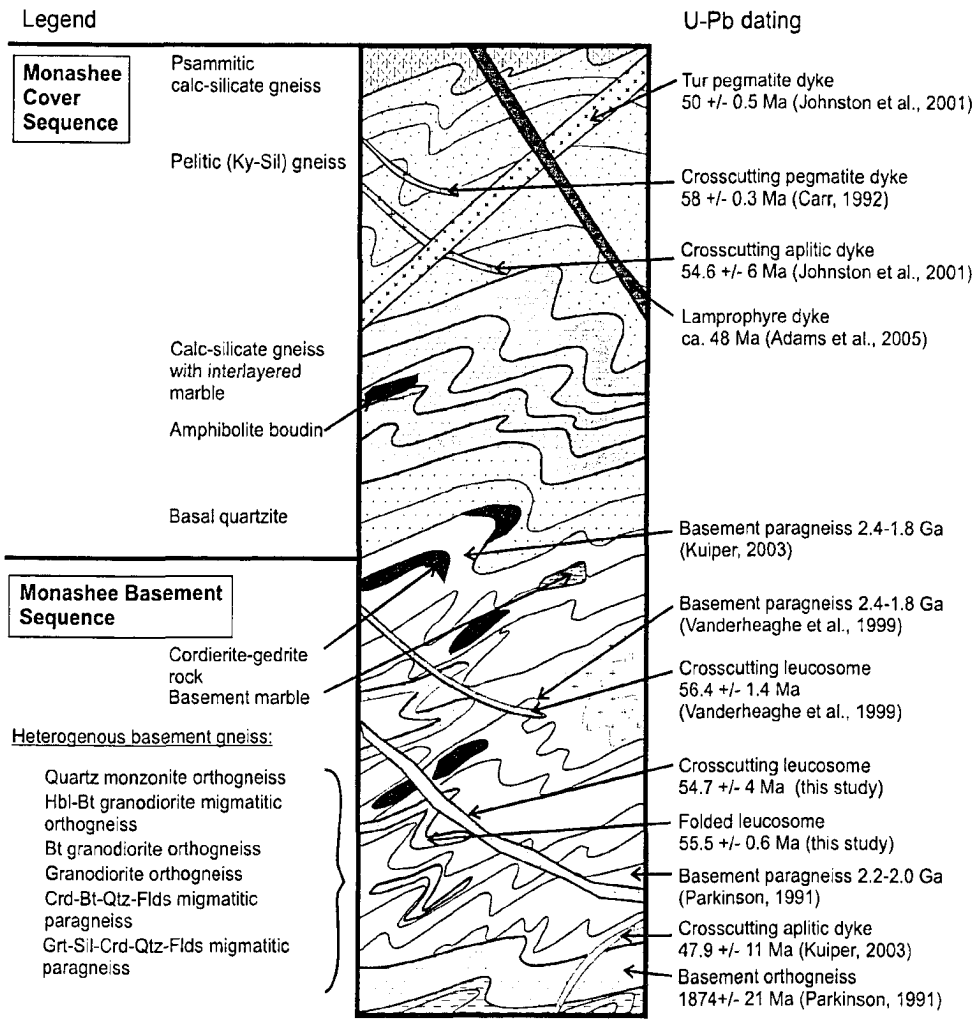


**Figure. 1-4.** Simplified tectonostratigraphic column of the lithological units in the Thor-Odin dome (modified after Parkinson, 1992). The location of the study area and results of previous geochronological studies in Thor-Odin are projected into the column. Geochronological data is from this study; Parkinson (1991); Carr (1992); Vanderhaeghe et al. (1999); Johnston et al. (2001); and Kuiper (2003).

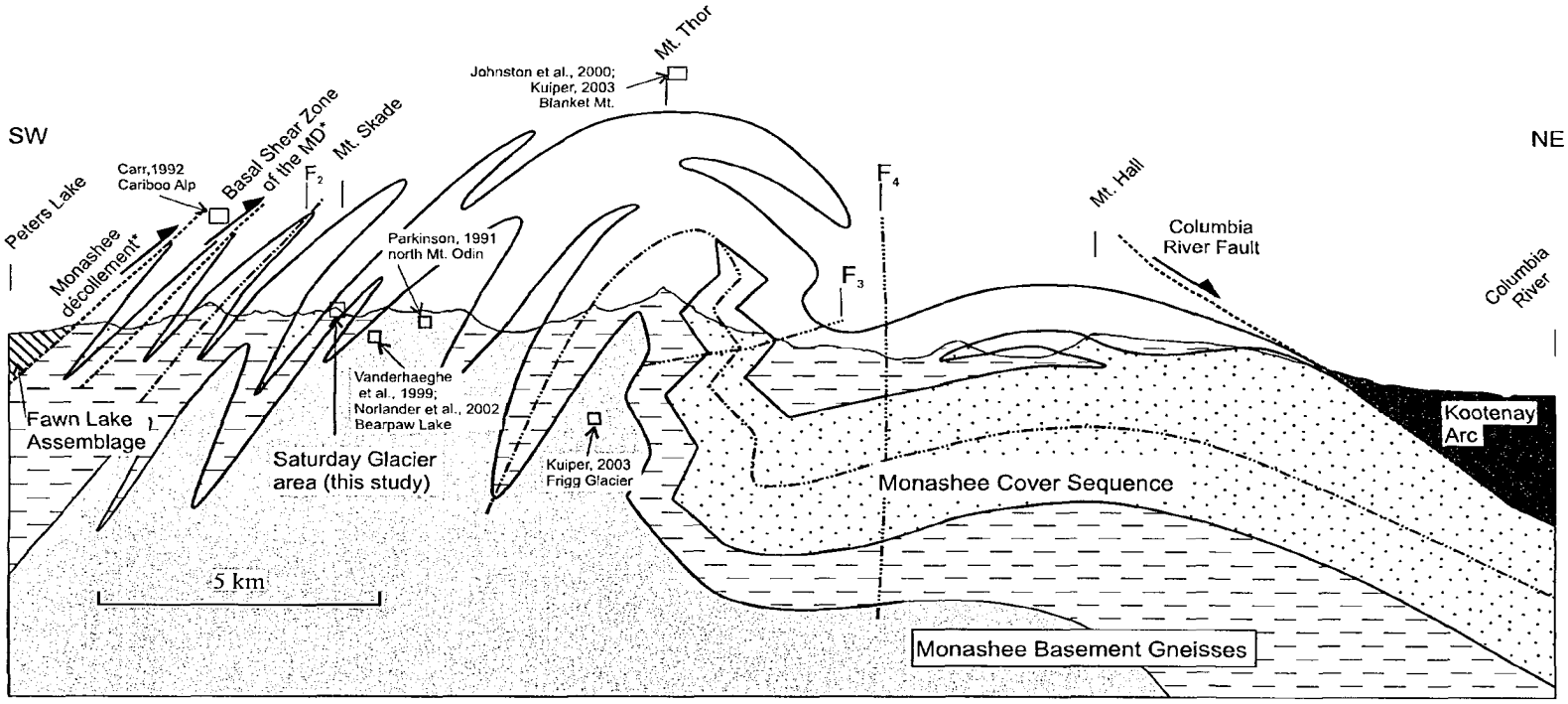


**Figure. 1-5.** A northeast cross section of Thor-Odin dome illustrating the complex fold patterns observed (modified after Williams and Jiang, in press). A type II fold interference pattern results from the superposition of $F_2$ and $F_4$ folds. The locations of geochronology sampling area (this study) and previous geochronological studies are projected into the plane of the cross section. Figure 1-2 shows the location of the cross section. Monashee décollement* (MD) is drawn based on mapping and interpretation of McNicoll and Brown (1995) at Cariboo Alp. Vertical scale equals horizontal scale.

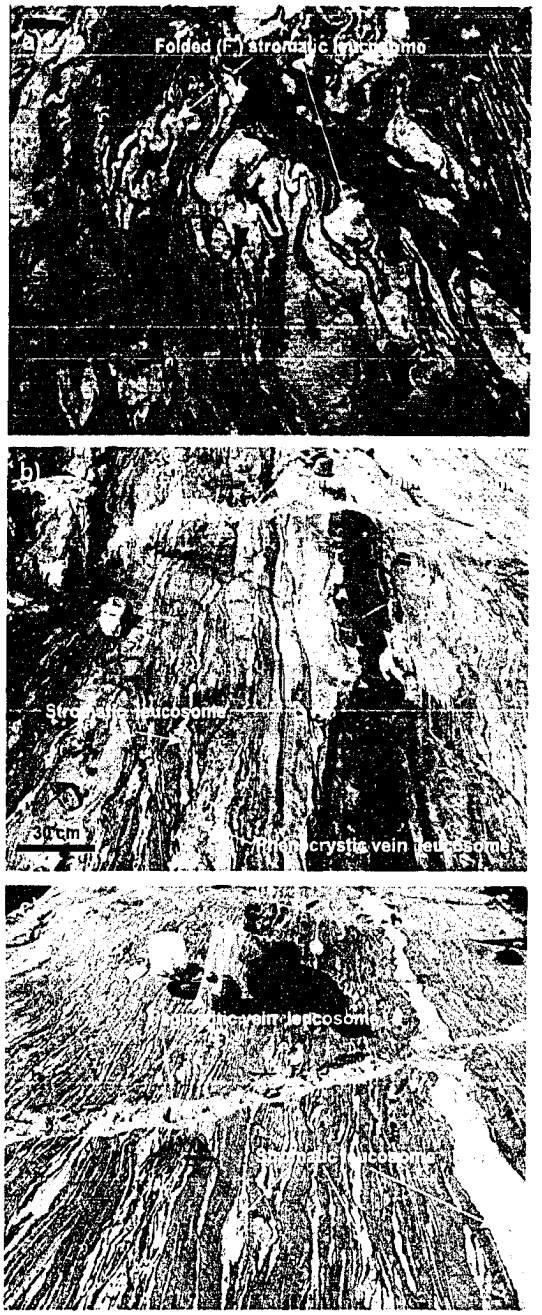


**Figure. 1-6.** Photographs of the representative types of leucosome (stromatic, phenocrystic and pegmatitic vein) preserved in the Saturday Glacier area, Thor-Odin dome. Photo (a) of folded stromatic leucosome hosted by the Crd-Bt quartzo-feldspathic paragneiss. Photo (b) depicts the phenocrystic vein leucosome crosscutting stromatic leucosome and the foliation in the Crd-Bt quartzo-feldspathic paragneiss. The phenocrystic vein leucosome is crosscut by the pegmatitic vein leucosome. The host gneiss is the Crd-Bt quartzo-feldspathic paragneiss. Photo (c) depicts the crosscutting relationship of the pegmatitic vein leucosome with the stromatic leucosome. The host gneiss is the Crd-Bt quartzo-feldspathic paragneiss.

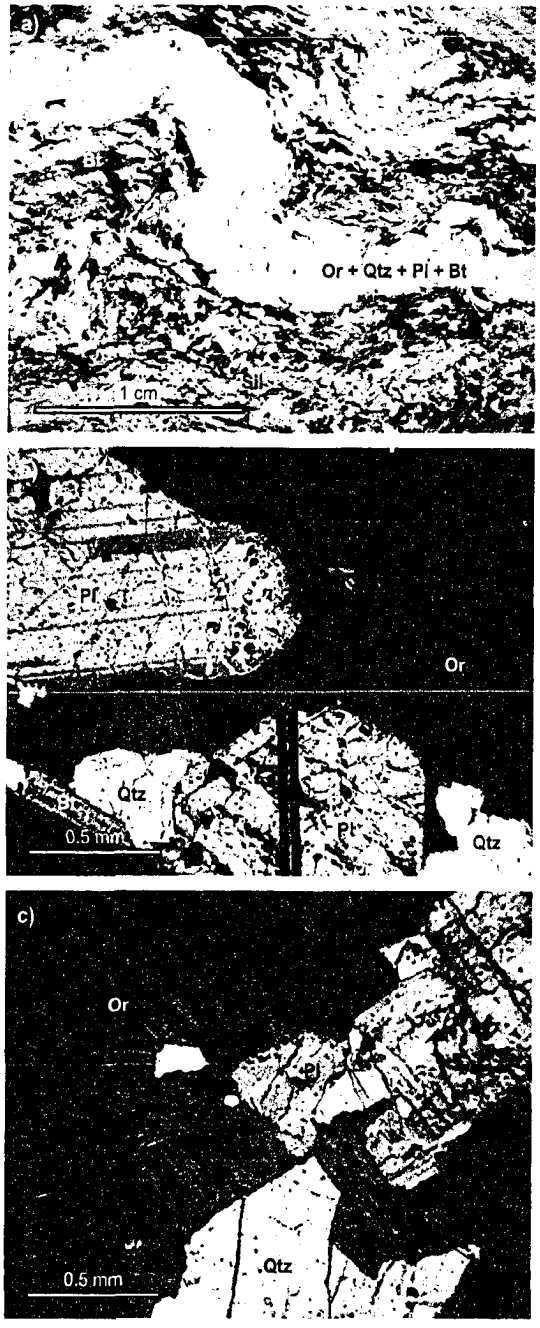


**Figure. 1-7.** Photomicrographs of leucosome exposed in Saturday Glacier area, Thor-Odin dome. Photo (a) is of folded ($F_2$) leucosome in the host Crd-Bt quartzo-feldspathic paragneiss. Photo (b) is of phenocrystic vein leucosome (sample AH-02-27) and shows the igneous nature of the leucosome as evidenced by euhedral to anhedral grains, primary twinning in plagioclase and in perthitic orthoclase, and myrmekite intergrowths of plagioclase and quartz. Photo (c) is of crosscutting pegmatitic vein leucosome (sample AH-02-29) and shows large euhedral grains of perthitic orthoclase surrounding euhedral to anhedral grains of plagioclase and quartz.

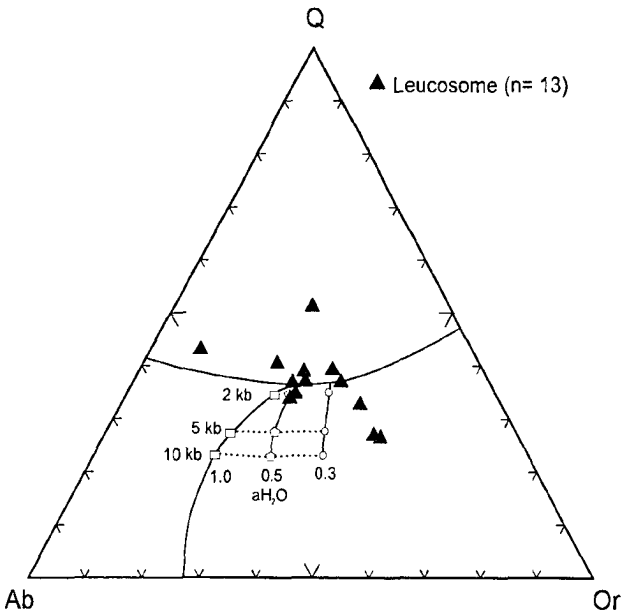


**Figure 1-8.** Diagram showing normalized proportions of quartz, albite and orthoclase for all leucosome samples. Minimum (first-formed) eutectic melt compositions are shown with varying pressures of 1, 2, 5 and 10 Kb with the $aH_2O$ values ranging between 0.3 and 1.0 (modified after Inger and Harris, 1993).

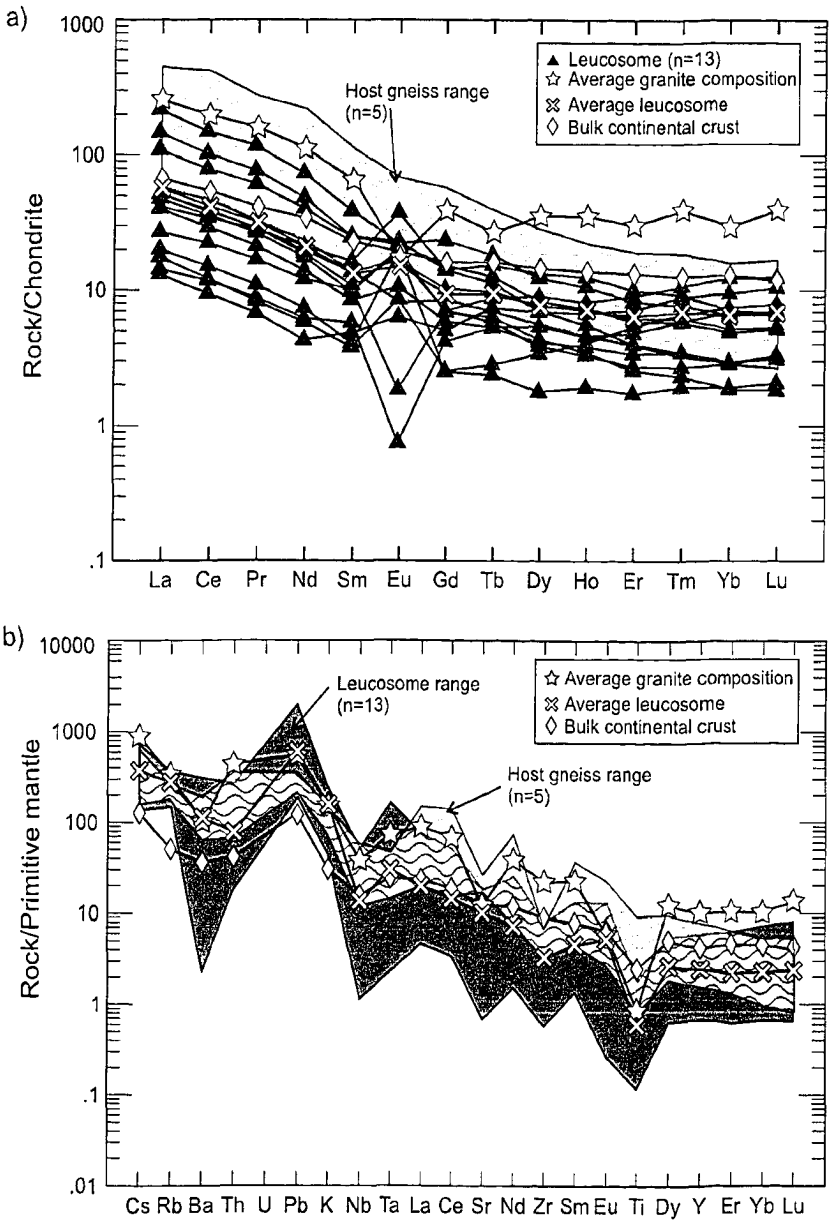


**Figure 1-9.** Trace element normalized diagrams showing the range of values for leucosome and host gneisses of the leucosome as well as for average granite and bulk continental crust compositions. (a) Chondrite normalization. (b) Primitive mantle normalization. Normalization values from Sun and McDonough (1989). Bulk continental crust from Taylor and McLennan (1995). Average granite composition from Govindaraju (1989). Trace element data for leucosome host gneiss from Hinchey (Chapter 2).

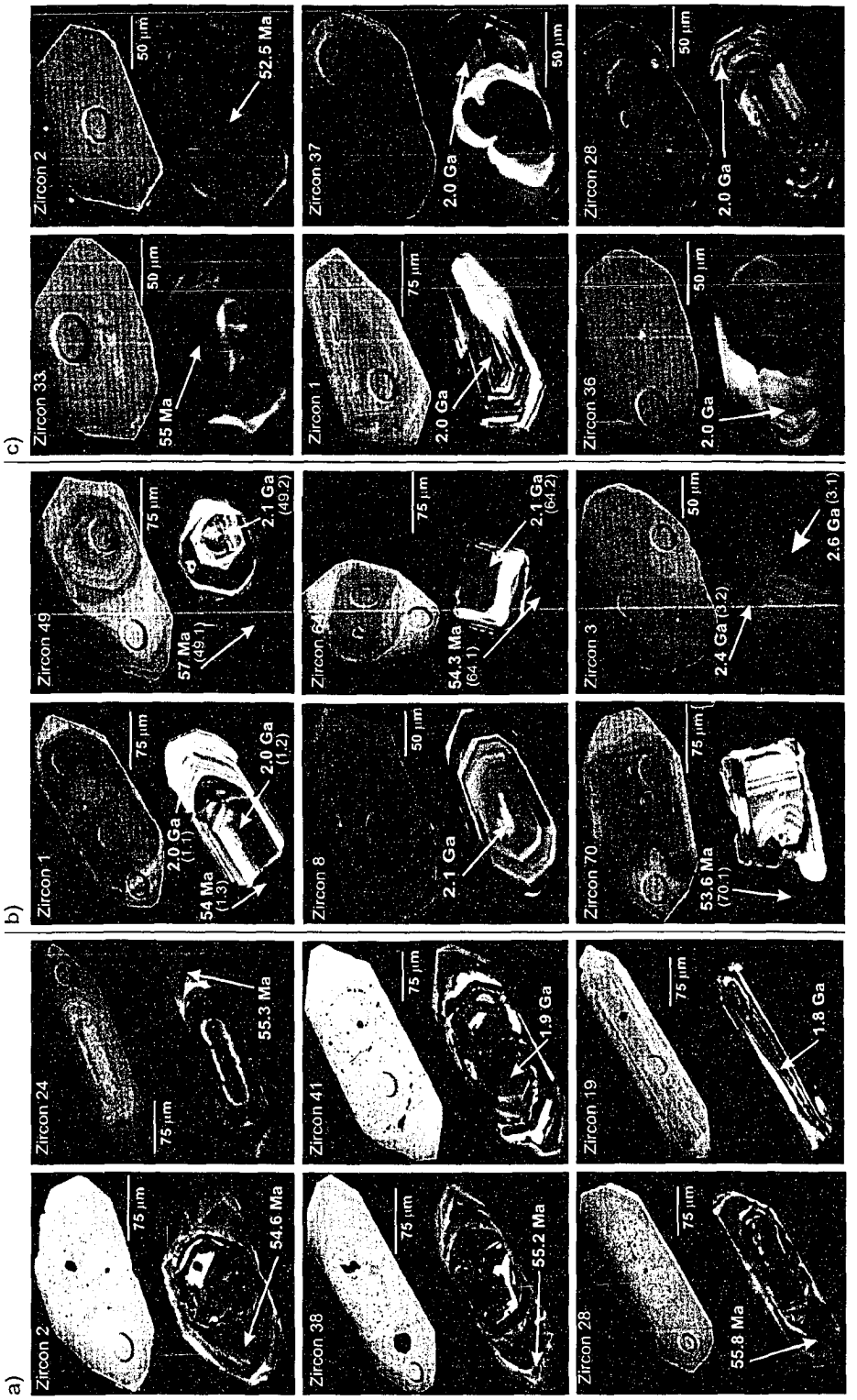

**Figure. 1-10.** Representative zircons from leucosome samples dated using the SHRIMP. The pit left by the ion beam on the zircon appears on the back scattered electron (BSE) images (top image) and the internal zoning of the zircons is most apparent in cathodo-luminescence (CL) images (bottom image). Zircon ages that are younger than 800 Ma are reported as $^{206}Pb/^{238}U$ ages and ages older then 800 Ma are reported as $^{207}Pb/^{206}Pb$ ages (see text for explanation). Zircon numbers correspond to spot numbers listed in Table 3 and zircons with multiple analytical sites have bracketed numbers after the age referring to specific analytical locations. See text for description and interpretation of intracrystalline domains and textures. (a) Folded stromatic type of leucosome (AH-02-26). (b) Phenocrystic vein type of leucosome (AH-02-27). (c) Pegmatitic vein type of leucosome (AH-02-29).

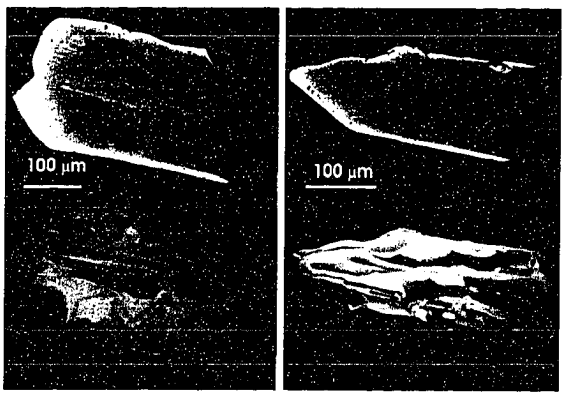


**Figure 1-12.** Back scattered electron (BSE) images (top image) and cathodoluminescence (CL) images (bottom image) of representative zircons from the cordierite-biotite-quartzo-feldspathic paragneiss that hosts the dated leucosome samples. In contrast to zircons from the leucosome sample, these zircons lack the cores bounded by bright alteration zones and the fine-scale oscillatory zoned (CL), euhedral, inclusion free magmatic growth.

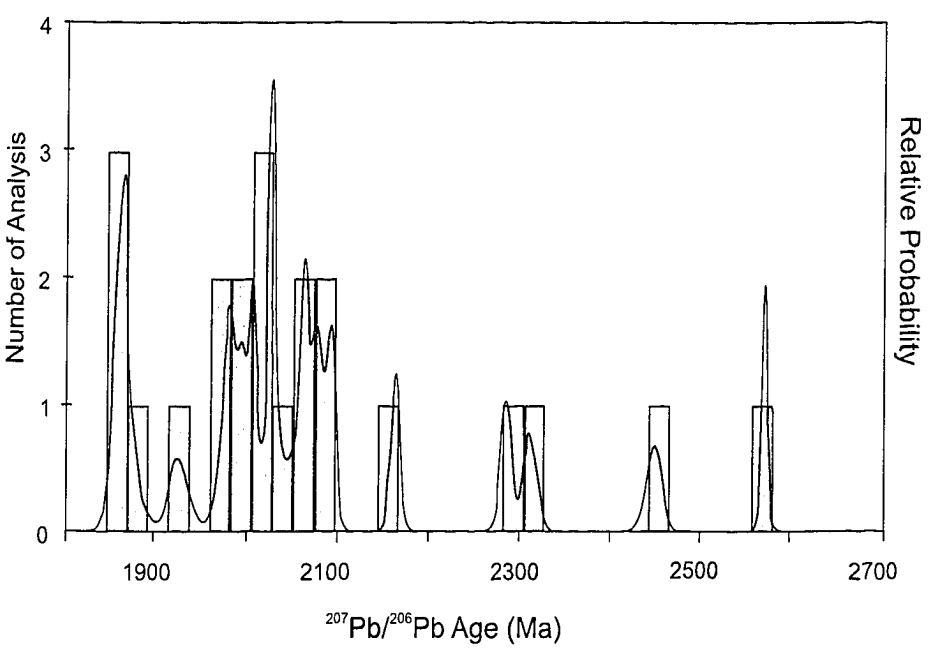


**Figure 1-13.** Histogram of $^{204}Pb$ corrected $^{207}Pb/^{206}Pb$ dates from 22 inherited cores within zircons from the three dated leucosome samples. Discordant $^{207}Pb/^{206}Pb$ ages are considered as minimum ages. Columns represent a frequency histogram of $^{207}Pb/^{206}Pb$ dates (scale on left), neglecting associated error, and are included as a visual aid to the data patterns. The curve represents a weighted cell-less summed probability histogram, into which errors of individual analysis have been incorporated.

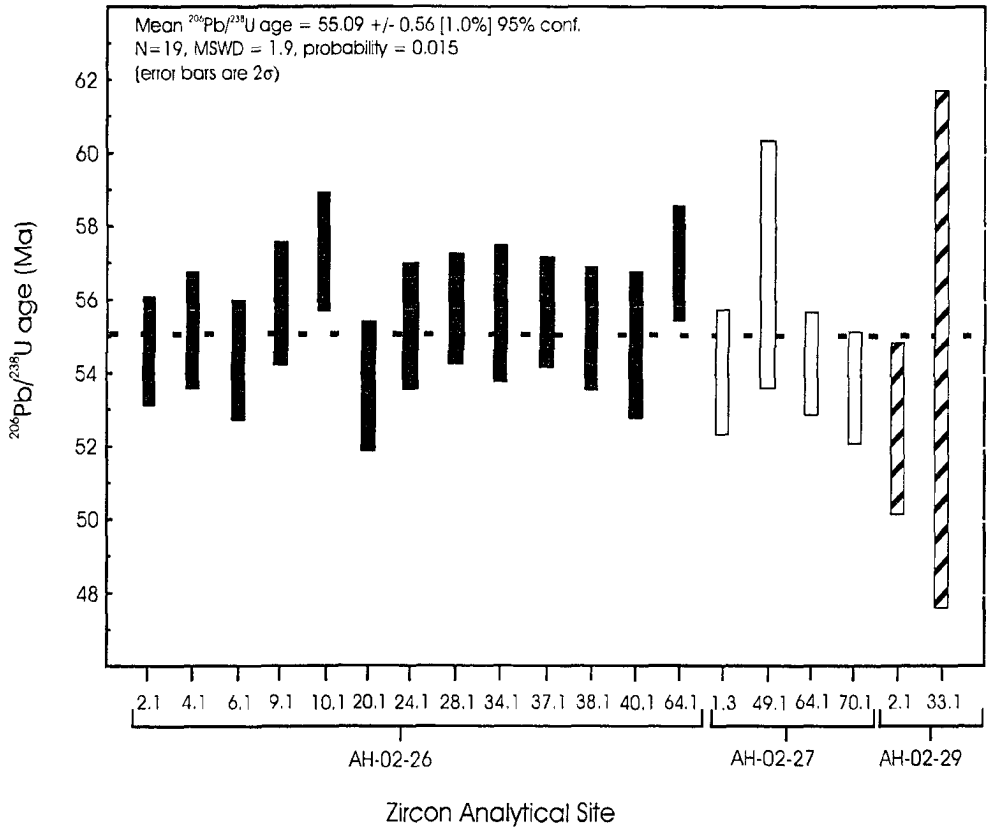


**Figure 1-11.** U-Pb SHRIMP analyses from zircons from the three leucosome samples excluding inherited grains and cores. Black bars are for the stromatic leucosome (AH-02-26), grey bars are phenocrystic leucosome (AH-02-27) and hatched bars are pegmatitic leucosome (AH-02-29). Errors are incorporated at the 2σ level. The mean weighted average age is calculated using only the analysis falling within the 95% confidence interval.

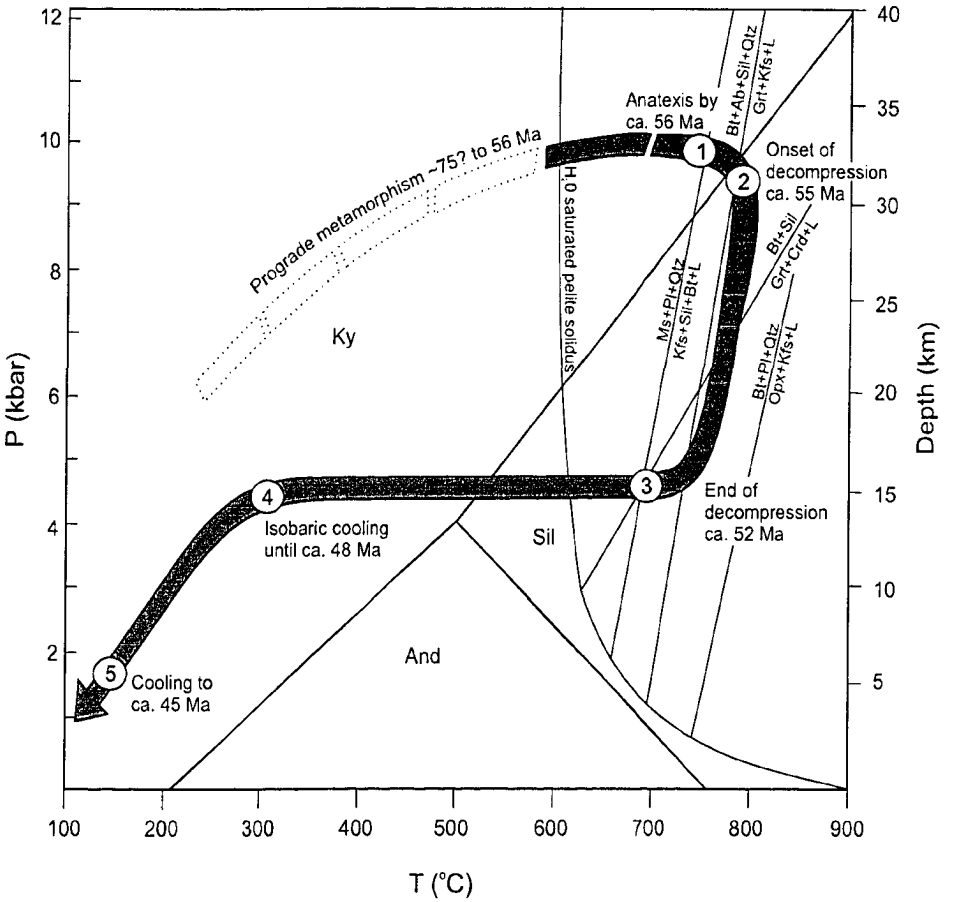


Events in the basement gneiss of Thor-Odin

① ca. 56 Ma - Baric peak metamorphism and anatexis

② ca. 55 Ma - Onset of isothermal decompression and continued anatexis

③ ca. 52 Ma - End of decompression and anatexis

④ ca. 48 Ma - Isobaric cooling

⑤ ca. 45 Ma - Continued cooling and decompression

**Figure 1-14.** Pressure-Temperature-time path proposed for the basement gneiss of Thor-Odin dome. The prograde path is uncertain; approximate timing constraints are labelled-for known parts of the path. Timing and geothermobarometric constraints are provided by this study and those of Reesor and Moore (1971); Duncan (1982); Vanderhaeghe et al.(1999); Norlander et al. (2001); Lorencak et al. (2001), and Vanderhaeghe et al. (2003). The locations of selected dehydration melting reactions are shown. Melt producing reactions are explained in Spear et al. (1999). Mineral symbols are from Kretz (1983).

**Table 1-1.** Description and location of geochemical and geochronological leucosome samples from Thor-Odin dome, Monashee complex. Mineral symbols are from Kretz (1983).

| Sample | Easting | Northing | Sample Description | Map Location |
|---|---|---|---|---|
| AH-03-017 | 419010 | 5598756 | Crosscutting pegmatitic Ms-Bt granitic leucosome | Bearpaw Lake |
| AH-03-019 | 418966 | 5598825 | Folded stromatic Ms-Bt granitic leucosome | Bearpaw Lake |
| AH-03-022 | 419149 | 5598883 | Crosscutting pegmatitic Ms-Bt granitic leucosome | Bearpaw Lake |
| AH-02-005 | 423299 | 5600302 | Stromatic Bt granitic leucosome | Frigg Glacier |
| AH-02-006 | 423299 | 5600302 | Folded stromatic Ms-Bt granitic leucosome | Frigg Glacier |
| AH-02-008 | 423307 | 5600311 | Folded stromatic Bt granitic leucosome | Frigg Glacier |
| AH-02-009 | 423239 | 5600301 | Crosscutting phenocrystic Bt granitic leucosome | Frigg Glacier |
| AH-02-010 | 423270 | 5600336 | Sheared, stromatic Bt granititc leucosome | Frigg Glacier |
| AH-02-011 | 423291 | 5600689 | Sheared, stromatic Bt granititc leucosome | Frigg Glacier |
| AH-02-013 | 423453 | 5600386 | Crosscutting phenocrystic Bt granitic leucosome | Frigg Glacier |
| AH-02-026 | 417252 | 5602040 | Folded stromatic Bt granitic leucosome | Saturday Glacier |
| AH-02-027 | 417245 | 5602034 | Phenocrystic Ms-Bt granitic leucosome | Saturday Glacier |
| AH-02-029 | 417252 | 5602034 | Crosscutting pegmatitic Ms-Bt granitic leucosome | Saturday Glacier |

**Table 1-2.** Major and trace element analyses of leucosome from Thor-Odin dome, Monashee complex.

| | AH-03-17 | AH-03-19 | AH-03-22 | AH-02-05 | AH-02-06 | AH-02-08 | AH-02-09 | AH-02-10 | AH-02-11 | AH-02-13 |
|---|---|---|---|---|---|---|---|---|---|---|
| (wt. %) | | | | | | | | | | |
| $SiO_2$ | 75.84 | 73.48 | 74.49 | 71.56 | 72.16 | 74.38 | 71.88 | 75.02 | 73.20 | 72.73 |
| $TiO_2$ | 0.09 | 0.03 | 0.07 | 0.39 | 0.10 | 0.05 | 0.24 | 0.06 | 0.03 | 0.21 |
| $Al_2O_3$ | 14.28 | 14.78 | 14.41 | 14.10 | 14.67 | 13.60 | 14.01 | 13.49 | 14.17 | 13.72 |
| $Fe_2O_3$* | 0.51 | 0.36 | 0.48 | 0.98 | 0.47 | 0.33 | 0.95 | 0.18 | 0.16 | 0.75 |
| FeO | 0.63 | 0.34 | 0.56 | 1.55 | 0.58 | 0.42 | 1.21 | 0.21 | 0.18 | 0.90 |
| MnO | 0.03 | 0.02 | 0.03 | 0.03 | 0.02 | 0.02 | 0.03 | 0.01 | 0.01 | 0.02 |
| MgO | 0.14 | 0.09 | 0.12 | 0.83 | 0.27 | 0.19 | 0.61 | 0.15 | 0.10 | 0.49 |
| CaO | 0.61 | 0.69 | 0.74 | 2.73 | 2.06 | 1.88 | 2.07 | 1.55 | 1.30 | 1.68 |
| $Na_2O$ | 3.91 | 2.90 | 3.80 | 4.41 | 3.70 | 3.32 | 3.24 | 2.86 | 2.72 | 2.73 |
| $K_2O$ | 3.73 | 7.54 | 4.40 | 1.28 | 4.27 | 4.29 | 4.27 | 5.11 | 6.37 | 5.32 |
| $P_2O_5$ | 0.18 | 0.07 | 0.15 | 0.04 | 0.04 | 0.03 | 0.13 | 0.02 | 0.03 | 0.08 |
| Sum | 99.94 | 100.31 | 99.25 | 97.91 | 98.33 | 98.51 | 98.65 | 98.65 | 98.26 | 98.63 |
| (ppm) | | | | | | | | | | |
| V | 7 | 10 | 11 | 30 | 15 | 8 | 21 | 5 | 12 | 16 |
| Cr | 39 | 2 | 5 | 29 | 7 | 5 | 6 | 5 | 5 | 10 |
| Co | 8 | 4 | 3 | 11 | 5 | 4 | 3 | <LD | <LD | 4 |
| Ni | 1 | <LD | 1.00 | 33 | 67 | 44 | 51 | 10 | 9 | 17 |
| Zn | 17 | 6 | 16 | 37 | 19 | 15 | 35 | 12 | 11 | 29 |
| Ga | 23 | 13 | 17 | 18 | 18 | 14 | 16 | 16 | 14 | 13 |
| As | <LD | <LD | <LD | 1 | 1 | 4 | 1 | 4 | <LD | 1 |
| Rb | 211.0 | 208.0 | 221.0 | 92.1 | 150.9 | 123.2 | 166.7 | 160.4 | 196.1 | 194.2 |
| Sr | 14.2 | 328.3 | 18.5 | 245.9 | 307.0 | 274.4 | 274.1 | 304.0 | 296.2 | 285.7 |
| Y | 8.2 | 6.4 | 14.4 | 6.2 | 10.7 | 11.1 | 16.3 | 3.1 | 5.3 | 8.6 |
| Zr | 18.4 | 8.9 | 33.2 | 84.8 | 64.1 | 23.8 | 19.3 | 6.4 | 37.7 | 24.7 |
| Nb | 36.9 | 1.0 | 13.5 | 14.9 | 5.0 | 3.3 | 12.6 | 2.9 | 1.4 | 9.1 |
| Cs | 2.7 | 1.1 | 5.8 | 3.2 | 1.9 | 1.1 | 3.4 | 1.9 | 2.0 | 2.9 |
| Ba | 23 | 1483 | 16 | 184 | 968 | 957 | 935 | 1203 | 1162 | 1328 |
| La | 3.5 | 4.2 | 6.5 | 9.7 | 26.2 | 12.4 | 51.9 | 4.8 | 12.5 | 34.9 |
| Ce | 7.3 | 7.6 | 13.8 | 18.1 | 48.6 | 23.6 | 91.2 | 9.3 | 24.2 | 62.7 |
| Pr | 0.8 | 0.8 | 1.6 | 2.0 | 5.8 | 2.8 | 11.1 | 1.1 | 2.8 | 7.4 |
| Nd | 2.9 | 2.8 | 5.7 | 6.6 | 19.0 | 9.3 | 34.6 | 3.5 | 8.9 | 22.9 |
| Sm | 0.89 | 0.59 | 1.57 | 1.31 | 3.80 | 2.12 | 5.98 | 0.63 | 1.69 | 3.87 |
| Eu | 0.04 | 0.50 | 0.11 | 0.62 | 1.27 | 0.96 | 1.30 | 1.12 | 1.05 | 1.34 |
| Gd | 0.87 | 0.53 | 1.46 | 1.23 | 3.15 | 2.12 | 4.85 | 0.52 | 1.48 | 2.94 |
| Tb | 0.20 | 0.11 | 0.33 | 0.20 | 0.48 | 0.37 | 0.69 | 0.09 | 0.22 | 0.43 |
| Dy | 1.39 | 0.88 | 2.32 | 1.07 | 2.13 | 1.96 | 3.16 | 0.46 | 1.00 | 1.81 |
| Ho | 0.26 | 0.23 | 0.47 | 0.22 | 0.42 | 0.42 | 0.61 | 0.11 | 0.19 | 0.32 |
| Er | 0.81 | 0.91 | 1.52 | 0.57 | 0.99 | 1.04 | 1.38 | 0.29 | 0.46 | 0.67 |
| Tm | 0.15 | 0.17 | 0.28 | 0.09 | 0.15 | 0.16 | 0.20 | 0.05 | 0.07 | 0.09 |
| Yb | 1.17 | 1.27 | 2.12 | 0.50 | 0.84 | 0.89 | 1.13 | 0.33 | 0.49 | 0.51 |
| Lu | 0.17 | 0.20 | 0.32 | 0.09 | 0.13 | 0.14 | 0.18 | 0.05 | 0.09 | 0.08 |
| Hf | 0.90 | 0.40 | 1.30 | 2.36 | 2.97 | 0.81 | 0.58 | 0.25 | 3.19 | 0.66 |
| Ta | 6.75 | 0.19 | 2.27 | 1.09 | 0.39 | <LD | 1.04 | 0.44 | <LD | 0.58 |
| Pb | 17 | 37 | 26 | 13 | 32 | 27 | 25 | 27 | 37 | 31 |
| Th | 1.52 | 1.91 | 2.68 | 5.31 | 16.21 | 6.30 | 22.86 | 3.64 | 9.01 | 15.54 |
| U | 4.89 | 1.39 | 6.76 | 2.97 | 5.34 | 1.87 | 4.31 | 3.87 | 2.18 | 2.52 |

Major element analyses by X-Ray Fluorescence. $Fe_2O_3$* and FeO recalculated from measured $Fe_2O_3T$ (total) using the procedure of LeMaitre (1976). Oxides normalized to 100 % (anhydrous). Totals of measured analysis are reported in "sum" column. Trace element analyses carried out by X-Ray Fluorescence and Inductively Coupled Plasma-Mass Spectrometry. LD = Limit of Detection.

**Table 1-2.** Continued.

| | AH-02-26 | AH-02-27 | AH-02-29 |
|---|---|---|---|
| (wt. %) | | | |
| $SiO_2$ | 70.29 | 74.37 | 74.07 |
| $TiO_2$ | 0.17 | 0.40 | 0.03 |
| $Al_2O_3$ | 14.91 | 12.00 | 14.00 |
| $Fe_2O_3$* | 0.57 | 1.16 | 0.25 |
| FeO | 0.57 | 1.77 | 0.29 |
| MnO | 0.02 | 0.02 | 0.02 |
| MgO | 0.40 | 1.05 | 0.09 |
| CaO | 1.26 | 1.61 | 0.74 |
| $Na_2O$ | 2.63 | 2.41 | 3.84 |
| $K_2O$ | 7.29 | 3.40 | 4.71 |
| $P_2O_5$ | 0.24 | 0.07 | 0.13 |
| Sum | 98.35 | 98.26 | 98.16 |
| (ppm) | | | |
| V | 16 | 39 | 9 |
| Cr | 3 | 23 | 3 |
| Co | 4 | 10 | 4 |
| Ni | 10 | 35 | 6 |
| Zn | 25 | 54 | 15 |
| Ga | 16 | 13 | 20 |
| As | 3 | <LD | 2 |
| Rb | 184.6 | 124.3 | 234.6 |
| Sr | 383.3 | 227.1 | 55.6 |
| Y | 19.3 | 5.6 | 12.2 |
| Zr | 39.5 | 90.2 | 14.7 |
| Nb | 5.5 | 15.1 | 14.8 |
| Cs | 2.2 | 2.3 | 5.0 |
| Ba | 2147 | 884 | 107 |
| La | 9.9 | 11.4 | 3.2 |
| Ce | 21.3 | 22.1 | 5.9 |
| Pr | 2.7 | 2.6 | 0.7 |
| Nd | 10.0 | 8.3 | 2.0 |
| Sm | 2.52 | 1.51 | 0.75 |
| Eu | 2.18 | 1.16 | 0.37 |
| Gd | 2.93 | 1.43 | 1.05 |
| Tb | 0.58 | 0.24 | 0.28 |
| Dy | 3.42 | 1.12 | 1.78 |
| Ho | 0.72 | 0.20 | 0.39 |
| Er | 1.68 | 0.43 | 1.19 |
| Tm | 0.24 | 0.06 | 0.23 |
| Yb | 1.21 | 0.32 | 1.63 |
| Lu | 0.18 | 0.05 | 0.27 |
| Hf | 1.17 | 2.30 | 0.74 |
| Ta | 0.32 | 0.81 | 3.74 |
| Pb | 59 | 36 | 52 |
| Th | 2.12 | 4.05 | 1.73 |
| U | 1.39 | 1.75 | 6.55 |

**Table 1-3.** U-Pb SHRIMP zircon data for leucosome samples from the Saturday Glacier area, Thor-Odin dome. $^{207}Pb/^{206}Pb$ dates are reported for zircon grains older than 800 Ma and $^{206}Pb/^{238}U$ for those younger than 800 Ma (see text for explanation).

| | | | | | | | | | | Ages (Ma)[c] | | | |
|---|---|---|---|---|---|---|---|---|---|---|---|---|---|
| spots[a] | U (ppm) | Th (ppm) | Th/U | Pb*[b] (ppm) | $^{204}Pb$ (ppb) | $^{204}Pb/^{206}Pb$ | $^{207*}Pb/^{235}U$ | $^{206*}Pb/^{238}U$ | $^{207*}Pb/^{206*}Pb$ | $^{206}Pb/^{238}U$ | $^{207}Pb/^{235}U$ | $^{207}Pb/^{206}Pb$ | Disc.[d] (%) |
| **Sample AH-02-26** Folded aplitic leucosome, verges in same direction as F2, contains transposition foliation | | | | | | | | | | | | | |
| **Rims** - Mean $^{206}Pb/^{238}U$ age 55.5 +/- 0.6 | | | | | | | | | | | | | |
| 2.1 | 1178 | 6.1 | 0.0053 | 9 | 7 | 0.0009 | 0.0521 ± 0.0031 | 0.0085 ± 0.0001 | 0.0444 ± 0.0025 | 54.6 ± 1 | | | |
| 4.1 | 1438 | 4.5 | 0.0032 | 11 | 8 | 0.0007 | 0.0538 ± 0.0044 | 0.0086 ± 0.0001 | 0.0454 ± 0.0036 | 55.2 ± 1 | | | |
| 6.1 | 1141 | 6.6 | 0.0060 | 9 | 5 | 0.0006 | 0.0559 ± 0.0031 | 0.0085 ± 0.0001 | 0.0479 ± 0.0025 | 54.4 ± 1 | | | |
| 9.1 | 1573 | 4.5 | 0.0030 | 12 | 8 | 0.0007 | 0.0578 ± 0.0043 | 0.0087 ± 0.0001 | 0.0481 ± 0.0034 | 55.9 ± 1 | | | |
| 10.1 | 1368 | 5.0 | 0.0038 | 11 | 7 | 0.0006 | 0.0646 ± 0.0029 | 0.0089 ± 0.0001 | 0.0524 ± 0.0021 | 57.3 ± 1 | | | |
| 20.1 | 677 | 4.5 | 0.0069 | 5 | 7 | 0.0014 | 0.0570 ± 0.0063 | 0.0084 ± 0.0001 | 0.0495 ± 0.0053 | 53.6 ± 1 | | | |
| 24.1 | 828 | 6.3 | 0.0079 | 7 | 9 | 0.0015 | 0.0655 ± 0.0075 | 0.0086 ± 0.0001 | 0.0552 ± 0.0061 | 55.3 ± 1 | | | |
| 28.1 | 1466 | 6.7 | 0.0048 | 11 | 11 | 0.0010 | 0.0562 ± 0.0026 | 0.0087 ± 0.0001 | 0.0469 ± 0.0020 | 55.8 ± 1 | | | |
| 34.1 | 1096 | 2.8 | 0.0027 | 9 | 8 | 0.0010 | 0.0575 ± 0.0036 | 0.0087 ± 0.0001 | 0.0482 ± 0.0028 | 55.6 ± 1 | | | |
| 37.1 | 1582 | 7.1 | 0.0046 | 12 | 9 | 0.0008 | 0.0589 ± 0.0029 | 0.0087 ± 0.0001 | 0.0493 ± 0.0022 | 55.7 ± 1 | | | |
| 38.1 | 860 | 5.1 | 0.0061 | 7 | 8 | 0.0013 | 0.0545 ± 0.0080 | 0.0086 ± 0.0001 | 0.0460 ± 0.0066 | 55.2 ± 1 | | | |
| 40.1 | 856 | 6.2 | 0.0075 | 7 | 8 | 0.0013 | 0.0600 ± 0.0046 | 0.0085 ± 0.0002 | 0.0510 ± 0.0037 | 54.8 ± 1 | | | |
| 64.1 | 1443 | 4.0 | 0.0029 | 12 | 11 | 0.0010 | 0.0573 ± 0.0028 | 0.0089 ± 0.0001 | 0.0468 ± 0.0021 | 57.0 ± 1 | | | |
| **Cores** | | | | | | | | | | | | | |
| 7.1 | 289 | 110.9 | 0.396 | 124 | 24 | 0.0002 | 8.0061 ± 0.1506 | 0.3961 ± 0.0062 | 0.1466 ± 0.0013 | 2151 ± 29 | 2232 ± 17 | 2307 ± 15 | 7 |
| 14.1 | 304 | 110.8 | 0.376 | 104 | 23 | 0.0003 | 5.0654 ± 0.0823 | 0.3227 ± 0.0042 | 0.1139 ± 0.0009 | 1803 ± 20 | 1830 ± 14 | 1862 ± 15 | 3 |
| 19.1 | 409 | 80.7 | 0.204 | 125 | 23 | 0.0002 | 4.7120 ± 0.0711 | 0.3011 ± 0.0038 | 0.1135 ± 0.0008 | 1697 ± 19 | 1769 ± 13 | 1856 ± 12 | 9 |
| 41.1 | 335 | 127.1 | 0.392 | 116 | 14 | 0.0002 | 5.3063 ± 0.1187 | 0.3265 ± 0.0058 | 0.1179 ± 0.0014 | 1821 ± 28 | 1870 ± 19 | 1924 ± 21 | 5 |
| **Sample AH-02-27** Coarse grained granitic leucosome, leucosome is not folded and crosscuts the main transposition foliation and pre-F2 leucosome | | | | | | | | | | | | | |
| **Rims** - Mean $^{206}Pb/^{238}U$ age 54.2 +/- 0.8 | | | | | | | | | | | | | |
| 1.3 | 2175 | 37.1 | 0.018 | 17 | 11 | 0.0007 | 0.0575 ± 0.0037 | 0.0084 ± 0.0001 | 0.0495 ± 0.0030 | 54.0 ± 1 | | | |
| 49.1 | 2255 | 44.6 | 0.020 | 18 | 15 | 0.0009 | 0.0529 ± 0.0035 | 0.0089 ± 0.0003 | 0.0432 ± 0.0024 | 57.0 ± 2 | | | |
| 64.1 | 2288 | 39.3 | 0.018 | 17 | 12 | 0.0007 | 0.0543 ± 0.0024 | 0.0085 ± 0.0001 | 0.0466 ± 0.0019 | 54.3 ± 1 | | | |
| 70.1 | 1782 | 31.3 | 0.018 | 13 | 10 | 0.0008 | 0.0537 ± 0.0021 | 0.0084 ± 0.0001 | 0.0467 ± 0.0016 | 53.6 ± 1 | | | |
| **Cores** | | | | | | | | | | | | | |
| 1.1 | 132 | 53.1 | 0.416 | 49 | 7 | 0.0002 | 5.876 ± 0.1111 | 0.3507 ± 0.0061 | 0.1215 ± 0.0007 | 1938 ± 29 | 1958 ± 17 | 1979 ± 10 | 2 |
| 1.2 | 224 | 123.4 | 0.569 | 76 | 5 | 0.0001 | 5.193 ± 0.1584 | 0.3075 ± 0.0089 | 0.1225 ± 0.0008 | 1728 ± 44 | 1852 ± 26 | 1993 ± 12 | 13 |
| 3.1 | 356 | 53.9 | 0.156 | 177 | 13 | 0.0001 | 11.211 ± 0.1457 | 0.4764 ± 0.0058 | 0.1707 ± 0.0006 | 2511 ± 25 | 2541 ± 12 | 2564 ± 6 | 2 |
| 3.2 | 191 | 44.3 | 0.240 | 81 | 17 | 0.0003 | 8.698 ± 0.2538 | 0.3973 ± 0.0103 | 0.1588 ± 0.0017 | 2157 ± 48 | 2307 ± 27 | 2443 ± 18 | 12 |
| 6.1 | 966 | 32.9 | 0.035 | 276 | 13 | 0.0001 | 4.640 ± 0.0663 | 0.2955 ± 0.0035 | 0.1139 ± 0.0008 | 1669 ± 17 | 1756 ± 12 | 1862 ± 12 | 10 |
| 8.1 | 277 | 38.9 | 0.145 | 95 | 9 | 0.0001 | 6.280 ± 0.0996 | 0.3383 ± 0.0048 | 0.1347 ± 0.0007 | 1878 ± 23 | 2016 ± 14 | 2160 ± 10 | 13 |
| 47.1 | 311 | 256.2 | 0.850 | 134 | 7 | 0.0001 | 6.464 ± 0.1285 | 0.3623 ± 0.0067 | 0.1294 ± 0.0007 | 1993 ± 32 | 2041 ± 18 | 2090 ± 10 | 5 |
| 49.2 | 448 | 187.4 | 0.432 | 167 | 16 | 0.0001 | 6.126 ± 0.0919 | 0.3466 ± 0.0044 | 0.1282 ± 0.0009 | 1918 ± 21 | 1994 ± 13 | 2073 ± 12 | 7 |
| 64.2 | 241 | 203.8 | 0.875 | 106 | 18 | 0.0002 | 6.448 ± 0.1341 | 0.3695 ± 0.0062 | 0.1266 ± 0.0013 | 2027 ± 29 | 2039 ± 18 | 2051 ± 18 | 1 |

[a]Analysis are denoted as follows: the first number refers to the zircon grain, the number after the decimal refers to location on grain. [b]Radiogenic Pb. [c]errors are 1σ reported as Ma. [d]Discordance = 100x[1-($^{206}Pb/^{238}U$ age)/($^{207}Pb/^{206}Pb$)]; values not quoted for grains younger than 800 Ma.

**Table 1-3.** Continued.

| spots[a] | U (ppm) | Th (ppm) | Th/U | Pb*[b] (ppm) | $^{204}$Pb (ppb) | $^{204}$Pb/$^{206}$Pb | $^{207*}$Pb/$^{235}$U | $^{206*}$Pb/$^{238}$U | $^{207*}$Pb/$^{206*}$Pb | Ages (Ma)[c] $^{206}$Pb/$^{238}$U | $^{207}$Pb/$^{238}$U | $^{207}$Pb/$^{206}$Pb | Disc.[d] (%) |
|---|---|---|---|---|---|---|---|---|---|---|---|---|---|
| **Sample AH-02-29** Coarse grained crosscuts all generation of leucosome and the main transposition foliation | | | | | | | | | | | | | |
| **Rims -** $^{206}$Pb/$^{238}$U age 53 +/- 1, 55 +/- 3 | | | | | | | | | | | | | |
| 2.1 | 374 | 2 | 0.01 | 3 | 28 | 0.0091 | 0.0367 ± 0.0137 | 0.0082 ± 0.0002 | 0.0325 ± 0.0120 | 52.5 ± 1 | | | |
| 33.1 | 110 | 0.5 | 0.005 | 1 | 29 | 0.0224 | 0.1152 ± 0.0530 | 0.0085 ± 0.0006 | 0.0981 ± 0.0439 | 54.7 ± 4 | | | |
| **Cores** | | | | | | | | | | | | | |
| 1.1 | 428 | 189 | 0.46 | 171 | 25 | 0.0002 | 6.2568 ± 0.0874 | 0.3679 ± 0.0046 | 0.1233 ± 0.0006 | 2020 ± 22 | 2012 ± 12 | 2005 ± 8 | -1 |
| 6.1 | 100 | 65 | 0.67 | 45 | 27 | 0.0008 | 6.9457 ± 0.1355 | 0.3918 ± 0.0058 | 0.1286 ± 0.0014 | 2131 ± 27 | 2105 ± 17 | 2079 ± 20 | -3 |
| 8.1 | 604 | 341 | 0.58 | 214 | 9 | 0.0001 | 5.4911 ± 0.0688 | 0.3193 ± 0.0038 | 0.1247 ± 0.0003 | 1786 ± 19 | 1899 ± 11 | 2025 ± 5 | 12 |
| 11.1 | 409 | 197 | 0.50 | 169 | 28 | 0.0002 | 6.6351 ± 0.1078 | 0.3780 ± 0.0057 | 0.1273 ± 0.0006 | 2067 ± 27 | 2064 ± 14 | 2061 ± 8 | 0 |
| 12.1 | 224 | 94 | 0.43 | 102 | 12 | 0.0001 | 8.3893 ± 0.1318 | 0.4214 ± 0.0057 | 0.1444 ± 0.0010 | 2267 ± 26 | 2274 ± 14 | 2280 ± 12 | 1 |
| 28.1 | 281 | 145 | 0.53 | 113 | 20 | 0.0002 | 6.1604 ± 0.1390 | 0.3675 ± 0.0062 | 0.1216 ± 0.0016 | 2018 ± 29 | 1999 ± 20 | 1979 ± 23 | -2 |
| 36.1 | 87 | 45 | 0.54 | 34 | 12 | 0.0005 | 6.0737 ± 0.1502 | 0.3555 ± 0.0059 | 0.1239 ± 0.0020 | 1961 ± 28 | 1986 ± 22 | 2013 ± 29 | 3 |
| 37.1 | 448 | 185 | 0.43 | 164 | 11 | 0.0001 | 5.8664 ± 0.1175 | 0.3407 ± 0.0059 | 0.1249 ± 0.0010 | 1890 ± 29 | 1956 ± 18 | 2027 ± 14 | 7 |
| 59.1 | 998 | 1077 | 1.11 | 414 | 10 | 0.0000 | 5.2812 ± 0.1195 | 0.3350 ± 0.0054 | 0.1143 ± 0.0016 | 1863 ± 26 | 1866 ± 20 | 1869 ± 26 | 0 |

[a]*Analysis are denoted as follows: the first number refers to the zircon grain, the number after the decimal refers to location on grain.* [b]Radiogenic Pb. [c]*errors are 1σ reported as* Ma. [d]Discordance = 100x[1-($^{206}$Pb/$^{238}$U age)/($^{207}$Pb/$^{206}$Pb)]; values not quoted for grains younger than 800 Ma.

# CHAPTER 2

## The S-type Ladybird leucogranite suite of southeastern British Columbia: geochemical and isotopic evidence for a genetic link with migmatite formation in North American basement gneiss of the Monashee complex


### Abstract

The 62-52 Ma Ladybird granite suite (LBG) is a peraluminous, leucocratic, S-type, leucoquartz monzonitic to granitic suite which occurs as batholiths, stocks, dikes, sills, and pegmatite veins predominantly in the high-grade rocks of the Shuswap complex, a Cordilleran metamorphic core complex in southeastern British Columbia. The emplacement of the LBG was synchronous with the production of abundant migmatites within Thor-Odin dome of the Monashee complex, an exposure of mid-crustal North American basement, exhumed from depths of ca. 26-33 km. The leucosome and the hosting ortho- and paragneiss basement migmatites were exhumed by Eocene extensional faults. The LBG suite and the leucosome from Thor-Odin dome have similar major and trace element trends, and are both characterized by zircons with inherited Precambrian cores. Whole rock Nd isotope compositions show a range of values for the LBG with $\varepsilon Nd_{(55\ Ma)}$ values from –5.0 to –17.2. The $\varepsilon Nd_{(55\ Ma)}$ of the leucosome samples range from –9.5 to –23.6, overlapping with those of the granitic suite. These data led to the interpretation of a genetic link between formation of the LBG suite and melting of North American basement rocks, such as those exposed in the core of Thor-Odin dome. The leucosome samples have lower high field strength element (HFSE) concentrations and positive Eu anomalies, while the LBG samples have higher HFSE concentrations and negative Eu anomalies. The distribution of trace elements suggests that the leucosome and LBG are related, whereby most of the leucosome samples are cumulates and the LBG samples represent residual melts. The initial $^{87}Sr/^{86}Sr$ isotope values for both the LBG and leucosome samples have a large range. However, the initial Sr isotopic ratios for the LBG suite are lower than those of the leucosome samples, with $^{87}Sr/^{86}Sr_{(55\ Ma)}$

ranging from 0.70603 to 0.73688 and 0.74256 to 0.76593, respectively. This isotopic heterogeneity suggests either: a) isotopic disequilibrium during partial melting in the mid to lower crust where the leucosome formed, b) the distribution of Sr during partial melting was controlled by different melt reactions, and/or c) isotopic heterogeneity in the source rocks. At least part of the LBG suite likely formed via melting of North American basement rocks dominated by rocks of sedimentary origin. Melting of the Proterozoic supracrustal metasedimentary rocks overlying North American basement may also have contributed regionally to the formation of phases of the suite. However, the abundant leucosome in the basement rocks of Thor-Odin dome may mark the melt migration paths for the structurally overlying Ladybird granites of the South Fosthall pluton.

## 2.1. Introduction

Peraluminous, crustally-derived granites were initially interpreted to be genetically related to migmatites, though in many instances this type of granite is now generally thought to be related to dehydration melting processes and granulite genesis (Menhert, 1968; Clemens, 1990). The latter theory is largely supported by the notion that migmatites are thought to be an ineffective way to move melt in the continental crust (Montel el al., 1992). However, exposures of migmatites and related granitic intrusions have provided, in certain instances, evidence of a link between migmatites and granitic plutons (i.e. Barbey et al., 1996; Kalsbeek et al., 2001; Johannes et al., 2003; Solar and Brown, 2001). This link is further supported by the interpretation that the leucosome portion of most migmatites represent a component of a partial melt and that migmatites can represent initial stages of crustal anatexis (Ashworth, 1985; Sawyer, 1987; Brown et al., 1995; Barbey et al., 1996; Jung et al., 2000; Kriegsman, 2001).

The relationship between spatially associated, coeval migmatites and granite plutons can be as follows: a) leucosome in migmatites may represent a link between high-grade metamorphism and large-scale granitic intrusions (Brown and D'Lemos, 1991); b) leucosome may have either fed, or represent crystal fractionation from, the spatially and temporally related granitic bodies (Kalsbeek et al., 2001; Johannes et al., 2003; Solar and Brown, 2001); c) leucosome may represent healed pathways that granitic melts followed during emplacement in the crust (Barbey et al., 1996); d) migmatites may represent the arrested stage of granite formation (Obata et al., 1994); e) migmatites may represent contact metamorphic effects induced by emplacement of temporally associated plutons (Pattison and Harte, 1988; Jung et al., 2000); or, f) there may be no genetic relationship between migmatite formation and spatially associated granites (White and Chappell, 1990). As there are a variety of possible interpretations of spatially and temporally associated migmatites and plutons, various field and laboratory methods are necessary to assess any relationship.

This paper evaluates the potential genetic link between coeval migmatites and Paleocene-Eocene S-type leucogranites in the Omineca Belt of southeastern British Columbia. Precambrian North American basement rocks of the Monashee complex are exposed in structural culminations that were exhumed during early Tertiary extension and tectonic denudation (Fig. 2-1; Parrish et al., 1988). The Monashee complex, consisting of high-grade migmatitic Paleoproterozoic basement rocks and overlying cover rocks, represents one of the deepest exposed structural levels in the southern Canadian Cordillera. In Thor-Odin dome, in the southern part of the complex, the basement rocks underwent progressive deformation and migmatization. The basement gneiss in the core of the dome was migmatized at ca. 56-52 Ma based on U-Pb zircon geochronology studies (Vanderhaeghe et al., 1999; Hinchey et al., 2004; Hinchey, Chapter 1). The production of leucosome was coincident with emplacement of part of the structurally overlying Ladybird granite suite (LBG) at ca. 62-52 Ma based on U-Pb zircon geochronology studies (Carr, 1992). Genetic linkages have been proposed between basement para- and orthogneiss melting and the formation of the extensive granitic bodies. Vanderhaeghe et al. (1999) and Hinchey and Carr (2003) have suggested that the melt leucosome in structurally deeper migmatites may have been the source of the LBG. This study evaluates the potential genetic link between melting in the basement rocks and granite emplacement through field relations, detailed petrography, major and trace element geochemistry, and Rb-Sr, Sm-Nd isotopic studies on samples from both the basement leucosome and LBG.

## 2.2. Regional Geology

The Canadian Cordillera formed as a result of the Paleozoic to Paleogene accretion of fragments of allochthonous and parautochthonous oceanic sequences, continental slivers, volcanic arcs and sedimentary sequences to the western edge of ancestral North America (Monger, 1989). Mesozoic – Paleogene crustal thickening occurred during collision with accreted terranes and westward underthrusting of the North American plate (Fig. 2-1;

Monger et al., 1982; Monger, 1989; Gabrielse and Campbell, 1991). By the Middle Jurassic, accreted terranes had begun overriding the pericratonic terranes and Proterozoic and Paleozoic to early Mesozoic platformal sedimentary sequences that had accumulated on the paleomargin of North America (Monger et al., 1982). By the mid-Cretaceous, a 50-60 km thick crustal welt and a foreland basin had formed and during the Cretaceous the Rocky Mountain fold and thrust belt (Foreland belt) formed (Price and Mountjoy, 1970; Coney and Harms, 1984; Brown et al., 1986; Price, 1986). Crustal thickening and burial of the North American sedimentary sequence and overriding terranes resulted in metamorphism and deformation of rocks in the hinterland of the Rocky Mountain fold and thrust belt (Foreland belt), termed the Omineca belt (Fig. 2-1; Reesor, 1970; Brown and Read, 1983 and references therein). In the Early Tertiary, southern British Columbia underwent a change from a transpressional to transtensional regime, attributed to changes in far field stresses related to the obliquity of the down-going Kula plate (Lonsdale, 1988; Andronicos et al., 2003). This resulted in Eocene regional extension, and the exhumation of some of the high-grade rocks of the southern Omineca belt via an array of generally north-south striking, brittle and ductile normal faults, which are linked to synchronous strike-slip fault systems that span the western Cordillera (Ewing, 1981; Tempelman-Kluit and Parkinson, 1986; Brown and Journeay, 1987; Parrish et al., 1988; Struik, 1993; Johnson and Brown 1996 and references therein). In the southern Omineca belt, the lower plates of regional extensional fault systems expose high-grade rocks with relatively young deformation and cooling histories in a Cordilleran metamorphic core complex (Armstrong, 1972; Coney, 1980; Parrish et al., 1988).

The southern Omineca belt is characterized by metamorphic and plutonic rocks, structural culminations and belts of high-grade rocks. The Shuswap complex (Fig. 2-1) is defined as a composite metamorphic core complex, bounded on the eastern and western margins by generally north-striking, outward-dipping Eocene normal faults. It is bounded by the 58-50 Ma Columbia River fault (CR) to the east and the 56-45 Ma Okanagan

Valley-Eagle River fault system (OV-ER) to the west (Okulitch, 1984; Brown and Journeay, 1987; Parrish et al., 1988; Parkinson, 1992; Bardoux, 1993; Johnson, 1994). The Shuswap complex contains individual gneiss complexes, most of which are bounded, at least on one side, by Eocene extensional faults (Parrish et al., 1988). The hanging wall rocks of both the CR and the OV-ER faults record older peak metamorphism (ca. 175 to 135 Ma) and are generally at lower grade than the footwall rocks (Parrish, 1995; Johnson and Brown, 1996). The Monashee complex, a basement-cored gneiss complex, and the structurally overlying metasedimentary rocks of the Middle Crustal Zone are contained within the Shuswap complex (Fig 2-1).

The Monashee complex contains two domal culminations, the Thor-Odin and Frenchmen Cap domes, that comprise Paleoproterozoic basement of North American cratonic affinity (Fig. 2-1; Armstrong et al., 1991) complexly infolded with unconformably overlaying Paleoproterozoic to Paleozoic platformal metasedimentary gneisses of the cover sequence (Wheeler, 1965; Reesor and Moore, 1971; Brown, 1980; Crowley, 1997). In both domes of the Monashee complex, Cordilleran orogenesis resulted in middle amphibolite to lower granulite facies metamorphism, km-scale isoclinal folds, and the development of penetrative planar and linear deformation fabrics (Wheeler, 1965; Reesor and Moore, 1971; Höy and Brown, 1980; Brown et al. 1986; Journeay, 1986; McNicoll and Brown, 1995). The dominantly metasedimentary rocks that structurally overlie and surround the Monashee complex are interpreted as an allochthonous, composite thrust sheet, termed the Selkirk allochthon. The boundary between these allochthonous rocks and the relatively more autochthonous rocks of the Monashee complex is referred to as the Monashee décollement (MD; Read and Brown, 1981; Brown et al., 1986; Journeay, 1986; Brown et al, 1992; McNicoll and Brown, 1995; Brown and Gibson, in press).

Periods of metamorphism, deformation and plutonism occurred within a 120 million year interval in the southern Omineca belt and events have been documented at ca. 175-

160, ca. 140, 100-90, 75-60 and 60-55 Ma (Digel et al., 1998; Sevigny et al., 1989, 1990; Scammell, 1993; Parrish, 1995; Vanderhaeghe et al., 1999; Gibson, 2003; Crowley et al., 2003; Reid, 2003; Carr and Simony, in review). Parrish (1995) synthesized known timing of deformation in the southern Omineca belt and suggested that there was a preservation of progressively younger strain and deformation with deeper structural levels, implying progressive incorporation of deeper and more inboard rocks through time. However, recent studies have shown that the relationships between structural level, deformation, and metamorphism are more complicated than this interpretation, and in order to understand the construction of the Omineca belt it is necessary to document these relationships at all structural levels. Metamorphic belts may overprint and crosscut older events. For example, the Cretaceous Cariboo – Monashee – Selkirk metamorphic high transects Middle Jurassic regional metamorphism, while in other locations younger, or successions of younger, events may reactivate, overprint and/or partially overlap with older events in a concordant fashion. (Digel et al., 1998; Gibson, 2003; Crowley et al., 2003; Reid, 2003; Carr and Simony, in review).

In southern British Columbia, periods of arc magmatism occurred during both the Middle Jurassic to late Paleocene transpressional history, as terranes were accreted to the North American continental margin, and during Eocene extensional tectonism (Armstrong, 1988; Carr et al., 1987; Parrish et al., 1988; Carr, 1992). The extensive plutonic activity throughout the southern Canadian Cordillera occurred from the Late Triassic to Eocene and is divided into four main magmatic episodes: a) Late-Triassic-Early Jurassic (215-190 Ma); b) Middle-Late Jurassic (180-150 Ma); c) Cretaceous (120-80 Ma); and d) Early Tertiary (60-45 Ma; Armstrong, 1988).

The Early Tertiary magmatic episode included widespread Paleocene - Eocene plutonism that varies in composition and structural style. Within the Shuswap complex, Paleocene - Eocene plutonism is dominated by the LBG (Fig. 2-1). This 62-52 Ma peraluminous leucogranite suite occurs as synkinematic sheets in both compressional

and extensional shear zones, and as late kinematic stocks, plutons and batholiths (Carr, 1992). The bulk of this suite is 55 Ma and occurs between the OV-ER fault system and the Slocan Lake fault (SL; Fig. 2-1). Sevigny et al. (1989) concluded that the 62 Ma peraluminous granites north of the Monashee complex likely formed via partial melting of a pelitic source. As these granites are geochemically similar and coeval with the LBG, they may represent a northern extension of the suite.

The generation of S-type leucogranites in the southern Omineca belt was followed by the intrusion of the 52 Ma, syn-extension to post-tectonic Coryell suite that is dominated by syenites. This suite has an isotopic signature that suggests incorporation of minor old crustal materials by more primitive, possibly mantle derived, magma (Ghosh, 1995). Extension is also marked in the region by intrusion of swarms of Eocene granitic and lamprophyre dykes (Parrish, 1991). Thermal cooling in the Shuswap complex generally occurred in the Early Tertiary (Parrish, 1995).

## 2.3. Geological setting of the study

The study encompasses the Thor Odin dome basement rocks and Middle Crustal Zone rocks in the structurally overlying Thor Odin - Pinnacles area in the southern Omineca belt (Fig. 2-1). The basement rocks of Thor-Odin dome are composed of heterogeneous migmatitic para- and orthogneisses (Fig. 2-2). Basement orthogneiss are dominated by migmatitic hornblende-biotite-quartzo feldspathic gneiss with a lesser volume of quartz monzonite gneiss. Basement paragneiss comprise: a) heterogeneous migmatitic garnet-sillimanite-quartzo feldspathic gneiss that are locally enriched in garnet and cordierite products of dehydration melting, b) migmatitic cordierite-biotite-quartzo feldspathic gneiss, and c) minor calc-silicates, marbles, and quartzites and are associated with minor cordierite-gedrite rocks and amphibolites (Reesor and Moore, 1971; Duncan, 1984). Though lithologically distinct, the basement ortho- and paragneisses are often interlayered at the scale of a few meters, due in large part to transposition by folding, with contacts that are complicated by the abundance of leucosome. Initial U/Pb geochronology

studies of zircons from basement orthogneiss yielded crystallization ages of 1934 ± 6 and 1874 ± 21 Ma (Parkinson, 1992). Deposition of the basement paragneiss in Thor-Odin dome likely began by 2.2 Ga, based on a detrital zircon study of a basement paragneiss (Parkinson, 1992) and continued to 1.8 Ga, based on the youngest detrital grains from basement paragneisses (Vanderhaeghe et al., 1999; Kuiper, 2003; Hinchey, Chapter 1). The sequence of supracrustal rocks interpreted to have been deposited on the basement rocks is termed the "cover rocks." The cover rocks comprise a heterogeneous assemblage of metasedimentary rocks that includes quartzites, pelitic schists, marbles, calc-silicates, and amphibolites. A preliminary detrital geochronology study on basal units of the cover gneiss yielded Paleoproterozoic zircons as young as 1825 ± 5 Ma (Kuiper, 2003). There are no constraints on an upper age limit for the cover sequence and the youngest depositional age in Thor-Odin dome is uncertain.

Leucosome occurs pervasively throughout the gneiss of Thor-Odin dome (Fig. 2-2). Leucosome is interpreted to have formed as a result of *in situ* melting of the adjacent gneisses (Hinchey, Chapter 1). Peak pressures on the order of 8 to 10 Kbar (Norlander et al., 2002) place constraints on depth of burial at 26-33 km. Leucosome formation was ongoing from ca. 56-52 Ma, coincident with peak metamorphism, formation of at least part of the $S_2$ foliation, and large $F_2$ folds, as well as $F_3$ and $F_4$ folds (Hinchey, Chapter 1). During the anatectic event, the basement paragneiss of Thor-Odin dome were rich in fertile pelites and greywackes, providing an obvious source material for the peraluminous, S-type leucogranites that are widespread in the Paleocene-Eocene of the southern Omineca belt.

The LBG suite is hosted as dykes, sills, sheets and plutons within predominantly supracrustal rocks of the Middle Crustal Zone of the Shuswap complex. The peraluminous nature of the granites led to the initial suggestion that the Ladybird granites likely formed via *in situ* melting (Carr, 1992). The South Fosthall pluton is part of the Ladybird granite suite and is the intrusion most proximal to Thor-Odin dome. The

South Fosthall pluton is predominantly composed of sheet-like bodies of dominantly pegmatitic leucogranites. Two locales in the South Fosthall pluton yielded U-Pb zircon and monazite ages of 55 ± 1.5 Ma, and 55 ± 0.1 Ma (Parrish et al., 1988; Carr et al., 1992) and large populations of Proterozoic detrital zircon (Vanderhaeghe et al., 1999). A third age constraint is from a pegmatite dyke of Ladybird granite near Sugar Lake that had a U-Pb zircon age of 60.5 +/- 0.5 Ma (Carr et al., 1992). These ages overlap with the range of Thor-Odin dome leucosome ages of ca. 56 to 52 Ma (Vanderhaeghe et al., 1999; Hinchey, Chapter 1). Due to its proximity to Thor-Odin dome, as well as its known structural setting and age relations, the South Fosthall pluton was chosen to study the link between melting of basement migmatitic gneisses and granite emplacement. Mapping and sampling was carried out east of Sugar Lake and Mt. Baldur (South Fosthall creek area; Fig. 2-1). The boundary of the South Fosthall pluton was originally mapped with a focus on screens of metasedimentary rocks with greater or less then 50% pegmatite dykes by Reesor and Moore (1971), and was extensively re-mapped with a focus on the strain variations within the Ladybird granite sheets and relationship with extensional structures by Carr (1990). An isotopic study by Ghosh (1995) of 3 samples of the Ladybird granite suite, from intrusions 120 km south of the South Fosthall pluton, was part of a regional study of the variation in magmatism across the southern Canadian Cordillera. One sample of the LBG was from within the Valhalla complex and two samples were from the LBG intrusion between the Greenwood Fault and the OV-ER. Ghosh (1995) reported high initial $^{87}Sr/^{86}Sr$ values ranging from 0.70642 to 0.78943, and low εNd values ranging from -6.8 to -13.7 characteristic of granitic melts that have significant crustal contributions.

### *2.3.1. Leucosome of Thor-Odin dome*

Leucosome occurs pervasively throughout the gneisses of Thor-Odin dome (Reesor and Moore, 1970; Spark, 2001; McNeill and Williams, 2003). Initial studies suggested there may be as many as three generations of leucosome production associated with two main melting events; one during the Precambrian and the other during the Cordilleran

orogeny (Reesor and Moore, 1970; Spark, 2001; McNeill and Williams, 2003). However, Hinchey et al. (2004) demonstrated based on U-Pb geochronology that leucosome production in Thor-Odin dome was restricted to a ca. 56 to 52 Ma Cordilleran event, findings consistent with data from Vanderhaeghe et al. (1999) and Kuiper (2003). Three styles of leucosome are preserved in the dome: folded stromatic leucosome, phenocrystic vein, and pegmatitic vein (Fig. 2-2a and b). Leucosome formation was a product of dehydration melting (Hinchey, Chapter 1). The following description of the leucosome is summarized from Hinchey (Chapter 1). Migmatite terminology and definitions are from Ashworth (1985) modified from Mehnert (1968).

The folded stromatic leucosome is the dominant type of leucosome and generally forms part of a stockwork of interconnected veinlets with a well-developed thin melanosome dominated by biotite (Fig. 2-2a and b). The leucosome parallels the main transposition foliation ($S_2$), contains a slight foliation defined by the alignment of biotite grains, and is tight to isoclinally folded. The phenocrystic vein type of leucosome is coarse grained, granitic in composition, and has a variable thickness of melanosome dominated by aggregates of coarse biotite crystals. This leucosome is dominated by phenocrysts of potassium feldspar, plagioclase and biotite. This type of leucosome is not folded, does not contain a foliation, and crosscuts the main transposition foliation and the folded stromatic leucosome. The third type of leucosome, pegmatitic vein type, is very coarse grained and granitic in composition. This leucosome is undeformed and crosscuts both concordant stromatic and phenocrystic leucosome types, as well as the main transposition foliation.

All leucosome types have similar modal mineralogy, characterized by quartz + potassium feldspar (orthoclase) + plagioclase ($An_{12}$ to $An_{33}$) + biotite ± apatite ± ilmenite ± rutile (Fig. 2-2c). The quartz, plagioclase, and potassium feldspar primarily occur as euhedral to anhedral grains and often contain abundant inclusions of smaller biotite grains and iron-titanium oxides. Myrmekitic intergrowths of plagioclase and quartz

are common, as are primary igneous albite and carlsbad twinning in plagioclase and potassium feldspar, phenocrysts and cumulate textures.

*2.3.2. South Fosthall pluton*

In the Mt. Baldur area, the LBG intrudes as sheets that contain extensive xenoliths of the host gneisses (Fig. 2-3a). This area is dominated by medium- to coarse-grained and locally pegmatitic biotite leucogranite, with 20 % xenolithic material that is generally 10-20 meter thick and as long as 500 meters. Some areas are rich in muscovite, tourmaline and garnet; these generally occur near zones of abundant xenoliths. Xenoliths include garnet amphibolite gneiss, and heterogeneous biotite quartzo-feldspathic paragneiss with interlayers of quartzite and calc-silicate. Despite the abundance of xenoliths, the LBG at Mt. Baldur is relatively homogenous in composition with only slight variations related to the presence of local mineral phases such as garnet and tourmaline. In the Sugar Lake area, the intrusion is characterized by a medium-grained leucogranite, with few xenoliths (Fig. 2-3b).

The South Fosthall pluton has a relatively consistent mineralogy. The rocks are dominantly medium- to coarse-grained muscovite-biotite leucogranite. The leucogranites characteristically contain equigranular, euhedral to subhedral, potassium feldspar (orthoclase), quartz, and plagioclase ($An_{21}$ to $An_{28}$), with accessory phases of biotite and muscovite (Fig. 2-3c). Potassium feldspar often contains biotite inclusions. Primary igneous albite and carlsbad twins are common in plagioclase and potassium feldspar. The fabric in the South Fosthall pluton is variable. Igneous textures such as euhedral grains, cumulate textures, and phenocrysts are preserved in low strain areas whereas the intensity of foliation and lineation varies depending on the proximity to shear zones that are Eocene or younger. Deformed samples often have a preferred orientation of biotite, muscovite, and undulose quartz.

## 2.4. Analytical data and interpretation

### *2.4.1. Major and trace element geochemistry*

Major elements, recalculated to an anhydrous total of 100%, and trace element compositions of 13 samples from all three types of leucosome and 16 samples from the Ladybird granite suite were analyzed. Three samples of the Ladybird granite were collected from the Slocan Lake area, in Valhalla complex, for comparison. In addition, six samples of basement gneisses including four samples of basement paragneiss and two samples of basement orthogneiss were analyzed for the purposes of comparison. Sample description and locations are listed in Table 2-1. Major and trace element data are presented in Table 2-2. Details of analytical methods are described in Appendix A.1.

#### *2.4.1.1.* Ladybird granite suite

On the basis of major and trace element analyses, there are no chemical distinctions between LBG samples from the South Fosthall pluton and LBG samples from the Valhalla complex; therefore, all samples are treated as one group. The compositions of the LBG samples define a tight cluster on a Q-A-P diagram with all samples falling in the granite category (Fig. 2-4). All samples are uniformly felsic and peraluminous on the Shand's index, with $K_2O$ of ~5.5 wt.%, $Na_2O$ of 3.4 wt.% and CaO of < 1.1 wt.% (Fig. 2-5). $SiO_2$ and $Al_2O_3$ contents range from 69 to 74 wt.% and from 14 to 16 wt.%, respectively. $Na_2O$ is constant despite increasing $SiO_2$ levels, while $Al_2O_3$, $Fe_2O_3$, CaO, MgO, and $TiO_2$ tend to decrease slightly with increasing $SiO_2$. The mean major element concentrations for the LBG samples are shown in Figure 2-6, and mean values and associated standard deviations are presented in Table 2-2. The trace element composition of these rocks exhibit large ranges in the low field strength elements, as defined by Saunders et al. (1980), of Ba (221-4032 ppm, mean = 1227) and Sr (88-1329 ppm, mean = 352; Fig. 2-7). Most trace element patterns, including those of Sr, Ba and Y, are consistent with major element trends, including those of CaO, MgO and $Fe_2O_3$, and show

a slight decrease in concentration with increasing $SiO_2$ content.

The chondrite-normalized rare earth element (REE) patterns of the LBG samples are fractionated. Most samples have $La_{(N)}/Yb_{(N)}$ between 80 and 150 times chondrite, whereas six samples have slightly lower ratios with values between 4 and 27 times chondrite, reflecting a localized enrichment of garnet (Fig. 2-8a). The samples have a slight to high negative Eu anomaly, with Eu/Eu* values of 0.06 to 0.04 (Table 2-2). On an extended trace element primitive-mantle normalized spider diagram, the LBG samples exhibit enrichments in elements such as Cs, Rb, Ba, Th, U, Pb and light REEs relative to primitive mantle, and negative Nb-Ta and Ti anomalies (Fig. 2-8c).

*2.4.1.2.* Leucosome from Thor-Odin dome

All but one of the leucosome samples fall within the granite category on a Q-A-P diagram, with the one sample falling in the tonalite category (Fig. 2-4). All of the samples are felsic and peraluminous on the Shand's index (Fig. 2-5), and show little variation in most major element compositions. $SiO_2$ contents range from 71 to 76 wt.% and $Al_2O_3$ ranges from 12 to 15 wt.% (Table 2-2). $Na_2O$ and $Al_2O_3$ remain constant despite increased $SiO_2$ levels, whereas $Fe_2O_3$, CaO, MgO, and $TiO_2$ tend to decrease with increasing $SiO_2$. The mean major element concentrations for the leucosome samples are shown in Figure 2-6. The trace element composition of these rocks exhibit large ranges in the low field strength elements of Ba (16-1483 ppm, mean = 877) and Sr (14-383 ppm, mean = 232; Fig. 2-7). Trace element variations, including those of Sr, Ba and Y, are consistent with major element trends, including those of CaO, MgO and $Fe_2O_3$, exhibiting a slight decrease in concentration with increasing $SiO_2$ content.

The chondrite-normalized REE patterns of the leucosome samples are fractionated with $La_{(N)}/Yb_{(N)}$ ranging between 1.5 and 50 times that of chondrite (Fig. 2-8b). In general, samples with higher $SiO_2$ concentrations exhibit less fractionation of $La_{(N)}/Yb_{(N)}$. Most leucosome samples show a flat to strongly positive Eu anomaly with Eu/Eu* values of 0.19 to 1.6; however, two samples show a conspicuous negative Eu anomaly with Eu/

Eu* values of 0.058 to 0.041 (Table 2-2). On an extended trace element primitive-mantle normalized spider diagram, the samples exhibit large enrichments in Cs, Rb, Ba, Th, U, Pb, Sr and light REEs relative to primitive mantle, and negative Nb-Ta and Ti anomalies (Fig. 2-8c).

*2.4.1.3.* Comparison of geochemistry of the Ladybird granite, leucosome, and basement gneiss

The major and trace element compositions of the LBG samples and leucosome are similar in that most samples are peraluminous and granitic in composition. In major element chemistry, the LBG and leucosome samples are generally indistinguishable and have similar concentrations of elements (Fig. 2-6). The leucosome samples do show a larger range in certain major elements, including $Al_2O_3$, CaO, and $K_2O$.The peraluminous nature is compatible with the LBG being an S-type leucogranite, as classified by Chappell and White (2001), with the leucosome samples also falling within this category. In terms of trace element chemistry, the LBG samples tend to have higher concentrations of the high field strength elements (HFSE) such as Hf, Zr, and Nb, than the leucosome samples (Fig. 2-7). In addition, the LBG samples generally have higher LREE concentrations and typically display negative Eu anomalies, whereas most of the leucosome samples have positive Eu anomalies. The implications of these characteristics are discussed below. The REE and extended trace element patterns of both the LBG and leucosomes, when compared with the average granite and average S-type granite composition (Fig. 2-8c), show very similar trends and concentrations of elements. The overall geochemical signature of the leucosome and LBG is compatible with granitic melts that are generated via partial melting (dehydration reactions) of the felsic middle to lower crust.

The basement gneiss exhibits a range in major and trace element chemistry which generally overlaps with that of the LBG and leucosome samples (Table 2-2). For most LFSE, the basement samples fall within the field of the LBG and leucosome samples; however, they often show distinct concentrations of certain HFSE, such as Nb and Ti.

Differences in the trace element concentration between the host basement gneiss and the leucosome samples likely reflect fractionation of elements and preferential melt migration of the LFSE relative to the HFSE and REE during partial melting (Sawyer, 1998). A similar chemistry of the host gneiss and *in situ* leucosome is not expected. Depending on degrees of partial melting, melt extraction, and equilibrium melting, the mass balance of leucosome and melanosome would not necessarily yield a protolith composition the same as the restitic composition (Sawyer, 1998; Kriegsman, 2001).

### *2.4.2. Whole rock radiogenic isotope geochemistry*

Rubidium-strontium and neodymium-samarium data for whole rock samples of selected LBG and leucosome are presented in Table 2-3. Analytical details are given in Appendix A.1. Ten leucosome and thirteen LBG whole rock samples were analyzed. In addition, four samples of basement gneiss were analyzed for the purposes of comparison, including two samples of basement paragneiss and two samples of basement orthogneiss (Table 2-3).

#### *2.4.2.1.* Sr isotopes

The LBG samples have highly variable and radiogenic $^{87}Sr/^{86}Sr$ ratios that range from 0.70626 to 0.73812 with initial ratios of 0.70603 to 0.73646, calculated at 55 Ma based on U-Pb zircon ages (Carr, 1992). The $^{87}Rb/^{86}Sr$ ratios range from 0.29 to 7.35 (Fig. 2-9). The leucosome samples have higher measured $^{87}Sr/^{86}Sr$ ratios ranging from 0.74341 to 0.76718 with initial ratios ranging from 0.74256 to 0.76593, calculated at 55 Ma for comparison with the LBG; details of the calculation are given in Table 2-3. The $^{87}Rb/^{86}Sr$ ratios of the leucosome define a tighter group than the LBG samples, with ratios that range from 0.56 to 1.98 (Fig. 2-9).

The four basement samples overlap with both the leucosome (basement samples AH-02-28 and AH-03-18) and the LBG samples (basement samples AH-02-07 and AH-02-12; Fig. 2-9). Basement samples have measured $^{87}Sr/^{86}Sr$ ratios ranging from 0.72418

to 0.75236 and $^{87}Rb/^{86}Sr$ ratios from 0.80 to 1.79 (Fig. 2-9). The Sr isotopic ratios demonstrate the highly radiogenic nature of the Paleoproterozoic basement gneisses in the Thor-Odin dome area.

At 55 Ma, the primitive mantle had an $^{87}Sr/^{86}Sr$ value of 0.70443, calculated assuming present day values of $^{87}Sr/^{86}Sr = 0.7045$ and a bulk silicate earth $^{87}Rb/^{86}Sr$ of 0.089. The LBG samples display a wide range in radiogenic values, as do the leucosome samples; suggesting that both rock types were derived in large part from old, heterogeneous crustal material (Fig. 2-9). The differences in the range of Sr values observed between the leucosome and LBG samples are discussed below (see section 2.5.2).

*2.4.2.2.* Nd isotopes

The LBG samples have a large range in $^{147}Sm/^{144}Nd$ ratios from 0.0996 to 0.15450 and $\varepsilon Nd_{(55\ Ma)}$ values from –5.0 to –17.2. The leucosome have a similar range with $^{147}Sm/^{144}Nd$ ratios from 0.1020- 0.1521 and $\varepsilon Nd_{(55\ Ma)}$ values from –9.5 to –23.6 (Fig. 2-10). The four basement gneiss samples have $^{147}Sm/^{144}Nd$ ratios of 0.0895 to 0.1176 and $\varepsilon Nd_{(55\ Ma)}$ values of –19.8 to –27.0. The εNd was calculated at 55 Ma for direct comparison with the LBG and leucosome samples, even though the basement gneiss samples are Paleoproterozoic in age (see Hinchey, Chapter 1).

The range in $\varepsilon Nd_{(55\ Ma)}$ values observed in the LBG and leucosome samples likely reflects heterogeneity in the source material. The strongly negative $\varepsilon Nd_{(55\ Ma)}$ of both the LBG and leucosome samples indicates that the parental magmas of these rocks likely formed via partial melting of old continental crust. In addition, the data trend toward higher εNd numbers suggesting a component of mixing, isotopic disequilibrium, and/or heterogeneous source material (Fig. 2-10).

*2.4.2.3.* Isotopic composition of potential sources

The majority of peraluminous muscovite-bearing granites are interpreted as being derived by partial melting, with exception given to very rare, extreme fractionation or

local contamination (Barbarin, 1996; Sylvester, 1998). The LBG is a muscovite-bearing peraluminous leucogranite with high initial Sr ratios and is interpreted to be derived by partial melting. This is supported by the $\varepsilon Nd_{(today)}$ and Sr ratios which are far too evolved to have formed via fractional crystallization of a mantle melt based on determined mantle values $\varepsilon Nd_{(today)}$ of +6 ±1.5 and $^{87}Sr/^{86}Sr$ of 0.7040 ± 0.0005. The mantle values beneath the Cordillera are based on data from mantle xenoliths, primitive Coast Belt granitoids, and primitive late Triassic to early Jurassic granitoids (Xue et al., 1990; Sun et al., 1991; Friedman et al., 1995; Ghosh, 1995). The most likely source material for the genesis of the LBG is the North American crust, which in this region can be essentially divided into two components the North American basement gneisses, and the overlying Proterozoic supracrustal sedimentary rocks. The isotopic composition of the each component is discussed below.

To assess the isotopic composition of the North American basement gneiss in the region, the data from this study is combined with data from basement gneisses from other locale in the Monashee complex. The upper part of the crystalline basement has a range in isotopic signatures. Armstrong et al. (1991) found that $^{87}Sr/^{86}Sr_{(measured)}$ ranges from 0.7114 to 2.179 and $\varepsilon Nd_{(today)}$ ranges from –6.2 to –29.4 for crystalline basement exposed in Frenchman Cap dome. Parkinson (1991) found a range in basement ortho- and paragneiss from Thor-Odin dome, with $^{87}Sr/^{86}Sr_{(measured)}$ from 0.76306 to 0.79493 and $\varepsilon Nd_{(today)}$ from –21.7 to –31.1. Basement samples from this study show a range of values with $^{87}Sr/^{86}Sr_{(measured)}$ of 0.72418 to 0.75236 and an $\varepsilon Nd_{(today)}$ of -19.8 to -27.0. The basement gneiss of Frenchman Cap dome and Thor-Odin dome have a range of isotopic compositions, and assigning an average composition is therefore not realistic, and the North American basement gneiss are treated as having a range of values as shown on figures (e.g. Fig. 2-11).

Several studies have constrained the isotopic signatures of the Proterozoic supracrustal rocks that were deposited on North American basement rocks. For the

purpose of this paper, we evaluate the Windermere and Belt-Purcell Supergroups, which are the metasedimentary sequences most likely to overly basement rocks in the area. In addition, the cover sequence of the Monashee complex is also evaluated as a potential source of melt. Samples of the cover sequence from Thor-Odin dome essentially overlap with basement samples and have a range of $^{87}Sr/^{86}Sr_{(measured)}$ from 0.7294 to 1.938 and $\varepsilon Nd_{(today)}$ from –6.7 to –25.1 (Parkinson, 1991). The isotopic signatures for the Windermere and Belt-Purcell Supergroups are taken from: Frost and O'Nions (1984); Devlin et al., 1985; Frost and Burwash (1986); Frost and Winston (1987); Burwash et al. (1988); Devlin et al. (1988); Burwash and Wagner (1989); Ross et al. (1993) and Anderson and Goodfellow (2000). The fields defined by this data are plotted in Figure 2-11.

## 2.5. Discussion

### *2.5.1. Petrogenesis of the Ladybird granite suite*

The geochemical, isotopic and petrographic characteristics of the LBG samples support the formation of these leucogranites by the melting of a crustal source. The peraluminous nature of the leucogranites, in combination with the inherited zircons with a wide range of ages (Carr, 1992), is typical of S–type granite and indicates that the crustal source was likely metasedimentary. The trace element composition of the LBG samples is compatible with granites that formed deep in the crust where garnet is stable, thus fractionating the HREE. This is supported by the enrichment of HREE in the two samples (AH-03-32 and AH-03-38) that contain xenocrysts of garnet. In addition, the positive Eu anomaly, negative Nb-Ta anomaly, negative Ti anomaly, and enrichment in incompatible element (i.e. Sr, La, and Ba) are all consistent with magmas that formed via partial melting of the continental crust. Considering all geochemical evidence, including major and trace element composition, isotopic composition, and peraluminous nature, a pelitic-dominated source material is likely for the leucogranites.

The range in values for both the Sr and Nd isotopes indicate that the LBG plutons are isotopically heterogeneous. Significant amounts of crustal contamination are required to explain the isotopic signatures. There were no observed correlations between the geochemistry or isotopic signature and sample locality or age (i.e. Sugar Lake, Mt Baldur or Valhalla complex). The magmas of the LBG are likely to have formed via *in situ* anatectic melting for the following reasons: a) leucogranites are not associated with mafic equivalents, which would be expected if the voluminous LBG formed via fractional crystallization from a more mafic magma; b) continental crust in this area was ~60-80 km thick prior to extension (Cook and Van der Velden, 1995; Clowes et al., 1995) and the over-thickened crust would have reached P-T conditions high enough to initiate melting of the middle to lower crust (Patino-Douce et al., 1990); c) the isotopic signature suggests melting of old, isotopically evolved crust; and d) the presence of abundant Proterozoic inherited zircon cores from samples of the LBG, dated by U-Pb technique (Parrish et al., 1988; Carr, 1990; Vanderhaeghe et al., 1999).

The two likely sources for the LBG are the North American basement gneiss and/ or the supracrustal rocks deposited on basement, including the Windermere and Belt-Purcell Supergroups, as well as the Monashee cover sequence. The extreme variation in Sr isotopic signature of the LBG samples, as well as the basement gneisses and the supracrustal rocks make it impossible to use this isotope system to distinguish between potential source materials for partial melting (Fig. 2-9).

The Nd isotopic signatures do not show the same extreme variation as the Sr isotopes; however, the isotopic compositions of most of the potential source materials overlap (Fig. 2-11). Comparing the Nd isotopic composition of the LBG with the basement gneiss of Thor-Odin and Frenchman Cap domes, the Nd systematics could be explained by partial melting of the basement gneiss. In addition, melting of the supracrustal rocks of Thor-Odin could also have produced the LBG, as they are isotopically indistinguishable from those of basement. However, the Windermere and Belt-Purcell Supergroups do

not display the same extensive range in isotopic composition as the LBG, and this, coupled with the limited known extent of these units in the Thor-Odin area, supports the conclusion that melting of these metasedimentary rocks was not likely a major contributor to the formation of the South Fosthall pluton. However, regionally, it cannot be ruled out that melting of these supracrustal rocks may have contributed to the formation of parts of the suite.

*2.5.2. Evidence for a genetic link between migmatites and leucogranites*

Melting in the basement rocks was synchronous with emplacement of the Ladybird granites at higher structural levels (Carr, 1992; Hinchey et al., 2004). This raises the question as to whether migmatites preserved in the basement rocks of Thor-Odin dome may be the source for the Ladybird granites. In terms of major and trace element composition, significant differences observed between the LBG and the leucosome samples are: a) slightly lower LREE concentration in the leucosome samples; and, b) lower concentrations of most of the HFSE in the leucosome. Similar REE relationships in other leucosome studies have been attributed to disequilibrium melting (Barbero et al., 1995; Watt et al., 1996; Jung et al., 1999; 2000). Sawyer (1987) attributed leucosome with high abundances of HFSE and negative Eu anomalies to represent fractionated melts, and leucosome with lower REE concentrations and positive Eu anomalies to represent cumulates. The cumulate model was supported by Ellis and Obata (1992) who found that the anhydrous nature of leucosome and the lack of retrograde reactions suggested that the leucosome does not represent frozen melt segregation but rather cumulates that precipitated from the melt. Johannes et al. (2003) documented the same chemical patterns of low abundance of HFSE and positive Eu anomaly in leucosome samples while the associated granites had higher HFSE concentrations and negative Eu anomalies. They also attributed this chemical pattern to the leucosome representing cumulates and the granites representing the final melts. The difference in geochemical signature of the Thor-Odin dome leucosome and the Ladybird granites can be explained

by a similar model, with the leucosome samples being cumulates and the LBG suite the residual melts that formed during deformation assisted dehydration melting. There are two samples of pegmatitic leucosome that have the same chemical pattern as the leucogranites (AH-03-17 and AH-03-22). These samples crosscut all of the host rock types and foliation in the area, and based upon this relationship and their chemistry are interpreted to represent residual melts.

The Nd isotopic data from the leucosome samples overlaps with those of the LBG suite, although their Sr isotopic composition is clearly more radiogenic. This seemingly contradictory data can be explained in a number of ways: a) The isotopic heterogeneity may reflect isotope variability in the source material, which can result in a large range in isotopic composition. Sr isotopic heterogeneity within source rocks has been shown to be preserved on the mineralogical scale before and during anatexis in some orogenic terranes (George and Bartlett, 1996), thus isotopic homogenization is not a necessary consequence of prograde metamorphism preceding anatexis (Knesel and Davidson, 2002). This variability of Sr signatures has been documented in the Himalayan Manaslu peraluminous leucogranites, which show an extreme range in signatures on the meter scale (Deniel et al., 1987). This signature is characteristic of granites derived by low-melt fractions in short-lived systems typical of pure crustal melts (Barbero et al., 1995). A larger number of samples from the LBG may likely show significantly more isotopic heterogeneity and consequently show more overlap with leucosome samples. b) The LBG samples may have a more homogenous isotopic signature as they were mobilized from their source and emplaced into higher structural levels; a process which has been found to have homogenizing affects on isotopic signatures (Barbero et al., 1995). c) The differences in Sr isotopic signatures between the leucosome and LBG may be due to partial isotopic resetting during partial melting. Incomplete isotopic resetting during migmatite formation has been observed in areas of high-grade anatexis. Pelite-derived anatectic leucogranites have been documented with slightly higher initial εNd and lower initial $^{87}Sr/^{86}Sr$ than

local leucosome, associated mesosome and granulite-facies pelitic material (Barbero et al., 1995). Isotopic disequilibrium is supported by experimental studies that show that the stoichiometry of melting reactions and the kinetics of melting are the major process controlling the isotopic composition of a melt, suggesting that isotopic composition is not controlled by the overall bulk composition of the source material (Hammouda et al., 1994). In a migmatite terrain, a relative enrichment of biotite and accessory minerals in the granites compared to the leucosome could explain isotopic differentiation and variability of Sr ratios. d) The Sr isotopic signature may be controlled by differences in melting reactions, which could control variations in the Sr isotopic composition of granite/leucosome melts from a single metapelitic source (Knesel and Davidson, 2002; Zeng et al., 2005). The experimental study of Knesel and Davidson (2002) showed that Ms-dehydration results in granites with higher $^{87}Sr/^{86}Sr_{(i)}$ and lower $Sr_{(ppm)}$ concentrations than the source rocks, whereas the fluid fluxed melting produced lower $^{87}Sr/^{86}Sr_{(i)}$ and higher $Sr_{(ppm)}$ concentrations than the source rocks. Rapid melt extraction, a function of feedback between melting and deformation, would stop the isotopic exchange between melt and source before equilibration, thus explaining batch melts from a single source with variable Sr isotopic signatures. These various models can explain the potential for slightly different Sr isotopic systematics in the Ladybird granite and leucosome samples.

Much of the geochemical and isotopic evidence presented here indicates a strong correlation between the leucosome and the Ladybird granite samples. These include major element concentrations, trace element concentrations, Nd isotopics, coeval U-Pb zircon ages, and the general restriction of the peraluminous leucogranites to amphibolite facies metamorphic zones. In addition, the leucosome samples also contain abundant inherited Precambrian zircons (Hinchey, Chapter 1) that are also abundant in the leucogranite suites (Carr, 1992). This evidence suggests that the melting in the basement gneisses that produced the anatectic leucosome may have also produced portions of the LBG suite. The chemical signatures suggest that most of the leucosome represents

cumulates and that the LBG are residual melts. The regional extent of the LBG and the difficulty in distinguishing, at least isotopically, between the different supracrustal sequences makes it impossible to rule out melting of the overlying supracrustal rocks as potential contributors to the formation of the Ladybird granites. However, the data presented in this paper strongly supports a genetic link between the melting of ca. 26-33 km deep North American basement gneisses and the emplacement of at least part of the peraluminous LBG.

## 2.6. Summary of conclusions

Based upon the geochemical, isotopic, and field data from the peraluminous Ladybird granites and the basement leucosome several conclusions can be drawn.

1) The ca. 55 Ma South Fosthall pluton is a peraluminous, S-type leucogranitic intrusion and is part of the ca. 62-52 Ma Ladybird granite suite.
2) Thor-Odin dome basement gneisses are an exposure of North American basement rocks exhumed from ca. 26-33 km depths that contain abundant anatectic leucosome (15-50 %) that formed via partial melting of the host paragneisses.
3) Anatexis and the formation of leucosome in Thor-Odin dome were ongoing from at least ca. 56 Ma to as young as ca. 52 Ma.
4) The Thor-Odin dome leucosome and Ladybird granite samples have similar major and trace element chemistry. They are classified in the peraluminous granitic fields on discrimination diagrams. Differences in HFSE concentrations and Eu anomalies suggest that the leucosome and leucogranites are related as cumulates and residual melts, respectively.
5) The initial Nd isotope values for the Ladybird granite suite overlap with those of the leucosome samples. Both suites of samples have a range in initial $\varepsilon Nd_{(55\ Ma)}$ values; -5.0 to –17.2 for the leucogranites and –9.5 to –23.6 for the leucosome samples. The similarity of initial isotopic ratios supports a genetic

link between the two.

6) The initial Sr isotope values for both the peraluminous leucogranites and leucosome samples show a large range in values. The initial Sr isotope ratios for the LBG suite (0.70603 to 0.73688) are slightly lower than those of the leucosome samples (0.74256 to 0.76593). This isotopic heterogeneity suggests either: a) isotopic disequilibrium during partial melting in the mid to lower crust where the leucosome formed, b) the distribution of Sr during partial melting was controlled by different melt reactions, and/or c) isotopic heterogeneity in the source rocks.

7) At least part of the LBG suite likely formed via partial melting of North American basement rocks. The abundant leucosome in the exhumed basement rocks of Thor-Odin dome, in addition to the geochemical, isotopic, and U-Pb data support this conclusion. The preservation of abundant melt leucosome might mark the melt migration paths for the overlying Ladybird granites. The platformal supracrustal metasedimentary rocks that overly basement may have also contributed regionally to the formation of parts of the suite.

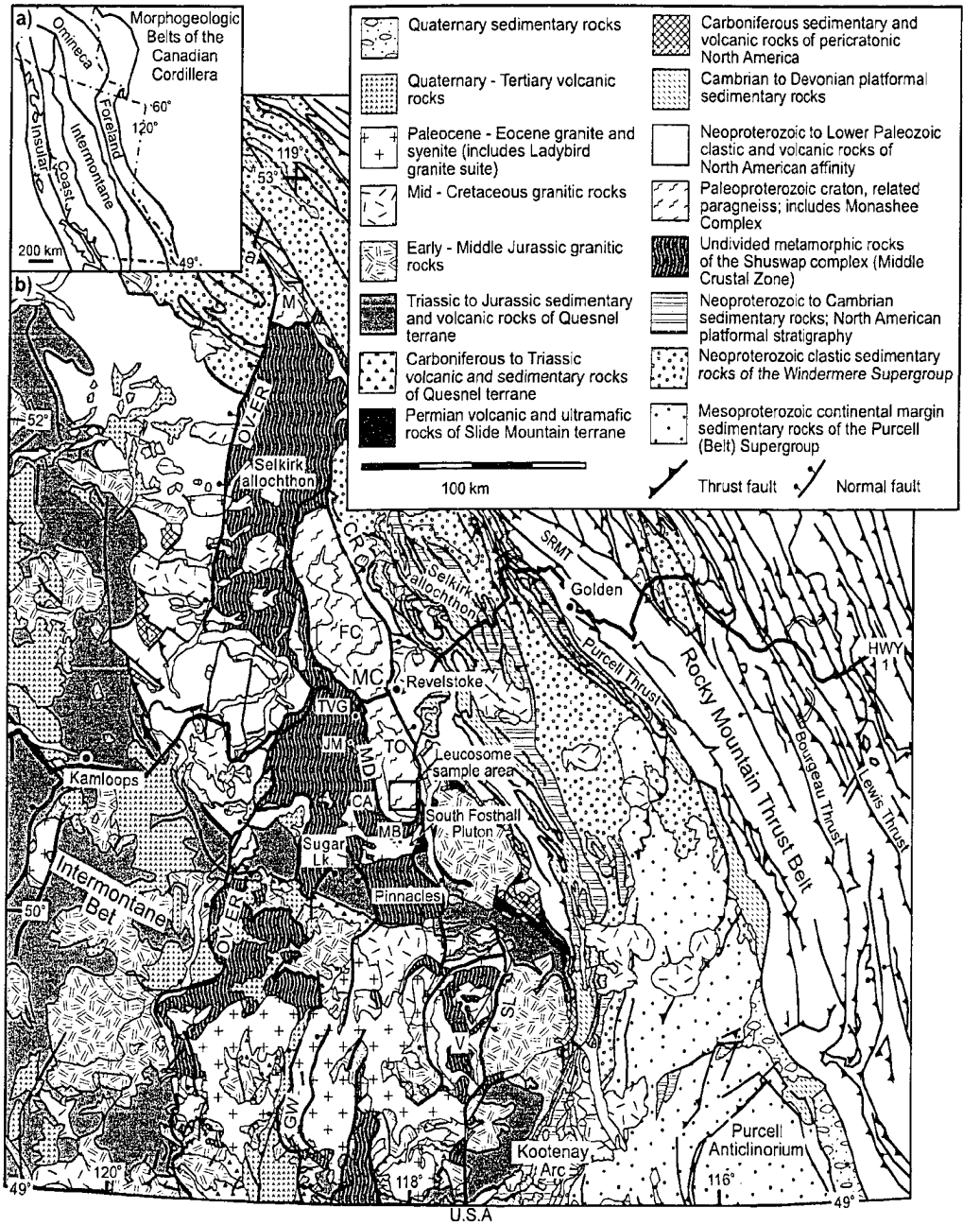


**Figure 2-1.** (a) Map highlights the five morphological belts of the Cordillera from Wheeler and McFeely (1991). (b) Tectonic assemblage map of the southeastern Canadian Cordillera (modified after Wheeler and McFeely, 1991). Shuswap complex was defined by Brown and Carr (1990), and is largely bounded by Eocene normal faults, including Okanagan Valley – Eagle River fault system (OV-ER), Columbia River Fault (CR), Greenwood Fault (GW), and Slocan Lake-Champion lake (SL) fault systems. SRMT = Southern Rocky Mountain Trench, M = Malton complex, MD = Monashee décollement, MC = Monashee complex, V = Valhalla complex, FC = Frenchman Cap dome, TO = Thor-Odin dome, TVG = Three Valley Gap, JM = Joss Mountain, MB = Mount Baldur. Sampling areas for the leucosome samples from Thor-Odin and Ladybird granite suite from the South Fosthall Pluton are delineated.

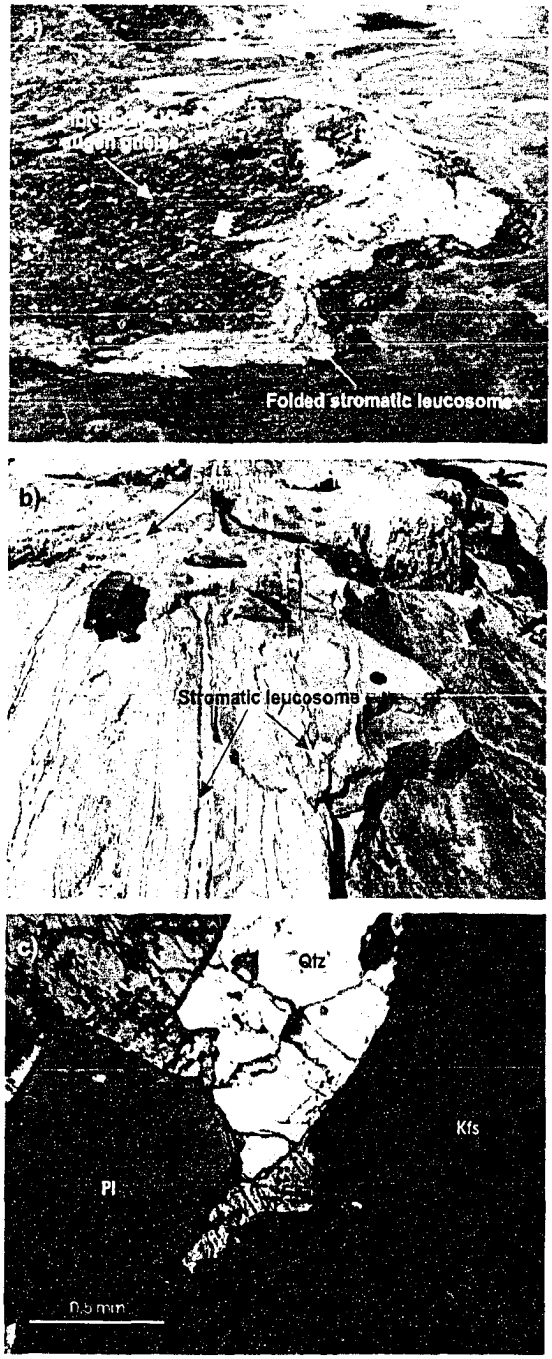


**Figure 2-2.** Representative types of leucosome preserved in migmatitic basement gneisses of Thor-Odin dome. (a) Host hornblende-biotite-quartz-feldspar augen gneiss surrounded by folded leucosome. (b) Host biotite-quartz-feldspar gneiss with phases of folded stromatic type and pegmatitic vein type of leucosome. (c) Photomicrographs in cross-polarized light of representative undeformed phenocrystic leucosome sample. Note euhedral to subhedral grains and lack of alteration in the perthitic orthoclase as evidence of igneous nature.

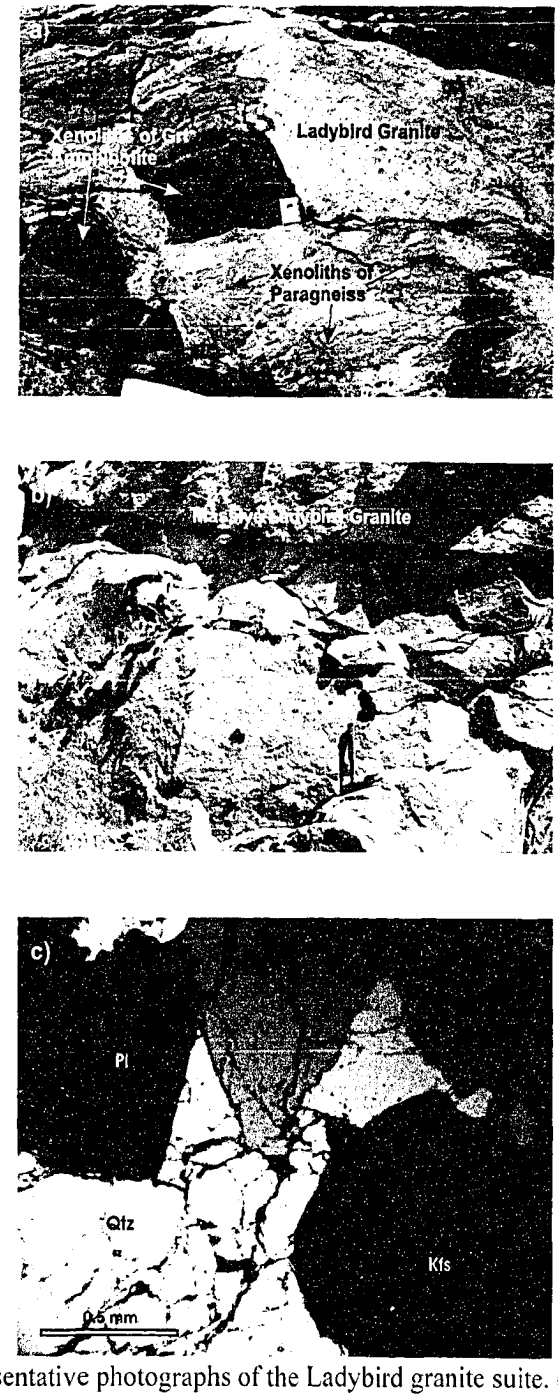


**Figure 2-3.** Representative photographs of the Ladybird granite suite. (a) Photo is from Mt Baldur and depicts the nature of the leucogranite in this area with xenoliths of garnet amphibolite and paragneiss. (b) Photo is from Sugar Lake and depicts the massive, homogenous nature of leucogranite in this area. (c) Photomicrographs in cross-polarized light of typical mineralogy of the Ladybird granite suite. Note euhedral to anhedral grains, primary albite twinning in plagioclase and lack of alteration of potassium feldspar as evidence of igneous rather than deformation textures.

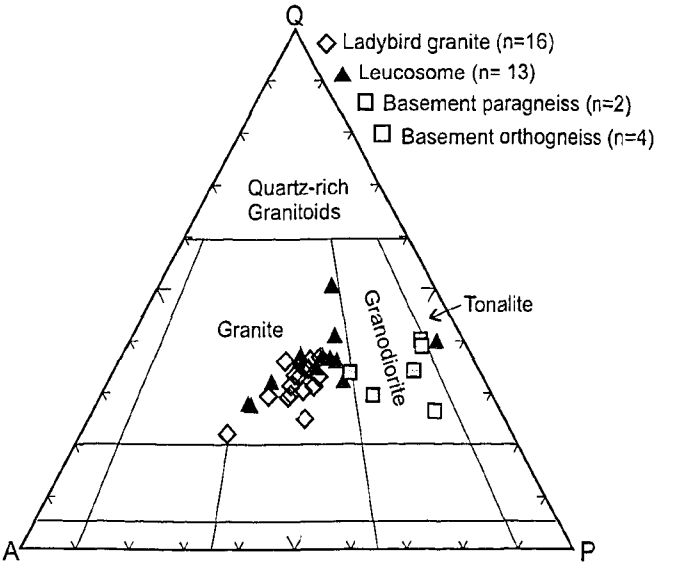


**Figure 2-4.** Leucosome from Thor-Odin dome and leucogranite from the Ladybird granite suite plotted on Quartz-Alkali feldspar-Plagioclase (QAP) classification diagram from Le Maitre (1989). All but one of the leucosome samples fall within the granite field.

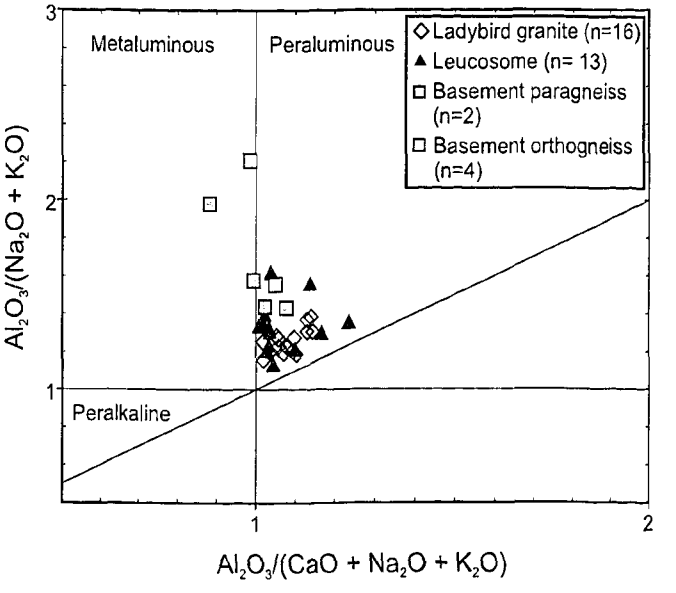


**Figure 2-5.** Samples of Ladybird leucogranite and leucosome plotted on Shand's plot of Al saturation index (molecular Al/(Ca + Na + K)) versus alkali saturation index (molecular Al/(Na + K)) from Manier and Piccoli (1989). All samples fall within the peraluminous field.

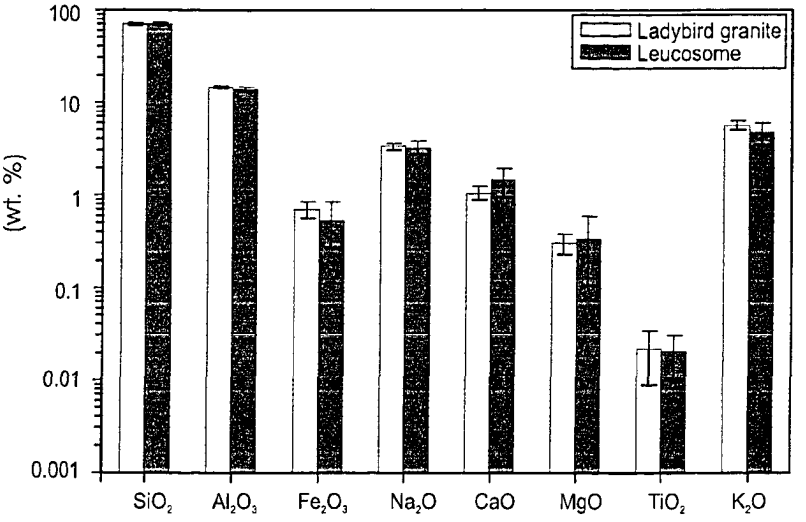


**Figure 2-6.** Graphical comparison of major element concentrations determined in Ladybird leucogranite and leucosome samples. Columns represent the mean concentration of each element, error bars are reported for the standard deviation for the mean. Values are listed in Table 2-2 with the associated standard deviation of the mean.

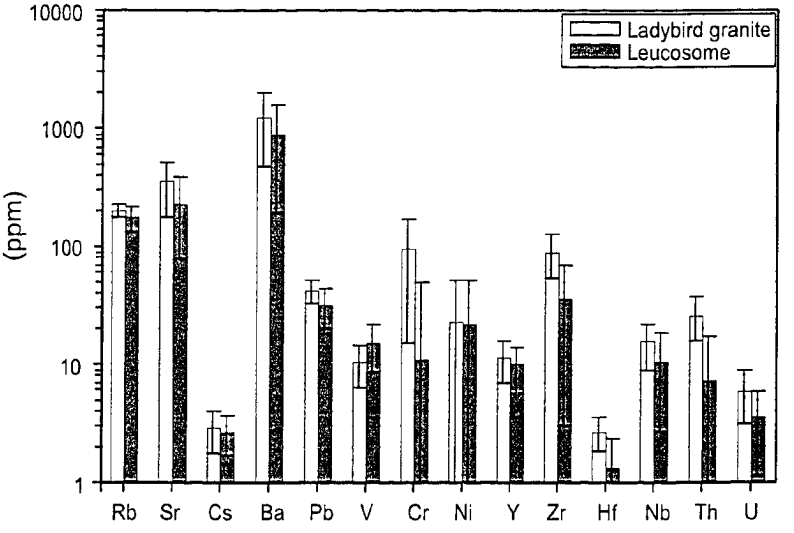


**Figure 2-7.** Graphical comparison of major element concentrations determined in Ladybird leucogranite and leucosome samples. Columns represent the average concentration of each element, error bars are reported for the standard deviation for the mean. Values are listed in Table 2-2 with the associated standard deviation of the mean.

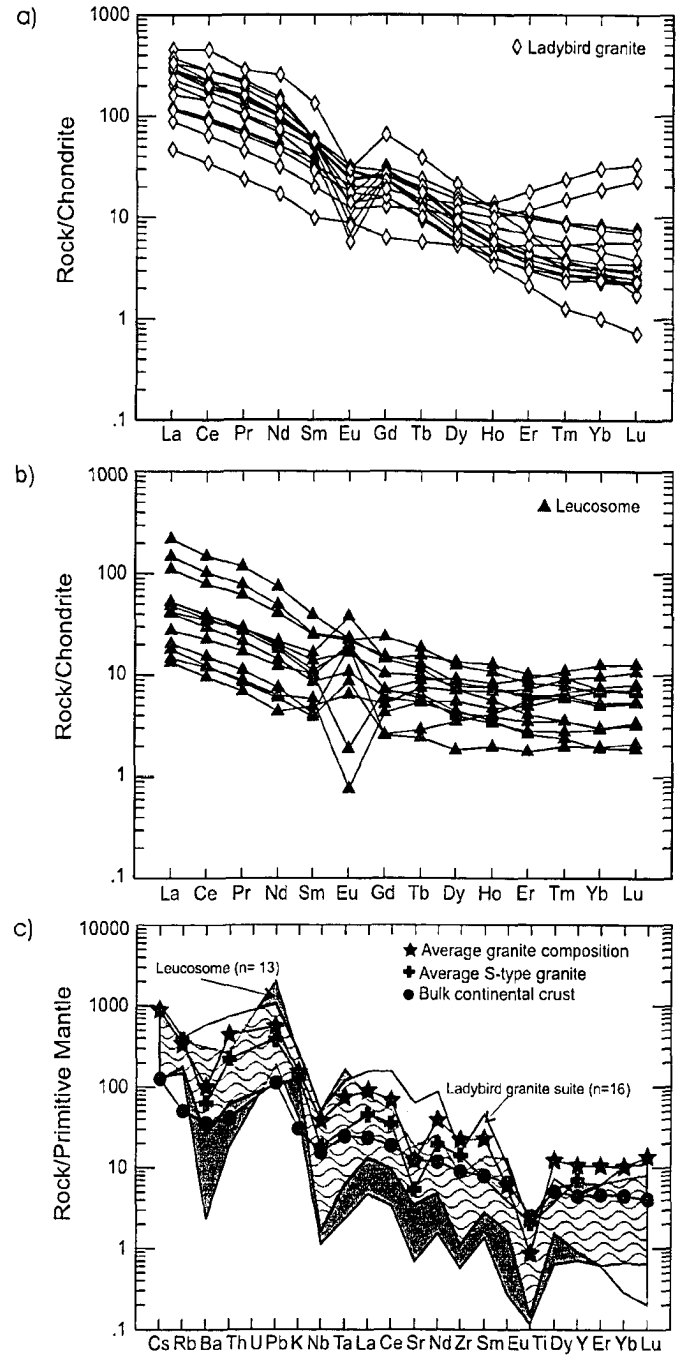


**Figure 2-8.** Trace element normalized diagrams for the Ladybird leucogranite and leucosome samples. (a) Chondrite normalized diagram of the Ladybird leucogranite samples. (b) Chondrite normalized diagram of the leucosome samples. (c) Primitive mantle normalized diagram for the range of leucosome and the range of Ladybird leucogranite samples. Normalization from Sun and McDonough (1989). Bulk continental crust data from Taylor and McLennan (1995), average granite composition data from Govindaraju (1989), and average S-type granite data from Chappell and White (1992).

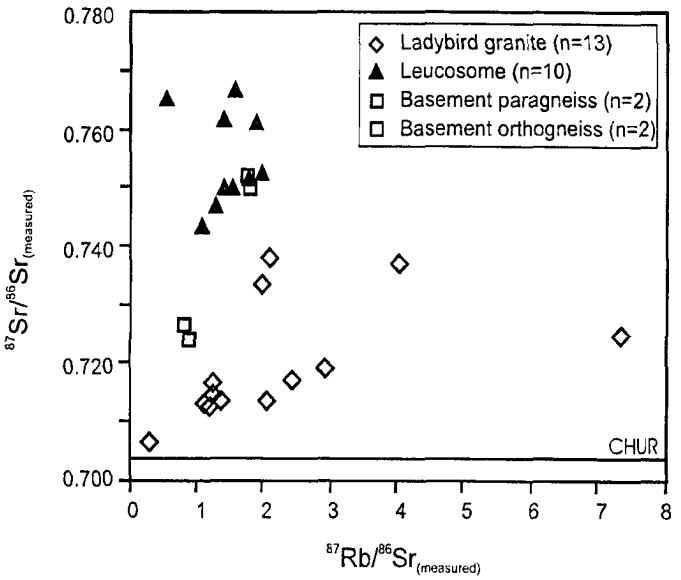


**Figure 2-9.** $^{87}Rb/^{86}Sr_{(measured)}$ versus $^{87}Sr/^{86}Sr_{(measured)}$ diagram for the Ladybird granite suite, leucosome samples and selected basement gneisses for comparison. CHUR = chondritic uniform reservoir. See text for interpretation.

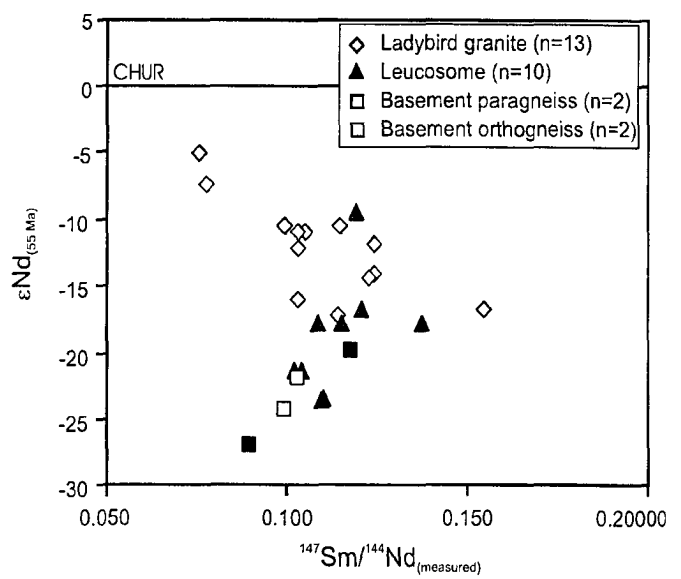


**Figure 2-10.** $^{147}Sm/^{144}Nd_{(measured)}$ versus $\varepsilon Nd_{(55\ Ma)}$ diagram for the Ladybird granite suite, leucosome samples and selected basement gneisses for comparison. CHUR = chondritic uniform reservoir. See text for interpretation.

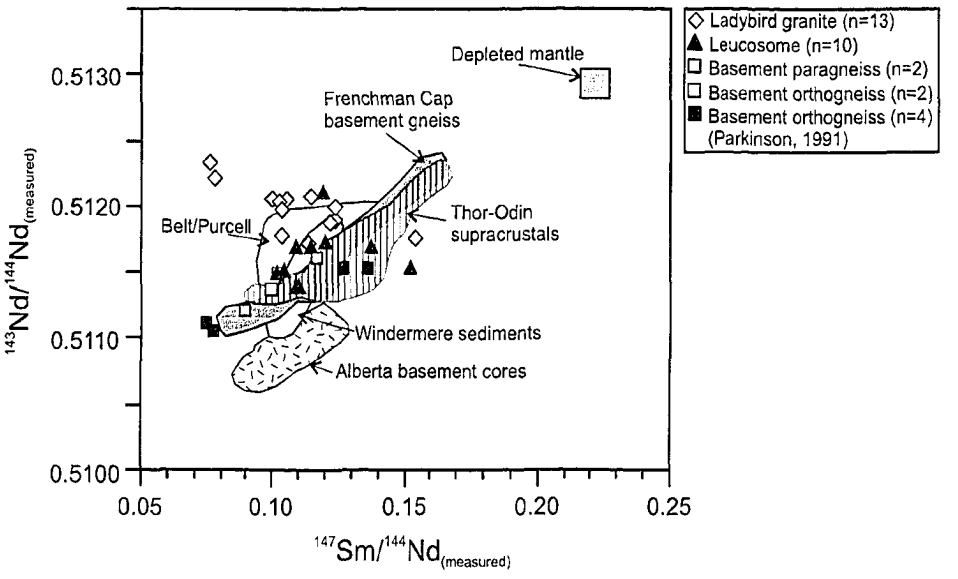


**Figure 2-11.** $^{147}Sm/^{144}Nd_{(measured)}$ versus $^{143}Nd/^{144}Nd_{(measured)}$ diagram for the Ladybird granite suite, and leucosome samples and selected basement gneisses from Thor-Odin dome. Basement orthogneiss from Thor-Odin (Parkinson, 1991; this study) are plotted for comparison. Fields for Thor-Odin supracrustals and Frenchman Cap basement gneisses are from Parkinson (1991) and Armstrong et al. (1991). Fields for Proterozoic Supergroups (Windermere, Belt-Purcell) and Archean basement cores for the Canadian Cordillera are also plotted for comparison. Data are from Frost and O'Nions (1984); Devlin et al. (1985); Frost and Burwash (1986); Frost and Winston (1987); Burwash et al. (1988); Devlin et al. (1988); Burwash and Wagner (1989); Ross et al., (1993); and Anderson and Goodfellow (2000). Depleted mantle values are from DePaolo (1988).

**Table 2-1.** Description and location of the geochemical samples of leucosome, Ladybird granite suite and basement gneisses from the Thor-Odin-Pinnacles area. Mineral symbols are from Kretz (1983).

| Sample | Easting | Northing | Sample Description | Map Location |
|---|---|---|---|---|
| Ladybird Granite Samples | | | | |
| LB-02-01 | 466600 | 5513350 | Bt Leucogranite | Slocan Lake |
| LB-02-02 | 466550 | 5513560 | Bt Leucogranite | Slocan Lake |
| LB-02-03 | 466700 | 5513220 | Bt Leucogranite | Slocan Lake |
| AH-03-03 | 466661 | 5518257 | Foliated Bt leucogranite | Slocan Lake |
| AH-03-05 | 466410 | 5517365 | Foliated Ms-Bt leucogranite | Slocan Lake |
| AH-03-06 | 391283 | 5587489 | Foliated Ms-Bt granite | Sugar Lake |
| AH-03-07 | 393055 | 5589929 | Bt granite | Sugar Lake |
| AH-03-13 | 401342 | 5588765 | Ms-Bt granite | Sugar Lake |
| AH-03-30 | 415498 | 5586175 | Ms Kfs-phenocrystic granite | Mt Baldur |
| AH-03-31 | 416123 | 5586216 | Bt granite | Mt Baldur |
| AH-03-32 | 416111 | 5586113 | Grt-Ms-Bt granite | Mt Baldur |
| AH-03-33 | 415822 | 5585582 | Ms granite | Mt Baldur |
| AH-03-34 | 416348 | 5585952 | Ms Kfs-phenocrystic granite | Mt Baldur |
| AH-03-35 | 424173 | 5578737 | Foliated Ms-Bt granite | Mt Baldur |
| AH-03-37 | 421983 | 5579663 | Bt granite | Mt Baldur |
| AH-03-38 | 423497 | 5581968 | Bt granite | Mt Baldur |
| Leucosome Samples | | | | |
| AH-02-05 | 423299 | 5600302 | Crosscutting pegmatitic Ms-Bt granitic leucosome | Frigg Glacier |
| AH-02-06 | 423299 | 5600302 | Folded stromatic Ms-Bt granitic leucosome | Frigg Glacier |
| AH-02-08 | 423307 | 5600311 | Crosscutting pegmatitic Ms-Bt granitic leucosome | Frigg Glacier |
| AH-02-09 | 423239 | 5600301 | Stromatic Bt granitic leucosome | Frigg Glacier |
| AH-02-10 | 423270 | 5600336 | Folded stromatic Ms-Bt granitic leucosome | Frigg Glacier |
| AH-02-11 | 423291 | 5600689 | Folded stromatic Bt granitic leucosome | Frigg Glacier |
| AH-02-13 | 423453 | 5600386 | Crosscutting phenocrystic Bt granitic leucosome | Frigg Glacier |
| AH-02-26 | 417252 | 5602040 | Sheared, stromatic Bt granititc leucosome | Saturday Glacier |
| AH-02-27 | 417245 | 5602034 | Sheared, stromatic Bt granititc leucosome | Saturday Glacier |
| AH-02-29 | 417252 | 5602034 | Crosscutting phenocrystic Bt granitic leucosome | Saturday Glacier |
| AH-03-17 | 419010 | 5598756 | Crosscutting pegmatitic Ms-Bt granitic leucosome | Bearpaw Lake |
| AH-03-19 | 418966 | 5598825 | Phenocrystic Ms-Bt granitic leucosome | Bearpaw Lake |
| AH-03-22 | 419149 | 5598883 | Crosscutting pegmatitic Ms-Bt granitic leucosome | Bearpaw Lake |
| Basement Gneisses | | | | |
| AH-02-07 | 423313 | 5600318 | Kfs augen granodiorite orthogneiss | Frigg Glacier |
| AH-02-12 | 423299 | 5600669 | Bt granodiorite orthogneiss | Frigg Glacier |
| AH-03-21 | 419186 | 5598790 | Hbl-Qtz-Kfs-Pl paragneiss | Bearpaw Lake |
| AH-03-18 | 419009 | 5598744 | Bt-Qtz-Kfs-Pl paragneiss | Bearpaw Lake |
| AH-02-28 | 417260 | 5602033 | Bt Qtz-Kfs paragneiss | Saturday Glacier |
| AH-02-30 | 417243 | 5602028 | Grt-Sil-Qtz-Kfs-Pl paragneiss | Saturday Glacier |

**Table 2-2.** Major and trace element chemistry of the leucosome, Ladybird granite suite, and basement gneiss samples from the Thor Odin-Pinnacles area.

| | Ladybird Granite | | | | | | | | | |
|---|---|---|---|---|---|---|---|---|---|---|
| | AH-03-03 | AH-03-05 | AH-03-06 | AH-03-07 | AH-03-13 | AH-03-30 | AH-03-31 | AH-03-32 | AH-03-33 | AH-03-34 |
| (wt.%) | | | | | | | | | | |
| $SiO_2$ | 72.54 | 74.29 | 73.85 | 72.50 | 74.37 | 68.95 | 72.14 | 72.10 | 72.81 | 72.64 |
| $TiO_2$ | 0.13 | 0.11 | 0.19 | 0.21 | 0.13 | 0.21 | 0.43 | 0.04 | 0.34 | 0.18 |
| $Al_2O_3$ | 14.73 | 14.22 | 14.10 | 14.29 | 14.61 | 16.31 | 14.37 | 15.90 | 14.22 | 14.80 |
| $Fe_2O_3$* | 0.51 | 0.51 | 0.67 | 0.64 | 0.67 | 0.82 | 1.19 | 0.79 | 0.94 | 0.58 |
| FeO | 0.55 | 0.55 | 0.74 | 0.65 | 0.76 | 0.72 | 1.46 | 0.89 | 1.08 | 0.58 |
| MnO | 0.02 | 0.02 | 0.02 | 0.02 | 0.02 | 0.01 | 0.02 | 0.07 | 0.02 | 0.01 |
| MgO | 0.21 | 0.25 | 0.24 | 0.30 | 0.21 | 0.43 | 0.58 | 0.24 | 0.46 | 0.34 |
| CaO | 1.52 | 1.01 | 0.87 | 0.92 | 0.90 | 0.69 | 1.27 | 1.37 | 0.97 | 0.83 |
| $Na_2O$ | 3.48 | 3.33 | 3.46 | 3.50 | 3.56 | 2.68 | 3.29 | 3.55 | 2.88 | 3.10 |
| $K_2O$ | 5.56 | 5.60 | 5.27 | 6.14 | 4.89 | 8.48 | 4.61 | 5.19 | 5.65 | 6.71 |
| $P_2O_5$ | 0.21 | 0.07 | 0.06 | 0.13 | 0.13 | 0.10 | 0.08 | 0.08 | 0.06 | 0.08 |
| Sum | 99.45 | 99.96 | 99.47 | 99.30 | 100.24 | 99.40 | 99.44 | 100.21 | 99.43 | 99.84 |
| (ppm) | | | | | | | | | | |
| V | 9 | 11 | 7 | 9 | 9 | 16 | 17 | 6 | 15 | 6 |
| Cr | 149 | 176 | 190 | 170 | 165 | 1 | 3 | 5 | 146 | 6 |
| Co | 5 | 5 | <LD | 4 | 3 | 2 | 7 | 3 | 10 | 2 |
| Ni | 12.0 | <LD | <LD | <LD | 183 | <LD | <LD | 56 | <LD | <LD |
| Zn | 24 | 16 | 40 | 31 | 47 | 24 | 52 | 10 | 39 | 14 |
| Ga | 24 | 19 | 22 | 27 | 29 | 18 | 17 | 14 | 16 | 17 |
| As | <LD | <LD | <LD | <LD | <LD | <LD | <LD | <LD | <LD | <LD |
| Rb | 232.0 | 218.0 | 203.0 | 252.0 | 224.0 | 223.0 | 170.0 | 138.4 | 164.0 | 225.0 |
| Sr | 327.1 | 239.1 | 240.1 | 247.2 | 88.3 | 322.9 | 397.1 | 189.2 | 383.8 | 162.3 |
| Y | 14.1 | 18.8 | 9.3 | 6.0 | 17.9 | 16.4 | 7.2 | 20.7 | 6.0 | 4.9 |
| Zr | 42.4 | 59.6 | 107.3 | 85.1 | 71.0 | 40.4 | 171.7 | 50.9 | 134.7 | 14.9 |
| Nb | 36.0 | 31.6 | 14.0 | 8.3 | 19.5 | 7.4 | 11.6 | 1.4 | 11.1 | 7.5 |
| Cs | 8.8 | 2.9 | 2.8 | 4.4 | 1.9 | 2.5 | 1.8 | 1.5 | 1.2 | 3.3 |
| Ba | 687 | 613 | 818 | 738 | 221 | 1706 | 3436 | 688 | 4032 | 711 |
| La | 20.9 | 53.9 | 66.7 | 47.9 | 27.7 | 107.0 | 88.0 | 28.1 | 79.0 | 27.0 |
| Ce | 39.3 | 105.8 | 125.2 | 88.6 | 56.7 | 275.0 | 172.0 | 58.6 | 172.0 | 54.4 |
| Pr | 4.3 | 11.8 | 13.5 | 9.3 | 6.5 | 27.0 | 21.3 | 6.7 | 19.7 | 6.1 |
| Nd | 14.7 | 40.9 | 45.8 | 31.5 | 22.9 | 118.0 | 71.0 | 24.3 | 65.9 | 21.5 |
| Sm | 3.03 | 8.34 | 8.66 | 5.40 | 5.87 | 20.20 | 8.93 | 5.00 | 8.48 | 4.37 |
| Eu | 0.71 | 0.99 | 0.73 | 0.81 | 0.33 | 1.73 | 1.60 | 1.18 | 1.68 | 1.01 |
| Gd | 2.60 | 6.38 | 6.02 | 3.21 | 5.03 | 13.28 | 4.82 | 3.86 | 4.70 | 3.20 |
| Tb | 0.44 | 0.88 | 0.69 | 0.35 | 0.75 | 1.43 | 0.49 | 0.56 | 0.46 | 0.37 |
| Dy | 2.56 | 4.22 | 2.74 | 1.45 | 3.79 | 5.36 | 1.88 | 3.43 | 1.69 | 1.51 |
| Ho | 0.45 | 0.70 | 0.37 | 0.23 | 0.65 | 0.67 | 0.28 | 0.78 | 0.23 | 0.19 |
| Er | 1.14 | 1.72 | 0.76 | 0.52 | 1.63 | 1.14 | 0.63 | 2.94 | 0.50 | 0.35 |
| Tm | 0.14 | 0.23 | 0.08 | 0.07 | 0.22 | 0.10 | 0.08 | 0.60 | 0.06 | 0.03 |
| Yb | 0.79 | 1.39 | 0.48 | 0.43 | 1.28 | 0.52 | 0.52 | 5.08 | 0.41 | 0.17 |
| Lu | 0.10 | 0.19 | 0.06 | 0.06 | 0.18 | 0.04 | 0.07 | 0.84 | 0.06 | 0.02 |
| Hf | 1.50 | 2.10 | 3.60 | 2.60 | 2.60 | 1.30 | 3.80 | 1.80 | 3.10 | 0.50 |
| Ta | 4.82 | 2.12 | 0.65 | 0.50 | 0.67 | 0.50 | 0.33 | 0.41 | 0.32 | 0.30 |
| Pb | 42 | 59 | 50 | 36 | 39 | 74 | 29 | 46 | 34 | 54 |
| Th | 9.02 | 31.30 | 39.29 | 21.68 | 15.59 | 62.13 | 28.82 | 10.67 | 27.56 | 11.53 |
| U | 13.43 | 8.32 | 15.62 | 4.14 | 5.89 | 4.93 | 2.59 | 2.72 | 1.92 | 1.84 |
| Eu/Eu* | 0.20 | 0.11 | 0.08 | 0.15 | 0.05 | 0.08 | 0.18 | 0.21 | 0.20 | 0.21 |

Major element analyses by X-Ray Fluorescence. $Fe_2O_3$* and FeO recalculated from measured $Fe_2O_3T$ (total) using the procedure of LeMaitre (1976). Oxides normalized to 100 % (anhydrous). Totals of measured analysis are reported in "sum" column. Trace element analyses carried out by X-Ray Fluorescence and Inductively Coupled Plasma-Mass Spectrometry. LD = Limit of Detection. $Eu/Eu^* = Eu_{(N)}/[(Sm_{(N)}+Gd_{(N)})/2]$; normalized using values from Sun and McDonough (1989). [a]SEM is the standard error of the mean.

**Table 2-2.** Continued.

| | Ladybird Granite | | | | | | | | Leucosome | |
|---|---|---|---|---|---|---|---|---|---|---|
| | AH-03-35 | AH-03-37 | AH-03-38 | LB-02-01 | LB-02-02 | LB-02-03 | Mean | SEM[a] | AH-02-05 | AH-02-06 |
| (wt. %) | | | | | | | | | | |
| $SiO_2$ | 73.55 | 71.15 | 73.04 | 72.50 | 72.46 | 72.70 | 72.60 | 0.81 | 71.56 | 72.16 |
| $TiO_2$ | 0.21 | 0.13 | 0.17 | 0.24 | 0.17 | 0.12 | 0.19 | 0.06 | 0.39 | 0.10 |
| $Al_2O_3$ | 14.37 | 15.89 | 14.66 | 14.01 | 13.91 | 14.23 | 14.66 | 0.54 | 14.10 | 14.67 |
| $Fe_2O_3$* | 0.77 | 0.71 | 0.76 | 0.71 | 0.59 | 0.49 | 0.71 | 0.13 | 0.98 | 0.47 |
| FeO | 0.87 | 0.70 | 0.79 | 0.82 | 0.67 | 0.56 | 0.77 | 0.16 | 1.55 | 0.58 |
| MnO | 0.01 | 0.04 | 0.07 | 0.02 | 0.01 | 0.01 | 0.02 | 0.01 | 0.03 | 0.02 |
| MgO | 0.26 | 0.24 | 0.26 | 0.33 | 0.30 | 0.33 | 0.31 | 0.08 | 0.83 | 0.27 |
| CaO | 1.01 | 1.14 | 1.08 | 1.33 | 0.97 | 1.23 | 1.07 | 0.18 | 2.73 | 2.06 |
| $Na_2O$ | 3.43 | 3.90 | 3.42 | 3.15 | 3.31 | 3.62 | 3.35 | 0.22 | 4.41 | 3.70 |
| $K_2O$ | 5.23 | 6.03 | 6.08 | 5.29 | 5.31 | 4.89 | 5.68 | 0.63 | 1.28 | 4.27 |
| $P_2O_5$ | 0.11 | 0.04 | 0.07 | 0.06 | 0.07 | 0.06 | 0.09 | 0.03 | 0.04 | 0.04 |
| Sum | 99.83 | 99.97 | 100.39 | 98.46 | 97.77 | 98.25 | | | 97.91 | 98.33 |
| (ppm) | | | | | | | | | | |
| V | 5 | 17 | 7 | 15 | 14 | 4 | 10 | 4 | 30 | 15 |
| Cr | 161 | 155 | 172 | 2 | 4 | 5 | 94 | 79 | 29 | 7 |
| Co | 1 | 4 | <LD | 5 | 2 | 5 | 4 | 2 | 11 | 5 |
| Ni | 52 | <LD | <LD | 8 | 23 | 30 | 52 | 39 | 33 | 67 |
| Zn | 31 | 24 | 22 | 44 | 22 | 33 | 30 | 10 | 37 | 19 |
| Ga | 25 | 21 | 21 | 22 | 18 | 22 | 21 | 3 | 18 | 18 |
| As | <LD | <LD | <LD | <LD | 2 | 2 | | | 1 | 1 |
| Rb | 255.0 | 135.8 | 208.0 | 196.3 | 209.7 | 187.1 | 202.6 | 28.0 | 92.1 | 150.9 |
| Sr | 177.9 | 1329.0 | 146.1 | 513.0 | 438.1 | 442.7 | 352.7 | 173.4 | 245.9 | 307.0 |
| Y | 8.5 | 8.3 | 14.1 | 8.2 | 9.6 | 8.7 | 11.2 | 4.4 | 6.2 | 10.7 |
| Zr | 92.3 | 140.6 | 63.8 | 141.2 | 116.3 | 107.1 | 90.0 | 36.4 | 84.8 | 64.1 |
| Nb | 11.6 | 13.1 | 14.9 | 17.4 | 26.1 | 16.3 | 15.5 | 6.7 | 14.9 | 5.0 |
| Cs | 3.5 | 1.2 | 2.8 | 2.6 | 3.4 | 2.1 | 2.9 | 1.1 | 3.2 | 1.9 |
| Ba | 590 | 1651 | 331 | 1320 | 1012 | 1084 | 1227 | 751 | 184 | 968 |
| La | 67.2 | 11.0 | 38.0 | 79.4 | 65.4 | 70.6 | 54.9 | 23.0 | 9.7 | 26.2 |
| Ce | 136.0 | 20.9 | 87.5 | 136.7 | 114.5 | 121.7 | 110.3 | 46.3 | 18.1 | 48.6 |
| Pr | 13.9 | 2.2 | 9.8 | 17.5 | 14.3 | 15.3 | 12.4 | 5.4 | 2.0 | 5.8 |
| Nd | 46.8 | 7.9 | 34.3 | 55.2 | 44.7 | 47.5 | 43.3 | 18.6 | 6.6 | 19.0 |
| Sm | 8.11 | 1.49 | 7.51 | 9.13 | 7.81 | 8.10 | 7.53 | 2.50 | 1.31 | 3.80 |
| Eu | 0.73 | 0.51 | 0.47 | 1.83 | 1.35 | 1.40 | 1.07 | 0.41 | 0.62 | 1.27 |
| Gd | 4.84 | 1.29 | 5.34 | 5.80 | 5.20 | 5.43 | 5.06 | 1.50 | 1.23 | 3.15 |
| Tb | 0.53 | 0.21 | 0.64 | 0.68 | 0.65 | 0.69 | 0.61 | 0.19 | 0.20 | 0.48 |
| Dy | 2.19 | 1.35 | 2.92 | 2.24 | 2.30 | 2.35 | 2.62 | 0.84 | 1.07 | 2.13 |
| Ho | 0.32 | 0.29 | 0.56 | 0.30 | 0.33 | 0.33 | 0.42 | 0.16 | 0.22 | 0.42 |
| Er | 0.72 | 0.89 | 1.94 | 0.57 | 0.69 | 0.56 | 1.04 | 0.53 | 0.57 | 0.99 |
| Tm | 0.09 | 0.14 | 0.38 | 0.07 | 0.10 | 0.07 | 0.15 | 0.10 | 0.09 | 0.15 |
| Yb | 0.55 | 0.96 | 3.16 | 0.45 | 0.59 | 0.39 | 1.07 | 0.83 | 0.50 | 0.84 |
| Lu | 0.08 | 0.14 | 0.58 | 0.06 | 0.09 | 0.06 | 0.16 | 0.14 | 0.09 | 0.13 |
| Hf | 2.90 | 3.90 | 2.30 | 4.19 | 3.56 | 3.30 | 2.69 | 0.85 | 2.36 | 2.97 |
| Ta | 0.49 | 0.90 | 0.96 | 0.66 | 1.72 | 0.48 | 0.99 | 0.71 | 1.09 | 0.39 |
| Pb | 45 | 9 | 46 | 39 | 40 | 38 | 43 | 10 | 13 | 32 |
| Th | 28.93 | 6.37 | 25.79 | 36.07 | 30.28 | 34.35 | 26.21 | 10.35 | 5.31 | 16.21 |
| U | 5.91 | 1.92 | 7.30 | 5.63 | 7.25 | 5.67 | 5.94 | 2.78 | 2.97 | 5.34 |
| Eu/Eu* | 0.09 | 0.30 | 0.06 | 0.19 | 0.16 | 0.16 | | | 0.40 | 0.29 |

**Table 2-2.** Continued.

| | Leucosome | | | | | | | | | |
|---|---|---|---|---|---|---|---|---|---|---|
| | AH-02-08 | AH-02-09 | AH-02-10 | AH-02-11 | AH-02-13 | AH-02-26 | AH-02-27 | AH-02-29 | AH-03-17 | AH-03-19 |
| (wt. %) | | | | | | | | | | |
| $SiO_2$ | 74.38 | 71.88 | 75.02 | 73.20 | 72.73 | 70.29 | 74.37 | 74.07 | 75.84 | 73.48 |
| $TiO_2$ | 0.05 | 0.24 | 0.06 | 0.03 | 0.21 | 0.17 | 0.40 | 0.03 | 0.09 | 0.03 |
| $Al_2O_3$ | 13.60 | 14.01 | 13.49 | 14.17 | 13.72 | 14.91 | 12.00 | 14.00 | 14.28 | 14.78 |
| $Fe_2O_3$* | 0.33 | 0.95 | 0.18 | 0.16 | 0.75 | 0.57 | 1.16 | 0.25 | 0.51 | 0.36 |
| FeO | 0.42 | 1.21 | 0.21 | 0.18 | 0.90 | 0.57 | 1.77 | 0.29 | 0.63 | 0.34 |
| MnO | 0.02 | 0.03 | 0.01 | 0.01 | 0.02 | 0.02 | 0.02 | 0.02 | 0.03 | 0.02 |
| MgO | 0.19 | 0.61 | 0.15 | 0.10 | 0.49 | 0.40 | 1.05 | 0.09 | 0.14 | 0.09 |
| CaO | 1.88 | 2.07 | 1.55 | 1.30 | 1.68 | 1.26 | 1.61 | 0.74 | 0.61 | 0.69 |
| $Na_2O$ | 3.32 | 3.24 | 2.86 | 2.72 | 2.73 | 2.63 | 2.41 | 3.84 | 3.91 | 2.90 |
| $K_2O$ | 4.29 | 4.27 | 5.11 | 6.37 | 5.32 | 7.29 | 3.40 | 4.71 | 3.73 | 7.54 |
| $P_2O_5$ | 0.03 | 0.13 | 0.02 | 0.03 | 0.08 | 0.24 | 0.07 | 0.13 | 0.18 | 0.07 |
| Sum | 98.51 | 98.65 | 98.65 | 98.26 | 98.63 | 98.35 | 98.26 | 98.16 | 99.94 | 100.31 |
| (ppm) | | | | | | | | | | |
| V | 8 | 21 | 5 | 12 | 16 | 16 | 39 | 9 | 7 | 10 |
| Cr | 5 | 6 | 5 | 5 | 10 | 3 | 23 | 3 | 39 | 2 |
| Co | 4 | 3 | <LD | <LD | 4 | 4 | 10 | 4 | 8 | 4 |
| Ni | 44 | 51 | 10 | 9 | 17 | 10 | 35 | 6 | 1 | <LD |
| Zn | 15 | 35 | 12 | 11 | 29 | 25 | 54 | 15 | 17 | 6 |
| Ga | 14 | 16 | 16 | 14 | 13 | 16 | 13 | 20 | 23 | 13 |
| As | 4 | 1 | 4 | <LD | 1 | 3 | <LD | 2.00 | <LD | <LD |
| Rb | 123.2 | 166.7 | 160.4 | 196.1 | 194.2 | 184.6 | 124.3 | 234.6 | 211.0 | 208.0 |
| Sr | 274.4 | 274.1 | 304.0 | 296.2 | 285.7 | 383.3 | 227.1 | 55.6 | 14.2 | 328.3 |
| Y | 11.1 | 16.3 | 3.1 | 5.3 | 8.6 | 19.3 | 5.6 | 12.2 | 8.2 | 6.4 |
| Zr | 23.8 | 19.3 | 6.4 | 37.7 | 24.7 | 39.5 | 90.2 | 14.7 | 18.4 | 8.9 |
| Nb | 3.3 | 12.6 | 2.9 | 1.4 | 9.1 | 5.5 | 15.1 | 14.8 | 36.9 | 1.0 |
| Cs | 1.1 | 3.4 | 1.9 | 2.0 | 2.9 | 2.2 | 2.3 | 5.0 | 2.7 | 1.1 |
| Ba | 957 | 935 | 1203 | 1162 | 1328 | 2147 | 884 | 107 | 23 | 1483 |
| La | 12.4 | 51.9 | 4.8 | 12.5 | 34.9 | 9.9 | 11.4 | 3.2 | 3.5 | 4.2 |
| Ce | 23.6 | 91.2 | 9.3 | 24.2 | 62.7 | 21.3 | 22.1 | 5.9 | 7.3 | 7.6 |
| Pr | 2.8 | 11.1 | 1.1 | 2.8 | 7.4 | 2.7 | 2.6 | 0.7 | 0.8 | 0.8 |
| Nd | 9.3 | 34.6 | 3.5 | 8.9 | 22.9 | 10.0 | 8.3 | 2.0 | 2.9 | 2.8 |
| Sm | 2.12 | 5.98 | 0.63 | 1.69 | 3.87 | 2.52 | 1.51 | 0.75 | 0.89 | 0.59 |
| Eu | 0.96 | 1.30 | 1.12 | 1.05 | 1.34 | 2.18 | 1.16 | 0.37 | 0.04 | 0.50 |
| Gd | 2.12 | 4.85 | 0.52 | 1.48 | 2.94 | 2.93 | 1.43 | 1.05 | 0.87 | 0.53 |
| Tb | 0.37 | 0.69 | 0.09 | 0.22 | 0.43 | 0.58 | 0.24 | 0.28 | 0.20 | 0.11 |
| Dy | 1.96 | 3.16 | 0.46 | 1.00 | 1.81 | 3.42 | 1.12 | 1.78 | 1.39 | 0.88 |
| Ho | 0.42 | 0.61 | 0.11 | 0.19 | 0.32 | 0.72 | 0.20 | 0.39 | 0.26 | 0.23 |
| Er | 1.04 | 1.38 | 0.29 | 0.46 | 0.67 | 1.68 | 0.43 | 1.19 | 0.81 | 0.91 |
| Tm | 0.16 | 0.20 | 0.05 | 0.07 | 0.09 | 0.24 | 0.06 | 0.23 | 0.15 | 0.17 |
| Yb | 0.89 | 1.13 | 0.33 | 0.49 | 0.51 | 1.21 | 0.32 | 1.63 | 1.17 | 1.27 |
| Lu | 0.14 | 0.18 | 0.05 | 0.09 | 0.08 | 0.18 | 0.05 | 0.27 | 0.17 | 0.20 |
| Hf | 0.81 | 0.58 | 0.25 | 3.19 | 0.66 | 1.17 | 2.30 | 0.74 | 0.90 | 0.40 |
| Ta | <LD | 1.04 | 0.44 | <LD | 0.58 | 0.32 | 0.81 | 3.74 | 6.75 | 0.19 |
| Pb | 27 | 25 | 27 | 37 | 31 | 59 | 36 | 52 | 17 | 37 |
| Th | 6.30 | 22.86 | 3.64 | 9.01 | 15.54 | 2.12 | 4.05 | 1.73 | 1.52 | 1.91 |
| U | 1.87 | 4.31 | 3.87 | 2.18 | 2.52 | 1.39 | 1.75 | 6.55 | 4.89 | 1.39 |
| Eu/Eu* | 0.37 | 0.19 | 1.57 | 0.54 | 0.31 | 0.67 | 0.65 | 0.35 | 0.04 | 0.73 |

**Table 2-2.** Continued.

| | Leucosome | | | Basement Orthogneiss | | Basement Paragneiss | | | |
|---|---|---|---|---|---|---|---|---|---|
| | AH-03-22 | Mean | SEM[a] | AH-02-07 | AH-02-12 | AH-03-18 | AH-02-28 | AH-02-30 | AH-03-21 |
| (wt. %) | | | | | | | | | |
| $SiO_2$ | 74.49 | 73.34 | 1.27 | 67.91 | 70.15 | 71.36 | 58.21 | 68.32 | 57.54 |
| $TiO_2$ | 0.07 | 0.14 | 0.11 | 0.53 | 0.34 | 0.17 | 2.01 | 0.16 | 2.04 |
| $Al_2O_3$ | 14.41 | 14.01 | 0.50 | 14.77 | 14.59 | 16.33 | 15.19 | 17.16 | 13.63 |
| $Fe_2O_3$* | 0.48 | 0.55 | 0.25 | 1.82 | 1.18 | 0.73 | 3.00 | 0.68 | 3.28 |
| FeO | 0.56 | 0.71 | 0.40 | 2.67 | 1.52 | 0.88 | 5.51 | 0.90 | 5.99 |
| MnO | 0.03 | 0.02 | 0.01 | 0.07 | 0.04 | 0.03 | 0.13 | 0.03 | 0.13 |
| MgO | 0.12 | 0.35 | 0.25 | 1.15 | 0.74 | 0.46 | 2.58 | 0.62 | 2.83 |
| CaO | 0.74 | 1.46 | 0.52 | 3.06 | 2.31 | 2.11 | 4.76 | 2.96 | 4.75 |
| $Na_2O$ | 3.80 | 3.27 | 0.52 | 3.96 | 3.42 | 4.45 | 2.20 | 5.23 | 2.11 |
| $K_2O$ | 4.40 | 4.77 | 1.20 | 2.60 | 4.12 | 3.72 | 2.98 | 2.21 | 3.13 |
| $P_2O_5$ | 0.15 | 0.09 | 0.06 | 0.15 | 0.11 | 0.07 | 0.86 | 0.10 | 0.97 |
| Sum | 99.25 | | | 98.69 | 98.52 | 100.32 | 97.44 | 98.36 | 96.40 |
| (ppm) | | | | | | | | | |
| V | 11 | 15 | 7 | 44 | 32 | 10 | 109 | 18 | 117 |
| Cr | 5 | 11 | 9 | 12 | 7 | 6 | 25 | 5 | 130 |
| Co | 3 | 5 | 2 | 8 | 5 | 7 | 19 | 3 | 23 |
| Ni | <LD | 22 | 19 | 27 | 52 | <LD | 36 | 31 | 87 |
| Zn | 16 | 22 | 10 | 69 | 45 | 29 | 148 | 35 | 143 |
| Ga | 17 | 16 | 2 | 22 | 16 | 19 | 15 | 18 | 23 |
| As | <LD | 2 | 1 | 3 | 4 | <LD | 2 | 4 | <LD |
| Rb | 221.0 | 174.4 | 35.2 | 155.1 | 181.9 | 117.8 | 168.9 | 79.3 | 140.7 |
| Sr | 18.5 | 231.9 | 94.2 | 255.6 | 295.6 | 426.7 | 557.0 | 617.0 | 454.7 |
| Y | 14.4 | 9.8 | 3.9 | 32.2 | 16.2 | 6.9 | 25.7 | 5.7 | 32.1 |
| Zr | 33.2 | 35.8 | 21.1 | 47.1 | 79.5 | 36.9 | 65.9 | 38.0 | 78.2 |
| Nb | 13.5 | 10.5 | 6.9 | 23.5 | 11.2 | 8.5 | 41.4 | 5.4 | 33.8 |
| Cs | 5.8 | 2.7 | 1.0 | 4.8 | 4.1 | 1.3 | 5.0 | 1.5 | 3.9 |
| Ba | 16 | 877 | 489 | 441 | 854 | 909 | 1300 | 672 | 1129 |
| La | 6.5 | 14.7 | 10.6 | 60.4 | 62.2 | 13.6 | 103.0 | 6.3 | 65.0 |
| Ce | 13.8 | 27.3 | 18.5 | 102.8 | 110.8 | 27.1 | 249.0 | 12.0 | 202.0 |
| Pr | 1.6 | 3.2 | 2.2 | 12.5 | 13.5 | 2.9 | 25.0 | 1.4 | 27.0 |
| Nd | 5.7 | 10.5 | 6.9 | 39.3 | 41.8 | 10.3 | 99.7 | 4.8 | 87.0 |
| Sm | 1.57 | 2.09 | 1.20 | 6.71 | 6.92 | 2.01 | 14.82 | 1.04 | 16.30 |
| Eu | 0.11 | 0.92 | 0.46 | 1.34 | 1.35 | 0.45 | 3.82 | 0.52 | 2.96 |
| Gd | 1.46 | 1.89 | 1.01 | 6.24 | 5.07 | 1.66 | 10.62 | 1.02 | 11.41 |
| Tb | 0.33 | 0.32 | 0.14 | 1.05 | 0.71 | 0.25 | 1.38 | 0.18 | 1.42 |
| Dy | 2.32 | 1.73 | 0.69 | 5.60 | 3.09 | 1.36 | 5.51 | 0.98 | 6.99 |
| Ho | 0.47 | 0.35 | 0.14 | 1.22 | 0.60 | 0.25 | 1.00 | 0.19 | 1.23 |
| Er | 1.52 | 0.92 | 0.35 | 3.08 | 1.44 | 0.63 | 2.13 | 0.44 | 3.09 |
| Tm | 0.28 | 0.15 | 0.06 | 0.46 | 0.21 | 0.08 | 0.30 | 0.06 | 0.40 |
| Yb | 2.12 | 0.95 | 0.43 | 2.61 | 1.21 | 0.47 | 1.68 | 0.36 | 2.48 |
| Lu | 0.32 | 0.15 | 0.07 | 0.41 | 0.20 | 0.06 | 0.24 | 0.05 | 0.34 |
| Hf | 1.30 | 1.36 | 0.83 | 1.20 | 2.17 | 1.30 | 1.57 | 1.20 | 2.00 |
| Ta | 2.27 | 1.60 | 1.45 | 1.33 | 0.67 | 0.59 | 1.92 | 0.35 | 1.65 |
| Pb | 26 | 32 | 9 | 18 | 25 | 23 | 20 | 22 | 16 |
| Th | 2.68 | 7.14 | 5.39 | 23.66 | 30.18 | 5.72 | 18.70 | 0.73 | 15.30 |
| U | 6.76 | 3.52 | 1.63 | 10.93 | 4.00 | 1.05 | 3.07 | 0.68 | 2.11 |
| Eu/Eu* | 0.058 | | | 0.17 | 0.18 | 0.20 | 0.24 | 0.42 | 0.17 |

**Table 2-3.** Whole rock Nd and Sr isotope data of the leucosome, the Ladybird granite suite and basement gneiss samples from the Thor Odin-Pinnacles area.

| Sr Isotopes | | | | | | | | |
|---|---|---|---|---|---|---|---|---|
| Sample no. | Location | Rock Type | Rb (ppm) | Sr (ppm) | $^{87}Sr/^{86}Sr$ (m)[ab] | $2\sigma$[c] (+/-) | $^{87}Rb/^{86}Sr$ (calc)[d] | $^{87}Sr/^{86}Sr$ (55 Ma) |
| LB-02-01 | Slocan Lake | Ladybird Granite | 196.3 | 513.0 | 0.713177 | 09 | 1.11 | 0.71231 |
| LB-02-02 | Slocan Lake | Ladybird Granite | 209.7 | 438.1 | 0.713340 | 10 | 1.39 | 0.71226 |
| LB-02-03 | Slocan Lake | Ladybird Granite | 187.1 | 442.7 | 0.712551 | 10 | 1.22 | 0.71160 |
| AH-03-03 | Slocan Lake | Ladybird Granite | 232.0 | 327.1 | 0.713635 | 12 | 2.05 | 0.71203 |
| AH-03-06 | Sugar Lake | Ladybird Granite | 203.0 | 240.1 | 0.716841 | 34 | 2.45 | 0.71493 |
| AH-03-07 | Sugar Lake | Ladybird Granite | 252.0 | 247.2 | 0.719191 | 21 | 2.95 | 0.71688 |
| AH-03-13 | Sugar Lake | Ladybird Granite | 224.0 | 88.3 | 0.724540 | 18 | 7.35 | 0.71880 |
| AH-03-30 | Mt. Baldur | Ladybird Granite | 223.0 | 322.9 | 0.733146 | 23 | 2.00 | 0.73158 |
| AH-03-31 | Mt. Baldur | Ladybird Granite | 170.0 | 397.1 | 0.714386 | 17 | 1.24 | 0.71342 |
| AH-03-32 | Mt. Baldur | Ladybird Granite | 138.4 | 189.2 | 0.738118 | 33 | 2.12 | 0.73646 |
| AH-03-33 | Mt. Baldur | Ladybird Granite | 164.0 | 383.8 | 0.716813 | 22 | 1.24 | 0.71585 |
| AH-03-34 | Mt. Baldur | Ladybird Granite | 225.0 | 162.3 | 0.736805 | 25 | 4.02 | 0.73366 |
| AH-03-37 | Mt. Baldur | Ladybird Granite | 135.8 | 1329.0 | 0.706258 | 17 | 0.30 | 0.70603 |
| AH-02-05 | Frigg Glacier | Leucosome | 92.1 | 245.9 | 0.743413 | 14 | 1.09 | 0.74256 |
| AH-02-06 | Frigg Glacier | Leucosome | 150.9 | 307.0 | 0.750247 | 15 | 1.43 | 0.74913 |
| AH-02-08 | Frigg Glacier | Leucosome | 123.2 | 274.4 | 0.747273 | 19 | 1.30 | 0.74625 |
| AH-02-09 | Frigg Glacier | Leucosome | 166.7 | 274.1 | 0.751479 | 12 | 1.77 | 0.75010 |
| AH-02-10 | Frigg Glacier | Leucosome | 160.4 | 304.0 | 0.750216 | 11 | 1.53 | 0.74902 |
| AH-02-11 | Frigg Glacier | Leucosome | 196.1 | 296.2 | 0.761240 | 11 | 1.92 | 0.75974 |
| AH-02-13 | Frigg Glacier | Leucosome | 194.2 | 285.7 | 0.752558 | 17 | 1.98 | 0.75101 |
| AH-02-26 | Saturday Glacier | Leucosome | 184.6 | 383.3 | 0.761799 | 65 | 1.40 | 0.76070 |
| AH-02-27 | Saturday Glacier | Leucosome | 124.3 | 227.1 | 0.767178 | 11 | 1.59 | 0.76593 |
| AH-03-20 | Saturday Glacier | Leucosome | 36.5 | 191.2 | 0.765469 | 16 | 0.56 | 0.76504 |
| AH-02-07 | Frigg Glacier | Orthogneiss | 155.1 | 255.6 | 0.752361 | 16 | 1.76 | 0.75098 |
| AH-02-12 | Frigg Glacier | Orthogneiss | 181.9 | 295.6 | 0.750427 | 24 | 1.79 | 0.74903 |
| AH-02-28 | Saturday Glacier | Paragneiss | 168.9 | 557.0 | 0.724180 | 10 | 0.88 | 0.72349 |
| AH-03-18 | Saturday Glacier | Paragneiss | 117.8 | 426.7 | 0.726997 | 24 | 0.80 | 0.72637 |

[a] measurements by TIMS. [b] measured and corrected for mass fractionation. [c] errors refer to last one or two digits and are propogated to include reproducibility of standard analysis and run errors. [d] calculated using ppm concentrations from ICP-MS trace element analysis.

**Table 2-3.** Continued.

| Nd Isotopes | | | | | | | | | |
|---|---|---|---|---|---|---|---|---|---|
| Sample no. | Location | Rock Type | Sm (ppm) | Nd (ppm) | $^{143}Nd/^{144}Nd$ (m)[ab] | 2σ[c] (+/-) | $^{147}Sm/^{144}Nd$ (calc)[d] | $^{143}Nd/^{144}Nd$ (55 Ma) | εNd[e] (55 Ma) |
| LB-02-01 | Slocan Lake | Ladybird Granite | 9.13 | 55.18 | 0.512062 | 15 | 0.09964 | 0.51203 | -10.6 |
| LB-02-02 | Slocan Lake | Ladybird Granite | 7.81 | 44.72 | 0.512047 | 10 | 0.10517 | 0.51201 | -10.9 |
| LB-02-03 | Slocan Lake | Ladybird Granite | 8.10 | 47.45 | 0.512040 | 14 | 0.10280 | 0.51200 | -11.0 |
| AH-03-03 | Slocan Lake | Ladybird Granite | 3.03 | 14.72 | 0.511890 | 68 | 0.12396 | 0.51185 | -14.1 |
| AH-03-06 | Sugar Lake | Ladybird Granite | 8.66 | 45.82 | 0.511727 | 57 | 0.11381 | 0.51169 | -17.2 |
| AH-03-07 | Sugar Lake | Ladybird Granite | 5.40 | 31.54 | 0.511785 | 37 | 0.10310 | 0.51175 | -16.0 |
| AH-03-13 | Sugar Lake | Ladybird Granite | 5.87 | 22.88 | 0.511768 | 24 | 0.15450 | 0.51171 | -16.7 |
| AH-03-30 | Mt. Baldur | Ladybird Granite | 20.20 | 118.00 | 0.511980 | 13 | 0.10309 | 0.51194 | -12.2 |
| AH-03-31 | Mt. Baldur | Ladybird Granite | 8.93 | 71.01 | 0.512340 | 18 | 0.07573 | 0.51231 | -5.0 |
| AH-03-32 | Mt. Baldur | Ladybird Granite | 5.00 | 24.26 | 0.512007 | 30 | 0.12411 | 0.51196 | -11.8 |
| AH-03-33 | Mt. Baldur | Ladybird Granite | 8.48 | 65.94 | 0.512218 | 15 | 0.07744 | 0.51219 | -7.4 |
| AH-03-34 | Mt. Baldur | Ladybird Granite | 4.37 | 21.51 | 0.511875 | 13 | 0.12234 | 0.51183 | -14.4 |
| AH-03-37 | Mt. Baldur | Ladybird Granite | 1.49 | 7.85 | 0.512069 | 49 | 0.11430 | 0.51203 | -10.5 |
| AH-02-05 | Frigg Glacier | Leucosome | 1.31 | 6.62 | 0.512123 | 29 | 0.11916 | 0.51208 | -9.5 |
| AH-02-06 | Frigg Glacier | Leucosome | 3.8 | 19 | 0.511749 | 23 | 0.12044 | 0.51171 | -16.8 |
| AH-02-08 | Frigg Glacier | Leucosome | 2.12 | 9.29 | 0.511704 | 25 | 0.13742 | 0.51165 | -17.8 |
| AH-02-09 | Frigg Glacier | Leucosome | 5.98 | 34.57 | 0.511513 | 18 | 0.10417 | 0.51148 | -21.3 |
| AH-02-10 | Frigg Glacier | Leucosome | 0.63 | 3.49 | 0.511697 | 20 | 0.10871 | 0.51166 | -17.7 |
| AH-02-11 | Frigg Glacier | Leucosome | 1.69 | 8.86 | 0.511700 | 16 | 0.11487 | 0.51166 | -17.7 |
| AH-02-13 | Frigg Glacier | Leucosome | 3.87 | 22.85 | 0.511510 | 28 | 0.10199 | 0.51147 | -21.3 |
| AH-02-26 | Saturday Glacier | Leucosome | 2.52 | 9.98 | 0.511533 | 22 | 0.15206 | 0.51148 | -21.2 |
| AH-02-27 | Saturday Glacier | Leucosome | 1.51 | 8.31 | 0.511395 | 44 | 0.10942 | 0.51136 | -23.6 |
| AH-03-20 | Saturday Glacier | Leucosome | 0.27 | 1.48 | 0.511406 | 15 | 0.10986 | 0.51137 | -23.4 |
| AH-02-07 | Frigg Glacier | Orthogneiss | 6.71 | 39.26 | 0.511479 | 16 | 0.10292 | 0.51144 | -22.0 |
| AH-02-12 | Frigg Glacier | Orthogneiss | 6.92 | 41.78 | 0.511359 | 19 | 0.09974 | 0.51132 | -24.3 |
| AH-02-28 | Saturday Glacier | Paragneiss | 14.82 | 99.71 | 0.511216 | 17 | 0.08950 | 0.51118 | -27.0 |
| AH-03-18 | Saturday Glacier | Paragneiss | 2.01 | 10.29 | 0.511594 | 62 | 0.11763 | 0.51155 | -19.8 |

[a] measurements by TIMS. [b] measured and corrected for mass fractionation.
[c] errors refer to last one or two digits and are propogated to include reproducibility of standard analysis and run errors.
[d] calculated using ppm concentrations from ICP-MS trace element analysis.
[e] calculated using present day chondritic uniform reservoir with $^{143}Nd/^{144}Nd = 0.512638$ and $^{147}Sm/^{144}Nd = 0.1967$.

# CHAPTER 3

## Cordierite-gedrite basement rocks and associated garnet amphibolites of Thor-Odin dome, Monashee complex: protolith composition and implications for the petrogenesis of the North American basement


### Abstract

The Precambrian history of the Thor-Odin dome area is poorly constrained due to the pervasive overprinting of high-grade metamorphism, deformation, and anatexis associated with Cretaceous-Tertiary events during the Cordilleran orogeny. The occurrence of cordierite-gedrite rocks and associated garnet amphibolites in the North American basement rocks of Thor-Odin dome were the focus of major and trace element geochemical, Rb-Sr and Sm-Nd isotopic, petrographic and field studies to constrain the origin of the cordierite-gedrite rocks and of the garnet amphibolites, and from these data constrain the Precambrian evolution of the basement gneisses.

The cordierite-orthoamphibole, dominantly gedrite, rocks are primarily preserved on the limbs of Paleogene $F_2$ folds in the basement paragneiss in the southwestern area of the Thor-Odin dome, Monashee complex. This unit appears to define a discontinuous marker horizon within the Paleoproterozoic North American basement paragneiss, which were metamorphosed to peak conditions of 8-10 kbar and 800 °C during the Late Cretaceous to Paleocene Cordilleran orogeny. The cordierite-gedrite rocks occur as discontinuous lenses, 15 to 50 meters thick, and up to 500 meters long that are concordant with the pervasive $S_2$ transposition foliation. These rocks have unique bulk rock chemistry that is characterized by depletions in the alkalies, notably CaO, and enrichments in $Al_2O_3$, MgO and $Fe_2O_3$. They have flat rare earth element (REE) patterns, depletions in most low field strength elements, such as Cs, Rb, Ba and Sr, and enrichments in high field strength elements such as Zr, Hf, and Nb. The $^{87}Sr/^{86}Sr$ ratios for these rocks vary from 0.74923 to 0.85962 and the $\varepsilon Nd_{(today)}$ vary from −15.3 to −20.6. The cordierite-gedrite rocks are interpreted as Paleoproterozoic mafic volcanics that were hydrothermally altered,

likely syn-depositional. This hydrothermal alteration explains their distinctive bulk rock chemistry.

The cordierite-gedrite rocks are interlayered and spatially associated with lenses of garnet amphibolites of uncertain, although likely Precambrian based on Nd isotopic composition, protolith age. In the Bearpaw Lake area, Thor-Odin dome, the garnet amphibolites are boudinaged, 10-20 meters thick, up to 400 meters long, and are concordant with the pervasive $S_2$ transposition foliation. The garnet amphibolites have high MgO and $TiO_2$ values and depletions in the alkalies. They have flat REE patterns, depletions in most low field strength elements and enrichments in high field strength elements. The garnet amphibolites have $^{87}Sr/^{86}Sr$ ratios varying from 0.70953 to 0.74319 and $\varepsilon Nd_{(today)}$ from –0.8 to –7.3. The garnet amphibolites are interpreted as Proterozoic metamorphosed mafic (basaltic) rocks that either post-date the formation of the protolith of the cordierite-gedrite rocks or escaped the hydrothermal alteration.

On the basis of chemistry and Nd isotopic signatures, neither the cordierite-gedrite rocks nor the garnet amphibolites can be correlated with regional mafic suites known to have intruded the rocks of North American basement and platformal sequence in the southern Omineca belt. The mafic suites include: the Moyie sills of the Belt-Purcell Supergroup, volcanics of the Horsethief creek group of the Windermere Supergroup, and Eocene lamprophyre dykes. The chemical and isotopic signatures of the garnet amphibolites and cordierite-gedrite samples show a range of values that overlap with these suites.

## 3.1. Introduction

Cordierite-orthoamphibole rocks occur as lenses and boudinaged layers in Paleoproterozoic basement paragneiss of Thor-Odin dome, Monashee complex, southeastern British Columbia. The origin of cordierite-orthoamphibole (gedrite-anthophyllite) rocks is enigmatic as their chemistry is not easily explained as being either of sedimentary or igneous origin. Their chemistry is distinctive in that it is marked by enrichments in MgO, $Al_2O_3$, and FeO, and depletions in the alkalies, particularly CaO. These rocks are of interest because the Precambrian history of this area is poorly constrained due to the pervasive overprinting of high-grade metamorphism, deformation, and anatexis associated with Cretaceous-Tertiary events during the Cordilleran orogeny. Constraining the origin of the cordierite-orthoamphibole rocks will help to further understand the Precambrian geologic history of the area.

Genetic models for the evolution of cordierite-orthoamphibole rocks are diverse but can generally be classified into two groups based on whether the protoliths were affected by chemical alteration before or during metamorphism. The most commonly employed models for the formation of these rocks are described below. The first two models attribute the chemical signature of cordierite-orthoamphibole rocks to alteration during metamorphism. The first model involves synmetamorphic metasomatic alteration, which introduces FeO and MgO by diffusion or hydrothermal fluid infiltration into a range of rock types (i.e. Eskola, 1914; Irving and Ashley, 1976). The second model invokes partial melting, in which these rocks are the residuum, likely of a pelitic sediment or a metavolcanic, after extraction of granitic melt (i.e. Grant, 1968; Hoffer and Grant, 1980). The remaining genetic models invoke alteration prior to metamorphism. In the third model, the cordierite-orthoamphibole rocks form via the metamorphism of an ancient weathering horizon and these rocks are a paleoregolith or paleosol (Gable and Sims, 1969; Young, 1973). In the fourth model, the cordierite-orthoamphibole rocks represent volcanic rocks that were hydrothermally altered prior to metamorphism (i.e. Vallance,

1967; James et al., 1978; Schumacher, 1988; Smith et al., 1992). This is the most common model invoked for the formation of the cordierite-orthoamphibole rocks, and usually involves sea water as the hydrothermal fluid (Spear, 1993).

This paper addresses the origin and geological significance of the cordierite-gedrite rocks in Thor-Odin dome. Major and trace element geochemical studies, in combination with Rb-Sr and Sm-Nd isotopic studies, were carried out to address the question of their petrogenesis. It has previously been suggested that this unit may define a pseudo-stratigraphy within the basement paragneiss, and outcrop on the limbs of a fold (Duncan, 1984), thus further understanding for their formation may have implications on the tectonic evolution of the Thor-Odin dome.

### 3.2. Geological setting

Thor-Odin dome is one of two structural culminations of the Monashee complex that contain a core of Paleoproterozoic orthogneiss and paragneiss basement rocks of North America cratonic affinity (Fig. 3-1; Parrish, 1991). The basement rocks are unconformably overlain by and infolded with a Paleoproterozoic to Paleozoic supracrustal cover sequence of dominantly metasedimentary siliciclastic and carbonate rocks (Fig. 3-2; Wheeler, 1965; McMillan 1973; Brown, 1980; Read, 1980; Scammell and Brown, 1990, Armstrong et al., 1991; Parkinson, 1992; Parrish, 1995; Crowley; 1997). The rocks are exposed in a tectonic window beneath the Monashee décollement, the boundary between the structurally overlying allochthonous rocks of the Selkirk allochthon and the relatively more autochthonous rocks of the Monashee complex (Read and Brown, 1981; Brown et al., 1986; Journeay, 1986; Brown et al, 1992; McNicoll and Brown, 1995; Brown and Gibson, in press). Cordilleran orogenesis in the Monashee complex resulted in middle amphibolite to lower granulite facies metamorphism, km-scale isoclinal folds, anatexis, and the development of penetrative planar and linear deformation fabrics (Wheeler, 1965; Reesor and Moore, 1971; Höy and Brown, 1980; Brown et al. 1986; Journeay, 1986; McNicoll and Brown, 1995; Hinchey, Chapter 1).

Paleocene-Eocene extension of the southern Omineca belt resulted in the exhumation of the Monashee complex via an array of brittle and ductile normal faults (Tempelman-Kluit and Parkinson, 1986; Brown and Journeay, 1987; Parrish et al., 1988; Struik, 1993; Johnson and Brown 1996 and references therein). At the latitude of the Monashee complex, the lower plates of the extensional faults expose high-grade rocks with a relatively young deformation and cooling history termed the Shuswap complex (Fig. 3-1; Okulitch, 1984; Brown and Journeay, 1987; Parrish et al., 1988; Parkinson, 1992; Johnson, 1994).

### *3.2.1. Geology of Thor-Odin dome*

The basement rocks of Thor-Odin dome are composed of Paleoproterozoic heterogeneous migmatitic para- and orthogneiss (Fig. 3-2). Basement orthogneiss are dominated by migmatitic, hornblende-biotite-quartzo feldspathic gneiss with a lesser volume of quartz monzonite gneiss. Basement paragneiss comprise: a) heterogeneous migmatitic garnet-sillimanite-quartzo feldspathic gneiss locally enriched in garnet and cordierite, b) migmatitic cordierite-biotite-quartzo feldspathic gneiss, c) minor calc-silicates, marbles, and quartzites, and are associated with minor cordierite-gedrite rocks and garnet amphibolites (Reesor and Moore, 1971; Duncan, 1984). Though lithologically distinct, the basement ortho- and paragneiss are often interlayered at the scale of a few meters, due in large part to transposition by folding, with contacts that are complicated by the abundance of leucosome. The cover sequence comprises a heterogeneous assemblage of metasedimentary rocks that includes quartzites, pelitic schists, marbles, calc-silicates and amphibolites.

### *3.2.2. Precambrian geological history*

The basement orthogneiss are interpreted to have intruded into the basement paragneiss during the Paleoproterozoic (Parkinson, 1992). Although the homogenous orthogneiss generally have concordant contacts with basement paragneiss, Parkinson

(1992) reported local contacts which are intrusive. Initial U/Pb geochronology studies of zircons from basement orthogneiss yielded crystallization ages of 1934 ± 6 and 1874 ± 21 Ma (Parkinson, 1992). Based on a detrital zircon study, deposition of the basement paragneiss in Thor-Odin dome likely began by 2.2 Ga (Parkinson, 1992) and continued until at least 1.8 Ga, based on the youngest detrital zircon grains from basement paragneisses (Vanderhaeghe et al., 1999; Kuiper, 2003; this study). The Monashee cover sequence was subsequently deposited on the basement para- and orthogneiss after 1825 Ma, the youngest known zircon age in the basal quartzite from a preliminary detrital zircon study (Kuiper, 2003). There are no constraints on an upper age limit for the cover sequence and the youngest depositional age in Thor-Odin dome is uncertain. Precambrian metamorphism and deformation has been pervasively overprinted by Cordilleran deformation and metamorphism. A focus of this paper is elucidating the Precambrian history by understanding the formation of the cordierite-gedrite basement rocks. The rocks studied are exposed in the Bearpaw Lake area (Fig. 3-3) in the southwest portion of the dome.

### *3.2.3. Cretaceous – Eocene Cordilleran metamorphic history*

Basement and cover rocks in Thor-Odin dome experienced high pressure and temperature metamorphism of upper amphibolite to lower granulite facies conditions in the Paleogene at ca. 56 Ma (Hinchey, this study and Chapter 4), and may have reached high grade conditions as early as 75 Ma, on the basis of the age of zircons in leucosome from migmatitic paragneiss near Three Valley gap on the north flank of Thor Odin dome (Parish, 1995; Kuiper, 2003). Throughout the dome, the mineral assemblages are relatively uniform with stable sillimanite-potassium feldspar-melt assemblages (Reesor and Moore, 1971). Kyanite and cordierite occur in aluminous basement gneiss and orthopyroxene occurs in granitic and aluminum-poor basement gneiss (Reesor and Moore, 1971). The sillimanite-potassium feldspar isograd approximately encloses the dome, and rocks of the surrounding Selkirk allochthon are at lower grade

with sillimanite-almandine-muscovite assemblages (Reesor and Moore, 1971). U-Pb geochronology studies indicate that metamorphism and penetrative deformation of the Thor-Odin dome basement rocks were ongoing during the Paleogene (Vanderhaeghe et al., 1999; Johnston et al., 2000; Kuiper, 2003) at ca. 56 to 52 Ma based on the ages of anatectic migmatites (Hinchey, Chapter 1) and of metamorphic monazites (this study). Peak metamorphism culminated in the onset of melting and the production of abundant leucosome (Hinchey, Chapter 1).

Thermobarometry studies in the Bearpaw Lake area indicate that the basement rocks underwent isothermal decompression from the kyanite-potassium feldspar zone ($P > 8$ to 10 kbar) into the sillimanite-cordierite zone ($P < 5$ kbar) at $T \sim 750$ °C, with a maximum temperature of ~ 800 °C (Norlander et al., 2002). Based on complex symplectic textures preserved in basement cordierite-gedrite rocks and in garnet amphibolite boudins, Norlander et al. (2002) concluded that the peak regional metamorphic episode occurred in the Tertiary, as these textures could not have survived a subsequent metamorphic event. This argument, coupled with the ages of zircon crystallization in leucosome from the sampling area (Vanderhaeghe et al., 1999; Hinchey, Chapter 1), and zircon in leucogranites from structurally higher levels (Carr, 1992; Vanderhaeghe et al., 1999), is consistent with the interpretation that metamorphism coincided with the onset of a major partial melting event. Reaction textures indicate that leucocratic melt interacted with minerals growing in the boudins during decompression, preserving cordierite reaction rims around mafic phases such as garnet and corundum (Norlander et al., 2002).

### *3.2.4. Cretaceous – Eocene Cordilleran structural evolution*

Basement and cover gneiss are characterized by at least four folding events, and the map-pattern distribution of basement and cover is controlled by large-scale fold interference patterns (Fig. 3-2). These superimposed folds produced interference patterns at all scales and all structural levels (Read, 1980; Duncan, 1982). The dominant foliation dips to the west on the western margin of the dome and to the east on the eastern margin,

and it wraps around the southern end, producing outward dips (Reesor and Moore, 1971). $F_1$ folds are preserved at outcrop scale, and may represent either relict Precambrian deformation or formation during a progressive $D_{1-2}$ thickening and burial. Kilometre-scale isoclinal $F_2$ fold nappes infold the cover sequence with the underlying basement gneisses (Reesor and Moore, 1971; Read, 1979, 1980; McNeill and Williams, 2004) and are, at least in part, Paleogene in age (Hinchey, Chapter 1). The $S_2$ transposition foliation is the dominant planar fabric throughout the 4-5 km thick exposed section of Thor-Odin dome and is defined by domainal schistosity, compositional banding, and gneissic foliation. Leucosome occurs pervasively throughout the gneisses in Thor-Odin dome. Leucosome is interpreted to have formed as a result of *in situ* melting of the host paragneiss (Hinchey, Chapter 1). Leucosome formation was ongoing from ca. 56-52 Ma, coincident with peak metamorphism, formation of part of the $S_2$ foliation and $F_2$, as well as $F_3$ and $F_4$ (Hinchey et al., 2004).

## 3.3. Bearpaw Lake area

### *3.3.1. Geology*

The Bearpaw Lake area (Fig. 3-2 and 3-3) is characterized by basement rocks dominated by: a) hornblende-biotite granodiorite migmatitic orthogneiss, and, b) compositionally heterogeneous garnet-sillimanite-quartzo feldspathic migmatitic paragneiss. The garnet-sillimanite-quartzo-feldspathic paragneiss is interlayered at the scale of 10's of meters with a muscovite-biotite-quartzo feldspathic diatexite paragneiss and hornblende-biotite-quartzo feldspathic paragneiss. In addition, this unit is characterized by boudinaged layers of cordierite-gedrite rocks, garnet amphibolites, infolded quartzites and calc-silicates. This package of gneiss strikes southeast and dips at ~70° to the west. The lenses of cordierite-gedrite rocks and garnet amphibolites were likely boudinaged during deformation associated with $F_2$ folding, which was ongoing ca. 56 Ma (Fig. 3-3; Hinchey, Chapter 1).

The cordierite-gedrite rocks occur as boudinaged lenses 15 to 50 meters thick and up to 500 meters long (Fig. 3-3). They parallel the pervasive $S_2$ transposition foliation and strike at 135-142° to the southeast. In the southwestern portion of the dome, known occurrences of these rocks are plotted in Figure 3-2. The cordierite-gedrite rocks are documented only within the basement paragneiss, where they occur on the limbs of $F_2$ isoclines and appear to at least locally define a discontinuous marker horizon. Based on mineralogy, it has been suggested that the cordierite-gedrite rocks in Thor-Odin dome may be the product of hydrothermal alteration of mafic volcanics, or that they may represent a restite of partial melting (Duncan, 1982; 1984).

The garnet amphibolites occur as discontinuous boudinaged lenses that range from 10 to 20 meters thick and up to 400 meters long (Fig. 3-3). They parallel the pervasive $S_2$ transposition foliation and strike at 133-150° to the southeast. In the study area, the garnet amphibolites are documented only within the basement paragneisses and are not observed crosscutting the cordierite-gedrite rocks. Garnet amphibolites have been documented throughout Thor-Odin dome (Reesor and Moore, 1971; Parkinson, 1992) and, in contrast to the cordierite-gedrite rocks, the amphibolites in Thor-Odin dome have been studied. They occur as boudinaged lenses that are concordant with the $S_2$ transposition foliation and have been documented within both the basement para- and orthogneiss. Attempts have been made to correlate these amphibolites with the regional mafic suites. Specifically, comparisons were carried out of Nd isotopic signatures of the amphibolites and: a) the mafic Moyie sills (1.5 Ga) of the Middle Proterozoic Belt-Purcell Supergroup, and b) the mafic volcanic rocks associated with the Horsethief Creek Group (~760 Ma; Devlin et al., 1988; Sevigny and Thériault, 2003) of the Late Proterozoic Windermere Supergroup. However, due to a wide range in isotopic values of the amphibolites and limited data set a correlation was not possible (Parkinson, 1991).

For the purpose of evaluating the petrogenesis of the cordierite-gedrite rocks (section 3-4) and discussion (section 3-5), the cordierite-gedrite samples are plotted

with, and compared, to the garnet amphibolite samples. This is because the amphibolites occur regionally, they have been part of previous geochemical studies (Parkinson, 1992; Sevigny, 1988), and their chemistry more closely approximates that of a typical metamorphosed mafic rock. There are no geochronological age constraints on either the cordierite-gedrite rocks or the amphibolites in Thor-Odin dome. For the purpose of evaluating the isotopic signatures, specifically the epsilon values, values are calculated at an age of ~760 Ma, which is the Nd $T_{DM}$ model age of the Horsethief Creek mafic volcanics (Devline et al., 1988). This is interpreted as the lower age constraint for the garnet amphibolites based on $T_{Nd}$ model age (Parkinson, 1992) and regional correlations (Sevigny and Thériault, 2003).

### *3.3.2. Lithology and petrology*

The cordierite-gedrite rocks have very coarse grained textures and complex simplectic intergrowths. The gedrite crystals are up to 25 cm long and garnet occurs up to 15 cm. This coarse grained nature, coupled with their variable mineralogy, makes it difficult to collect hand samples that contain all of the minerals present within individual boudinaged layers. In hand samples, typical mineralogy includes: biotite, sillimanite, kyanite, quartz, spinel, garnet and cordierite (Fig. 3-4a). Norlander et al. (2002) distinguished between gedrite rocks that contain garnet and those that were sapphirine-bearing, however, this distinction is not possible at the outcrop scale. All exposures of the cordierite-gedrite boudins contain garnet at least locally, and thus the absence of garnet in thin section may reflect a local small-scale breakdown reaction or may reflect compositional heterogeneity within the protolith. The contact between the cordierite-gedrite rocks and the paragneiss often contain mats of randomly orientated, coarse grained sillimanite mantled by cordierite and corundum.

Gedrite is the most abundant mineral in the cordierite-gedrite rocks and occurs as prismatic crystals that define the $S_2$ foliation. Garnet occurs as porphyroblasts that often contain abundant inclusions of cordierite, spinel, gedrite, and apatite (Fig. 3-4b). Cracks

in the garnet grains are filled with grains of cordierite, gedrite, ilmenite, plagioclase and spinel. Kyanite is partially to entirely replaced by a corundum + cordierite + ilmenite symplectite in the cores of the grains and spinel + cordierite ± sapphirine in the rims of the grains (Norlander et al., 2002). Cordierite occurs dominantly as an interstitial mineral between blades of gedrite. Sillimanite occurs as prismatic crystals or as fibrous overgrowths on kyanite. Accessory phases of biotite, quartz, apatite, spinel, ilmenite, and monazite are common. Further petrological descriptions related to detailed pressure-temperatures conditions are described in Norlander et al. (2002).

The garnet amphibolites are medium grained garnet hornblende amphibolites with a typical mineralogy of garnet-hornblende-quartz-plagioclase +/- clinopyroxene (Fig. 3-4c). Hornblende occurs both as interstitial grains in the matrix and as euhedral, tabular grains that often define the $S_2$ foliation. Garnet porphyroblasts are 1-3 mm in diameter and contain few inclusions, which when present are dominated by plagioclase, biotite, ilmenite and rutile (Norlander et al., 2002). Garnets are often rimmed by quartz and plagioclase symplectites. Accessory phases are ilmenite, biotite, apatite and monazite. Plagioclase and quartz are granoblastic, anhedral grains that dominate the matrix. Plagioclase commonly displays albite twinning and quartz often contains subgrains. Further petrological descriptions related to detailed pressure-temperatures conditions for the garnet amphibolites are described in Norlander et al. (2002).

## 3.4. Analytical data and interpretation

### *3.4.1. Major and trace element chemistry*

Major element, recalculated to an anhydrous total of 100%, and trace element compositions were determined for all major units in the Bearpaw Lake area. Six samples of the cordierite-gedrite rock and 4 samples of garnet amphibolite were analyzed. The cordierite-gedrite samples are plotted with the garnet amphibolite for comparison, as the amphibolite chemistry more closely approximates a typical metamorphosed mafic rock.

Sample descriptions and locations are listed in Table 3-1. Representative compositions are presented in Table 3-2, and analytical details are given in Appendix A.1. Four samples of quartzo-feldspathic basement paragneiss and 2 samples of granodioritic basement orthogneiss are plotted for comparison (data from Hinchey, Chapter 2).

The cordierite-gedrite rocks show a large range in $SiO_2$ contents from 28 to 53 wt.% (Table 3-2), with one of the samples (AH-03-25) having notably low $SiO_2$ concentration of 28 wt.%, attributed to the large percentage of hercynite, approximately 25 wt.% of the bulk rock composition of that sample. In all samples, $Al_2O_3$ ranges from 13 to 23 wt.%. CaO and $Na_2O$ concentrations are low with values ranging from 6 to 0.2 wt.% and 0.2 to 0.9 wt.%, respectively. The samples are enriched in MgO, 12-18 wt.%; $Fe_2O_3$, 2-5 wt.%; MnO, 0.1-0.3 wt.%, and $TiO_2$, 0.3-3.7 wt.% (Table 3-2). Compared to the cordierite-gedrite samples, the garnet amphibolite samples have a narrower range in $SiO_2$ from 46-51 wt.%, and have lower $Al_2O_3$ contents from 9 to 15 wt.% (Table 3-2). In addition, the garnet amphibolites do not have a marked depletion in CaO or $Na_2O$, with values ranging from 8 to 10 wt.% and 1 to 3 wt.%, respectively. MgO content of the garnet amphibolites is notably less than in the gedrite samples, ranging from 6.0 to 11.2 wt.% and enrichments are observed in $Fe_2O_3$, MnO, and $TiO_2$.

On an AFM diagram (Fig. 3-5), the gedrite samples are more aluminous and define a tighter cluster of values compared to the garnet amphibolite samples. On the ACF diagram (Fig. 3-6a), the cordierite-gedrite rocks dominantly plot along the A-F tieline, reflecting the limited amount of plagioclase in these samples and low CaO content. The garnet amphibolite samples plot more centrally in the diagram, reflecting the presence of more plagioclase. Extreme depletion of $K_2O$ of the cordierite-gedrite rocks is reflected in the AKF diagram (Fig. 3-6b) with samples plotting along the A-F line reflecting a lack of potassium feldspar, while most of the garnet amphibolite samples plot near the F apex or below.

Trace element signatures of the cordierite-gedrite rocks display depletions in most

low field strength elements (LFSE; field strength elements as defined by Saunders et al., 1980) such as Cs, Ba, Sr and Pb (Table 3-2). Samples are enriched in most high field strength elements (HFSE) such as Zr, Hf, Nb and Ta. In addition, the samples show enrichments in the transition elements of Cr, Ni, V, and Zn. In general, the garnet amphibolite samples show the same trace element trends and variation in concentrations (Table 3-2).

The chondrite-normalized rare earth element (REE) patterns of the cordierite-gedrite samples are relatively flat, with $La_{(N)}/Yb_{(N)}$ ratios between 1 and 16 times chondrite (Fig. 3-7a). The samples all have slightly negative Eu anomalies. The garnet amphibolites have similar flat chondrite-normalized REE patterns, with $La_{(N)}/Yb_{(N)}$ ratios between 0.5 and 7 times chondrite (Fig. 3-7b). On an extended trace element primitive-mantle normalized spider diagram, the cordierite-gedrite samples exhibit marked depletions in Rb, Ba, and Sr, and enrichments in Cs, Th, U and the heavy rare earth elements (HREE; Fig. 3-7c). The garnet amphibolite samples also show the same general pattern of enrichments and depletions in the above noted elements, with the exception that they lack the Th enrichment and the extreme degree of Sr depletion of the gedrite samples (Fig. 3-7c).

### *3.4.2. Whole rock radiogenic isotope geochemistry*

Rubidium-strontium and samarium-neodymium data for whole rock samples from the Bearpaw Lake area are presented in Table 3-3. Analytical details are given in Appendix A.1. Three samples of cordierite-gedrite rock and three samples of garnet amphibolite were analyzed. Two samples of both the basement paragneiss and the basement orthogneiss are plotted for comparison (data from Hinchey, Chapter 2).

#### *3.4.2.1.* Sr isotopes

The amphibolite and gedrite samples have radiogenic measured $^{87}Sr/^{86}Sr$ ratios (Table 3-3). The cordierite-gedrite rocks have a range of $^{87}Sr/^{86}Sr$ ratios from 0.74923 to 0.85962, and measured $^{87}Rb/^{86}Sr$ ratios from 0.44 to 12.24. The garnet amphibolite

samples have a range of $^{87}Sr/^{86}Sr$ ratios from 0.70953 to 0.74319, and measured $^{87}Rb/^{86}Sr$ ratios from 0.40 to 1.51. The four basement samples have measured $^{87}Sr/^{86}Sr$ ratios from 0.72418 to 0.75236 and $^{87}Rb/^{86}Sr$ ratios range from ~0.80 to 1.79 (Hinchey, Chapter 2). The Sr data demonstrate the highly radiogenic nature of the Paleoproterozoic basement gneisses of the Thor-Odin area.

The primitive mantle has a present day $^{87}Sr/^{86}Sr$ value of 0.7045 and the bulk silicate earth has a $^{87}Rb/^{86}Sr$ value of 0.089. The Sr data for both the garnet amphibolites and cordierite-gedrite rocks have a wide range of radiogenic values (Fig. 3-8), likely reflecting disturbance of the Sr isotopic system during high-grade metamorphism. Data for basement gneisses and amphibolites from Parkinson (1991; 1992) are plotted for comparison. The Rb-Sr isotope system appears to have been disturbed; perhaps by Cordilleran metamorphism, and therefore the data cannot be used to determine the protolith composition of the garnet amphibolites or cordierite-gedrite rocks.

*3.4.2.2.* Nd isotopes

The garnet amphibolite and cordierite-gedrite samples have different Nd isotopic compositions (Table 3-3). The cordierite-gedrite samples display a range in $^{147}Sm/^{144}Nd$ ratios from 0.1084 to 0.1224, $\varepsilon Nd_{(today)}$ values from –15.3 to –20.6, and Nd model ages of $T_{(DM)}$ = 2.2 to 3.5 Ga. The garnet amphibolite samples have a range in $^{147}Sm/^{144}Nd$ ratios from 0.1502 to 0.1685, $\varepsilon Nd_{(today)}$ values from –0.8 to –7.3, and Nd model ages of $T_{(DM)}$ = 1.3 to 2.2 Ga. The four basement gneiss samples have $^{147}Sm/^{144}Nd$ ratios of 0.0895 to 0.1176, and $\varepsilon Nd_{(today)}$ values of –20.4 to –27.4 (Hinchey, Chapter 2). Data for the basement gneiss and garnet amphibolite samples from Parkinson (1991, 1992) are plotted for comparison (Fig. 3-9). εNd is calculated at 760 Ma, the lower age constraint on the garnet amphibolites (see section 3.3.1). The $^{147}Sm/^{144}Nd$ ratios appear to have retained their original isotopic signature, with the garnet amphibolite and cordierite-gedrite samples plotting homogeneously into two groups (Fig. 3-9). There is no differential mobility of Sm and Nd observed in the REE chemistry (Fig. 3-7). This supports the

interpretation that the differences in εNd signatures between the garnet amphibolite and cordierite-gedrite samples are inherited and are not a result of alteration during Cordilleran metamorphism.

The data for the garnet amphibolites from this study and Parkinson's study (1992) define a tight group with $\varepsilon Nd_{(760\ Ma)}$ values ranging from -0.3 to –4.6, suggesting only a limited interaction with crustal material. The cordierite-gedrite samples fall outside this group and appear to mirror the isotopic systematics of the basement gneiss. The variation in Nd systematics between the cordierite-gedrite and amphibolite samples may be due to: a) Precambrian metamorphic alteration; b) difference in age; c) alteration by fluids; or d) a primary feature of crustal contamination. The implications of each will be discussed below.

## 3.5. Discussion

### *3.5.1. Interpretation of the protolith composition*

#### *3.5.1.1.* Cordierite-gedrite rocks

The major element composition of these rocks may reflect either: a) protolith composition; or b) element mobilization, before or during metamorphism. It is not possible to distinguish between these two processes and therefore, the major element composition can only provide limited constraints on the protolith composition. The trace element chemistry provides more information as certain trace elements particularly the HFSE and transition elements are generally considered relatively immobile, and thus are more resistant to secondary alteration (Jenner, 1996). These elements are therefore more likely to reflect primary protolith composition. The low abundance of LFSE such as K, Sr, and Ba, suggests that these mobile elements have been affected by secondary alteration. This interpretation is supported by the Sr isotopic signatures which are also disturbed.

The cordierite-gedrite rocks show general systematic variations between most

trace element concentrations and silica weight percent (Fig. 3-10a and 3-10b). On the Th-Hf-Co ternary diagram of Taylor and McLennan (1985), most of the cordierite-gedrite samples plot close to the Co apex (Fig. 3-11). The ratio of Th/Hf in most rocks types (igneous, sedimentary and metamorphic) varies little, and therefore most crustal materials will plot along a linear array. Mafic material will plot close to the Co apex with more felsic material becoming more displaced and plotting towards the opposite end. The cordierite-gedrite rocks have an average Th/Hf ratio of 2.4 and this is interpreted to reflect a primary mafic composition. In addition, the flat REE patterns and slightly negative Eu anomaly are consistent with basaltic to andesitic signatures (Taylor and McLennan, 1985; Rollinson, 1996). On the tectonic discrimination diagram of $Zr/TiO_2$ versus Nb/Y, the cordierite-gedrite samples mostly fall in the basalt field, with one sample falling in the rhyolite field (Fig. 3-12). The major and trace element chemistry of the cordierite-gedrite rocks indicate that these rocks are altered mafic volcanics.

The variable Nd isotopic signature of the cordierite-gedrite rocks can be interpreted several ways: a) the isotope system was affected by secondary alteration resulting in the preferential mobility of the parent or daughter element; or b) the signatures are primary, and are the product of significant crustal contamination or heterogeneous source. Based on trace element chemistry, the cordierite-gedrite rocks are interpreted to be mafic volcanics. There does not appear to be any significant fractionation of Sm and Nd in their chemistry. The Nd isotopic values could therefore be primary and the range in values could represent minor crustal contamination; however, minor alteration cannot be precluded.

*3.5.1.2.* Garnet amphibolites

The garnet amphibolite samples have a basaltic composition (Table 3-2). The major and trace element compositions are similar to those of modern basaltic rocks (Rollinson, 1996). The amphibolite samples dominantly plot in the basalt field on the Nb/Y versus $Zr/TiO_2$ diagram (Fig. 3-12). The trace and major element compositions of the garnet

amphibolites suggest that they represent the metamorphic equivalent of such rocks, and that high-grade Late Cretaceous to Eocene metamorphism had little effect on their chemical composition. This conclusion is supported by the high average Cr/Th ratio of 380.5 and the high average La/Th ratio of 7.4. These values are different from those of typical sedimentary rocks with Cr/Th = 7.5 and La/Th = 2.6 (Taylor and McLennan, 1985), but are typical for mafic magmatic rocks (Rollinson, 1996). The interpretation of a mafic protolith is further supported by the high MgO and $TiO_2$ values, and general major element trends (Table 3-2).

The amphibolites have flat REE patterns; the lack of a HREE depletion suggesting that the primitive melt either formed: a) at shallow depths in the mantle outside the stability field of garnet, or b) by high degrees of partial melting (Fig. 3-7b). Although, the LFSE are fractionated with respect to HFSE (Fig. 3-7c), some of the LFSE may have been remobilized during metamorphism and therefore caution must be exercised in interpreting the igneous evolution using these elements. The trace element compositions suggest that the garnet amphibolites either had a source influenced by an enriched mantle, or that the protolith melts were contaminated with minor crustal material.

The garnet amphibolite samples have a more primitive Nd isotopic signature than the cordierite-gedrite rocks. The signatures can be interpreted in several ways: a) the signatures are primary, and reflect either the model age of intrusion, or were only slightly affected by crustal contamination; or, b) the system was affected by secondary alteration, which did not disturb these rocks as extensively as the cordierite-gedrite rocks. The lack of a notable disturbance in the trace element chemistry of these samples indicates that secondary alteration was not a significant process affecting these rocks. Therefore, the Nd isotopic ratios are interpreted as primary in origin. The $T_{Nd}$ model ages range from 1.3 to 2.2 Ga, supporting a Precambrian age of formation. The range in values may reflect: a) minor crustal contamination during emplacement, or b) the garnet amphibolites include more than one suite of volcanic rocks or of mafic dykes.

*3.5.2. Evaluating genetic models for the cordierite-gedrite rocks*

Genetic models outlined in section 3.1 for the cordierite-gedrite rocks are largely distinguished based on whether alteration occurred before or during metamorphism. Cordierite-gedrite rocks in Thor-Odin dome are most likely hydrothermally altered mafic volcanics, and may have been altered during or shortly after their formation in the Proterozoic. Hydrothermal alteration of volcanic rocks ranging from basalts to rhyolites will generally result in the loss of Ca and gain of Mg (Smith et al., 1992). The effects of the alteration depend on several factors including but not limited to: temperature of fluids, initial composition of the protolith, and water to rock ratio (Smith et al., 1992). However, the end result is the equivalent of a "chlorite schist" and its subsequent prograde metamorphism would result in the spectrum of cordierite-orthoamphibole assemblages (Smith et al., 1992). This is consistent with most occurrences of these rocks, which are interpreted to have achieved their chemical composition before metamorphism (Spear and Schumacher, 1982). Hydrothermal fluids, likely seawater, would have local access along faults, and thus fracture density would control the extent of hydrothermal alteration of a volcanic pile, providing a mechanism whereby altered volcanics could easily be interlayered with unaltered rocks, a relationship often observed in the field (Spear and Schumacher, 1982). If the garnet amphibolites are part of the same volcanic package as the cordierite-gedrite rocks, then this mechanism could explain the preservation of the garnet amphibolites and the alteration of the cordierite-gedrite rocks. However, the difference in degree of alteration could also be explained if the garnet amphibolites are younger, and formed after the cordierite-gedrite rocks were altered. Regardless, the cordierite-gedrite rocks of Thor-Odin dome are interpreted as being hydrothermally altered prior to being metamorphosed at upper amphibolite grade during Late Cretaceous to Eocene Cordilleran orogenesis.

Metasomatic processes synchronous with Late Cretaceous to Eocene Cordilleran metamorphism are unlikely candidates to have formed the cordierite-gedrite rocks of

Thor-Odin dome. The cordierite-gedrite rocks are part of a regionally metamorphosed, deformed and transposed basement complex, which does not contain a source for metasomatic fluids. In addition, if metasomatism occurred at this time, it would have affected other rocks including the garnet amphibolite boudins which have essentially the same protolith composition. The role and extent of a Precambrian metamorphism is not known in these rocks, and therefore the potential involvement of metasomatic fluids during the Precambrian cannot be fully evaluated. It is reasonable to entertain a model that the rocks were altered in a sea floor setting shortly after, or during, their original formation.

The synmetamorphic model that attributes formation of these rocks as a byproduct or residuum of partial melting of a pelitic sediment or metavolcanic does not apply in this situation, for the following reasons: a) the basement rocks of Thor-Odin dome experienced partial melting from 56 to 52 Ma, and the onset of anatexis was concomitant with Late Cretaceous to Eocene metamorphism and continued during isothermal decompression (Hinchey, Chapter 1); and b) the coarse grained textures, petrography, and geochronology (Hinchey, Chapter 4) of the cordierite-gedrite rocks indicate that these minerals grew during Cordilleran metamorphism, as the textures would not have survived subsequent metamorphism (Norlander et al., 2002). For these reasons, the chemical composition of these rocks must have been established prior to the Late Cretaceous to Eocene metamorphism and anatexis.

The paleoregolith model is unlikely for several reasons. First, the weathering profiles often have enrichments in residual Zr in paleosols formed by the alteration of mafic volcanics (Moore and Waters, 1990). Average values for bauxites are on the order of ~690 ppm of Zr and kaolinites are known to have excessive Zr, with levels as high as 10000 ppm (Degenhardt, 1957). The cordierite-gedrite samples of this study contain 58-264 ppm of Zr, which is not enriched and is comparable to average continental crust values of 100 ppm (Taylor and McLennan, 1985). Second, residual soils often show

large enrichments in $TiO_2$ (up to 30%) and can show LREE enrichments, notably Ce if derived in humid climates (Moore and Waters, 1990). The cordierite gedrite samples are not excessively enriched in $TiO_2$ and do not have a LREE enrichment. Based on their chemical signatures it seems unlikely that these rocks formed from the metamorphism of a paleosol or paleoregolith.

*3.5.3. Regional correlation*

Within the Shuswap complex, the cordierite-gedrite rocks are restrictive to the southwest portion of Thor-Odin dome; however, the amphibolites are known to occur throughout the region. Regional correlations can therefore be attempted with the amphibolites from Thor-Odin dome and those that occur in the surrounding geology. Similar amphibolites are documented south of the Malton complex and north of the Monashee complex, and intruded into Windermere to Lower Paleozoic platformal strata. These amphibolites are interpreted as Late Proterozoic mantle derived basalt on the basis of geochemistry (Sevigny, 1988). In comparing the major and trace element chemistry of the amphibolites from Sevigny's (1988) study with this study, the signatures show considerable overlap (Fig. 3-13). This includes enrichments in CaO and MgO, similar trace element concentrations, and relatively flat REE concentrations. On the Zr/Nb versus $Ce_{(N)}/Sm_{(N)}$ diagram, samples from both this study and Sevigny (1988) all fall in a similar range (Fig. 3-13). These parallels in chemistry suggest that the amphibolites from this study and those of Sevigny (1988) may represent one mafic suite; however, additional radiogenic isotope and/or U-Pb studies would be required to clearly illustrate if these amphibolites reflect one suite.

Other Proterozoic mafic volcanic suites in the southern Omineca belt include volcanics of the Windermere and mafic intrusions of the Belt-Purcell Supergroups. The Nd isotopic signatures of mafic suites from these two supergroups were compared with the garnet amphibolite and cordierite-gedrite rocks to evaluate whether or not any correlation is possible (Fig. 3-14). In addition, samples of Eocene lamprophyre dykes

from south of the Valhalla complex and from the Three Valley suite from northern Thor-Odin dome have been plotted for comparison (Fig. 3-12 and 14), as these rocks have distinct chemical and Nd isotopic signatures (Sevigny and Thériault, 2003; Adams et al., 2005).

The major and trace element signatures from the garnet amphibolites and cordierite-gedrite rocks overlap with those of the Moyie Sills (Belt-Purcell Supergroup) and volcanics of the Horsethief creek group (Windermere Supergroup). These data cannot form the basis for a correlation. The Nd isotopic signatures of the garnet amphibolite and cordierite-gedrite samples overlap with both the volcanics of Horsethief creek group and the Moyie sills (Fig. 3-14); and therefore the Nd isotopic data set cannot form the basis for a correlation. In addition, the garnet amphibolites are not correlated with the Eocene lamprophyre dykes, as the lamprophyres have a less evolved Nd isotopic signatures, are ca. 50 Ma and intruded into the Omineca belt following the onset of extension (Sevigny and Thériault, 2003; Adams et al., 2005). Neither the cordierite-gedrite rocks nor the garnet amphibolites could be correlated with other mafic suites known to have intruded the southern Omineca belt.

### 3.6. Conclusions

The cordierite-gedrite rocks, in the southwest portion of Thor-Odin dome, occur as discontinuous layers that are locally boudinaged within Paleoproterozoic basement paragneiss. Previous studies have established that the basement rocks were metamorphosed to peak conditions of 8-10 kbar and 800 °C during the Late Cretaceous to Paleocene Cordilleran orogeny. The lenses of cordierite-gedrite rocks are 15 to 50 meters thick and up to 500 meters long in the Bearpaw Lake area. They are concordant with the pervasive $S_2$ transposition foliation, are preserved on the limbs of $F_2$ isoclines, and appear to be a discontinuous marker horizon within the basement paragneiss of Thor-Odin dome. The contact between the cordierite-gedrite rocks and the basement paragneiss often contain mats of randomly orientated, coarse grained sillimanite mantled by cordierite and

corundum. In the Bearpaw Lake area, the cordierite-gedrite rocks are interlayered and spatially associated with garnet amphibolite boudins. The garnet amphibolites occur as discontinuous boudinaged lenses that range from 10 to 20 meters thick, up to 400 meters long, and parallel the pervasive $S_2$ transposition foliation. The garnet amphibolites occur within the Paleoproterozoic basement paragneisses and are not observed crosscutting the cordierite-gedrite rocks.

Based on field evidence, major element signatures, trace element signatures, and Nd isotopic signatures, the cordierite-gedrite rocks are interpreted as Paleoproterozoic lenses of mafic volcanics that are part of the North America basement paragneiss of Thor-Odin dome. These rocks were likely boudinaged during deformation attributed to $F_2$ folding which was ongoing ca. 56 Ma. The distinctive bulk rock chemistry of the cordierite-gedrite rocks is characterized by depletions in the alkalies, notably CaO, and enrichments in $Al_2O_3$, MgO and $Fe_2O_3$. They have flat rare earth element (REE) patterns, depletions in most low field strength elements, such as Cs, Rb, Ba, and Sr, and enrichments in high field strength elements, such as Zr, Hf, and Nb. The $^{87}Sr/^{86}Sr$ ratios for these rocks vary from 0.74923 to 0.85962 and the $\varepsilon Nd_{(today)}$ vary from –15.3 to –20.6. Their unique chemical signature is interpreted to have resulted from hydrothermal alteration, likely by sea water.

The garnet amphibolites have a chemical signature typical of mafic volcanic rocks, with high MgO and $TiO_2$ values and depletions in the alkalies. They display flat REE patterns, depletions in most low field strength elements and enrichments in high field strength elements. The garnet amphibolites have $^{87}Sr/^{86}Sr$ ratios varying from 0.70953 to 0.74319 and $\varepsilon Nd_{(today)}$ from -0.8 to –7.3. On the basis of field evidence, major element signatures, trace element signatures and Nd isotopic signatures, the garnet amphibolites are interpreted as Proterozoic metamorphosed mafic rocks that either post date the formation of the protolith of the cordierite-gedrite rocks or escaped the hydrothermal alteration.

Due to overlapping signatures of major elements, trace elements and Nd isotopic ratios, neither the garnet amphibolites nor cordierite-gedrite rocks could be correlated regionally with similar mafic suites that are known to have intruded the rocks of North American basement and platformal sequences, such as lithologically similar candidates of the Moyie Sills of the Belt-Purcell Supergroup; volcanics of the Horsethief creek group of the Windermere Supergroup; or the Eocene lamprophyre dykes.

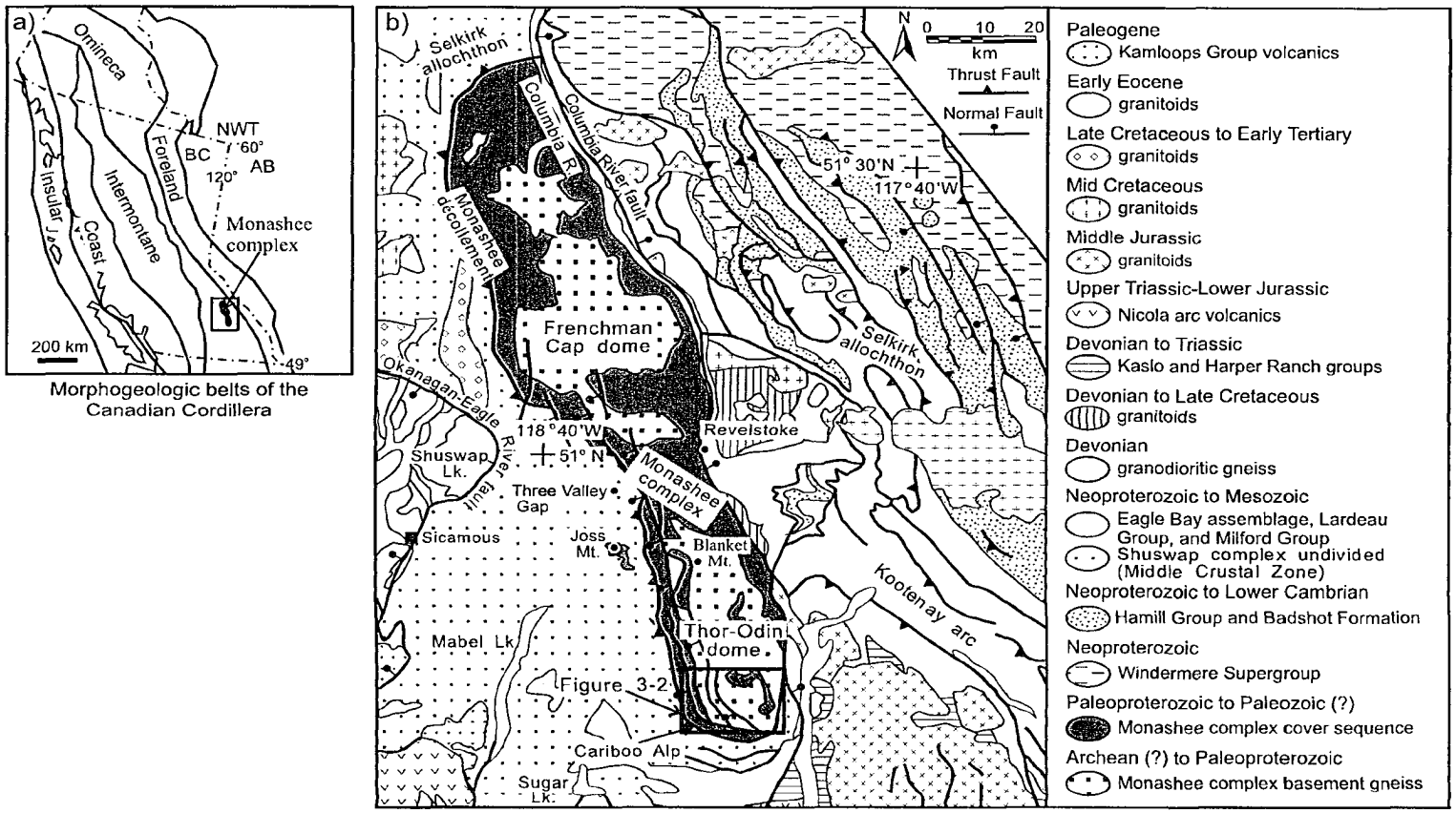


**Figure 3-1.** (a) Map highlights the five morphogeological belts of the Cordillera from Wheeler and McFeely (1991). B) Regional map of the Monashee complex and surrounding area, southeastern Omineca belt (modified after Scammell and Brown, 1990; Wheeler and McFeely, 1991; Gibson, et al., 1999). The box inThor-Odin dome delineates Figure 3-2.

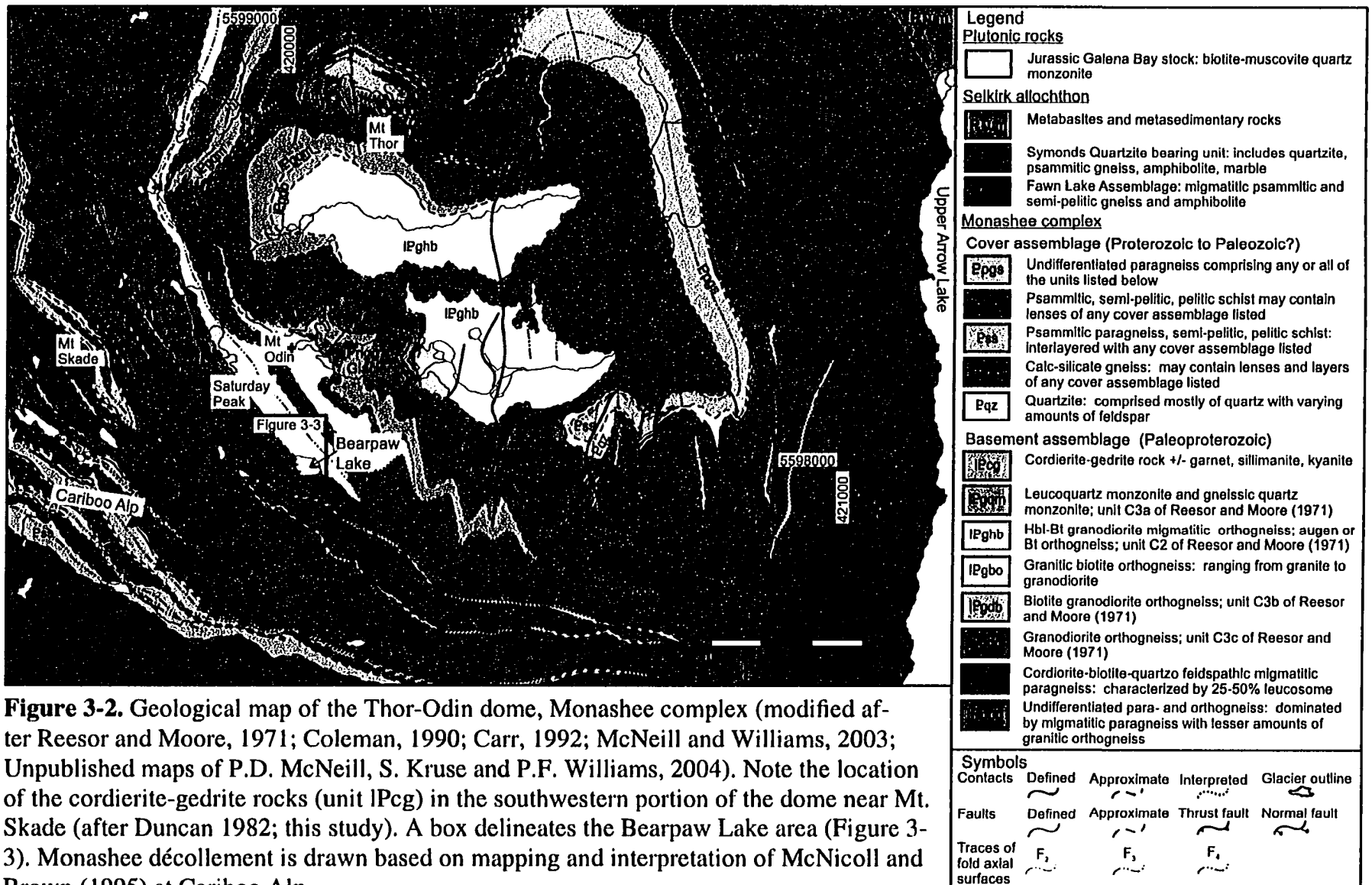


**Figure 3-2.** Geological map of the Thor-Odin dome, Monashee complex (modified after Reesor and Moore, 1971; Coleman, 1990; Carr, 1992; McNeill and Williams, 2003; Unpublished maps of P.D. McNeill, S. Kruse and P.F. Williams, 2004). Note the location of the cordierite-gedrite rocks (unit lPcg) in the southwestern portion of the dome near Mt. Skade (after Duncan 1982; this study). A box delineates the Bearpaw Lake area (Figure 3-3). Monashee décollement is drawn based on mapping and interpretation of McNicoll and Brown (1995) at Cariboo Alp.

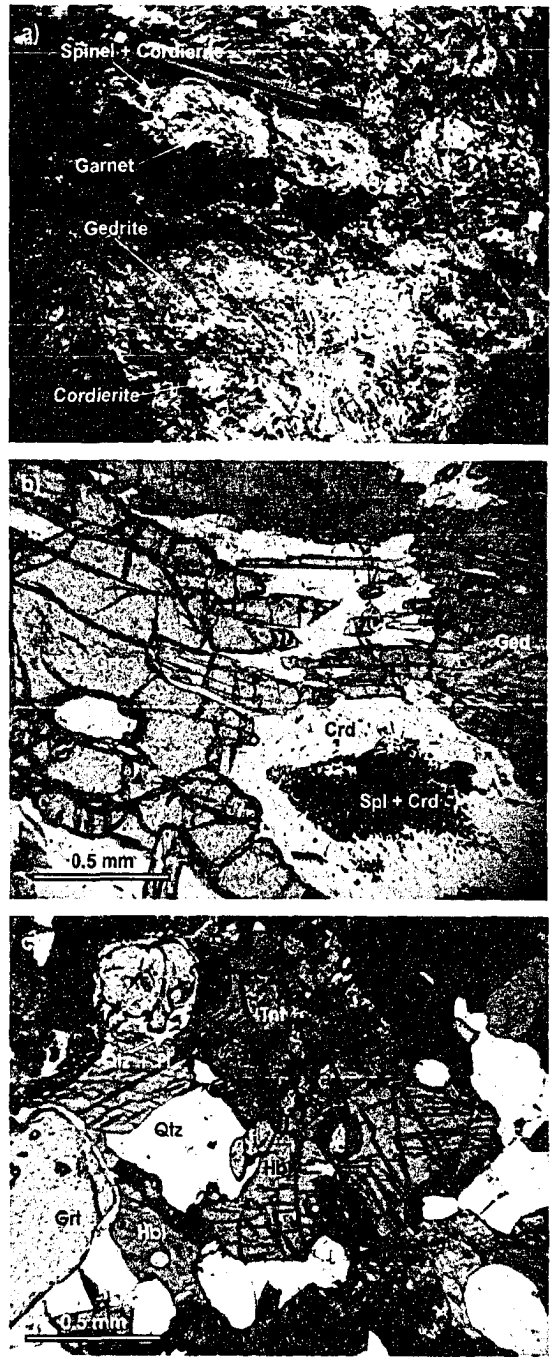


**Figure 3-4.** Field photo (a) of cordierite gedrite rock and photomicrographs in plane-polarized light of (b) cordierite-gedrite rock (AH-03-26) and (c) garnet amphibolite exposed in the Bearpaw Lake area, Thor-Odin dome. Photo (a) shows garnet porphyroblast with reaction rims of cordierite-spinel surrounded by coarse grained gedrite crystals. Photo (b) shows garnet porphyroblasts, symplectite of spinel and cordierite, interstitial cordierite grains and euhedral gedrite crystals. Photo (c) shows garnet porphyroblasts rimmed by quartz and plagioclase, euhedral hornblende and titanite, and interstitial quaartz grains.

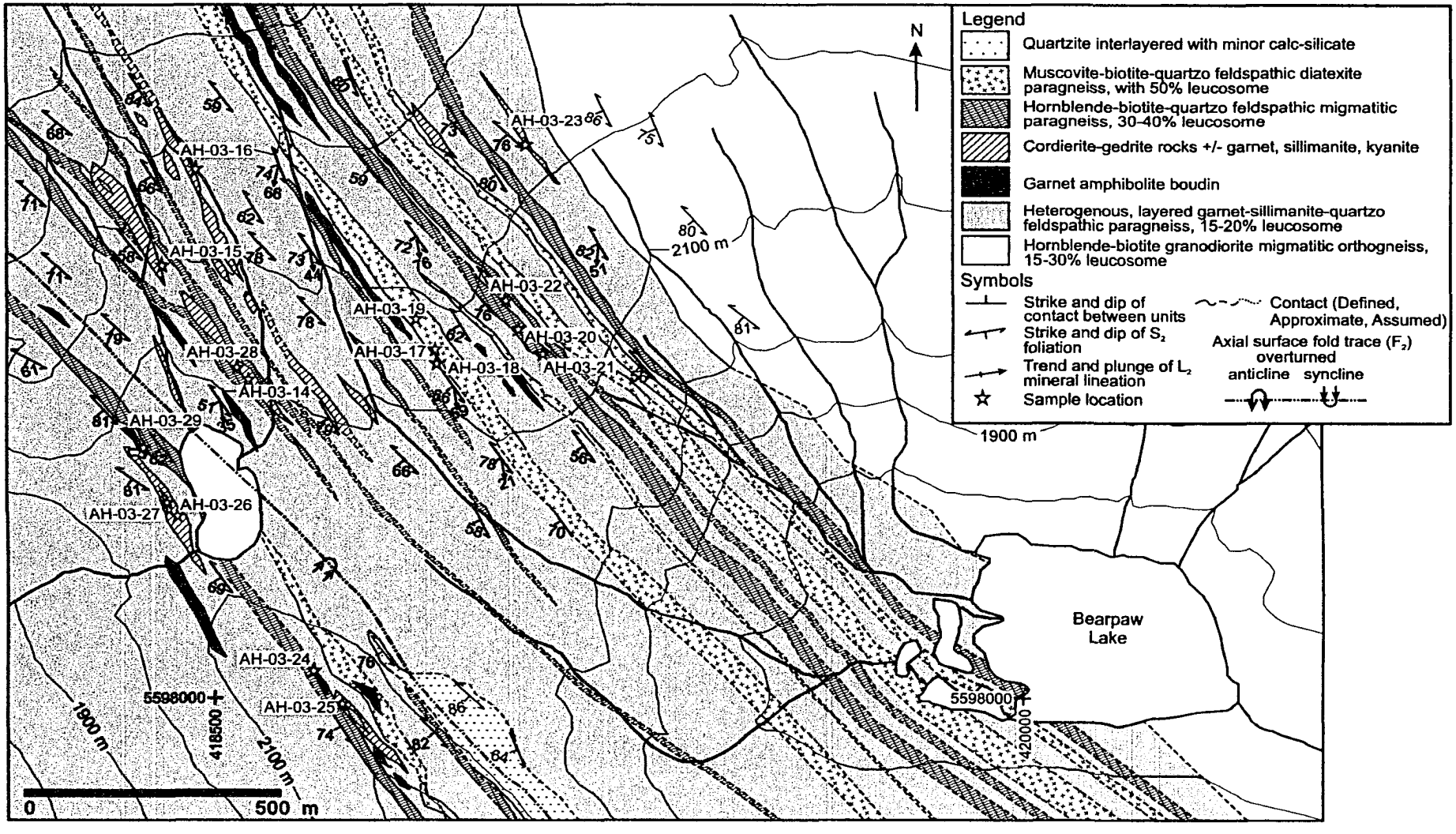


**Figure 3-3.** Geological map of the Bearpaw Lake area, Thor-Odin dome, Monashee complex (mapping by A.M. Hinchey).

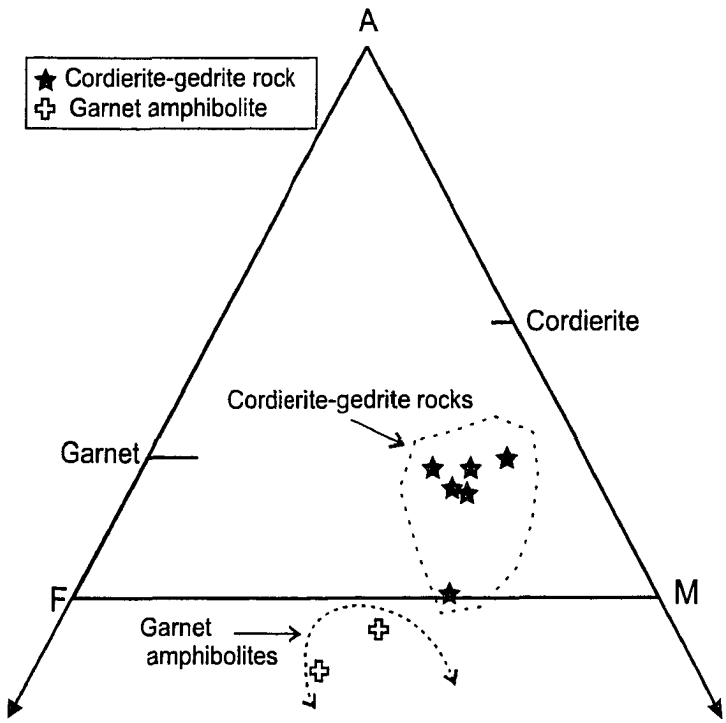


**Figure 3-5.** An AFM diagram for the garnet amphibolite and cordierite-gedrite samples from Thor-Odin dome. The parameters are (in mole percent, with total iron as FeO): A= $Al_2O_3$-CaO-$K_2O$-$Na_2O$+3.33*$P_2O_5$; F = FeO+MnO+$TiO_2$; M = MgO.

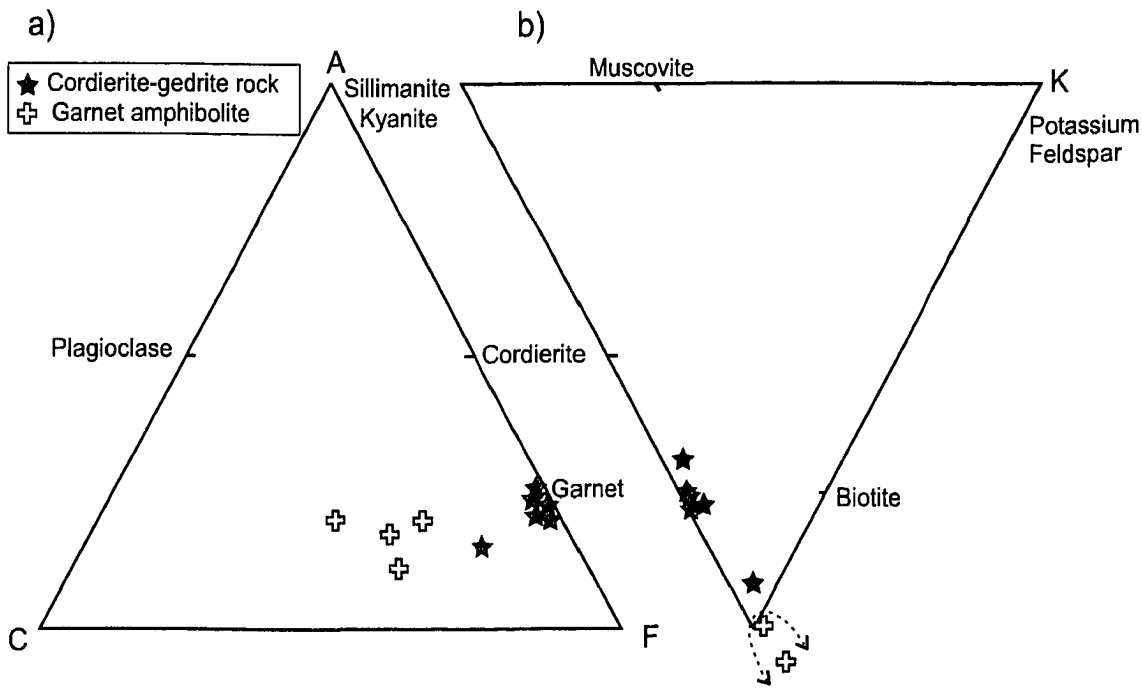


**Figure 3-6.** Projections for the garnet amphibolite and cordierite-gedrite samples from Thor-Odin dome. The parameters are in mole percent and total iron is plotted as FeO. (a) An ACF diagram, with the following parametres: A = $Al_2O_3$-$K_2O$; C = CaO+$Na_2O$-3.33*$P_2O_5$; F = FeO+MnO+MgO-$TiO_2$. (b) An AKF diagram, with the following parameters: A = $Al_2O_3$-CaO-$Na_2O$-3.33*$P_2O_5$; K = $K_2O$; F = FeO+MnO+MgO-$TiO_2$.

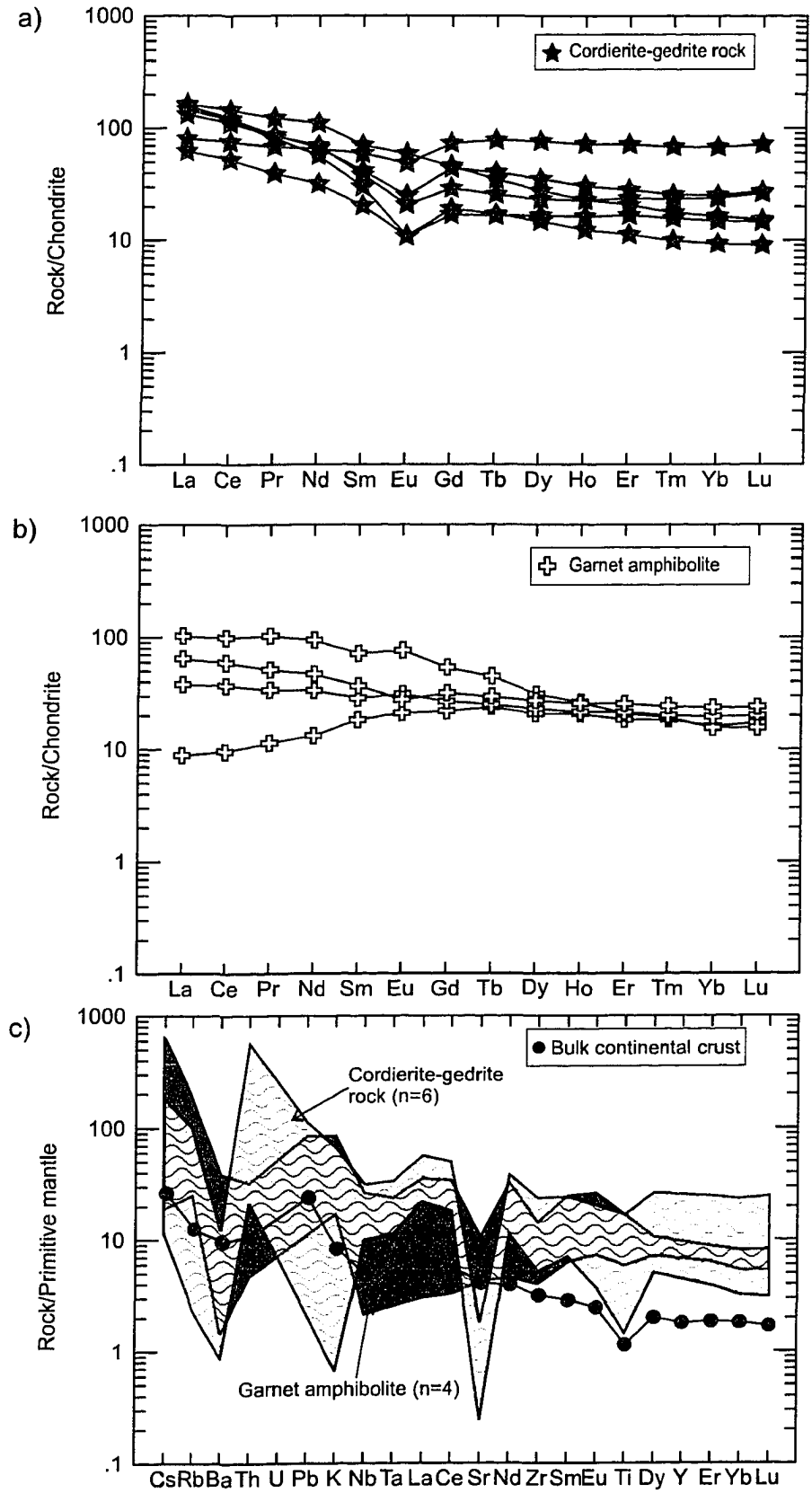


**Figure 3-7.** Trace element normalized diagrams. (a) Chondrite normalized diagram for the cordierite-gedrite samples. (b) Chondrite normalized diagram for the garnet amphibolite. (c) Primitive mantle normalized diagram for the range of cordierite-gedrite and garnet amphibolite samples. Normalization is from Sun and McDonough (1989). Average bulk continental crust data from Taylor and McLennan (1995).

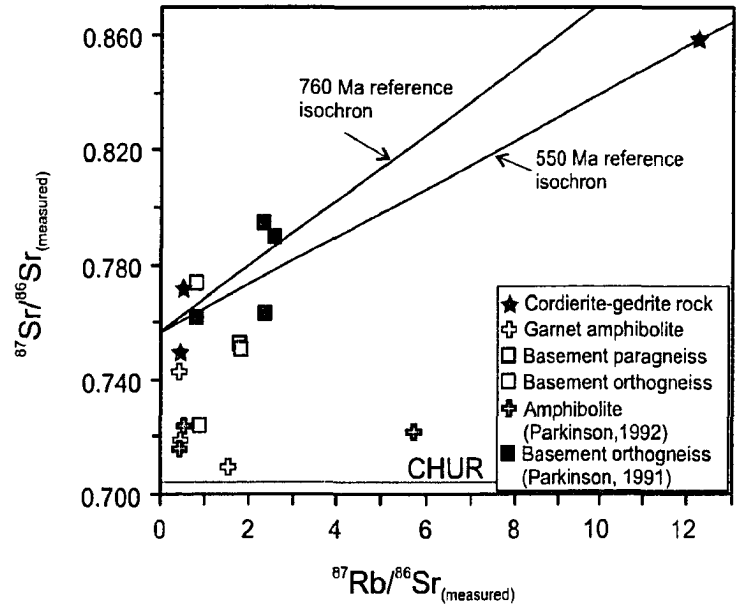


**Figure 3-8.** $^{87}Rb/^{86}Sr_{(measured)}$ versus $^{87}Sr/^{86}S_{r(measured)}$ diagram for the cordierite-gedrite rocks, garnet amphibolite and select basement gneiss for comparison. Amphibolite and basement orthogneiss from Parkinson (1992 and 1991, respectively) are plotted for comparison. CHUR = chondritic uniform reservoir.

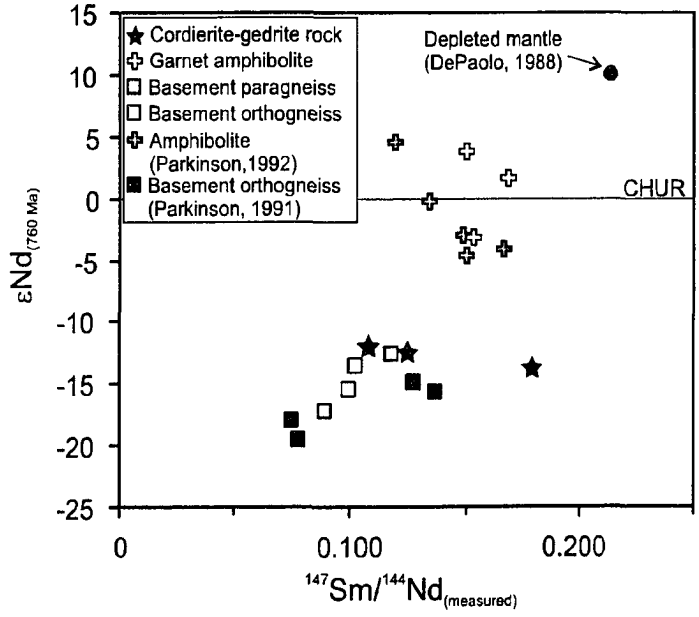


**Figure 3-9.** $^{147}Sm/^{144}Nd_{(measured)}$ versus $\varepsilon Nd_{(760\ Ma)}$ diagram for the cordierite-gedrite rocks, garnet amphibolite and select basement gneiss for comparison. Amphibolite and basement orthogneiss from Parkinson (1992 and 1991, respectively) are plotted for comparison. Depleted mantle from DePaolo (1988) is plotted. CHUR = chondritic uniform reservoir.

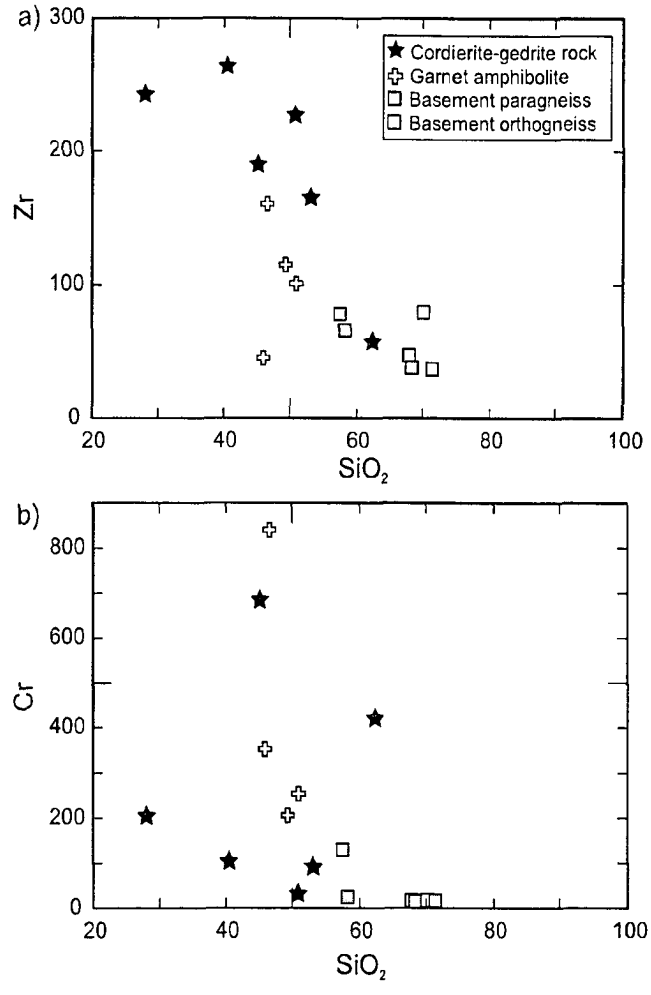


**Figure 3-10.** $SiO_2$ versus (a) Zr; and, (b) Cr, for the garnet amphibolite, cordierite-gedrite rocks and selected basement gneiss from Thor-Odin dome.

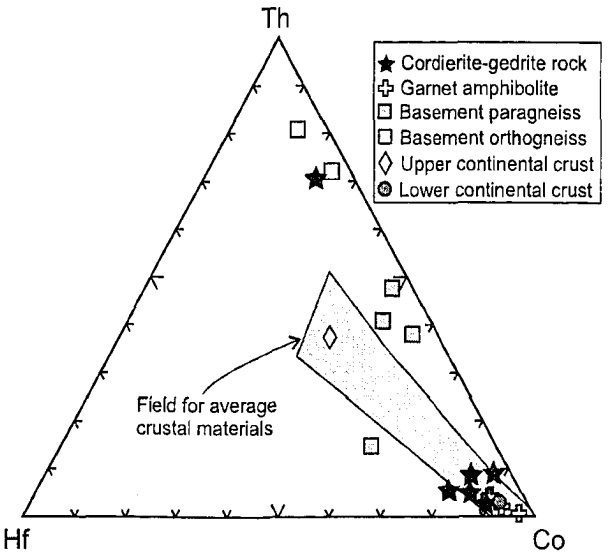


**Figure 3-11.** Ternary diagram for Hf-Th-Co data from the garnet amphibolite, cordierite-gedrite rocks, and selected basement gneisses. Average upper and lower continental crust and the field for average crustal material is from Taylor and McLennan (1985).

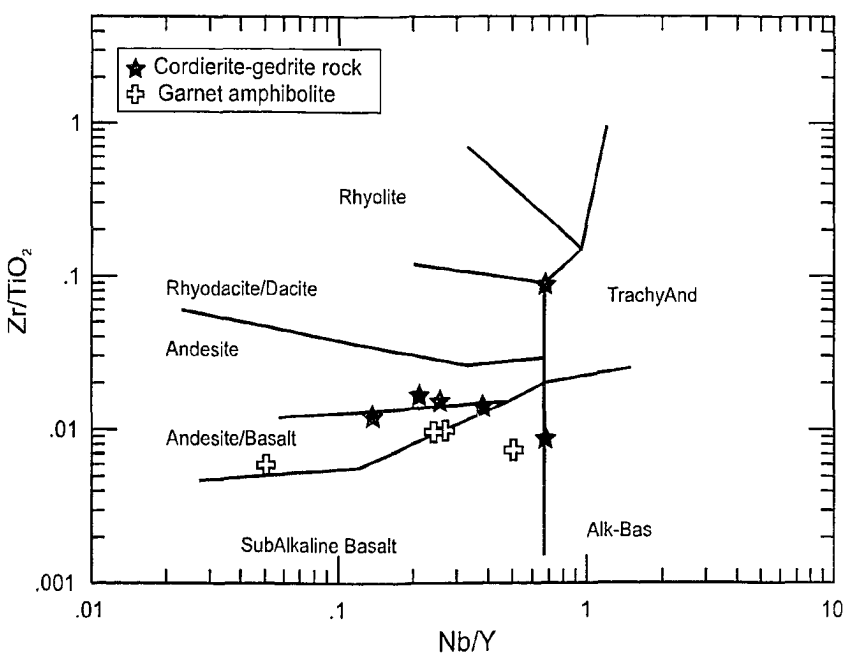


**Figure 3-12.** A plot of Nb/Y versus $Zr/TiO_2$ for garnet amphibolite and cordierite-gedrite samples. Volcanic rock classification fields are from Winchester and Floyd (1977).

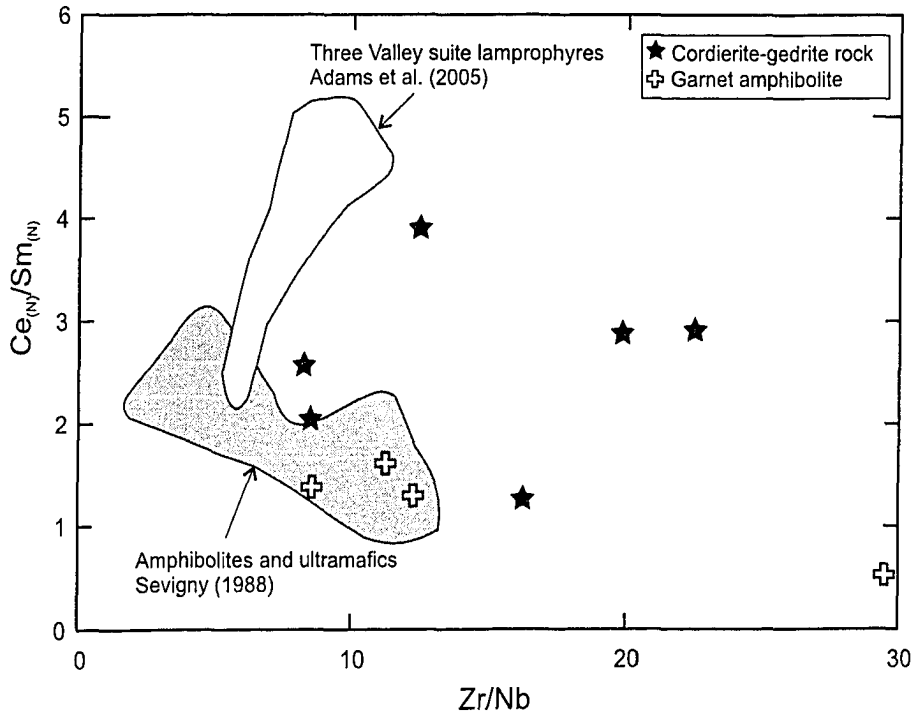


**Figure 3-13.** Comparison of Zr/Nb versus $Ce_{(N)}/Sm_{(N)}$ for garnet amphibolite and cordierite-gedrite rocks from this study. For comparison fields are plotted for amphibolites from south of the Malton complex (data from Sevigny, 1988) and Three Valley suite lamprophyres from northern Thor-Odin dome (data from Adams et al., 2005). Normalization values are from Sun and McDonough (1989).

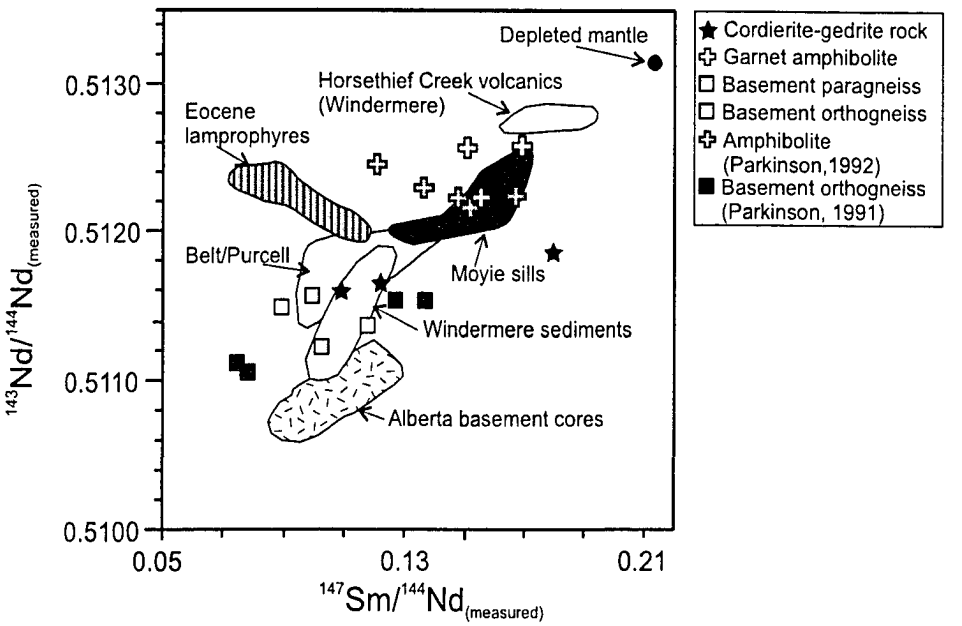


**Figure 3-14.** $^{147}Sm/^{144}Nd_{(measured)}$ versus $^{143}Nd/^{144}Nd_{(measured)}$ diagram for the garnet amphibolite, cordierite-gedrite rocks and selected basement gneiss from Thor-Odin dome. Amphibolite and basement orthogneiss from Parkinson (1992 and 1991, respectively) are plotted for comparison. Eocene lamprophyre data is from Sevigny and Thériault (2003) and Adams et al. (2005). Isotopic data for Paleoproterozoic Supergroups (Windermere, Belt-Purcell) and Archean basement cores for the Canadian Cordillera are plotted for comparison. Data are from Frost and O'Nions (1984); Devlin et al. (1985); Frost and Burwash (1986); Frost and Winston (1987); Burwash et al. (1988); Devlin et al. (1988); Burwash and Wagner (1989); Ross et al., (1993); and Anderson and Goodfellow (2000). Depleted mantle values are from DePaolo (1988).

**Table 3-1.** Description and location of geochemical and geochronological samples from Thor-Odin dome, Monashee complex. Mineral symbols are from Kretz (1983).

| Sample | Easting | Northing | Sample Description | Location |
|---|---|---|---|---|
| AH-03-14 | 418667 | 5598701 | Grt-Crd-Ged rock | Bearpaw Lake |
| AH-03-15 | 418472 | 5598934 | Sil-Crd-Grt-Ged rock | Bearpaw Lake |
| AH-03-16 | 418563 | 5599096 | Sil-Crd-Grt-Ged rock | Bearpaw Lake |
| AH-03-23 | 419192 | 5599189 | Crd-Ged rock | Bearpaw Lake |
| AH-03-25 | 418836 | 5598004 | Grt-Crd-Ged rock | Bearpaw Lake |
| AH-03-26 | 418513 | 5598418 | Sil-Grt-Crd-Ged rock | Bearpaw Lake |
| AH-03-24 | 418812 | 5598068 | Grt amphibolite | Bearpaw Lake |
| AH-03-29 | 418497 | 5598511 | Grt amphibolite | Bearpaw Lake |
| AH-02-03 | 423426 | 5600049 | Grt amphibolite | Frigg Glacier |
| AH-02-04 | 423299 | 5600302 | Grt amphibolite | Frigg Glacier |

**Table 3-2.** Major and trace element analyses of garnet amphibolite and cordierite-gedrite samples from Thor-Odin dome, Monashee complex.

| | Cordierite-gedrite rock | | | | Garnet amphibolite | | | | | |
|---|---|---|---|---|---|---|---|---|---|---|
| | AH-03-14 | AH-03-15 | AH-03-16 | AH-03-23 | AH-03-25 | AH-03-26 | AH-03-24 | AH-03-29 | AH-02-03 | AH-02-04 |
| (wt%) | | | | | | | | | | |
| $SiO_2$ | 40.52 | 53.10 | 45.14 | 62.31 | 28.11 | 50.85 | 49.39 | 50.96 | 46.59 | 45.91 |
| $TiO_2$ | 3.15 | 0.31 | 3.65 | 0.63 | 3.36 | 2.29 | 1.95 | 1.74 | 3.63 | 1.27 |
| $Al_2O_3$ | 17.78 | 20.01 | 12.98 | 12.75 | 23.07 | 15.76 | 13.23 | 14.48 | 9.00 | 13.40 |
| $Fe_2O_3$* | 3.64 | 1.55 | 3.94 | 2.33 | 3.50 | 2.24 | 4.30 | 3.70 | 3.99 | 4.93 |
| FeO | 11.99 | 4.27 | 11.36 | 7.02 | 17.15 | 8.21 | 11.70 | 10.41 | 9.60 | 11.32 |
| MnO | 0.11 | 0.08 | 0.19 | 0.19 | 0.25 | 0.11 | 0.24 | 0.24 | 0.17 | 0.22 |
| MgO | 18.09 | 16.54 | 12.53 | 12.35 | 18.87 | 13.60 | 5.96 | 7.97 | 11.19 | 6.83 |
| CaO | 0.99 | 0.21 | 5.96 | 0.37 | 2.04 | 1.07 | 10.12 | 7.53 | 8.96 | 9.55 |
| $Na_2O$ | 0.89 | 0.23 | 0.66 | 0.75 | 0.15 | 0.45 | 1.99 | 1.73 | 1.08 | 2.57 |
| $K_2O$ | 0.88 | 2.05 | 1.76 | 0.34 | 0.02 | 0.02 | 0.59 | 0.51 | 2.59 | 1.50 |
| $P_2O_5$ | 0.74 | 0.12 | 0.45 | 0.10 | 1.48 | 0.74 | 0.20 | 0.20 | 0.39 | 0.05 |
| Sum | 98.78 | 98.48 | 98.63 | 99.14 | 97.99 | 95.33 | 99.66 | 99.47 | 97.18 | 97.54 |
| (ppm) | | | | | | | | | | |
| V | 334 | 25 | 306 | 156 | 451 | 200 | 345 | 329 | 283 | 264 |
| Cr | 104 | 92 | 685 | 421 | 205 | 32 | 206 | 254 | 840 | 352 |
| Co | 53 | 15 | 52 | 43 | 62 | 31 | 46 | 47 | 60 | 60 |
| Ni | 135 | 28 | 139 | 304 | 105 | 31 | 58 | 145 | 326 | 183 |
| Zn | 106 | 55 | 162 | 83 | 198 | 75 | 121 | 91 | 122 | 127 |
| Ga | 34 | 18 | 23 | 21 | 42 | 28 | 19 | 17 | 16 | 11 |
| As | <LD | <LD | <LD | <LD | <LD | <LD | <LD | <LD | <LD | <LD |
| Rb | 29.67 | 63.64 | 59.84 | 17.45 | 1.52 | 1.66 | 15.82 | 16.19 | 117.46 | 27.45 |
| Sr | 7.1 | 5.1 | 38.2 | 11 | 9.5 | 11 | 114.4 | 118.8 | 225.14 | 87.74 |
| Y | 34.97 | 19.5 | 33.12 | 27.17 | 108.95 | 47.66 | 37.87 | 32.6 | 37.11 | 30.24 |
| Zr | 263.9 | 164.8 | 189.7 | 57.5 | 242.6 | 226.9 | 114.9 | 100.9 | 160.09 | 45.13 |
| Nb | 13.3 | 13.2 | 22.4 | 7.0 | 14.9 | 10.1 | 10.2 | 8.2 | 18.7 | 1.53 |
| Cs | 0.79 | 0.73 | 1.41 | 0.93 | 0.15 | 0.09 | 0.15 | 0.82 | 5.00 | 0.50 |
| Ba | 6 | 80 | 87 | 67 | 9 | 9 | 139 | 10 | 271 | 59 |
| La | 31.55 | 34.95 | 38.80 | 14.80 | 19.14 | 37.92 | 15.28 | 9.00 | 24.34 | 2.09 |
| Ce | 67.40 | 71.62 | 88.38 | 31.86 | 45.97 | 74.04 | 36.19 | 22.63 | 60.47 | 5.83 |
| Pr | 8.10 | 7.71 | 11.65 | 3.74 | 6.46 | 8.19 | 4.86 | 3.21 | 9.74 | 1.08 |
| Nd | 32.56 | 26.68 | 51.57 | 14.85 | 30.58 | 31.33 | 21.90 | 15.62 | 43.89 | 6.18 |
| Sm | 5.86 | 4.59 | 10.81 | 3.10 | 9.10 | 6.37 | 5.61 | 4.37 | 10.95 | 2.80 |
| Eu | 1.21 | 0.63 | 3.43 | 0.63 | 2.82 | 1.46 | 1.60 | 1.80 | 4.40 | 1.22 |
| Gd | 5.97 | 3.92 | 9.45 | 3.48 | 15.04 | 9.02 | 6.52 | 5.48 | 11.00 | 4.49 |
| Tb | 0.96 | 0.64 | 1.31 | 0.62 | 2.93 | 1.51 | 1.10 | 0.94 | 1.67 | 0.89 |
| Dy | 5.90 | 3.75 | 7.03 | 4.22 | 19.47 | 8.95 | 6.89 | 5.85 | 7.86 | 5.27 |
| Ho | 1.29 | 0.70 | 1.30 | 0.92 | 4.08 | 1.73 | 1.45 | 1.22 | 1.49 | 1.17 |
| Er | 3.92 | 1.87 | 3.43 | 2.77 | 11.87 | 4.67 | 4.21 | 3.55 | 3.44 | 3.04 |
| Tm | 0.60 | 0.25 | 0.45 | 0.40 | 1.74 | 0.65 | 0.62 | 0.51 | 0.49 | 0.47 |
| Yb | 4.06 | 1.58 | 2.79 | 2.54 | 11.56 | 4.29 | 4.00 | 3.33 | 2.63 | 2.73 |
| Lu | 0.67 | 0.23 | 0.39 | 0.37 | 1.83 | 0.69 | 0.61 | 0.51 | 0.39 | 0.44 |
| Hf | 6.20 | 5.00 | 4.90 | 1.60 | 5.60 | 5.30 | 3.20 | 2.70 | 4.59 | 1.66 |
| Ta | 0.58 | 1.38 | 1.33 | 0.47 | 0.65 | 0.46 | 0.63 | 0.49 | 0.97 | <LD |
| Pb | 7.0 | 8.0 | 8.0 | <LD | 5.0 | 6.0 | <LD | 1.0 | 5.0 | 6.0 |
| Th | 3.01 | 47.78 | 5.36 | 4.42 | 1.79 | 2.06 | 2.23 | 1.04 | 2.75 | 0.40 |
| U | 5.42 | 9.37 | 1.10 | 1.56 | 4.97 | 3.87 | 0.59 | 0.55 | 0.84 | 0.82 |

Major element analyses by X-Ray Fluorescence. $Fe_2O_3$* and FeO recalculated from measured $Fe_2O_3T$ (total) using the procedure of LeMaitre (1976). Oxides normalized to 100% (anhydrous). Totals of measured analysis are reported in "sum" column. Trace element analyses carried out by X-Ray Fluorescence and Inductively Coupled Plasma-Mass Spectrometry. LD = Limit of Detection.

**Table 3-3.** Whole rock Nd and Sr isotope data of the cordierite-gedrite rocks and garnet amphibolites from the Thor-Odin dome, Monashee complex.

Sr Isotopes[a]

| Sample no. | Location | Sample Description | Rb (ppm) | Sr (ppm) | $^{87}Sr/^{86}Sr$ (m)[b] | $2\sigma$[d] (+/-) | $^{87}Rb/^{86}Sr$ (calc)[c] | $^{87}Sr/^{86}Sr$ (760 Ma) |
|---|---|---|---|---|---|---|---|---|
| AH-03-14 | Bearpaw Lake | Grt-Crd-Ged rock | 29.6 | 7.1 | 0.859617 | 15 | 12.242 | 0.72679 |
| AH-03-25 | Bearpaw Lake | Grt-Crd-Ged rock | 1.52 | 9.5 | 0.771449 | 24 | 0.466 | 0.76639 |
| AH-03-26 | Bearpaw Lake | Sil-Grt-Crd-Ged rock | 1.66 | 11 | 0.749230 | 28 | 0.438 | 0.74447 |
| AH-03-24 | Bearpaw Lake | Grt Amphibolite | 15.82 | 114.4 | 0.718968 | 47 | 0.401 | 0.71462 |
| AH-03-29 | Bearpaw Lake | Grt Amphibolite | 16.19 | 118.8 | 0.743187 | 24 | 0.396 | 0.73889 |
| AH-02-03 | Frigg Glacier | Grt Amphibolite | 117.46 | 225.14 | 0.709529 | 15 | 1.510 | 0.69315 |

Nd Isotopes[a]

| Sample no. | Location | Sample Description | Sm (ppm) | Nd (ppm) | $^{143}Nd/^{144}Nd$ (m)[b] | $2\sigma$[d] (+/-) | $^{147}Sm/^{144}Nd$ (calc)[c] | $^{143}Nd/^{144}Nd$ (760 Ma) | $\varepsilon Nd$[e] (760 Ma) |
|---|---|---|---|---|---|---|---|---|---|
| AH-03-14 | Bearpaw Lake | Grt-Crd-Ged rock | 5.86 | 32.56 | 0.511583 | 13 | 0.10838 | 0.51104 | -12.0 |
| AH-03-25 | Bearpaw Lake | Grt-Crd-Ged rock | 9.1 | 30.58 | 0.511853 | 14 | 0.17920 | 0.51096 | -13.6 |
| AH-03-26 | Bearpaw Lake | Sil-Grt-Crd-Ged rock | 6.37 | 31.33 | 0.511635 | 24 | 0.12244 | 0.51102 | -12.4 |
| AH-03-24 | Bearpaw Lake | Grt Amphibolite | 5.61 | 21.9 | 0.512262 | 14 | 0.15426 | 0.51149 | -3.2 |
| AH-03-29 | Bearpaw Lake | Grt Amphibolite | 4.37 | 15.62 | 0.512583 | 11 | 0.16847 | 0.51174 | 1.7 |
| AH-02-03 | Frigg Glacier | Grt Amphibolite | 10.95 | 43.89 | 0.512598 | 10 | 0.15024 | 0.51185 | 3.7 |

[a] measurements by TIMS

[b] measured and corrected for mass fractionation

[c] calculated using ppm concentrations from ICP-MS trace element analysis

[d] errors refer to last one or two digits and are propogated to include reproducibility of standard analysis and run errors

[e] calculated using present day chondritic uniform reservoir with $^{143}Nd/^{144}Nd = 0.512638$ & $^{147}Sm/^{144}Nd = 0.1967$

# CHAPTER 4

## Paleocene-Eocene monazite ages in cordierite-gedrite basement rocks and associated quartzites from the Thor-Odin dome, Monashee complex: constraints on the timing of isothermal decompression


### Abstract

Thor-Odin dome of the Monashee complex is an exposure of North American basement that preserves rocks from the deepest exposed structural level within the Shuswap complex of the Omineca belt. Ortho- and paragneiss of the basement rocks are infolded within overlying metasedimentary rocks of the Monashee cover sequence. Basement gneiss preserve sillimanite-potassium feldspar-melt assemblages, were buried to depths of 26-33 km, and were completely transposed and migmatized during the Late Cretaceous to Eocene Cordilleran orogenesis. The basement paragneiss are comprised of: a) heterogeneous, migmatitic garnet-sillimanite-quartzo feldspathic paragneiss that are locally rich in cordierite, b) migmatitic cordierite-biotite-quartzo feldspathic gneiss, and c) minor calc-silicates, marbles, and quartzites, and are associated with minor cordierite-gedrite rocks and garnet amphibolites. To constrain the timing of metamorphism in the basement rocks, monazite from cordierite-gedrite rocks and interlayered quartzite from the basement paragneiss were dated by U-Pb Sensitive High Resolution Ion Microprobe (SHRIMP) method. These cordierite-gedrite rocks are preserved on the limbs of $F_2$ folds in the southwestern portion of Thor-Odin dome. Monazites were chemically X-ray mapped on the electron microprobe prior to analysis, to identify potential age domains within single monazite crystals. Chemical maps of Y, U, Ca and Th were created for each grain and the maps were used to select SHRIMP analytical sites. Most monazite grains show a range of chemical patterns, including sector zoning, concentric zoning, discontinuous or irregular patches with embayments and cores varying in composition relative to the rims. The three samples analyzed had mean $^{206}Pb/^{238}U$ ages that ranged from ca. 56 to 52 Ma. The distinct chemical domains in the monazite grains did not

appear to correspond to discernable age domains. Monazite growth or recrystallization occurred over a few million years, and thus the complex internal chemical patterns are likely a result of changing composition of the rocks during formation synchronous with high-grade metamorphism and anatexis. Peak metamorphism in the basement gneiss of Thor-Odin dome occurred by ca. 56 Ma, with basement rocks undergoing subsequent isothermal decompression to < 5kbar ending by ca. 52 Ma. This was followed by near isobaric cooling of the dome to < 300 °C by 48 Ma. Decompression is attributed to erosion and extension within the Shuswap complex.

## 4.1. Introduction

The Monashee complex in southeastern British Columbia is located in the hinterland of the Rocky Mountain fold and thrust belt and contains exposures of North American basement rocks that are part of the deepest exposed structural levels in the southern Canadian Cordillera (Fig. 4-1). The complex contains two structural culminations, Frenchman Cap and Thor-Odin domes that consist of high-grade Paleoproterozoic basement rocks and an overlying cover sequence. The domes appear to have experienced different tectono-thermal histories during the Late Cretaceous to Eocene stage of the Cordilleran orogeny. Thor-Odin dome experienced pervasive anatexis and deformation at ca. 56 Ma to 52 Ma (Hinchey, Chapter 1). Peak metamorphic conditions in Thor-Odin have been established as 800 °C and 8-10 kbar (Norlander et al., 2002), and this paper aims to put direct timing constraints on these metamorphic conditions. In addition, the following questions are addressed. a) Did these rocks experience multiple metamorphic events recorded in monazite growth?; b) Is a Precambrian metamorphic event preserved?; and, c) Are distinct age domains, reflecting different metamorphic events, documented in the compositions of the monazite grains? In order to address these questions, a combination of field, petrography, chemical mapping and geochronology studies were utilized.

Monazite from cordierite-orthoamphibole (dominantly gedrite) rocks and quartzite from the basement paragneisses were dated by U-Pb SHRIMP method in order to constrain the timing of metamorphism. The cordierite-orthoamphibole rocks contain complex metamorphic textures and were selected for dating for several reasons. The metamorphic paragenesis and pressure-temperature (P-T) relationships of the cordierite-orthoamphibole rocks are reasonably well understood (see Spear, 1993). The mineral assemblages in these rocks are characteristic of particular P-T conditions and usually contain a well-preserved history of metamorphic reactions in mineral inclusions, coronas, and reaction textures (Spear, 1993). For these reasons, they make excellent rocks to place

timing constraints on the P-T paths. In the cordierite-gedrite rocks from Thor-Odin dome, Norlander et al. (2002) documented decompression from a kyanite zone (P> 8-10 kbar) to a sillimanite-cordierite zone (P<5 kbar) at temperatures ca. 750°C to a maximum of 800 °C based on the mineral assemblages and reaction textures. This high-temperature decompression event is interpreted to be coeval with partial melting in the basement gneiss of Thor-Odin dome on the basis of petrology by Norlander et al. (2002) and on the basis of geochronology and geochemistry by Hinchey (Chapter 1). The current study also analyzed monazite from a quartzite that is interlayered with the cordierite-gedrite rocks. A quartzite sample was selected because monazites in these rocks were thought to possibly be less susceptible to complete or partial resetting of the U-Pb systematics during repeated metamorphic events, and therefore would most likely contain a complete record of monazite growth events (M. Williams, personal communication 2003).

## 4.2. Regional geology

The Canadian Cordillera formed as a result of the Paleozoic to Paleogene accretion of fragments of allochthonous and paraautochthonous oceanic sequences, continental slivers, volcanic arcs and sedimentary sequences to the western edge of ancestral North America, and Mesozoic – Paleogene crustal thickening during collision and westward underthrusting of the North American plate (Fig. 4-1; Monger et al., 1982; Monger, 1989; Gabrielse and Campbell, 1991). By the Middle Jurassic, accreted terranes had begun overriding the pericratonic terranes and Proterozoic and Paleozoic to early Mesozoic platformal sedimentary sequences that had accumulated on the paleomargin of North America (Monger et al., 1982). By the Late Cretaceous, a 50-60 km thick crustal welt was created along with a flexural foreland basin at the front of the Rocky Mountain fold and thrust belt (Foreland belt; Price and Mountjoy, 1970; Coney and Harms, 1984; Brown et al., 1986; Price, 1986). Crustal thickening and burial of the North American sedimentary sequence and overriding terranes resulted in metamorphism and deformation of rocks in the hinterland of the Rocky Mountain fold and thrust belt, termed the

Omineca belt (Fig. 4-1; Reesor, 1970; Brown and Read, 1983 and references therein). Subsequently, southern British Columbia underwent a change from a transpressional to transtensional regime, attributed to changes in far field stresses related to the obliquity of the down-going Kula plate (Lonsdale, 1988; Andronicos et al., 2003). This resulted in Eocene regional extension, and exhumation of some of the high-grade rocks of the southern Omineca belt by an array of generally north-south striking, brittle and ductile normal faults, which are linked to synchronous strike-slip fault systems that span the western Cordillera (Ewing, 1981; Tempelman-Kluit and Parkinson, 1986; Brown and Journeay, 1987; Parrish et al., 1988; Struik, 1993; Johnson and Brown 1996 and references therein). In the southern Omineca belt, the lower plates of regional extensional fault systems expose high-grade rocks with relatively young deformation and cooling histories in a Cordilleran metamorphic core complex, termed the Shuswap complex (Armstrong, 1972; Coney, 1980; Parrish et al., 1988).

The southern Omineca belt is characterized by metamorphic and plutonic rocks and contains structural culminations and belts of high-grade rocks. The Shuswap complex is bounded on the eastern and western margins by generally north-striking, outward-dipping Eocene normal faults. It is bounded by the 58-50 Ma Columbia River fault (CR) to the east and the 56-45 Ma Okanagan Valley-Eagle River fault system (OV-ER) to the west (Okulitch, 1984; Brown and Journeay, 1987; Parrish et al., 1988; Parkinson, 1992; Bardoux, 1993; Johnson, 1994). The hanging wall rocks of both the CR and the OV-ER faults generally record older peak metamorphism (ca. 175 to 135 Ma) and are generally at lower metamorphic grade than the footwall rocks (Parrish, 1995; Johnson and Brown, 1996). The Monashee complex, a basement-cored gneiss complex, and structurally overlying metasedimentary rocks are contained within the Shuswap complex (Fig 4-1).

The two domal culminations of the Monashee complex comprise Paleoproterozoic basement of North American cratonic affinity (Fig. 4-1; Armstrong et al., 1991) complexly infolded with unconformably overlaying Paleoproterozoic to Paleozoic

platformal metasedimentary gneisses of the cover sequence (Wheeler, 1965; Reesor and Moore, 1971; Brown, 1980; Crowley, 1997). In both domes of the complex, Cordilleran orogenesis resulted in middle amphibolite to lower granulite facies metamorphism, km-scale isoclinal folding, and the development of penetrative planar and linear deformation fabrics (Wheeler, 1965; Reesor and Moore, 1971; Höy and Brown, 1980; Brown et al. 1986; Journeay, 1986; McNicoll and Brown, 1995). The dominant sedimentary rocks that structurally overlie and surround the Monashee complex are interpreted as an allochthonous, composite thrust sheet, termed the Selkirk allochthon (Read and Brown, 1981). The boundary between these allochthonous rocks and the relatively more autochthonous rocks of the Monashee complex is referred to as the Monashee décollement (MD; Read and Brown, 1981; Brown et al., 1986; Journeay, 1986; Brown et al, 1992; McNicoll and Brown, 1995; Brown and Gibson, in press).

Periods of metamorphism, deformation, and plutonism occurred within a 120 million year interval in the southern Omineca belt and events have been documented at ca. 175-160, ca. 140, 100-90, 75-60 and 60-55 Ma (Digel et al., 1998; Sevigny et al., 1989, 1990; Scammell, 1993; Parrish, 1995; Vanderhaeghe et al., 1999; Gibson, 2003; Crowley et al., 2003; Reid, 2003; Carr and Simony, in review). Parrish (1995) synthesized known timing of deformation in the southern Omineca belt and suggested that there was a preservation of progressively younger strain and deformation with deeper structural levels, implying progressive incorporation of deeper and more inboard rocks through time. However, recent studies have shown that the relationships between structural level, deformation and metamorphism are more complicated than this interpretation, and metamorphic belts may overprint and crosscut older events. In order to understand the construction of the Omineca belt it is necessary to document these relationships at all structural levels. For example the Cretaceous Cariboo – Monashee – Selkirk metamorphic high transects Middle Jurassic regional metamorphism, while in other locations younger, or successions of younger, events may reactivate, overprint and/or partially overlap with older events in

a concordant fashion (Digel et al., 1998; Gibson, 2003; Crowley et al., 2003; Reid, 2003; Carr and Simony, in review).

The panel of rocks that structurally overlies and in map view surrounds Thor-Odin dome on the southern and western sides, is referred to as the Middle Crustal Zone (after Carr 1991). It is characterized by Late Cretaceous to Eocene ductile strain, plutonism, and thermal quenching (Carr, 1991). The rocks of the upper structural levels of Frenchman Cap dome experienced high-grade metamorphism from ca. 80 to 50 Ma; however, a boundary delimiting the base of Eocene Cordilleran deformation has been located at deep structural levels below which Precambrian relationships > 1.8 Ga are preserved (Parrish, 1995; Gibson et al., 1999; Crowley and Parrish, 1999). In contrast, this study confirms that rocks throughout Thor-Odin dome experienced high-grade metamorphism during the Paleocene to Eocene (Vanderhaeghe et al., 1999; Norlander et al. 2003; Kuiper, 2003; this study), synchronous with anatexis (Hinchey, Chapter 1). However, the timing of the onset of metamorphism in the basement rocks of the Thor-Odin dome remains an outstanding question.

## 4.3. Geological setting of Thor-Odin dome

### *4.3.1. Lithology*

The basement rocks of Thor-Odin dome are composed of heterogeneous migmatitic para- and orthogneiss. Basement orthogneiss are dominated by migmatitic, hornblende-biotite-quartzo feldspathic gneiss with a lesser volume of quartz monzonite gneiss. Basement paragneiss comprise: a) heterogeneous migmatitic garnet-sillimanite-quartzo feldspathic gneiss that are locally rich in cordierite, b) migmatitic cordierite-biotite-quartzo feldspathic gneiss, and c) minor calc-silicates, marbles, and quartzites, and minor cordierite-gedrite rocks and amphibolites (Reesor and Moore, 1971; Duncan, 1984). Though lithologically distinct, the basement ortho- and paragneiss are often interlayered at the scale of a few meters, due in large part to transposition by folding, with contacts

that are further complicated by the abundance of leucosome. Initial U/Pb geochronology studies of zircons from basement orthogneiss yielded crystallization ages of 1934 ± 6 and 1874 ± 21 Ma (Parkinson, 1992). Deposition of the basement supracrustal sequence likely began by 2.2 Ga, based on a detrital zircon study of a basement paragneiss (Parkinson, 1992), and continued to at least 1.8 Ga, based on the youngest detrital grains from basement paragneisses (Vanderhaeghe et al., 1999; Kuiper, 2003; Hinchey, Chapter 1). The Monashee cover sequence was subsequently deposited on the basement para- and orthogneiss after 1825 Ma, based on the youngest detrital grain in the basal quartzite (Kuiper, 2003). There are no constraints on an upper age limit for the cover sequence, and the youngest depositional age in Thor-Odin dome is uncertain. The cover sequence comprises a heterogeneous assemblage of metasedimentary rocks that includes quartzites, pelitic schists, marbles, calc-silicates and amphibolites. The focus of this paper is on basement paragneiss from the Bearpaw Lake area in the southwest portion of the Thor-Odin dome (Fig. 4-1 and 2).

*4.3.2. Cretaceous – Eocene Cordilleran metamorphic history*

Basement and cover rocks experienced upper amphibolite to lower granulite facies metamorphic conditions in the Late Cretaceous to Eocene, during the Cordilleran orogen. Precambrian metamorphism and deformation has been pervasively overprinted by Cordilleran events. Throughout the dome, the mineral assemblages are relatively uniform with stable sillimanite-potassium feldspar-melt assemblages (Reesor and Moore, 1971). Kyanite and cordierite occur in aluminous basement gneiss and orthopyroxene occurs in granitic and aluminum-poor basement gneiss (Reesor and Moore, 1971). The sillimanite-potassium feldspar isograd approximately encloses the dome. Peak P-T conditions for the basement gneiss are > 8-10 kbar and 750-800 °C (Norlander et al., 2002), corresponding to depths of 26-30 km. Based on complex symplectic textures preserved in basement cordierite-gedrite rocks and in garnet amphibolite boudins, Norlander et al. (2002) concluded that the peak regional metamorphic episode occurred in the Tertiary, as these

textures would not have survived a subsequent metamorphic event. This is consistent with U-Pb geochronology studies that indicate that metamorphism and penetrative deformation of Thor-Odin dome basement rocks was ongoing during the Paleogene at ca. 56 to 52 Ma (Vanderhaeghe et al., 1999; Hinchey, Chapter 1; this study). Peak metamorphism culminated in the onset of melting and the production of leucosome (Hinchey, Chapter 1).

### *4.3.3. Cretaceous – Eocene Cordilleran structural evolution*

Basement and cover gneiss are characterized by at least four folding events, and the map-pattern distribution of basement and cover is controlled by large-scale fold interference patterns. The dominant foliation dips to the west on the western margin of the dome and to the east on the eastern margin, and it wraps around the southern end, producing outward dips (Reesor and Moore, 1971). $F_1$ folds are preserved at outcrop scale, and may be either relict Precambrian deformation, or formed during a progressive $D_{1-2}$ thickening and burial. Kilometre-scale isoclinal $F_2$ fold nappes infold the cover sequence with the underlying basement gneisses (Reesor and Moore, 1971; Read, 1979, 1980; McNeill and Williams, 2004). The $S_2$ transposition foliation is the dominant planar fabric throughout the 4-5 km thick exposed section of Thor-Odin dome and is defined by domainal schistosity, compositional banding and gneissic foliation. Leucosome occurs pervasively throughout the gneiss in Thor-Odin dome. Leucosome is interpreted to have formed as a result of *in situ* melting of the host gneiss, with formation ongoing from ca. 56-52 Ma, coincident with peak metamorphism, formation of part of the $S_2$ foliation and $F_2$, as well as $F_3$ and $F_4$ (Hinchey et al., 2004; Hinchey, Chapter 1).

### *4.3.4. Geology of the Bearpaw Lake area*

The Bearpaw Lake area (Fig. 4-2) is characterized by basement rocks dominated by: a) hornblende-biotite granodiorite migmatitic orthogneiss, and, b) compositionally heterogeneous garnet-sillimanite-quartzo feldspathic migmatitic paragneiss. The garnet-

sillimanite quartzo-feldspathic paragneiss is interlayered at the scale of 10's of meters with a muscovite-biotite-quartzo feldspathic diatexite paragneiss and hornblende-biotite-quartzo feldspathic paragneiss. In addition, this unit is characterized by boudinaged layers of cordierite-gedrite rocks, garnet hornblende amphibolites, infolded quartzites and calc-silicates. This package of gneiss strikes southeast and dips ~70° to the west. The lenses of cordierite-gedrite rocks and garnet amphibolites dykes were likely boudinaged during deformation associated with $F_2$ folding, which was ongoing ca. 56 Ma (Fig. 4-2; Hinchey, Chapter 1).

The cordierite-gedrite mafic rocks occur as discontinuous layers that are locally boudinaged. The lenses of cordierite-gedrite rocks are 15 to 50 meters thick and up to 500 meters long (Fig. 4-2). They parallel the pervasive $S_2$ transposition foliation and strike at 135-142° to the southeast. The cordierite-gedrite rocks are documented only within the basement paragneiss and occur on the limbs of $F_2$ isoclines. They appear, at least locally, to define a discontinuous marker horizon within the basement paragneiss. The cordierite-gedrite rocks are interpreted as hydrothermally altered Proterozoic mafic volcanics (Hinchey, Chapter 3).

The textures and mineralogy of the cordierite-gedrite rocks and surrounding lithologies of Bearpaw Lake are best explained by decompression from peak metamorphism at 8-10 kbar to < 5 kbar at temperatures of ~750-800 °C (Norlander et al., 2002). Petrologically, this is supported by both the replacement of garnet by cordierite and anorthite-amphibole-biotite, and the replacement of kyanite by sillimanite with the accompanied reaction of kyanite + gedrite to cordierite + spinel ± corundum ± sapphirine (Norlander et al., 2002). Near isothermal decompression also explains the abundance of melt leucosome in the basement rocks, as this would cause the production of melt through several melt generating reactions (Hinchey, Chapter 1).

## 4.4. Analytical data and interpretation

### *4.4.1. U-Pb geochronology*

U-Pb isotopic ratios of monazites from two samples of cordierite-gedrite rocks, and one sample of quartzite were analyzed using the Sensitive High Resolution Ion Microprobe (SHRIMP). Representative field photos are presented in Figure 4-3. Analytical procedures are described in Appendix A.1. Backscattered electron (BSE) images and high-resolution Y-Ca-Th-U X-ray maps of the metamorphic monazite crystals were produced prior to analysis (Fig. 4-4). Analytical procedures for creating the chemical maps are described in Appendix A.1. Each analyzed sample is described in detail below.

The geochronological data are presented in Table 4-1 and on Tera-Wasserburg diagrams in Figure 4-5 (diagram from Tera and Wasserburg, 1972). In Table 4-1, the isotopic ratios are uncorrected for common Pb. However, in Table 4-1 and Figure 4-4, the $^{206}Pb/^{238}U$ ages are reported corrected for common Pb using the $^{207}Pb$ method of Stern and Berman (2000), with errors reported at the 1$\sigma$ level. This correction uses the $^{207}Pb$ isotope to correct for common Pb because the counting statistics on $^{204}Pb$ are extremely low, which can impart a significant error on the calculate age (see Stern, 1997). In Figure 4-4, $^{206}Pb/^{238}U$ SHRIMP ages are located beside the analytical site. In Figure 4-5, the data is plotted in a Tera-Wasserburg diagram (Tera and Wasserburg, 1972) in which the $^{207}Pb^*/^{206}Pb^*$ ratio, uncorrected for common lead, is plotted against the uncorrected $^{238}U/^{206}Pb^*$ ratio with error ellipses reported at the 2$\sigma$ level. In this case, the Tera-Wasserburg plots provide a means to assess the common Pb component in the monazite analyzed, since the further the ellipse plots away from the concordia curve, the larger the common Pb component (see Stern, 1997). U-Pb SHRIMP analytical sites were selected on monazite grains using the chemical X-ray maps (see Fig. 4-4).

*1.4.1.1.* Garnet cordierite-gedrite rock (AH-03-14)

Sample AH-03-14 is from a coarse grained cordierite-gedrite rock from a 400 meter long and 5 meter wide lens on the southwest side of Bearpaw Lake (Fig. 4-2). The contact of this lens with the host gneiss is characterized by very coarse grained gedrite and prismatic aggregates of sillimanite mantled by cordierite and corundum. This sample contains 4-7 cm long, fanlike growths of gedrite crystals, 2-5 cm garnet porphyroblasts, and interstitial cordierite crystals. In thin section, gedrite is characterized by prismatic, euhedral grains that define the $S_2$ foliation (Fig. 4-6a). Garnet poikiloblasts contain inclusions of cordierite, spinel, gedrite, and apatite. Cracks within the garnet are filled with grains of cordierite, gedrite, ilmenite, plagioclase and spinel. Cordierite dominates the matrix as anhedral, interstitial grains. Biotite crystals are euhedral and randomly oriented. Accessory phases of apatite, spinel, ilmenite and monazite are common. Monazite grains occur as inclusions in garnet and cordierite, as well as along the grain boundaries of ilmenite, biotite, cordierite, garnet, apatite and gedrite.

The monazite population in sample AH-03-14 is dominated by euhedral to subhedral, equant grains. Fourteen grains from this sample, varying in shape and internal structure, were analyzed (Table 4-1). In BSE, most grains appear homogenous, although some grains have a narrow bright rim. The chemical maps show a range of internal structures. The cores of many grains have lower concentrations of Ca-U-Th and higher Y relative to the rims which have higher concentrations of Ca-U-Th and lower Y (Fig. 4-4a). Embayments are also common (see monazite 10 in Fig. 4-4a). Monazite grains have a range of $^{206}Pb/^{238}U$ ages from 62.3 ± 1.4 Ma to 52.9 ± 1 Ma (1σ error; Table 4-1). The weighted mean $^{206}Pb/^{238}U$ age of all the grains is 56.2 ± 1.2 Ma (2 σ error, n=17), with a mean-square of weighted deviates (MSWD) of 3.8 (Fig. 4-5a). The relatively high MSWD likely reflects a real spread of ages with continued growth or recrystallization of monazite over the course of several million years rather than an analytical effect. In this sample, the chemical domains do not appear to correspond to distinct age domains. The

monazite formation likely occurred during a protracted event and does not appear to be linked to one particular metamorphic reaction, such as the breakdown of garnet.

*1.4.1.2.* Garnet cordierite-gedrite rock (AH-03-26)

Sample AH-03-26 is from a coarse grained cordierite-gedrite rock that occurs in a 200 meter long and 25 metre thick lens on the west side of Bearpaw Lake (Fig. 4-2). The boudins trend to the northwest and parallel the main $S_2$ transposition foliation which is defined by the alignment of gedrite and biotite crystals in this sample. The sample is characterized by 2-4 cm long tabular gedrite crystals, 1-3 cm garnet porphyroblasts and interstitial cordierite crystals. In thin section, gedrite occurs as tabular euhedral crystals that are riddled with inclusions (Fig. 4-6b). Garnet poikiloblasts contain abundant inclusions of cordierite, gedrite, ilmenite, spinel and apatite. Many of the garnets are oblate in shape, with their long axis concordant with the $S_2$ foliation. Garnets often contain cracks that are filled with gedrite, plagioclase and cordierite. Cordierite dominates the matrix and occurs predominantly as interstitial grains between blades of gedrite. Fibrolite rims relict kyanite grains and prismatic sillimanite occurs as euhedral grains in the matrix. Biotite crystals are euhedral and randomly oriented. Accessory phases of apatite, spinel, ilmenite and monazite are common. Monazite occurs as inclusions in garnet and gedrite, as well as along grain boundaries of gedrite, ilmenite, cordierite and rutile.

The monazite population in this sample is dominated by euhedral to subhedral grains, varying from 120 to 250 μm in length. A total of thirteen grains from this sample, varying in shape and internal structure, were analyzed (Table 4-1). BSE imaging of the monazites shows that most of the grains are homogenous; however, some grains show a faint sector zoning. Chemical maps show a range in compositional patterns (Fig. 4-4b). Sector and patchy irregular zoning with embayments are also common and some grains appear to have centres that are depleted in Y-U with rims more enriched in these elements (grain 18; Fig. 4-4b). Monazite grains have a range of $^{206}Pb/^{238}U$ ages from 57.0 ± 1 Ma

to 51 ± 1 Ma (1σ error; Table 4-1). The grains have a weighted mean $^{206}Pb/^{238}U$ age of 54.27 ± 1.0 Ma (2 σ error, n=17; MSWD = 3.3; Fig. 4-5b). The relatively high MSWD can be explained by monazite growth or recrystallization during a protracted event. The chemical domains in the monazite do not appear to correspond to distinct age domains. Monazite formation does not appear to be linked to a specific metamorphic reaction.

*1.4.1.3.* Quartzite (AH-03-27)

Sample AH-03-27 is from a 75 meter long and 25 meter wide, coarse grained quartzite lens from the west side of Bearpaw Lake. The quartzite is interlayered within a lens of the cordierite-gedrite rock from which sample AH-03-26 was taken (Fig. 4-2). Monazite from this sample was thought to most likely contain a complete record of monazite growth during multiple metamorphic events. The quartzite is characterized by 0.5-1 cm grains of quartz with pods of biotite and muscovite. In thin section, quartz occurs as euhedral to anhedral interlocking crystals with minor amounts of potassium feldspar which occurs as anhedral, highly altered grains (Fig. 4-6c). Biotite occurs as tabular crystals parallel to $S_2$. Muscovite occurs as randomly oriented tabular grains. Biotite and muscovite are often rimmed by secondary chlorite alteration. Accessory phases of apatite, monazite and zircon are common.

The monazite grains are equant and euhedral to subhedral in shape. In BSE images, the grains show either a weak sector zoning or appear homogeneous. The chemical maps show a range of patterns (Fig. 4-4c), including oscillatory zoning, marked sector zoning, irregular patchy zoning with embayments, discontinuous zones, and cores that are enriched or depleted in Y-Ca-Th-U relative to their rims. Fourteen monazite grains from this sample were analyzed and have a range of $^{206}Pb/^{238}U$ ages from 55.1 ± 1 Ma to 50.1 ± 1 Ma (1σ error; Table 4-1). The monazite grains have a weighted mean $^{206}Pb/^{238}U$ age of 52.5 ± 0.8 Ma (2 σ error, n=17; MSWD = 2.7; Fig. 4-5c). As with the other samples, the relatively high MSWD in this sample is explained by protracted monazite growth or recrystallization over the course of several million years, and the chemical domains in

the monazite do not correspond with distinct age domains that were identifiable using the SHRIMP.

## 4.5. Discussion

The Y, Ca, Th and U chemical zoning observed in the monazite grains do not appear to be related to distinct age domains that are discernable by SHRIMP analysis. In other studies of monazite, the chemical patterns observed are similar to those of this study in that most metamorphic monazites contain a patchwork of chemical zones, with truncation of earlier zones and juxtaposition of different chemical zones (Parrish, 1990, Pyle and Spear, 1999; Williams et al., 1999; Pyle et al., 2001; Pyle and Spear, 2003; Gibson et al., 2004). These chemical zones are often attributed to dissolution and re-precipitation during multiple monazite growth events at different times. Some studies (Foster et al., 2002; Gibson et al., 2004) have linked specific chemical zones, usually Y, with distinct age domains. However, in this study, there was no systematic pattern of older and/or younger ages corresponding to specific chemical domains. The chemical domains are likely controlled by local heterogeneities in the bulk rock chemistry and range of phases present, which would have exerted considerable control over the availability or local mobility of certain elements during prograde metamorphism (Pyle and Spear, 2003). In addition, common silicates such as plagioclase, muscovite and biotite, can host sufficient light rare earth elements (LREE) and phosphorous to stabilize and grow monazite (Kohn and Malloy, 2004). During decompression, the P-T-t path of the basement gneisses crosses several reactions that could control the Y and heavy rare earth elements (HREE) distribution via garnet growth, such as Bt + Sil = Grt + Crd + melt (Fig. 4-7). The presence of garnet and cordierite in the basement gneisses support the involvement of this melt-producing reaction. Basement rocks were subsequently isobarically cooled, which resulted in the reversal of these reactions potentially releasing HREE and Y during the breakdown of garnet. In this way, the rapid decompression and subsequent isobaric cooling would have resulted in rapid and/or partial metamorphic reactions that

would have controlled the distributions of trace elements during monazite growth or recrystallization. The chemical patterns observed in the monazite grains are likely a result of changes in pressure, temperature and composition of the rocks, related to mineral breakdown and growth during metamorphism and anatexis, and the enhanced mobility of elements due to the presence of a ubiquitous melt phase.

The Paleocene-Eocene ages from the cordierite-gedrite and quartzite samples are interpreted to date the time of the peak P-T conditions and subsequent ca. 5 kbar decompression in the basement rocks of Thor-Odin dome. Precambrian metamorphism has been penetratively overprinted in these rocks and any record of earlier events is not preserved within the monazite grains. The mean $^{206}Pb/^{238}U$ ages of the samples range from ca. 56 Ma to 52 Ma, and likely reflect the progressive growth or recrystallization of monazite over the course of several million years. The P-T-t path for the basement gneiss of Thor-Odin dome is shown in Figure 4-7.

The timing of monazite formation records ca. 56 Ma peak metamorphism of 800 °C and 8-10 kbar and subsequent decompression of the basement gneisses of Thor-Odin dome. The timing of the onset of prograde metamorphism in Thor-Odin dome is uncertain; however, deformation and prograde metamorphism were ongoing in the Late Cretaceous in structurally overlying rocks surrounding Thor-Odin dome and on the north flank of the dome near Three Valley gap (Carr, 1990; Parrish, 1995; Johnston et al., 2000; Kuiper, 2003) and was likely ongoing by this time in Thor-Odin dome as well (Fig. 4-1). Prograde metamorphism had begun in Thor-Odin dome, possibly as early as 75 Ma due to thickening of the crust, and the rocks were at thermal peak by ca. 56 Ma. This was synchronous with anatexis in the basement rocks that had begun by ca. 56 Ma a based on zircon ages in leucosome (Hinchey, Chapter 1). Thor-Odin dome underwent near isothermal decompression from 10 kbar to < 5 kbar ca. 52 Ma. This decompression was synchronous with continued leucosome generation and resulted in the preservation of symplectitic textures in cordierite-gedrite rocks and mafic basement

gneisses. Decompression was followed by near isobaric cooling to 300 °C from ca. 52 to 48 Ma (Parkinson, 1992; Lorencak et al., 2001; Vanderhaeghe et al., 2003), likely a result of rapid cooling due to extensional denudation, with final stages of cooling continuing to ~45 Ma (Lorencak et al., 2001; Vanderhaeghe et al., 2003). There does not appear to be any metamorphic diachroneity within the basement gneisses of Thor-Odin dome.

## 4.6. Conclusions

The chemical patterns of Y, Ca, Th and U in monazite from the cordierite-gedrite and quartzite samples are complex, preserving distinct patterns, discontinuous zones, truncations, and embayments. The chemical domains do not correlate with age domains and are likely caused by local changes in the composition of the bulk rock and phases due to mineral breakdown and growth during metamorphism and anatexis. There are several metamorphic and melt-producing reactions that were likely operative, such as the growth and breakdown of garnet (see Fig. 4-7), that would have exerted control on the availability of HREE and Y for the formation of monazite grains.

The basement gneiss of Thor-Odin dome preserve sillimanite-potassium feldspar-melt assemblages, were buried to depths of 26-33 km, and were completely transposed and migmatized during the Cordilleran orogenesis from the Late Cretaceous to Eocene. Prograde metamorphism in the basement gneisses of Thor-Odin dome was likely on going by ca. 75 Ma on the basis of metamorphic ages of structurally overlying rocks of the Middle Crustal Zone. The basement gneiss of Thor-Odin dome experienced peak metamorphism of 800 °C and 8-10 kbar by 56.2 ± 1.2 Ma, based on the mean $^{206}Pb/^{238}U$ age of monazite from the cordierite-gedrite basement gneiss. The basement subsequently underwent near isothermal decompression to < 5 kbar ending by 52.5 ± 0.8 Ma, based on the mean $^{206}Pb/^{238}U$ age of monazite from a sample of quartzite in the basement paragneiss. Any older metamorphic event, such as a Precambrian metamorphism, is not preserved in the monazite grains from the samples of either cordierite-gedrite rock or quartzite from the basement paragneiss. In Thor-Odin dome, ca. 56 to 52 Ma monazite

records the culmination of peak metamorphism, synchronous with the onset of anatexis, and also records the timing of decompression.

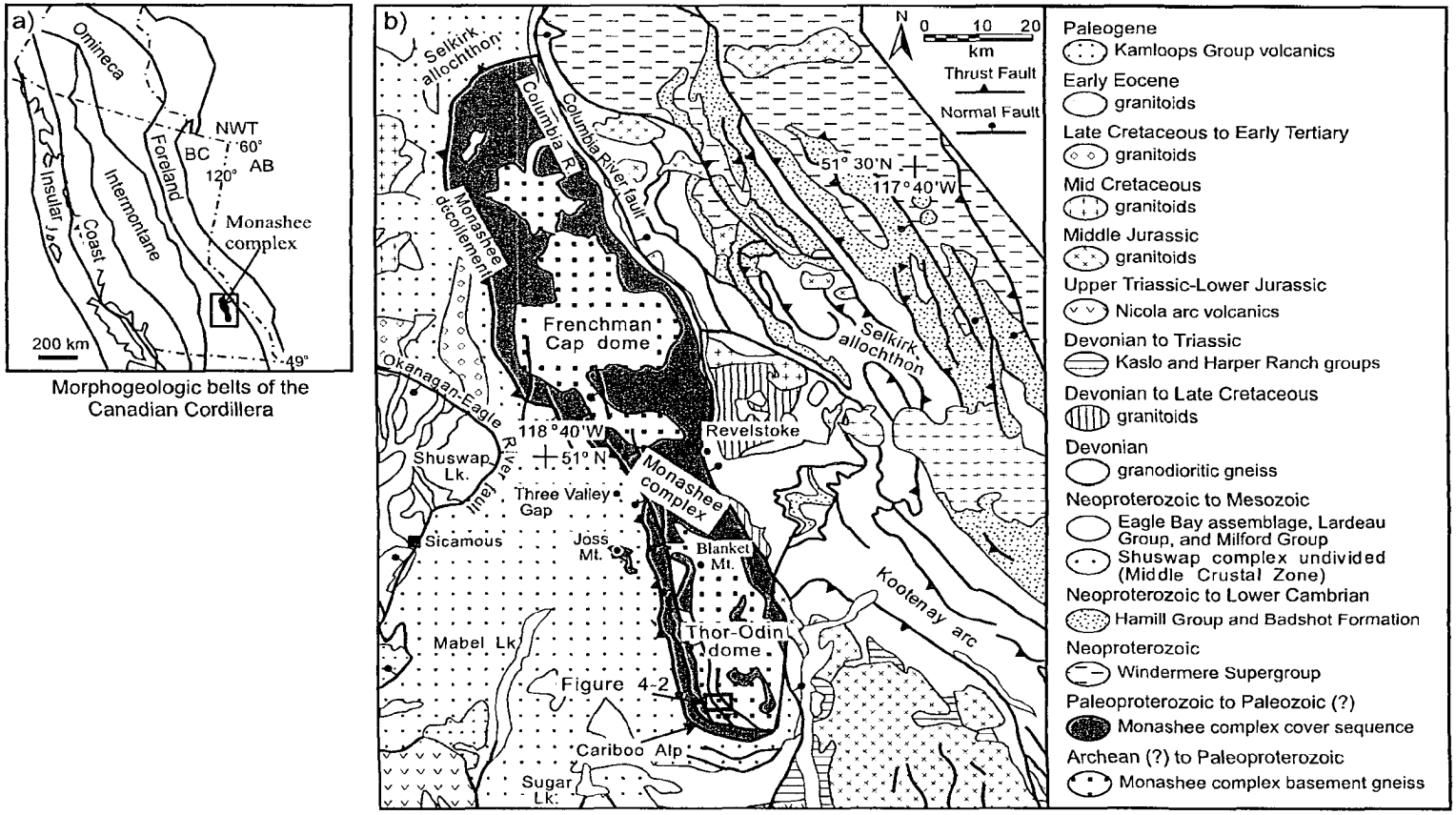


**Figure 4-1.** (a) Map highlights the five morphogeological belts of the Cordillera from Wheeler and McFeely (1991). (b) Regional map of the Monashee complex and surrounding area, southeastern Omineca belt (modified after Scammell and Brown, 1990; Wheeler and McFeely, 1991; Gibson, et al., 1999). The box in southern Thor-Odin dome delineates Figure 4-2.

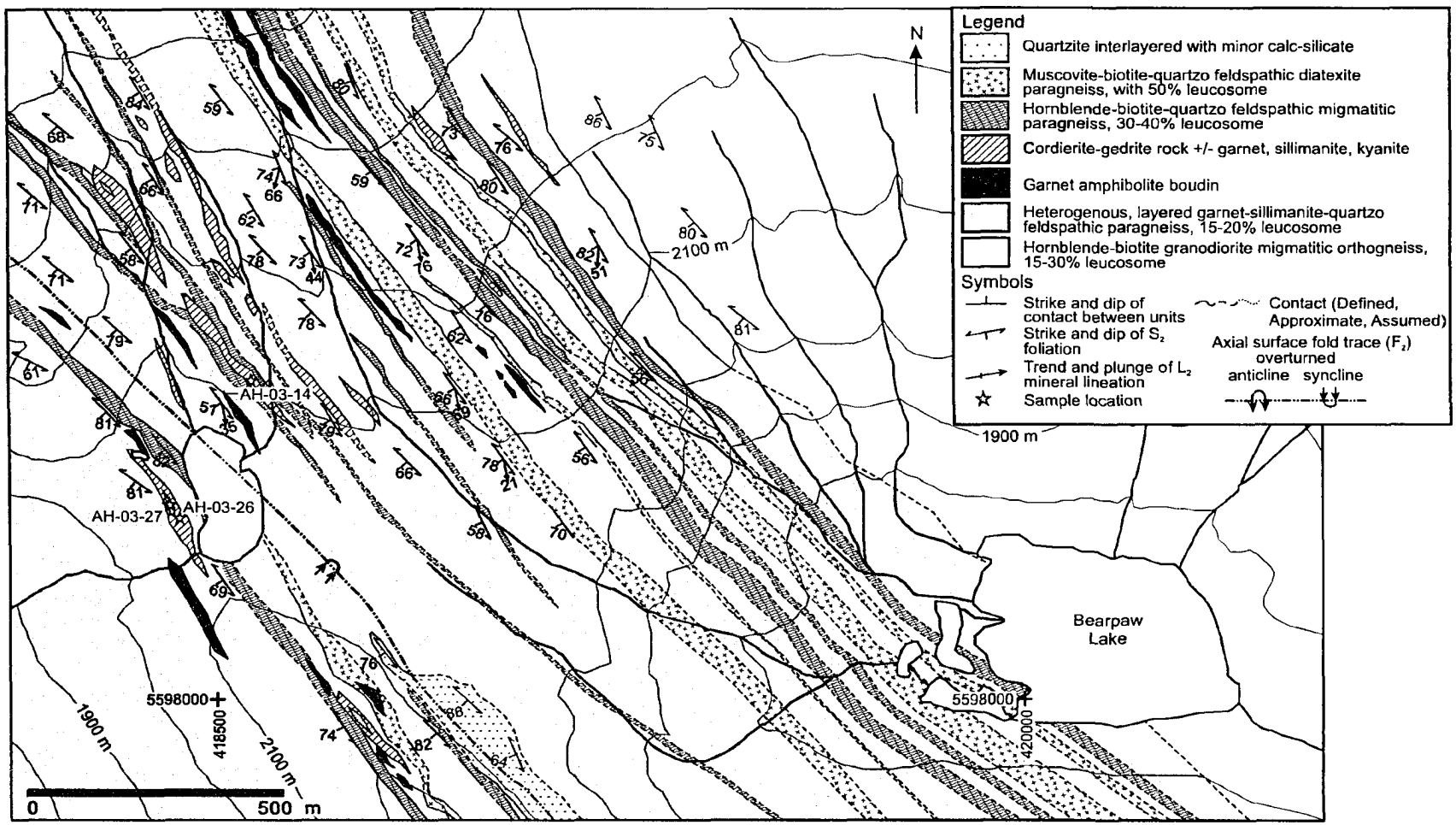


**Figure 4-2.** Geological map of the Bearpaw Lake area, Thor-Odin dome, Monashee complex (mapping by A.M. Hinchey).

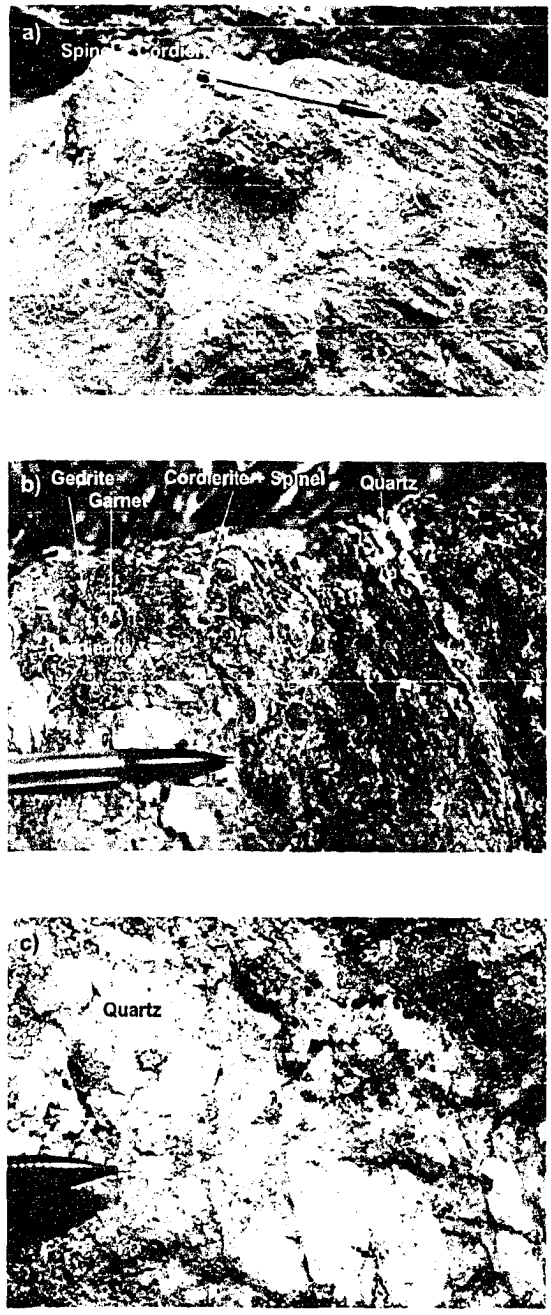


**Figure 4-3.** Field photo (a) cordierite-gedrite rock (AH-03-14), (b) cordierite-gedrite rock (AH-03-26), and (c) quartzite (AH-03-27) exposed in the Bearpaw Lake area, Thor-Odin dome. Photo (a) shows garnet porphyroblast with reaction rims of cordierite-spinel surrounded by coarse grained, radial, gedrite crystals. Photo (b) shows garnet porphyroblasts, symplectite of spinel and cordierite, interstitial cordierite grains and euhedral gedrite crystals. Photo (c) shows medium grained massive quartzite that is interlayered within the cordierite-gedrite rocks.

**Figure 4-4.** Representative monazite grains from two cordierite-gedrite samples and a quartzite sample dated using the SHRIMP. Each monazite shows four chemical maps: Y= yttrium, Th= thorium, Ca = calcium and U = uranium. The pit left by the ion beam on the monazite is drawn on the yttrium chemical map (top left). Monazite ages are reported as $^{206}Pb/^{238}U$ ages that are corrected for common Pb (see text for explanation). Bracketed numbers after the age refer to analytical locations listed in Table 4-1. See text for description and interpretation of intracrystalline domains and textures. Errors on ages are reported in Table 4-1 and in text. (a) Coarse grained cordierite-gedrite rock (AH-03-14). (b) Coarse grained cordierite-gedrite rock (AH-03-26). (c) Medium grained quartzite (AH-03-27) that is interlayered with the cordierite-gedrite rock (AH-03-26).

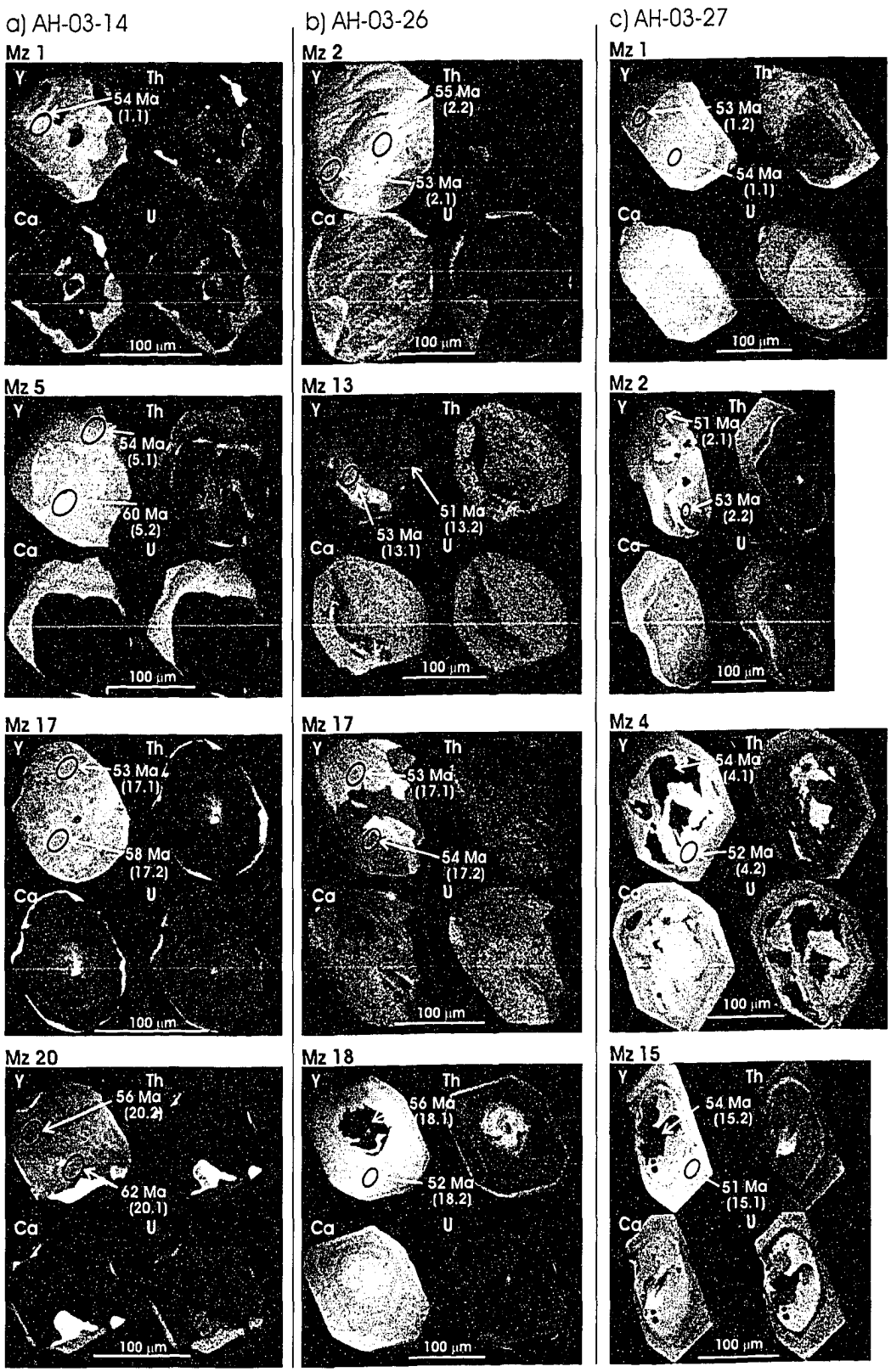

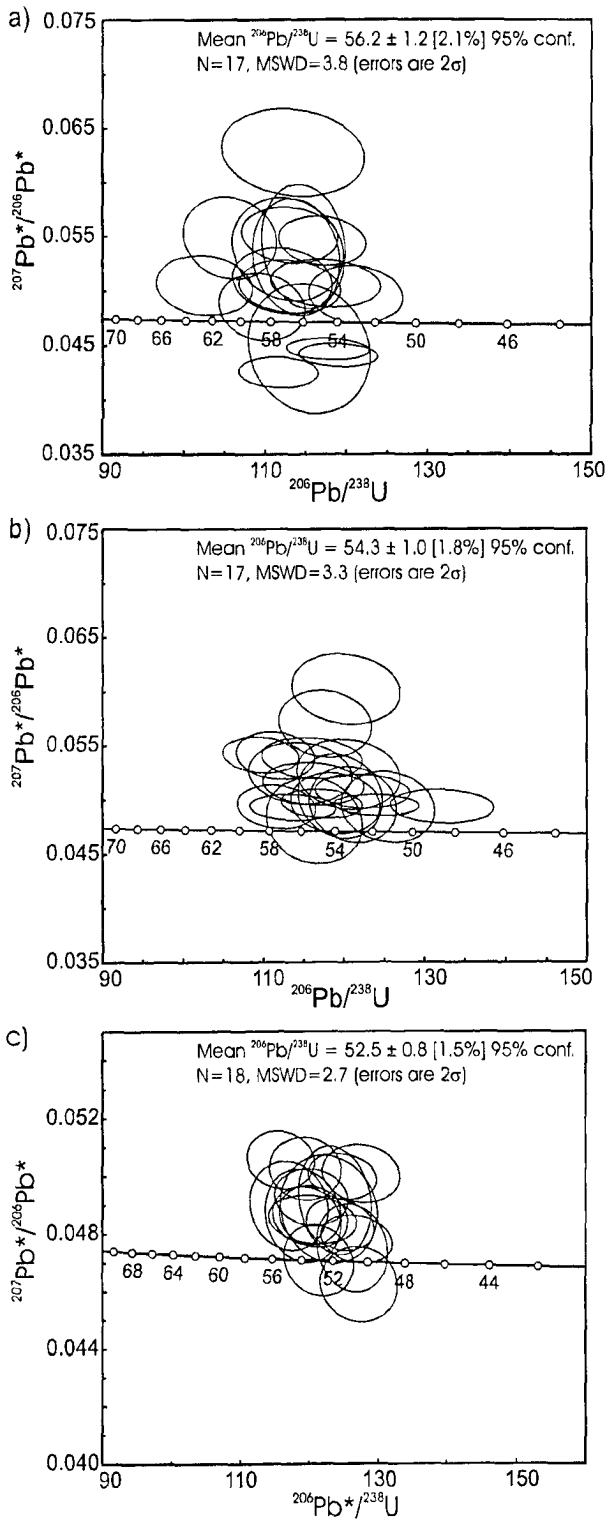


**Figure 4-5.** U-Pb Tera-Wasserburg diagrams for each sample dated by U-Pb SHRIMP analysis. (a) Coarse grained cordierite-gedrite rock (AH-03-14). (b) Coarse grained cordierite-gedrite rock (AH-03-26). (c) Medium grained quartzite (AH-03-27) that is interlayered within the cordierite-gedrite rock (AH-03-26).

**Figure 4-6.** Photomicrographs of cordierite-gedrite rocks and interlayered quartzite Bearpaw Lake area, Thor-Odin dome. Photo (a) is of sample AH-03-14 and shows prismatic, euhedral gedrite crystals that define the $S_2$ foliation. Interstitial cordierite grains dominate the matrix, with minor spinel. Photo (b) is of sample AH-03-26 and shows tabular, euhedral crystals of gedrite crystals that are riddled with inclusions. Garnet grains contain abundant inclusions of cordierite, gedrite, ilmenite, spinel and apatite with cracks that are filled with gedrite, plagioclase and cordierite. Cordierite dominates the matrix and occurs predominantly as interstitial grains between blades of gedrite. Photo (c) is of sample AH-03-27 and shows euhedral to anhedral interlocking quartz crystals. Biotite occurs as tabular crystals parallel to $S_2$. Muscovite occurs as randomly oriented tabular grains.

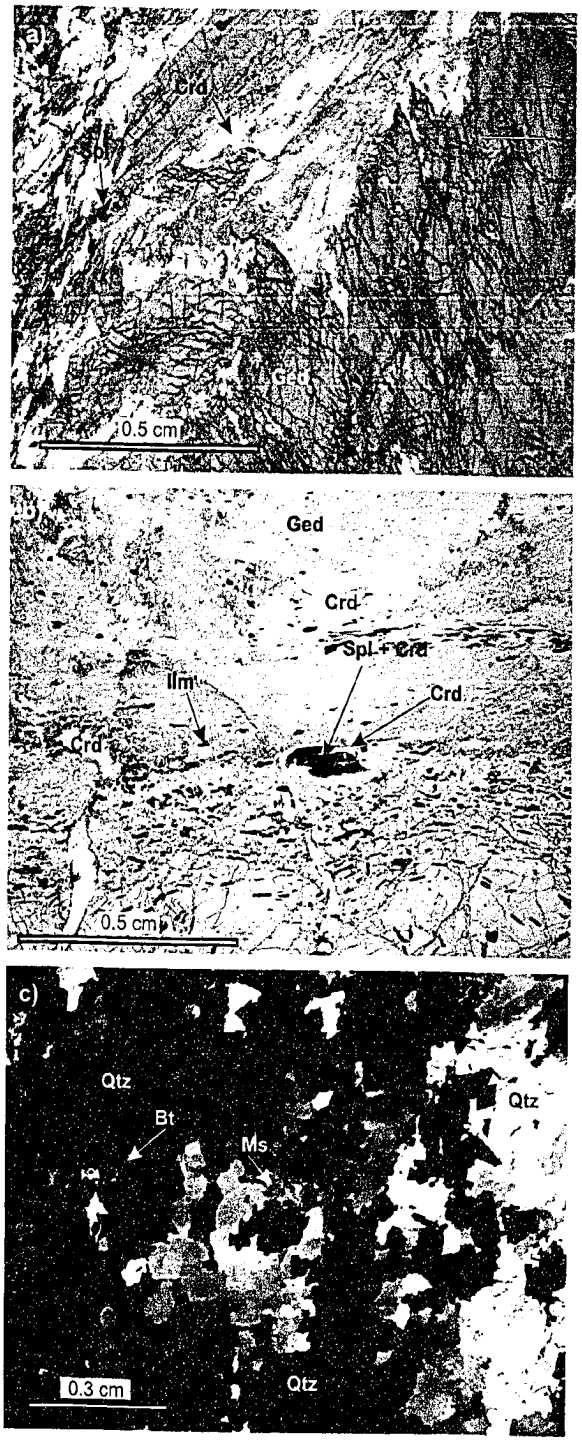

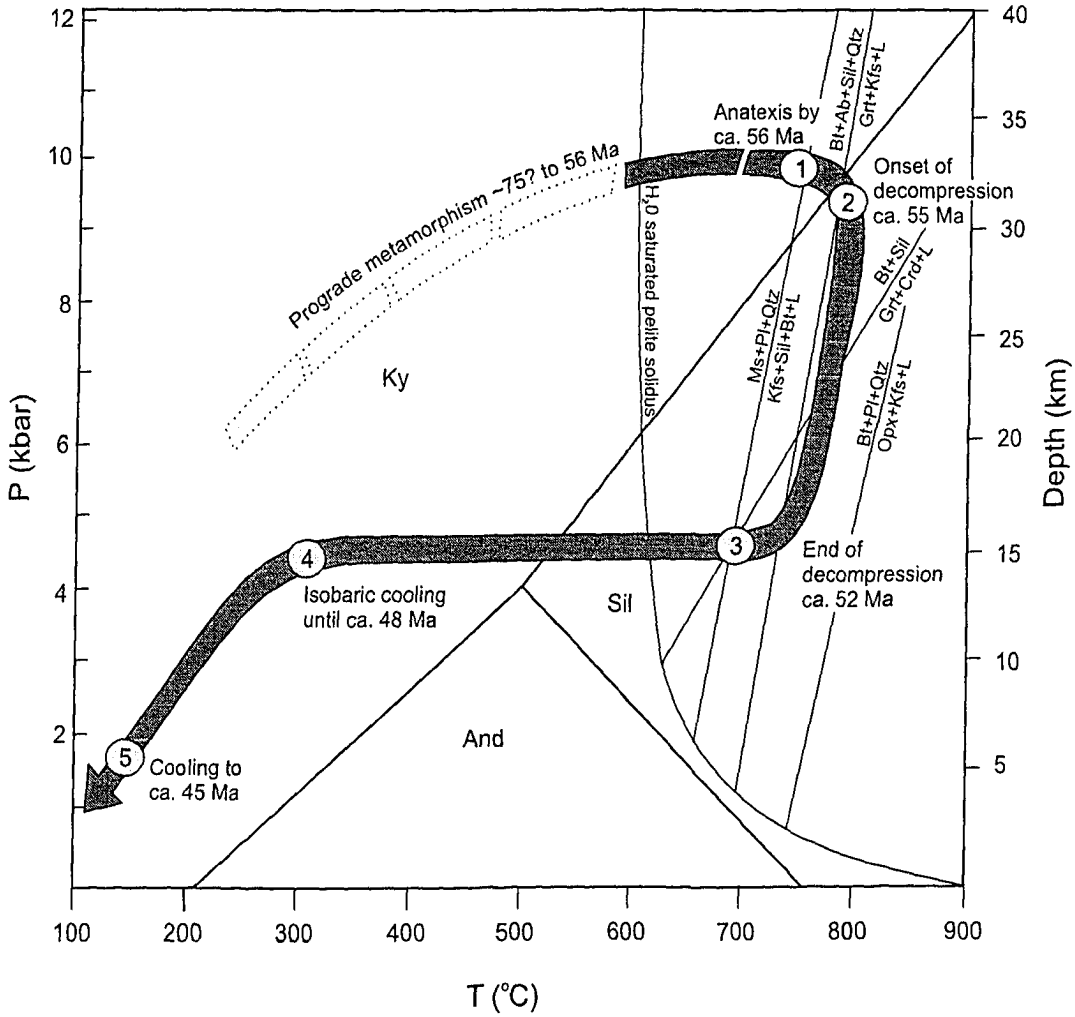


Events in the basement gneiss of Thor-Odin

① ca. 56 Ma - Baric peak metamorphism and anatexis
② ca. 55 Ma - Onset of isothermal decompression and anatexis
③ ca. 52 Ma - End of decompression and anatexis
④ ca. 48 Ma - Isobaric cooling
⑤ ca. 45 Ma - Continued cooling and decompression

**Figure 4-7.** Pressure-Temperature-time path proposed for the basement gneiss of Thor-Odin dome. The prograde path is unconstrained; approximate timing constraints are labelled for known parts of the path. Timing and geothermobarometric constraints are provided by this study and those of Reesor and Moore (1971); Duncan (1982); Vanderhaeghe et al. (1999); Norlander et al. (2001); Lorencak et al. (2001) and Vanderhaeghe et al. (2003). The locations of selected dehydration melting reactions are shown. Melt producing reactions are explained in Spear et al. (1999). Mineral symbols are from Kretz (1983).

**Table 4-1.** U-Pb SHRIMP monazite data for the cordierite-gedrite and quartzite samples from Bearpaw Lake area, Thor-Odin dome. $^{206}Pb/^{238}U$ ages are reported corrected for common lead (see text for explanation).

| | | | | | | | | *Ages* |
|---|---|---|---|---|---|---|---|---|
| | Th | Pb[a] | $^{204}Pb$[b] | $^{208}Pb$[b] | $^{207}Pb$[b] | $^{206}Pb$[b] | $^{207}Pb$[b] | $^{206}Pb$[c] |
| Spots | U | (ppm) | $^{206}Pb$ | $^{206}Pb$ | $^{235}U$ | $^{238}U$ | $^{206}Pb$ | $^{238}U$ |
| **Sample AH-03-14** Coarse grained garnet-cordierite-gedrite rock. UTM: 418667E, 5598701N | | | | | | | | |
| 1.1 | 2.02 | 64 | 0.00086 ± 0.00024 | 0.64740 ± 0.00801 | 0.06433 ± 0.00173 | 0.00855 ± 0.00016 | 0.05460 ± 0.00093 | 54.3 ± 1.0 |
| 2.1 | 2.06 | 59 | 0.00078 ± 0.00015 | 0.64573 ± 0.00971 | 0.06504 ± 0.00318 | 0.00872 ± 0.00016 | 0.05408 ± 0.00233 | 55.5 ± 1.0 |
| 3.1 | 6.09 | 40 | 0.00205 ± 0.00049 | 1.92030 ± 0.02920 | 0.07630 ± 0.00337 | 0.00882 ± 0.00028 | 0.06271 ± 0.00165 | 55.5 ± 1.8 |
| 5.1 | 0.51 | 210 | 0.00009 ± 0.00003 | 0.14049 ± 0.00138 | 0.05116 ± 0.00105 | 0.00841 ± 0.00014 | 0.04410 ± 0.00044 | 54.2 ± 0.9 |
| 5.2 | 3.64 | 53 | 0.00091 ± 0.00021 | 1.13550 ± 0.01377 | 0.07166 ± 0.00271 | 0.00947 ± 0.00021 | 0.05490 ± 0.00154 | 60.1 ± 1.3 |
| 6.1 | 1.79 | 24 | 0.00088 ± 0.00020 | 0.53030 ± 0.01157 | 0.05345 ± 0.00339 | 0.00867 ± 0.00023 | 0.04470 ± 0.00243 | 55.8 ± 1.5 |
| 7.1 | 0.86 | 41 | 0.00080 ± 0.00019 | 0.24863 ± 0.00358 | 0.06147 ± 0.00197 | 0.00885 ± 0.00020 | 0.05039 ± 0.00099 | 56.5 ± 1.3 |
| 9.1 | 2.97 | 237 | 0.00017 ± 0.00003 | 0.85660 ± 0.00340 | 0.05235 ± 0.00109 | 0.00850 ± 0.00015 | 0.04466 ± 0.00039 | 54.7 ± 1.0 |
| 13.1 | 1.33 | 34 | 0.00028 ± 0.00012 | 0.40719 ± 0.00435 | 0.05955 ± 0.00186 | 0.00852 ± 0.00020 | 0.05071 ± 0.00089 | 54.4 ± 1.3 |
| 14.1 | 2.40 | 47 | 0.00062 ± 0.00018 | 0.75256 ± 0.00755 | 0.06722 ± 0.00206 | 0.00885 ± 0.00019 | 0.05509 ± 0.00106 | 56.2 ± 1.2 |
| 16.1 | 3.36 | 131 | 0.00030 ± 0.00005 | 0.89791 ± 0.00611 | 0.05257 ± 0.00123 | 0.00896 ± 0.00016 | 0.04257 ± 0.00058 | 57.8 ± 1.0 |
| 17.1 | 1.72 | 39 | 0.00044 ± 0.00023 | 0.53741 ± 0.00477 | 0.05653 ± 0.00173 | 0.00826 ± 0.00016 | 0.04963 ± 0.00107 | 52.9 ± 1.0 |
| 17.2 | 1.73 | 38 | 0.00040 ± 0.00010 | 0.53955 ± 0.00535 | 0.06110 ± 0.00212 | 0.00913 ± 0.00018 | 0.04854 ± 0.00127 | 58.5 ± 1.2 |
| 18.2 | 6.62 | 136 | 0.00067 ± 0.00020 | 2.00010 ± 0.02814 | 0.06262 ± 0.00220 | 0.00892 ± 0.00020 | 0.05091 ± 0.00123 | 57.0 ± 1.3 |
| 19.1 | 2.27 | 41 | 0.00039 ± 0.00033 | 0.72335 ± 0.01171 | 0.06435 ± 0.00307 | 0.00879 ± 0.00017 | 0.05312 ± 0.00219 | 56.0 ± 1.1 |
| 20.1 | 8.51 | 154 | 0.00095 ± 0.00017 | 2.55820 ± 0.02550 | 0.06794 ± 0.00231 | 0.00976 ± 0.00023 | 0.05048 ± 0.00111 | 62.3 ± 1.4 |
| 20.2 | 1.69 | 40 | 0.00099 ± 0.00028 | 0.53963 ± 0.01241 | 0.06581 ± 0.00306 | 0.00887 ± 0.00022 | 0.05379 ± 0.00194 | 56.5 ± 1.4 |
| **Sample AH-03-26** Coarse grained garnet-cordierite-gedrite rock. UTM: 418513E, 5598418N | | | | | | | | |
| 1.1 | 1.85 | 34 | 0.00052 ± 0.00014 | 0.57428 ± 0.01613 | 0.06312 ± 0.00212 | 0.00873 ± 0.00020 | 0.05243 ± 0.00117 | 55.7 ± 1.3 |
| 2.1 | 0.61 | 75 | 0.00013 ± 0.00007 | 0.19725 ± 0.00380 | 0.05761 ± 0.00182 | 0.00841 ± 0.00016 | 0.04967 ± 0.00114 | 53.8 ± 1.0 |
| 2.2 | 0.79 | 32 | 0.00020 ± 0.00008 | 0.25539 ± 0.00359 | 0.05703 ± 0.00238 | 0.00860 ± 0.00018 | 0.04810 ± 0.00162 | 55.1 ± 1.1 |
| 7.1 | 5.18 | 55 | 0.00083 ± 0.00012 | 1.63760 ± 0.01183 | 0.06398 ± 0.00180 | 0.00862 ± 0.00019 | 0.05384 ± 0.00077 | 54.9 ± 1.2 |
| 9.1 | 3.40 | 92 | 0.00049 ± 0.00010 | 1.04190 ± 0.00675 | 0.05840 ± 0.00129 | 0.00853 ± 0.00015 | 0.04968 ± 0.00053 | 54.6 ± 1.0 |
| 10.1 | 0.58 | 23 | 0.00021 ± 0.00006 | 0.19677 ± 0.00183 | 0.05726 ± 0.00140 | 0.00818 ± 0.00016 | 0.05076 ± 0.00064 | 52.3 ± 1.0 |
| 11.2 | 4.25 | 62 | 0.00068 ± 0.00038 | 1.29170 ± 0.00979 | 0.06101 ± 0.00159 | 0.00896 ± 0.00016 | 0.04937 ± 0.00081 | 57.4 ± 1.1 |
| 12.1 | 0.39 | 41 | 0.00070 ± 0.00019 | 0.14573 ± 0.00340 | 0.06908 ± 0.00233 | 0.00832 ± 0.00019 | 0.06019 ± 0.00133 | 52.6 ± 1.2 |
| 13.1 | 2.34 | 43 | 0.00034 ± 0.00007 | 0.71076 ± 0.00892 | 0.05643 ± 0.00203 | 0.00826 ± 0.00015 | 0.04955 ± 0.00143 | 52.9 ± 1.0 |
| 13.2 | 2.04 | 59 | 0.00036 ± 0.00015 | 0.60935 ± 0.00416 | 0.05420 ± 0.00188 | 0.00797 ± 0.00015 | 0.04933 ± 0.00134 | 51.0 ± 1.0 |
| 15.1 | 2.86 | 117 | 0.00039 ± 0.00010 | 0.88855 ± 0.01175 | 0.06108 ± 0.00176 | 0.00861 ± 0.00019 | 0.05144 ± 0.00080 | 55.0 ± 1.2 |
| 16.1 | 1.75 | 163 | 0.00091 ± 0.00013 | 0.53734 ± 0.00666 | 0.06692 ± 0.00174 | 0.00897 ± 0.00016 | 0.05412 ± 0.00090 | 57.0 ± 1.0 |
| 17.1 | 3.77 | 34 | 0.00080 ± 0.00041 | 1.13180 ± 0.01713 | 0.05987 ± 0.00210 | 0.00830 ± 0.00018 | 0.05229 ± 0.00133 | 53.0 ± 1.1 |
| 17.2 | 1.98 | 64 | 0.00078 ± 0.00014 | 0.61526 ± 0.00458 | 0.05809 ± 0.00222 | 0.00837 ± 0.00015 | 0.05032 ± 0.00157 | 53.5 ± 1.0 |
| 18.1 | 2.32 | 453 | 0.00029 ± 0.00005 | 0.68308 ± 0.00312 | 0.05983 ± 0.00136 | 0.00880 ± 0.00017 | 0.04931 ± 0.00048 | 56.3 ± 1.1 |
| 18.2 | 2.01 | 298 | 0.00033 ± 0.00012 | 0.65135 ± 0.00269 | 0.05501 ± 0.00109 | 0.00806 ± 0.00014 | 0.04951 ± 0.00039 | 51.6 ± 0.9 |
| 20.1 | 1.14 | 44 | 0.00073 ± 0.00016 | 0.36461 ± 0.00531 | 0.06683 ± 0.00210 | 0.00850 ± 0.00017 | 0.05702 ± 0.00127 | 53.9 ± 1.1 |
| **Sample AH-03-27** Medium granite quartzite interlayered with AH-03-26. UTM: 418513E, 5598391N | | | | | | | | |
| 1.1 | 1.78 | 351 | 0.00028 ± 0.00003 | 0.56782 ± 0.00392 | 0.05605 ± 0.00111 | 0.00836 ± 0.00014 | 0.04865 ± 0.00041 | 53.5 ± 0.9 |
| 1.2 | 2.37 | 363 | 0.00031 ± 0.00005 | 0.74483 ± 0.00249 | 0.05550 ± 0.00133 | 0.00830 ± 0.00018 | 0.04848 ± 0.00034 | 53.2 ± 1.2 |
| 2.1 | 3.22 | 361 | 0.00035 ± 0.00004 | 0.98971 ± 0.00310 | 0.05195 ± 0.00100 | 0.00788 ± 0.00013 | 0.04780 ± 0.00034 | 50.6 ± 0.9 |
| 2.2 | 2.79 | 275 | 0.00040 ± 0.00006 | 0.87641 ± 0.00312 | 0.05555 ± 0.00114 | 0.00829 ± 0.00014 | 0.04860 ± 0.00043 | 53.1 ± 0.9 |
| 3.1 | 8.53 | 225 | 0.00165 ± 0.00019 | 2.04980 ± 0.16406 | 0.06638 ± 0.00375 | 0.00845 ± 0.00019 | 0.05697 ± 0.00281 | 53.6 ± 1.2 |
| 4.1 | 4.40 | 341 | 0.00041 ± 0.00004 | 1.42340 ± 0.00484 | 0.05645 ± 0.00116 | 0.00831 ± 0.00015 | 0.04925 ± 0.00040 | 53.2 ± 1.0 |
| 4.2 | 2.94 | 302 | 0.00036 ± 0.00004 | 0.94930 ± 0.00417 | 0.05476 ± 0.00137 | 0.00808 ± 0.00014 | 0.04917 ± 0.00076 | 51.7 ± 0.9 |
| 5.1 | 2.35 | 306 | 0.00050 ± 0.00008 | 0.63590 ± 0.00442 | 0.05012 ± 0.00110 | 0.00786 ± 0.00014 | 0.04624 ± 0.00054 | 50.5 ± 0.9 |
| 7.1 | 4.58 | 340 | 0.00085 ± 0.00010 | 1.25060 ± 0.03877 | 0.05767 ± 0.00143 | 0.00854 ± 0.00017 | 0.04895 ± 0.00063 | 54.7 ± 1.1 |
| 11.1 | 3.19 | 387 | 0.00034 ± 0.00004 | 0.98932 ± 0.00580 | 0.05349 ± 0.00115 | 0.00824 ± 0.00014 | 0.04709 ± 0.00051 | 52.9 ± 0.9 |
| 12.1 | 2.75 | 360 | 0.00029 ± 0.00003 | 0.85594 ± 0.00709 | 0.05483 ± 0.00162 | 0.00814 ± 0.00019 | 0.04888 ± 0.00076 | 52.1 ± 1.2 |
| 13.1 | 2.55 | 339 | 0.00034 ± 0.00006 | 0.80286 ± 0.00815 | 0.05625 ± 0.00140 | 0.00839 ± 0.00016 | 0.04860 ± 0.00066 | 53.8 ± 1.0 |
| 14.1 | 2.92 | 416 | 0.00028 ± 0.00006 | 0.85963 ± 0.00237 | 0.05188 ± 0.00116 | 0.00792 ± 0.00013 | 0.04752 ± 0.00062 | 50.8 ± 0.8 |
| 15.1 | 2.87 | 267 | 0.00042 ± 0.00004 | 0.88877 ± 0.00259 | 0.05521 ± 0.00102 | 0.00801 ± 0.00013 | 0.04999 ± 0.00032 | 51.2 ± 0.9 |
| 15.2 | 3.85 | 256 | 0.00050 ± 0.00010 | 1.19370 ± 0.00726 | 0.05800 ± 0.00119 | 0.00837 ± 0.00015 | 0.05027 ± 0.00045 | 53.5 ± 0.9 |
| 17.1 | 4.32 | 258 | 0.00059 ± 0.00006 | 1.38310 ± 0.00446 | 0.06017 ± 0.00120 | 0.00863 ± 0.00015 | 0.05060 ± 0.00041 | 55.1 ± 0.9 |
| 18.1 | 2.75 | 335 | 0.00039 ± 0.00007 | 0.84419 ± 0.00354 | 0.05350 ± 0.00103 | 0.00803 ± 0.00013 | 0.04831 ± 0.00036 | 51.5 ± 0.9 |
| 20.1 | 3.04 | 268 | 0.00047 ± 0.00007 | 0.95842 ± 0.00431 | 0.05414 ± 0.00111 | 0.00784 ± 0.00014 | 0.05011 ± 0.00041 | 50.1 ± 0.9 |

[a]Radiogenic Pb. [b]Ratios are uncorrected for common Pb. [c]Corrected for common Pb according to procedure oulined by Stern and Berman (2000); uncertainties are reported at 1σ and are calculated by numerical propogation of all known sources of error.

# CHAPTER 5

## Paleocene high-grade thermal peak, anatectic front and high strain in the Thor-Odin dome area, Monashee Complex: constraints for tectonic models of the southern Canadian Cordillera


### Abstract

Thor-Odin dome of the Monashee complex, located in the hinterland of the southern Canadian Rocky Mountain thrust belt, comprises a supracrustal sequence and > 1.8 Ga North American basement rocks that experienced polydeformation, high-grade metamorphism and anatexis during the Mesozoic-Eocene Cordilleran orogen. Pervasive Paleocene - Eocene deformation transposed and overprinted Precambrian relationships and structures. The timing of onset of Cordilleran events in Thor-Odin dome is uncertain; however, deformation and prograde metamorphism were likely ongoing in the Late Cretaceous. Peak P-T conditions of ~800 °C and 8-10 kb constrain the depth of burial of the basement rocks to 26-33 km. The ca. 56 Ma zircon ages of syntectonic leucosome from basement gneiss indicate that anatexis occurred in the Paleocene. This is part of the youngest deformation and metamorphic event in the hinterland, and was synchronous with the final stages of compression in the Foothills of the Foreland fold and thrust belt. Anatexis and isothermal decompression in Thor-Odin dome continued until ca. 52 Ma as the dome underwent exhumation during regional extension. Thor-Odin dome is the deepest exposed level of a panel of strained rocks that developed during progressive loading, thickening and heating of the crust. At structural levels above Thor-Odin dome, to the south, west, and north, referred to as the Middle Crustal Zone, the rocks preserve deformation, high-grade metamorphism and anatexis that is up to 20 m.y. older than that of Thor-Odin dome, and the boundary between these two, at Cariboo Alp, preserves deformation that is 2-4 m.y. older than that in Thor-Odin dome. This marked break in the timing of deformation supports the interpretation of a shear zone at Cariboo Alp, separating the older deformation of the Middle Crustal Zone from that of the basement

rocks of Thor-Odin dome. In the Paleocene, Thor-Odin dome was deeper (up to 6 km) and hotter than adjacent rocks of the Frenchman Cap dome, the northern culmination of the Monashee complex, indicating that there may be two different structural panels within the complex that were juxtaposed, likely during $F_2$ folding, late in the Paleogene tectonic evolution. The diachronous timing of the end of deformation, metamorphism and anatexis in the Middle Crustal Zone and Thor-Odin dome is explained by a tectonic model that invokes a ductile shear zone(s). This model includes, either: a) two distinct ductile shear zones, one in the Late Cretaceous affecting the Middle Crustal zone followed by a localized zone of Paleocene-Eocene of high strain affecting the lower structural panel of Thor-Odin dome; or, b) one diachronous strain zone that either migrated progressively downward and/or forward or a zone of strain where deformation at lower structural levels of Thor-Odin dome outlasted that of higher structural levels of the Middle Crustal Zone.

## 5.1. Introduction

Thor-Odin dome of the southern Omineca belt is a structural culmination of polydeformed high-grade migmatitic Paleoproterozoic basement rocks infolded with younger Paleoproterozoic to Paleozoic (?) supracrustal or cover rocks (Fig. 5-1). The dome is part of the Monashee complex, the deepest exposed structural level in the southern Canadian Cordillera, and was exhumed in the Early Tertiary during extensional denudation. Basement and cover gneiss of Thor-Odin dome were metamorphosed at 8-10 kbar and 800 °C (Norlander et al., 2002), penetratively deformed, and melted in the Late Cretaceous to Eocene during the Cordilleran orogeny (Hinchey, Chapter 1). This paper summarizes the Cretaceous – Eocene tectonic evolution of Thor-Odin dome in light of new field and geochronology constraints (Hinchey, Chapter 1 and 4), and integrates this data with that of structurally overlying metamorphic rocks of the Middle Crustal Zone of the Omineca belt (Carr 1991) and of the adjacent basement complex of Frenchman Cap dome (Parrish, 1995; Crowley, 1997; Gibson et al., 1999; Crowley and Parrish, 1999), the northern culmination of the Monashee complex. This synthesis provides a basis for discussion of tectonic models for the hinterland of the southeastern Canadian Cordillera.

The geology of the southern Omineca belt, in the region of Thor-Odin dome (Fig. 5-1), has been described in terms of three panels or crustal zones termed the Basement, Middle Crustal and Upper Crustal zones that experienced different deformation and thermal histories and were juxtaposed in the Cretaceous to Early Tertiary, late in the history of the Cordilleran orogen (see Carr, 1991). At the latitude of the Monashee complex, the Upper Crustal Zone is bounded at the bottom by crustal-scale Eocene normal faults and is characterized by Middle Jurassic and older structures, Middle Jurassic plutons and a Late Jurassic to Cretaceous cooling history (Carr, 1991). The Middle Crustal Zone is the panel of rocks that structurally overlies the Monashee complex, and is characterized by Late Cretaceous to Eocene ductile strain, plutonism, and Early Tertiary thermal quenching (Carr, 1991).

The Basement Zone was used by Carr (1991) to refer to the Thor-Odin and Frenchman Cap domes which were thought to be a basement cored complex. The domes are separated by a structural depression and interpreted to be bounded at the top by the Monashee décollement (MD; Wheeler, 1965; Reesor and Moore, 1971; Brown, 1980; Brown et al., 1986; Journeay, 1986; Brown et al, 1992; McNicoll and Brown, 1995 and references therein). Prior to the 1990s, the rocks of Thor-Odin dome were thought to have experienced limited or no penetrative deformation during the Late Cretaceous to Eocene (Carr, 1991; Parkinson, 1991). Direct timing constraints have been placed on the deformation history in Frenchman Cap dome (Parrish, 1995; Crowley, 1999; Crowley and Parrish, 1999; Crowley et al., 2001), and show that the core of the dome preserves Paleoproterozoic deformation, while the upper levels have been penetratively overprinted by Cretaceous to Eocene deformation and thermal events termed "Cordilleran deformation". Based on geochronological and geochemical data, it is now recognized that Thor-Odin dome was penetratively deformed, metamorphosed and underwent pervasive anatexis during the Late Cretaceous to Eocene Cordilleran orogenesis associated with the final stages of compressional tectonics (Vanderhaeghe et al., 1999; Norlander et al., 2002; Kuiper, 2003; Hinchey, Chapter 1 and 4). In light of new data from Thor-Odin dome, major differences in the Paleocene-Eocene thermal and deformation history of the two culminations have been revealed. This raises questions as to whether the domes can be part of the same basement complex, or whether they may represent two different structural domains that were not juxtaposed until the Paleogene. If the later is the case then the MD cannot be the upper boundary in both domes (see Fig. 5-1). For these reasons, Frenchman Cap and Thor-Odin domes will be described and discussed separately and the term Basement Zone will not be used.

There is no direct evidence for deformation or metamorphism in Thor-Odin dome prior to the Late Cretaceous. There is, however, direct evidence of Late Cretaceous to Eocene penetrative deformation and anatexis in the basement rocks of Thor-Odin dome.

Therefore this paper is restricted to discussing the Late Cretaceous to Eocene high strain, melting and metamorphism in Thor-Odin dome during final stages of compression, before extension.

Numerous tectonic models have been proposed for Thor-Odin dome and the Monashee complex. The timing and extent of penetrative basement involvement play a key role in distinguishing between these models. There are also debates over the extent and character of the Monashee décollement, which has traditionally been defined as a ductile thrust bounding the top of the Monashee complex (Brown et al., 1992) with differences in interpretation contributing to the variety of proposed tectonic models. Recent models for southern Omineca belt evolution and linkages with the Foreland fold and thrust belt to the east include: a critical wedge of ductile deformation (Brown, 2003), crustal boudinage (Monger and Price, 2000), channel flow (Williams, 1999; Beaumont et al., 2001; Kuiper, 2003; Brown and Gibson, in press), extrusion of channel flow (Johnson et al., 2001), domal culmination (Vanderhaeghe et al., 1999; Fayon et al., 2004; Whitney et al., 2004), diapiric domal culmination (Norlander et al., 2002), ductile wedge of material overriding a cold basement (Gibson et al., 1999; Crowley et al. 2001), and a rolling-hinge detachment model (Teyssier et al., in review). In order to discriminate among these varied tectonic models, new data from Thor-Odin dome are integrated with documented structural, metamorphic and geochronological data from the region, and a revised model is suggested.

## 5.2. Regional geological overview

The Canadian Cordillera formed as a result of the Paleozoic to Paleogene accretion of fragments of allochthonous and parautochthonous oceanic sequences, continental slivers, volcanic arcs and sedimentary sequences to the western edge of ancestral North America (Monger, 1989). Mesozoic – Paleogene crustal thickening occurred during collision with accreted terranes and westward underthrusting of the North American plate (Fig. 5-1; Monger et al., 1982; Monger, 1989; Gabrielse and Campbell, 1991). In the Middle

Jurassic, accreted terranes had begun overriding the pericratonic terranes and Proterozoic and Paleozoic to early Mesozoic platformal sedimentary sequences that had accumulated on the paleomargin of North America (Monger et al., 1982). By the mid-Cretaceous, a 50-60 km thick crustal welt and a foreland basin had formed and during the Cretaceous the Rocky Mountain fold and thrust belt (Foreland belt) formed (Price and Mountjoy, 1970; Coney and Harms, 1984; Brown et al., 1986; Price, 1986). Crustal thickening and burial of the North American sedimentary sequence and overriding terranes resulted in metamorphism and deformation of rocks in the hinterland of the Rocky Mountain fold and thrust belt, termed the Omineca belt (Fig. 5-1; Reesor, 1970; Brown and Read, 1983 and references therein). In the Early Tertiary, southern British Columbia underwent a change from a transpressional to transtensional regime, attributed to changes in far field stresses related to the obliquity of the down-going Kula plate (Lonsdale, 1988; Andronicos et al., 2003). This resulted in Eocene regional extension, and the exhumation of some of the high-grade rocks of the southern Omineca belt via an array of generally north-south striking, brittle and ductile normal faults, which are linked to synchronous strike-slip fault systems that span the western Cordillera (Ewing, 1981; Tempelman-Kluit and Parkinson, 1986; Brown and Journeay, 1987; Parrish et al., 1988; Struik, 1993; Johnson and Brown 1996 and references therein).

In the southern Omineca belt, the lower plates of the extensional faults, termed the Middle Crustal Zone (Carr, 1991), expose high-grade rocks with relatively young deformation and cooling histories in a Cordilleran metamorphic core complex, termed the Shuswap complex (Armstrong, 1972; Coney, 1980; Parrish et al., 1988). Thor-Odin dome is a structural culmination within the Shuswap complex. Eocene normal fault systems that bound the Shuswap complex include the 58-50 Ma east-dipping Columbia River fault (CR) to the east and the 56-45 Ma west-dipping Okanagan Valley-Eagle River fault system (OV-ER) to the west (Okulitch, 1984; Brown and Journeay, 1987; Parrish et al., 1988; Parkinson, 1992; Bardoux, 1993; Johnson, 1994). The Upper Crustal

Zone contains the hanging wall rocks of both the CR and the OV-ER faults. These rocks generally record older peak metamorphism and cooling (ca. 175 to 135 Ma), and are generally at lower metamorphic grade than the footwall Shuswap complex rocks of the Middle Crustal Zone (Parrish, 1995; Johnson and Brown, 1996). The timing of the last metamorphic overprint and associated deformation of the rocks in the Shuswap complex is shown in Figure 5-2.

The Middle Crustal Zone rocks and the Upper Crustal Zone rocks of the Selkirk Mountains to the east of the Monashee complex, and in part, in the hanging wall of the CR, have been interpreted as an allochthonous, composite thrust sheet, termed the Selkirk allochthon (Read and Brown, 1981). The Selkirk allochthon was interpreted as having been transported over the Monashee complex along the MD (Fig. 5-1; Brown et al., 1986; Journeay, 1986; Brown et al, 1992; McNicoll and Brown, 1995 and references therein). The MD was interpreted as a discrete 1-2 km thick zone of intense strain that separated the Monashee complex from the hanging-wall rocks of the Selkirk allochthon (Brown et al., 1992). The MD was correlated with the basal thrust beneath the Rocky Mountain Foreland belt on the basis of balanced cross-sections (Brown et al., 1986) and LITHOPROBE seismic reflection profiles (Cook et al., 1992), thus correlating middle crustal stain in the hinterland with a system of discrete upper crustal faults in the Foreland (Fig. 5-3).

The existence of the Monashee décollement has been recently questioned by several authors (Williams, 1999; Johnston et al., 2000; Spark, 2001; Kuiper, 2003). These studies suggested that in Thor-Odin dome, the MD is not a narrow shear zone of 1-2 km thick bounding the upper margin of the Monashee complex as interpreted by Brown et al. (1992). Instead, it was suggested that the rocks within Thor-Odin dome showed a penetrative foreland directed deformation characterized by transposition foliation and isoclinal folds throughout a 4-5 km thickness of crystalline rocks with no structural break at the upper boundary of the basement complex (Williams, 1999; Johnston et al., 2000;

Spark, 2001; Kuiper, 2003) leading to the interpretation that the MD does not exist. If the MD is not a discrete zone, or in fact does not exist, models for the tectonic development of the entire region will need to be revised. Recent definitions have defined the MD simply as the boundary between the allochthonous rocks of the Selkirk allochthon and the relatively more autochthonous rocks of the Monashee complex; and that at the latitude of Frenchman cap dome, the lower parts of the Selkirk allochthon structurally above the Monashee complex were deeply buried and mobilized through much of the Cretaceous epoch (Brown and Gibson, in press). For the purpose of this paper, it seems prudent to acknowledge the existence of the MD for Frenchman Cap dome, and to accept the more liberal definition of Brown and Gibson (in press) as the base of the zone of penetrative strain as young as Eocene said to be related to compressional orogenesis. However, results of this study, which indicate differences in the Paleocene-Eocene thermal and deformation history of the two culminations, raise questions such as: a) are Thor-Odin and Frenchman Cap domes part of the same structural level, or rather, do they represent two different domains juxtaposed in the Eocene; b) what is the relationship between Thor-Odin dome and the structurally overlying Middle Crustal Zone rocks; and c) what is the nature of the upper boundary of the Monashee complex in the southern part of Thor-Odin dome, originally mapped as a "disrupted zone" by Reesor and Moore (1971) and a ductile shear zone with a duplex structure by Coleman (1990) and McNicoll and Brown (1995), and correlated with the MD in Frenchman Cap.

## 5.3. Geological overview of Frenchman Cap dome

The rocks of the upper structural levels of Frenchman Cap dome experienced high-grade metamorphism from ca. 80 to 50 Ma; however, a boundary delimiting the base of Eocene Cordilleran deformation has been located at deep structural levels below which Precambrian relationships > 1.8 Ga are preserved (Parrish, 1995; Gibson et al., 1999; Crowley and Parrish, 1999).

### *5.3.1. Precambrian history*

In the Frenchman Cap dome, basement rocks are dominated by locally migmatitic augen granitic orthogneiss and granitic to tonalitic orthogneiss that are overlain by and intercalated with layers of hornblende biotite paragneiss and pelitic to semi-pelitic schist (Wheeler, 1965; Journeay, 1986; Crowley, 1999). Basement orthogneiss range in age from ca. 2.27 to 1.86 Ga (Armstrong et al., 1991; Crowley, 1997). Anatexis in the basement gneiss occurred during the Precambrian, between ca. 2080 and 2044 Ma (Crowley, 1999). In the deepest structural levels of Frenchman Cap there are basement gneisses preserving a ca. 2.06 Ga metamorphism, anatexis, and gneissosity (which is parallel to the Late Cretaceous to Eocene $S_2$ foliation) and is cut by the ca. 1.8 Ga Bourne granite (Crowley, 1999; Crowley and Parrish, 1999; Gervais et al, 2005; Crowley et al., 2005). At deep structural levels, Frenchman Cap was unaffected by Cordilleran deformation and metamorphism (Fig. 5-2).

The cover sequence is 2-3 km thick, laterally extensive and interpreted to be coeval with deposition of the Belt-Purcell and Windermere Supergroups to the east (Wheeler 1965; McMillan, 1973; Journeay, 1986, Gabrielse and Yorath, 1991). The cover sequence contains three fining-upward depositional assemblages referred to as the lower, middle, and upper parts (Journeay, 1986; Crowley, 1997). The lower cover sequence was deposited on basement gneiss between 1.99 and 1.85 Ga, and detrital zircon ages suggest a source from the Alberta basement of the western Canadian Shield (Crowley, 1997). The age of the upper cover sequence may be as young as Middle Devonian based on a single 388 Ma zircon U-Pb age from pyroclastic metavolcanic rocks (Scammell and Parrish, 1993).

### *5.3.2. Late Cretaceous to Eocene Cordilleran tectonic evolution*

In Frenchman Cap dome, there is a strain gradient or lower boundary of Cordilleran deformation below which extends a Cordilleran thermal overprint manifested by Eocene monazite growth and Pb loss in Paleoproterozoic titantites (Crowley, 1999). Frenchman

Cap dome experienced Late Cretaceous to Eocene metamorphism with peak P-T condition of 650-700 °C and ca. 6-8 kbar (Fig. 5-2; Journeay, 1986; Crowley and Parrish, 1999; Crowley et al., 2001). A progressive younging in thermal peak metamorphic ages from 64 to 49 Ma has been documented with increasing structural depth, down to the base of Cordilleran events (Parrish, 1995; Crowley and Parrish, 1999; Gibson et al., 1999). Rocks of the Selkirk allochthon, surrounding Frenchman Cap dome, preserve sillimanite-potassium feldspar-melt assemblages suggesting that they reached higher temperatures during the Late Cretaceous to Eocene than the structurally underlying Frenchman Cap dome rocks, which preserve kyanite-muscovite assemblages (Journeay, 1986; Scammell, 1987; Parrish, 1995; Gibson et al., 1999). The geometry of the isograds corresponds to the overall shape of the dome and the isograds are truncated by the MD (Journeay, 1986).

The following description of folding in Frenchman Cap dome is summarized from Brown (1980), Höy and Brown (1980), Journeay (1986), Scammell (1986), Crowley (1999) and Crowley et al. (2001). At upper structural levels, the basement and cover are dominated by regional, east-verging km-scale isoclinal $F_1$ folds. Syn-metamorphic $F_2$ rootless intrafolial folds are associated with the pervasive $S_2$ axial planar foliation. $F_3$ folds are post-metamorphic, generally northeast-verging and are best developed in the cover sequence, although they are also locally documented in the basement gneisses. The unconformity between basement and cover gneiss in the core of the Frenchman Cap is a simple dome surface that is locally affected by minor post-metamorphic $F_3$ folds.

## 5.4. Geological overview of Thor-Odin dome

Thor-Odin dome rocks preserve Late Cretaceous to Eocene penetrative deformation, metamorphism and anatexis that pervasively overprinted any Precambrian metamorphism or deformation (see below).

### *5.4.1. Precambrian geological history*

The basement rocks of Thor-Odin dome are composed of heterogeneous migmatitic para- and orthogneiss. Basement orthogneiss are dominated by migmatitic, hornblende-biotite-quartzo feldspathic gneiss with a lesser volume of quartz monzonite gneiss. Basement paragneiss comprise: a) heterogeneous, migmatitic, garnet-sillimanite-quartzo feldspathic gneiss that are locally rich in cordierite, b) migmatitic cordierite-biotite-quartzo feldspathic gneiss, and c) minor calc-silicates, marbles, and quartzites, and are associated with minor cordierite-gedrite rocks and garnet amphibolites (Reesor and Moore, 1971; Duncan, 1984). The cordierite-gedrite rocks are interpreted as mafic volcanics that experience hydrothermal alteration prior to metamorphism (Hinchey, Chapter 4). Though lithologically distinct, the basement ortho- and paragneiss are often interlayered at the scale of a few meters, due in large part to transposition by folding, and have contacts that are complicated by the abundance of leucosome. U/Pb geochronology studies of zircons from basement orthogneiss yielded crystallization ages of 1934 ± 6 and 1874 ± 21 Ma (Parkinson, 1992). Based on the detrital zircon studies, deposition of the basement supracrustal sequence likely began by ca. 2.2 Ga and continued to at least ca. 1.8 Ga (Parkinson, 1992; Vanderhaeghe et al., 1999; Kuiper, 2003; Hinchey, Chapter 1).

The cover sequence is a heterogeneous assemblage of metasedimentary rocks that includes quartzites, pelitic schists, marbles, calc-silicates and amphibolites (Reesor and Moore, 1971). A preliminary geochronology detrital zircon study on the basal quartzite of the cover gneiss yielded ages as young as 1825 ± 5 Ma (Kuiper, 2003). There is no documented angular unconformity beneath the cover sequence, but the occurrence of a basal quartzite in contact with basement gneisses has been interpreted as an erosional unconformity by Duncan (1982) and Parkinson (1992). However, the contact may also be tectonic or it may be that there are cover rocks beneath the quartzite marker that are unrecognized as of yet.

### *5.4.2. Late Cretaceous to Eocene Cordilleran tectonic evolution*

Basement and cover rocks experienced metamorphism of upper amphibolite to lower granulite facies conditions during the Late Cretaceous to Eocene Cordilleran orogeny (Fig. 5-2). Throughout the dome the mineral assemblages are relatively uniform, with stable sillimanite-potassium feldspar-melt assemblages (Reesor and Moore, 1971). Kyanite and cordierite occur in aluminous basement gneiss and orthopyroxene occurs in granitic and aluminum-poor basement gneiss (Reesor and Moore, 1971). U-Pb geochronology studies indicate that metamorphism and penetrative deformation of Thor-Odin dome basement rocks occurred during the Paleogene from ca. 56 to 52 Ma (Vanderhaeghe et al., 1999; Johnston et al., 2000; Kuiper, 2003; Hinchey, Chapter 1 and 4). Anatexis is pervasive throughout the basement of Thor-Odin dome and studies from a range of 4 kilometers of structural depth within the basement rocks all record a ca. 56 to 52 Ma anatectic event (Vanderhaeghe et al., 1999; Kuiper, 2003; Hinchey, Chapter 1).

On the northwestern margin of Thor-Odin dome, basement paragneiss experienced temperatures of ca. 725 °C (Johnston, 1997). Pressure-temperature studies in structurally deeper rocks from the southwestern part of the dome indicate that the basement rocks underwent near isothermal decompression from the kyanite-potassium feldspar zone ($P > 8$ to 10 kbar) into the sillimanite-cordierite zone ($P < 5$ kbar) at $T \sim 750$ °C, with a maximum temperature of ~ 800 °C (Norlander et al., 2002). Peak P-T conditions constrain depth of burial of Thor-Odin dome to 26-33 km (Fig. 5-4). Based on complex symplectic textures preserved in basement cordierite-gedrite rocks and amphibolite boudins, Norlander et al. (2002) concluded that the peak regional metamorphic episode occurred in the Tertiary, as the observed textures would not have survived a subsequent metamorphic event. This is consistent with U-Pb geochronology studies that indicate that anatexis, metamorphism and penetrative deformation of the basement rocks occurred during the Paleogene (Fig. 5-4; Vanderhaeghe et al., 1999; Hinchey, Chapter 1 and 4).

Basement and cover gneiss are characterized by at least four folding events with

the map-pattern distribution of these rocks controlled by large-scale fold interference patterns. These superposed folds produced interference patterns at all scales and all structural levels, and have been interpreted as the principal cause of doming and thickening of Thor-Odin dome exposing ~7 km thickness of rock (Read, 1980; Duncan, 1982). The dominant foliation dips to the west on the western margin of the dome and to the east on the eastern margin, and it wraps around the southern end producing outward dips (Reesor and Moore, 1971). The transposition foliation, which parallels $F_2$ isoclinal folds, is defined by the alignment of sillimanite, hornblende, and biotite in basement gneisses and at least part of the foliation development is syn-peak metamorphic. Some of the leucosome, ca. 56 Ma, was folded by $F_2$, $F_3$ and $F_4$ structures and contains a weak biotite foliation that is parallel to the transposition fabric; while other leucosome, ca. 55 to 52 Ma, crosscut $F_2$ folds and transposition foliation (Hinchey, Chapter 1). Melt may have been produced by several melt generating reactions as shown on Fig. 5-4 and including: Ms + Pl + Qtz = Bt + Kfs + Sil + melt; Bt + Ab + Sil + Qtz = Grt + Kfs + melt; and Bt + Sil = Grt + Crd + melt (Spear et al., 1999; Norlander et al., 2002). The presence of cordierite, millimeter-scale garnets and minor sillimanite, less than 1%, in the host gneiss support the involvement of these minerals in the melt-producing reactions. Metamorphic thermal peak accompanied folding, transposition and the onset of anatexis in Thor-Odin dome.

Anatexis in the basement continued after compressional tectonics changed to an extensional regime (Hinchey, Chapter 1) with the activation of faults such as the CR (Parrish et al., 1988). The onset of extension at higher structural levels is documented in the basement gneiss by the reactivation of foliation and the local development of shear bands ($D_5$), as the rocks were still hot and behaving ductilely at depth (Carr, 1992; Johnston et al., 2000; McNeill and Williams; 2003). As the basement rocks cooled, extension was manifested as late steep brittle faulting ($D_6$) such the Three Valley normal fault (Johnson, 1994; Johnston, 1997) and Victor Creek fault (Read, 1980; Kruse and

Williams, 2004).

Figure 5-5 summarizes the structural evolution, timing constraints and metamorphic mineral assemblages for Thor-Odin dome. The timing of onset of $F_2$ folding and prograde metamorphism in Thor-Odin dome is uncertain. However, in the immediately overlying rocks of the Middle Crustal Zone and on the north flank of Thor-Odin dome near Three Valley Gap, deformation and prograde metamorphism were ongoing in the Late Cretaceous; allowing the suggestion that similar conditions were likely ongoing in Thor-Odin dome rocks as well (Fig. 5-2; Carr, 1991; Parrish, 1995; Johnson, 1997; Kuiper, 2003). Prograde metamorphism likely began by ca. 75 Ma due to thickening of the crust, and the rocks were at thermal peak by ca. 56 Ma (Fig. 5-4). $F_2$ folds would have been forming by this time, based on the occurrence of $F_2$ folded leucosome (Hinchey, Chapter 1). The $F_2$ folding and associated metamorphism was synchronous with the final stages of compression in the Foreland belt. Movement on late thrust faults in the Foreland, specifically in the Foothills, continued to ca. 53 Ma (van der Pluijm et al. 2001a and 2001b). If Eocene strain in Thor-Odin dome was related to the Foreland displacement then it is likely linked via a detachment or high strain zone that passed underneath the rocks of the Selkirk and Purcell Mountains to the east, since they were not deformed at this time (Fig. 5-2). The $F_3$ folding had finished by ca. 52 Ma, based on crosscutting leucosome (Hinchey, Chapter 1 and 4).

Thor-Odin dome underwent near isothermal decompression, which ended by ca. 52 Ma (Fig. 5-4). $F_4$ may be the last stage of compressional folding or may represent folding in an extensional environment (see Harris et al., 2002). Decompression was synchronous with continued leucosome generation via biotite dehydration reactions (Fig. 5-4) and resulted in the preservation of symplectitic textures in mafic basement gneisses (Norlander et al., 2001; Hinchey et al., 2004). Isothermal decompression of Thor-Odin dome from ~750 °C to 300 °C (Norlander et al., 2002) was synchronous with, and likely caused by, the onset of extension in the southern Omineca belt. Movement along the CR

and OV-ER faults was synchronous with the ca. 52 to 45 Ma cooling of the basement rocks in Thor-Odin dome (Parkinson, 1991; Lorencak et al., 2001; Vanderhaeghe et al., 2003). The end of decompression was followed by near isobaric cooling from 300 °C to 150 °C at ca. 52 to 48 Ma as determined from zircon and monazite U-Pb ages, Ar thermochronology studies, and fission track zircon and apatite ages (Parkinson, 1992; Lorencak et al., 2001; Vanderhaeghe et al., 2003). The final stages cooling and decompression continued to ca. 45 Ma (Lorencak et al., 2001; Vanderhaeghe et al., 2003).

## 5.5. Geological setting of rocks surrounding Thor-Odin dome

East of Thor-Odin dome, rocks of the Upper Crustal Zone are mainly exposed to the east of the Columbia River fault (CR) in the Selkirk Mountains and Kootenay Arc (Fig. 5-1 and 5-3). The rocks east of the CR comprise Proterozoic to Mesozoic pericratonic and platformal sequences of North America. Metamorphism, generally at lower greenschist facies conditions, and compressional deformation primarily occurred in the Middle Jurassic and rocks preserve a Late Jurassic to Cretaceous cooling history (Carr, 1991; Greenwood et al., 1991). Rocks of this zone were intruded by Middle Jurassic plutons, such as the Kuskanax batholith and Galena Bay pluton (Carr, 1991; Parrish and Armstrong, 1987).

The Middle Crustal Zone, surrounding Thor-Odin dome on the southern and western margins, contains pericratonic, platformal sequence and Quesnel supracrustal rocks (Read and Brown, 1981; Carr, 1991; 1992; Johnson, 1994). Rocks of the Middle Crustal Zone lie in the footwall of the CR, are structurally above the belt of penetrative Late-Cretaceous to Paleocene deformation that affected Thor-Odin dome, and were juxtaposed with Thor-Odin dome in the Eocene. Lithologically, the Middle Crustal Zone dominantly contains paragneiss, sillimanite-bearing metapelite, amphibolite, and marble that were extensively intruded by sheets and pegmatites of the Ladybird granite suite (Read and Brown, 1981; Carr, 1991; 1992; Johnson, 1994; Coleman, 1990). The rocks are generally

polydeformed and contain medium- to high-grade metamorphism with grade generally increasing with structural depth (Carr, 1991). Timing constraints on metamorphism and deformation indicate that a penetrative Late Cretaceous event was superimposed on a complex Mesozoic history of terrane accretion, folding, faulting and metamorphism (Carr, 1991).

The structural style of Middle Crustal Zone rocks, south of Thor-Odin dome, is that of two generations of coaxial folds superimposed on a penetrative foliation with kilometer scale $F_3$ folds controlling the map pattern (Carr, 1991). Evidence that this deformation and thermal history is Late Cretaceous includes the deformed nature of the 77 Ma Whatshan batholith, south of the Pinnacles Peaks, and cross cutting contacts of post tectonic ca. 62–52 Ma stocks and plutons of the Ladybird granite suite (Carr 1995). This is consistent with the ca. 73 and 70 Ma ages of granitoids that bracket the timing of $F_3$ structures on Joss Mountain located to the west of Thor-Odin (Johnston et al., 2001; Kuiper, 2003). Thus rocks that structurally overly Thor-Odin dome, preserve a ca. 10 to 20 m.y. older deformation and thermal history relative to the dome.

The boundary between Thor-Odin dome and Middle Crustal Zone rocks, well exposed at Cariboo Alp on the southwest corner of the dome (Fig. 5-1), was extrapolated to extend northward on the west flank of Thor-Odin dome and was interpreted to be the continuation of the MD (Coleman, 1990; McNicoll and Brown, 1995). The boundary zone at Cariboo Alp is interpreted as an imbricated, crustal-scale, compressional shear zone active at sillimanite-potassium feldspar-melt assemblages (McNicoll and Brown, 1995). The shear zone culminated with syn-metamorphic $F_2$ folding, and final thrust movement occurred in the latest Paleocene with the associated shear zone having stopped moving by ca. 58 Ma (Carr, 1992; McNicoll and Brown, 1995). Deformation at Cariboo Alp is 2-4 m.y. older than that of the basement rocks of Thor-Odin dome. In addition, the Middle Crustal Zone preserves $F_3$ folds that control the distribution of units and preserves less penetrative strain, when compared to Thor-Odin dome rocks where $F_2$ folds control

the distribution of units. The marked break in timing and difference in deformation between rocks in the Middle Crustal Zone and those of Thor-Odin dome supports the existence of a boundary between the rocks of the Middle Crustal Zone and those of Thor-Odin dome.

At the latitude of Thor-Odin dome, rocks of the Middle Crustal Zone record deformation that is up to 20 m.y. older than that of Thor-Odin dome, and the boundary between the two at Cariboo Alp deformation is 2-4 m.y. older than Thor-Odin dome. This implies that there were either: a) two deformation events or shear zones at different structural levels; or, b) one progressive event. In the first alternative, one period of deformation and metamorphism was Late Cretaceous in age and affected the Middle Crustal Zone, including the Joss Mountain to Pinnacles area; and the second event was a structurally deeper and younger shear zone of Paleocene to Eocene age that affected the lower panel of rocks in Thor-Odin dome and Cariboo Alp. The second alternative is that there was one event in both the Middle Crustal Zone and Thor-Odin dome, and that strain at lower structural levels either: a) progressed downwards from Middle Crustal Zone to Thor-Odin dome basement; or, b) the Middle Crustal Zone was deactivated and the shear zone in Thor-Odin dome basement outlasted that of deformation in the Middle Crustal Zone.

## 5.6. Comparison of Frenchman Cap and Thor-Odin domes

Although there are similarities between Frenchman Cap and Thor-Odin domes, the following is a discussion of the significant differences. Lithologically, the basement rocks of Thor-Odin dome are dominantly paragneiss with lesser orthogneiss; whereas, basement rocks of Frenchman Cap dome contain more abundant orthogneiss. In addition, Thor-Odin dome basement gneiss contains distinctive cordierite-gedrite rocks, the metamorphosed equivalents of altered mafic rocks (Hinchey, Chapter 3) that are unrecognized in Frenchman Cap dome. In Thor-Odin dome, basement paragneiss were being deposited from at least ca. 2.2 Ga and continued to ca. 1.8 Ga (Vanderhaeghe et al.,

1999; Kuiper, 2003; Hinchey, Chapter 1), whereas in Frenchman Cap deposition started before ca. 2.27 and ceased by ca. 1.99 Ga (Armstrong et al., 1991; Crowley, 1997). The cover sequences of both Frenchman Cap and Thor-Odin domes are lithologically similar and have been correlated based on the preservation of a basal quartzite in both domes (Scammell and Brown, 1990). However, Frenchman Cap dome preserves three upward-fining depositional assemblages, whereas in Thor-Odin dome the cover is characterized by one quartzite unit and three sequences have not been recognized. The cover sequence of Thor-Odin dome is younger than ca. 1.8 Ga (Vanderhaeghe et al., 1999; Kuiper, 2003; Hinchey, Chapter 1), whereas in Frenchman Cap dome deposition is as old as ca. 1.99 Ga and continuing to as young as ca. 388 Ma (Scammell and Parrish, 1993; Crowley, 1997). Although the rocks are so transposed that primary sedimentary and volcanic features may not be preserved and the cover sequence of Thor-Odin dome has not been extensively studied, it is possible that the Thor-Odin dome cover sequence could be different from that of Frenchman Cap. These lithological and timing differences suggest that Thor-Odin dome may have a different Precambrian history than Frenchman Cap dome.

In Thor-Odin dome, Precambrian deformation and metamorphism was pervasively overprinted by the Late Cretaceous to Paleocene stages of the Cordilleran orogeny. However, in the deepest structural levels of Frenchman Cap dome there are basement gneisses that were not affected by Late-Cretaceous to Eocene Cordilleran deformation and metamorphism and there is a thermal and deformation front below which Precambrian relationships >1.8 Ga are preserved (Crowley, 1999; Crowley and Parrish, 1999; Gervais et al, 2005; Crowley et al., 2005). In contrast, the core of Thor-Odin dome preserves stable sillimanite-potassium feldspar-melt assemblages and cordierite overgrowths with Late Cretaceous – Eocene peak conditions of 750-800 °C and 8-10 kbar, and is of a higher metamorphic grade relative to that of Frenchman Cap dome which has stable assemblages of sillimanite-garnet-muscovite-melt and peak conditions of 650-700 °C and ca. 6-8 kbar (Reesor and Moore, 1970; Journeay, 1986; Crowley and

Parrish, 1999; Norlander et al., 2002). Differences in peak P-T suggests that Thor-Odin dome was up to 6 km deeper, and 50-100 °C hotter than Frenchman Cap dome, during the Late Cretaceous to Eocene Cordilleran orogenesis.

The onset of prograde metamorphism in the two domes may have overlapped in time. In Thor-Odin dome, peak metamorphism culminated with the onset of anatexis ca. 56 Ma with no diachroneity in the timing of thermal peak documented with structural depth. In contrast, in Frenchman Cap dome peak metamorphism was diachronous and synchronous with $D_2$ deformation and foliation formation, with higher structural levels having experienced metamorphism and deformation by ca. 64 Ma, while in the deeper rocks this occurred from ca. 52-49 Ma (Crowley et al., 2001). The basement rocks of Thor-Odin dome underwent isothermal decompression until ca. 52 Ma (Hinchey, Chapter 1), while Frenchman Cap dome was still being ductilely deformed by $F_2$ folding from ca. 52 Ma to 49 Ma (Crowley et al., 2001).

The structural style of both domes is similar in that both preserve kilometre-scale recumbent isoclines that infold basement gneiss with the cover sequence and control map patterns (termed $F_1$ in Frenchman Cap dome and $F_2$ in Thor-Odin dome). A noteworthy difference is in the vergence of these large folds, in Frenchman Cap dome the large-scale folds verge to the east (Scammell, 1987; Crowley, 2001). In Thor-Odin dome, the fold vergence is variable due to rotation, but $F_2$ folds generally have the same north-northeasterly vergence as the $F_3$ folds (McNeill and Williams, 2004; Williams and Jiang, in press).

On the basis of protolith of basement and cover lithology, and Late Cretaceous to Eocene Cordilleran thermo-tectonic history and deformation, there are significant differences between Thor-Odin and Frenchman Cap domes and it is permissible for the domes to represent two difference basement domains. Since at ca. 56 to 52 Ma Thor-Odin dome was likely deeper than Frenchman Cap dome, and was above the base of "Cordilleran deformation" while Frenchman Cap dome straddled the boundary,

the domes were likely at two different structural levels. In addition, the $F_2$ ($F_3$) Thor-Odin dome fold vergence is consistent with emplacement of Thor-Odin dome against Frenchman Cap dome. For these reasons, it is possible that Thor-Odin may represent a different basement level that was emplaced against Frenchman Cap dome in the Paleogene. Alternatively, Thor-Odin dome may have been exhumed from deeper levels, by more displacement/exhumation along Eocene faults, in the south than in the north.

In light of the difference between Thor-Odin dome and Frenchman Cap dome, the MD exposed at Cariboo Alp may represent a different shear zone or different structural level than the MD exposed on the western edge of Frenchman Cap dome. If there is a shear zone, such as the MD, in Thor-Odin dome and also in Frenchman Cap dome forming the upper boundary of the basement complex, it cannot be the same structure in both domes. If the MD in Frenchman Cap dome is really a basal décollement, then it must pass beneath Thor-Odin dome (Fig. 5-6). Alternatively, the MD may represent a thicker, high strain zone throughout Thor-Odin dome and may separate older deformation and metamorphism at higher structural levels of the Middle Crustal Zone from lower levels beneath the dome.

## 5.7. Proposed model for the tectonic evolution of the Thor-Odin dome area

A tectonic model for the evolution of the Thor-Odin dome area must account for: a) older deformation, anatexis and metamorphism preserved at higher structural levels of the Middle Crustal Zone; b) highly strained rocks, up to ~7 km in thickness, preserved in the lower structural levels of Thor-Odin dome; and, c) cold basement rocks uninvolved in the Cordilleran orogeny preserved in Frenchman Cap dome. The proposed tectonic model for this area suggests that Thor-Odin dome is part of a ductile shear zone.

In order to explain the differences in timing of deformation, style of deformation, metamorphism, and anatexis between the higher structural level of Middle Crustal Zone rocks and the lower structural level of Thor-Odin dome, at the same latitude, there were either: a) two shear zones at different structural levels; or, b) one progressive event. In (a)

a Late Cretaceous period of deformation and metamorphism affected the Middle Crustal Zone, and was followed by a second high-strain event at structurally deeper and younger shear zone of Paleocene to Eocene age that affected the lower panel of rocks in Thor-Odin dome. In (b) one shear zone that affected both the Middle Crustal Zone and Thor-Odin dome, and that strain at lower structural levels either: i) progressed downwards from Middle Crustal Zone to Thor-Odin dome basement; or, ii) the Middle Crustal Zone was deactivated and the shear zone in Thor-Odin dome basement outlasted that of deformation in the Middle Crustal Zone. If Thor-Odin dome is part of a ductile shear zone(s), this would explain the preservation of the transposition foliation ($S_2$), isoclinal $F_2$ folding and strain through a thick section of basement rocks. The occurrence of basement rocks in Frenchman Cap dome that were not affected by the Cordilleran orogeny can be explained by the rocks of Thor-Odin dome being emplaced against Frenchman Cap dome late in the Paleogene evolution of the dome by either $F_2$ folding, or possibly along a lateral ramp. In this manor, Thor-Odin dome may represent a different basement slice than Frenchman Cap dome, thus explaining the differences in Precambrian evolution and in Late Cretaceous-Eocene Cordilleran orogenesis.

## 5.8. Evaluation of alternative tectonic models for Thor-Odin dome

Numerous tectonic models that have been proposed for the region and the limitations of these models are discussed below. Models for the tectonic development of Thor-Odin dome can generally be classified into five major types and will be discussed as such: a) the crustal boudinage model (Monger and Price; 2000); b) orogenic wedge models (Brown et al., 1992; Parrish, 1995; Gibson et al., 1999; Crowley and Parrish, 1999; Crowley et al., 2001; Brown, 2003); c) domal culmination models, with or without diapirism (Vanderhaeghe et al., 1999; Norlander et al., 2002; Fayon et al., 2004; Whitney et al., 2004); d) channel flow models, which include versions of crustal-scale deformation (Williams, 1999; Kuiper, 2003), local development (Brown and Gibson, in press), extrusion (Johnston et al., 2001), and rolling-hinge detachment (Teyssier et al.,

in review); and, e) ductile shear zone(s) (Gibson, 2003; Carr and Simony, in review; this study)

Models that interpret Thor-Odin dome as a crustal boudin suggested that regional Eocene extension taken up by extensional faults at surface was balanced by ductile stretching of the lower crust, thereby forming boudins of basement representing major structural culminations (Monger and Price, 2000). Prior to extension, the North American basement rocks were uninvolved in shortening the Foreland belt, all shortening was accommodated in the detached supracrustal rocks thus suggesting a passive relationship between the basement and cover gneisses (Monger and Price, 2000). In this model, the implication is that Thor-Odin dome represents a ~ 45 km thick boudin of North American basement that is autochthonous and was not involved in the Cordilleran orogeny. However, in Thor-Odin dome the supracrustal cover gneiss were infolded with basement gneiss and this package was deformed into isoclinal folds during peak P-T conditions of the Late Cretaceous to Eocene Cordilleran orogeny, prior to the onset of extension, and therefore were not detached from basement rocks (Norlander et al., 2001; McNeill and Williams, 2004; Hinchey, Chapter 1 and 4). As such, a model with Thor-Odin dome representing a passive, crustal boudin is not supported by the deformation, anatexis and thermal data from the dome.

Orogenic wedge models have been suggested for formation of Frenchman Cap dome and have been inferred to include Thor-Odin dome. Models for Frenchman Cap dome have been modified over the years, but generally invoke ductile material overriding a cold, stiff basement that was only mildly affected by the Cordilleran events (Brown et al., 1992; Parrish, 1995; Gibson et al., 1999; Crowley and Parrish, 1999; Crowley et al., 2001; Brown, 2003). In a recent version of the model proposed by Brown (2003), supracrustal rocks were continuously underplated by folding, thrusting, and duplex formation. It was not until the Eocene that basement rocks of the Monashee complex were overridden by the advancing wedge along the MD. These models invoke: a)

uninvolved Precambrian basement rocks, b) a Cordilleran deformation boundary and c) accommodation of Cordilleran deformation within the near-basement shear zone of the MD (Brown et al., 1992; Parrish, 1995; Gibson et al., 1999; Crowley and Parrish, 1999; Crowley et al., 2001; Brown, 2003). These models do not adequately explain the data from Thor-Odin dome. In Thor-Odin dome, a strain gradient is not preserved. Strain was penetrative and intense through a ~7 km thick section of rocks pervasively overprinting and involving North American basement rocks. In addition, the deepest exposed structural levels in Thor-Odin dome preserve strain that outlasted that of higher structural levels of the Middle Crustal Zone. These observations are incompatible with orogenic wedge models that require a cold, stiff basement to achieve critical taper.

In domal culmination models, doming of Thor-Odin rocks has been explain by invoking extensional faulting or detachments at the surface which resulted in the formation of a dome of partially melted mid-crustal rocks (Vanderhaeghe et al., 1999; Whitney et al., 2004). In diapiric domal culmination, the dome was aided by diapiric assent of material from the mid-to lower crust resulting in decompression of the migmatitic rocks and leucosome crystallization (Norlander et al., 2002; Fayon et al., 2004). These models discount large-scale folding as the mechanism for creating Thor-Odin dome, and attribute creation of the dome via vertical thinning of the crust and buoyant upwelling of partially molten rocks (Vanderhaeghe et al., 1999; Norlander et al., 2002; Fayon et al., 2004). This mechanism to create Thor-Odin is inconsistent with the structural evolution of Thor-Odin dome, which documents km-scale isoclinal ($F_2$) folds infolding basement and cover, which are associated with the main transposition foliation ($S_2$) and $F_2$ folded leucosome (McNeill and Williams, 2003; Williams and Jiang, 2004; McNeill and Williams, 2005; Hinchey, Chapter 1). The occurrence of $F_2$ folded leucosome throughout Thor-Odin dome indicates that compressional tectonics was synchronous with melting, and that only small melt volumes were present at any one time, such that the rocks were still behaving as a composite unit. The geometry of

the Thor-Odin dome is controlled by polyphase folding and the orientation of folded lineations are inconsistent with models of diapirism (Read, 1980; Duncan, 1982; McNeill and Williams, 2003). These observations are incompatible with models of domal culmination in which the lower to middle crust must be partially molten and buoyantly rising via upwelling. In addition, these models cannot explain the timing and pattern of older deformation, metamorphism and anatexis at higher structural levels of the Middle Crustal Zone (Fig. 5-2). The domal culmination models require synchronous partially molten rocks in both the Middle Crustal Zone and Thor-Odin dome prior to the onset of extension. For the reasons outlined above, models of domal culmination are inadequate to explain the structural, anatectic, deformation and thermal history documented in the rocks of Thor-Odin dome.

Models for channel flow, are varied but generally require horizontal flow of the mid- to lower crust in a crustal scale shear zone localized as a channel with a decoupling of the lid (or upper crust) and lower crust (or mantle) from the channel (Williams, 1999; Beaumont et al., 2001; Johnston et al., 2001; Kuiper, 2003; Brown and Gibson, in press; Teyssier et al., in review). The various proposed versions of the channel flow model have different criteria but all require a ductile middle to lower crust.

In Frenchman Cap dome, basement rocks were not extensively deformed during the Cordilleran orogen (Crowley and Parrish, 1999; Crowley et al., 2001; Crowley et al., 2005; Gervais et al., 2005), suggesting that cold basement rocks underlie at least part of the Shuswap complex. This cold basement coupled with the preservation at higher structural levels (Middle Crustal Zone) of older deformation, metamorphism and anatexis is inconsistent with a regional channel that required a ductile middle to lower crust underlying the entire Shuswap complex (Williams, 1999; Johnston et al., 2001; Teyssier et al., in review). To accommodate the cold basement rocks in Frenchman Cap dome, Brown and Gibson (in press) have suggested a model of channel flow that interprets: a) the base of the channel as the MD; b) the channel to include part of the Selkirk

Allochthon or Middle Crustal zone, and c) top of the channel as the OV-ER fault system. Thus basement rocks of Frenchman Cap dome would lie below the channel. The base of the channel is interpreted to lie exposed in the upper structural levels of Frenchman Cap dome, but it has yet to be identified and neither has the expected reversal of fold vergence within the proposed channel. The channel proposed in this model cannot be projected southward above the Monashee complex given the young penetrative deformation within the basement rocks of Thor-Odin dome. In addition, the Brown and Gibson (in press) model proposes that the Selkirk fan is cut by the channel, and that most of the fan structure including the fan vergence reversal lies above the top of the channel. This is inconsistent with models put forth for the formation of the Selkirk fan above a subduction zone and transportation of the fan eastward (Gibson, 2003). If a channel cuts the Selkirk fan than the parts of fan that lie above the channel should have been dissected from the parts of the fan that lie within the channel.

If Thor-Odin dome is part of a regional channel, as proposed by Williams (1999) and Johnston et al. (2001), then the channel must be moving at ca. 55 Ma, to explain the timing of events in Thor-Odin dome. In models where the channel was long-lived and active from the Jurassic or Early Cretaceous to Tertiary, it is difficult to explain the geometry of Middle Jurassic to Late Cretaceous structures preserved at structural levels, that are now higher than Thor-Odin dome and documented throughout the southern Omineca belt, which record regional-scale recumbent nappes that formed early in the history of the hinterland, a change in vergence in the Middle Jurassic from west verging to generally northeast verging structures, changes in structural style through time and the diachronous superposition of deformation and metamorphism imposed on large-scale structures throughout a >100 m.y time period (see Fig. 5-2). This is more protracted than what has been considered thus far in channel flow models with channels that are generally $\leq$ 75 Ma (Beaumont et al., 2001). In addition, there is no evidence of melting

or high strain deformation in the Thor-Odin dome prior to the Paleocene (Vanderhaeghe et al., 1999; Hinchey, Chapter 1 and 4). Models with extrusion of a channel typically model the extruding zone as moving towards the subducting plate (prowedge) side of the orogen (Beaumont et al., 2001), whereas the model of Johnson et al. (2001) requires extrusion towards the retrowedge side (towards the Foreland belt).

The rolling-hinge detachment model of Teyssier et al. (in review) suggests that a channel develops in the hinterland, which evolves into a rolling-hinge detachment due to extension and is governed by the interface between the cold foreland and hot hinterland. In this model the activation of a rolling-hinge detachment drives rapid decompression and melting, resulting in the diapiric rise of a migmatite domes in the footwall of the detachment. The rolling-hinge detachment model of Teyssier et al. (in review) is unlikely for many of the same reasons as those presented against channel flow, including the preservation of cold basement rocks in Frenchman Cap dome. In addition, deformation and metamorphism of the Middle Crustal Zone records older ages > 70 Ma of anatexis, metamorphism and deformation while Thor-Odin dome basement preserves younger ages of ca. 56 Ma (see Fig. 5-2); this is inconsistent with this model which requires a partially molten crust in both the Middle Crustal Zone and Thor-Odin forming a rolling-hinge detachment in the Eocene. Models of channel flow and a rolling hinge detachment in the middle to lower crust of the Shuswap complex can not easily explain: a) the preservation of cold basement rocks in Frenchman Cap, and b) older deformation, anatexis and metamorphism in the Middle Crustal Zone relative to younger events in Thor-Odin dome.

Models of a ductile shear zone, such as those proposed for Valhalla complex and Frenchman Cap (Gibson, 2003; Carr and Simony, in review) can explain the data of Thor-Odin dome and the preservation of older anatexis, deformation and metamorphism in the Middle Crustal Zone. Valhalla complex is interpreted as a ductile crystalline nappe that was being deformed from 80-60 Ma where Cretaceous strain at depth is imposed on Jurassic events preserved at higher structural levels (Carr and Simony, in review). The

preservation of a thick section of rocks with strain at the base is likely analogous with Middle Crustal zone rocks on the southern flank of Thor-Odin dome to Pinnacles area. The implications of Thor-Odin dome being part of a ductile shear is presented above (see section 5.7).

## 5.9. Conclusions

The favoured model for development of Thor-Odin dome is as follows (Fig. 5-6). During the Mesozoic to Paleocene Cordilleran orogen, the crust was thickened resulting in the internal deformation, crustal thickening and regional metamorphism of the Omineca Belt hinterland, including burial of the rocks of Thor- Odin dome, and formation of the structures of the Rocky Mountain fold and thrust belt. Rocks of Thor-Odin dome were penetratively deformed as the orogen underwent shortening driven by far-field stresses at the plate boundaries. The restored location of Thor-Odin dome during the Early Cretaceous is unknown and there is no direct evidence of Late Jurassic or Early Cretaceous events in these rocks; as a result the timing of the onset of prograde metamorphism and onset of penetrative deformation in the rocks of Thor-Odin dome is uncertain. It is likely that the rocks were metamorphosed and deformed by ca. 75 Ma on the basis of the age of deformation and metamorphism in immediately structurally overlying rocks in the Middle Crustal Zone and near Three Valley gap on the north flank of Thor-Odin dome (Parish, 1995; Kuiper, 2003); however, it is clear that peak metamorphic conditions of 800 °C and 8-10 kbar, anatexis and penetrative deformation had occurred by ca. 56 Ma (Hinchey, Chapter 1 and 4). Paleogene deformation in Thor-Odin dome is interpreted to have accommodated shortening in the orogen and is synchronous with the youngest deformation in the Foreland belt, suggesting that deformation and shortening in the hinterland and the Foreland is somehow linked. Decompression melting had begun in the Eocene and had ended by 52 Ma, synchronous with exhumation of the rocks via regional extension and erosion.

The most probable tectonic model invokes a ductile shear zone(s) to explain the

diachronous timing of the end of deformation, metamorphism and anatexis in the Middle Crustal Zone and Thor-Odin dome. This model includes, either: a) two distinct ductile shear zones, one in the Late Cretaceous affecting the higher structural panel of the Middle Crustal zone followed by a localized zone of Paleocene-Eocene of high strain affecting the lower structural panel of Thor-Odin dome; or, b) one diachronous strain zone that either migrated progressively downward and/or forward or a zone of strain where deformation at lower structural levels of Thor-Odin dome outlasted that of higher structural levels of the Middle Crustal Zone. In either case, Late Cretaceous - Eocene deformation would have followed a period of progressive loading, thickening and heating of the crust and accommodated translation of the hinterland of the orogen during shortening. The onset of Eocene extension and decompression melting in the Middle Eocene helped facilitate the exhumation and cooling of the dome.

**Figure 5-1.** (a) Map highlights the five morphogeological belts of the Cordillera from Wheeler and McFeely (1991). (b) Tectonic assemblage map of the southeastern Canadian Cordillera (modified after Wheeler and McFeely, 1991; Carr, 1991, and Johnson, 1994). Shuswap complex was defined by Brown and Carr (1990), and is largely bounded by Eocene normal faults, including Okanagan Valley – Eagle River fault system (OV-ER), Columbia River Fault (CR), Greenwood Fault (GW), and Slocan Lake-Champion Lake (SL) fault systems. SRMT = southern Rocky Mountain Trench, M = Malton complex, MD = Monashee décollement, FC = Frenchman Cap dome, TO = Thor-Odin dome, MC = Monashee complex, V = Valhalla complex, TVG = Three Valley Gap, JM = Joss Mountain, CA = Cariboo Alp.

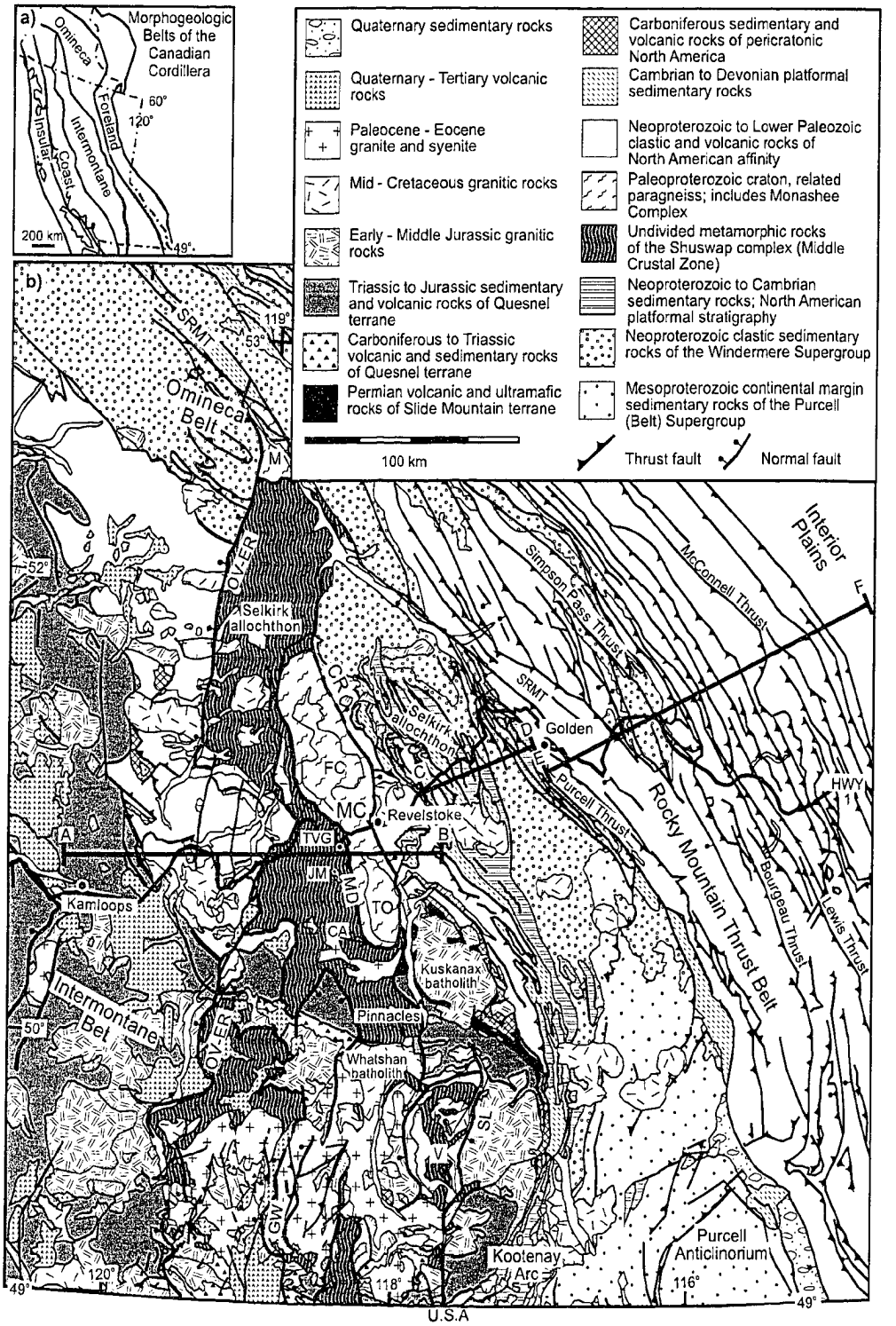

**Timing of metamorphism, anatexis and deformation in the southern Omineca belt**

<60 Ma Paleogene metamorphic overprint

A Metamorphism, deformation and high-strain shearing of MD ongoing at 62 and 59 Ma, and ceased by 58 Ma (Carr, 1992)

B Metamorphic zircon growth at 59 Ma (Parrish and Scammell, 1988)

C Metamorphic zircon growth at 52 Ma (Parrish, 1995)

D Metamorphic zircon growth at 57-55 Ma (Parrish, 1995)
Pegmatite crystallization at 58 Ma (Parrish, 1995)

E Metamorphic monazite/titanite at 64 (highest structural level) to 50 Ma (lower structural level) in the cover sequence (Crowley and Parrish, 1999)
Deformation part of $D_2$ ($F_2$) - on going at 58 Ma and ceased by 55 Ma (Crowley et al., 2001)

F Metamorphic (sil-ky-kfs assemblage) monazite and titanite growth 52 to 49 Ma at deepest structural levels (Crowley and Parrish, 1999)
Deformation part of $D_2$($F_2$)<52 Ma, ceased by 49 Ma at deepest structural levels (Crowley et al., 2001)

G Metamorphic (sil-kfs-melt assemblage) monazite growth 56-52 Ma (Hinchey, Chapter 4)
Anatexis in basement gneiss 56-52 Ma, zircon ages(Hinchey, Chapter 1)
Deformation part of $D_2$($F_2$) on going at 56 ceased by 55 Ma (Hinchey, Chapter 1)

H Anatexis in basement gneiss 55 Ma (Vanderhaeghe et al., 1999)

I Anatexis in basement gneiss 48+/- 11 Ma (Kuiper, 2003)
Metamorphic (sil-kfs-melt assemblages) monazite growth 55-52 Ma (Kuiper, 2003)

J Leucosome crystallization 53-52 Ma zircon (Kuiper, 2003
Metamorphic (sil-kfs-melt assemblages) monazite growth 55-52 Ma (Kuiper, 2003)

K Metamorphic monazite growth at 57-50 Ma (Johnston et al., 2000)
Deformation $F_2$ to $D_5$ < 55 Ma and > 50 Ma (Johnston et al., 2000)

100-60 Ma Late Cretaceous to Early Paleocene metamorphic overprint

1 Amphibolite facies (sil-mus-kfs) conditions persisted to 75-65 Ma (Scammell, 1993; Parrish, 1995)
Migmatization at 89-86 Ma (Parrish, 1995)
Ductile deformation ceased between 65 Ma and 57 Ma (Scammell, 1993; Parrish, 1995)

2 Deformation of MD as ealier as ~70 Ma and ceased by 59 Ma (Gibson, 1997)

3 Peak metamorphism by 78 Ma, continued to 58 Ma (Gibson, 1997)

4 Metamorphism from 67-65 Ma, monazite ages (Johnson, 1994)
Anatexis at 60 Ma, zircon ages (Johnson, 1994)
Intense shearing to <60 Ma (Johnson, 1994)

5 Peak metamorphism by 73 Ma, monazite ages (Parrish, 1995)
Leucosome crystallization, zircon 79 Ma, monazite 73-79 Ma (Kuiper, 2003)

6 Metamorphism from 65-59 Ma, monazite ages (Digel et al., 1998)

7 Peak Metamorphism >73 Ma, monazite ages (Crowley et al, 2003)
Anatexis 61 Ma, zircon ages (Crowley et al., 2003)

8 Deformation superimposed on Jurassic deformation on the east side of Selkirk fan (Gibson, 2003)

9 Peak metamorphism ~75 Ma, monazite ages (Spear and Parrish, 1996)

10 Prograde metamorphism 85-67 Ma (Spear and Parrish, 1996; Schaubs et al., 2002; Spear, 2004)
Anatexis and high-strain shearing 72-60 Ma (Spear, 2004; Carr and Simony, in review)

11 Metamorphism ~70 Ma to ~56 Ma, zircon and monazite ages (Bardoux, 1993)

12 Ductile deformation $F_3$>70 Ma and <73 Ma (Johnston et al., 2000; Kuiper, 2003)
Peak metamorphism ~93 Ma, monazite age (Johnston, 2000)

175-100 Ma Late Jurassic to Early Cretaceous metamorphic overprint

Jurassic metamorphism Kootney Arc and Purcell Anticlinorium (Archibald et al., 1983)

Jurassic metamorphism (165-175 Ma) Selkirk Mountains (Archibald et al.,1983; Colpron et al., 1996; Parrish and Wheeler(1983); Brown et al., 1992; Digel et al.,1998)

Jurassic to Early Cretaceous metamorphism in the Cariboo and Monashee Mtns. (Pigage, 1977; Murphy, 1987; Mortensen et al., 1987; Gerasimoff, 1988; Murphy et al., 1995; Sevigny et al., 1989; Scammell, 1993, Reid, 2003; Crowley et al., 2003; Gibson, 2003)

Late Triassic to Middle Jurassic low-grade metamorphism

Proterozoic metamorphism

a Metamorphic monazite growth 2060 Ma (Crowley, 1999)
Anatexis in basement gneiss between 2044-2080 Ma, zircon ages (Crowley, 1999)

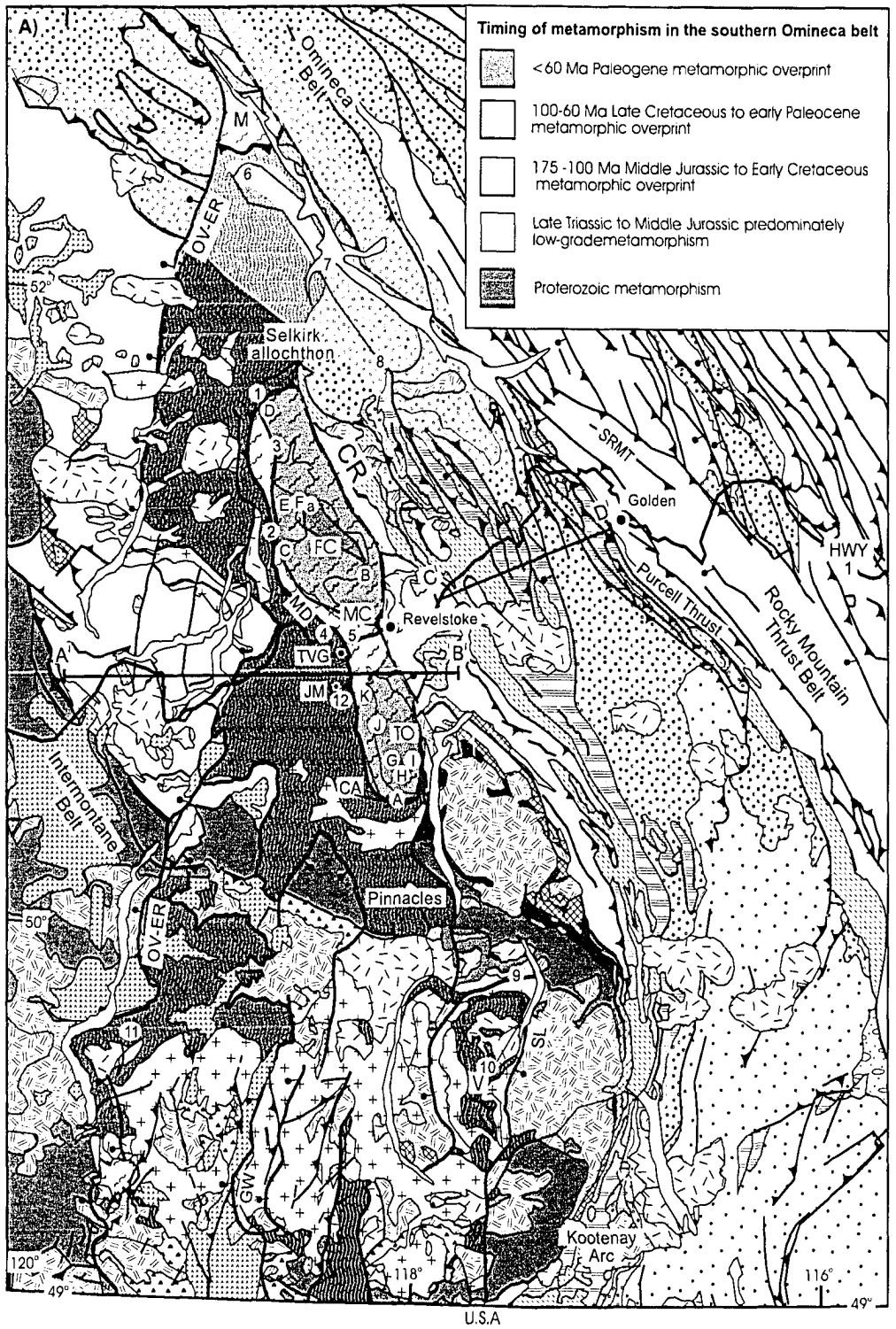


**Figure 5-2.** The timing of the last metamorphic overprint mainly in the Shuswap complex, southern Omineca belt. Most of the rocks within the Shuswap complex (with the exception of the younger plutonic suites) experienced a Late Triassic to Jurassic predominately low-grade greenschist facies metamorphism, and some parts were subsequently metamorphosed to higher grade. Details of timing, theromobarometric, anatectic and deformation constraints are provided in the adjacent legend and in the text. The lithological units are as in Figure 5-1.

| | | Shuswap Complex | | | |
|---|---|---|---|---|---|
| Intermontane Belt | Western Omineca | Hunters Range | Monashee Complex | Selkirk and Purcell Mtns. | Rocky Mountains and Foothills |
| Cretaceous granite and qtz monzonite | Lower Paleozoic granodioritic gneiss | Lower Paleozoic Griffin gneiss | Proterozoic to Paleozoic Monashee cover sequence | Lower Paleozoic Clachacudainn gneiss | Cenozoic clastic rocks of the Foothills |
| Triassic granite and syenite | Lower Paleozoic Eagle Bay assblg. (pericratonic?) | Upper Paleozoic Hunters Range assblg. (N.A. affinity?) | North American basement | Lower Paleozoic platformal sequence and pericratonic rocks | Mesozoic clastic rocks of the Foothills and Rockies |
| Devonian to Triassic Quesnel terrane | Lower Paleozoic Tsalkom Fm., Sicamous Fm. (pericratonic?) | Paleozoic Three Valley assblg. (N.A. affinity?) | | Lower Cambrian platformal sequence rocks (Hamill Gp., Badshot Fm.) | Upper Paleozoic platformal sequence rocks |
| North American basement | Paleoproterozoic to Lower Paleozoic Silver Creek assblg. (pericratonic?) | North American basement | | Upper Proterozoic Windermere Sgp. | Lower Paleozoic platformal sequence rocks |
| | Upper Paleozoic Hunters Range assblg. (N.A. affinity?) | | | Middle Proterozoic Purcell Sgp. | Upper Proterozoic Windermere Sgp. |
| | North American basement | | | North American basement | North American basement |

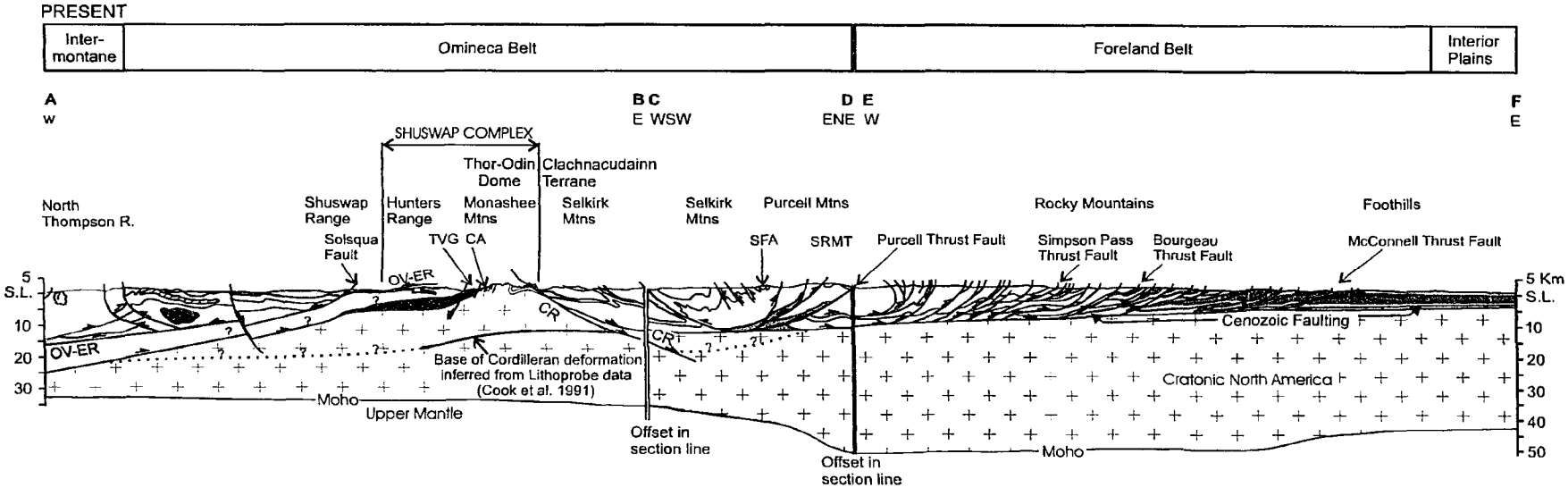


**Figure 5-3.** Cross section through the Intermontane Belt, Omineca Belt, Foreland Belt and Interior Plains. Modified after Price and Mountjoy, 1970; Okulitch, 1979; Sears, 1979; Monger et al. 1985; Monger, 1989; Cook et al., 1992; Brown et al., 1992; Johson, 1994; Johnson and Brown, 1996; Kruse et al., 2003; Williams and Jiang, in press; Cook and Van der Velden (unpublished geophysical cross section). The cross section lines are located in Figure 1. OV-ER = Okanagan Valley – Eagle River fault system, CR = Columbia River Fault, TVG = Three Valley Gap, CA = Cariboo Alp, SRMT = southern Rocky Mountain Trench, NA = North America, SFA = Selkirk Fan axis.

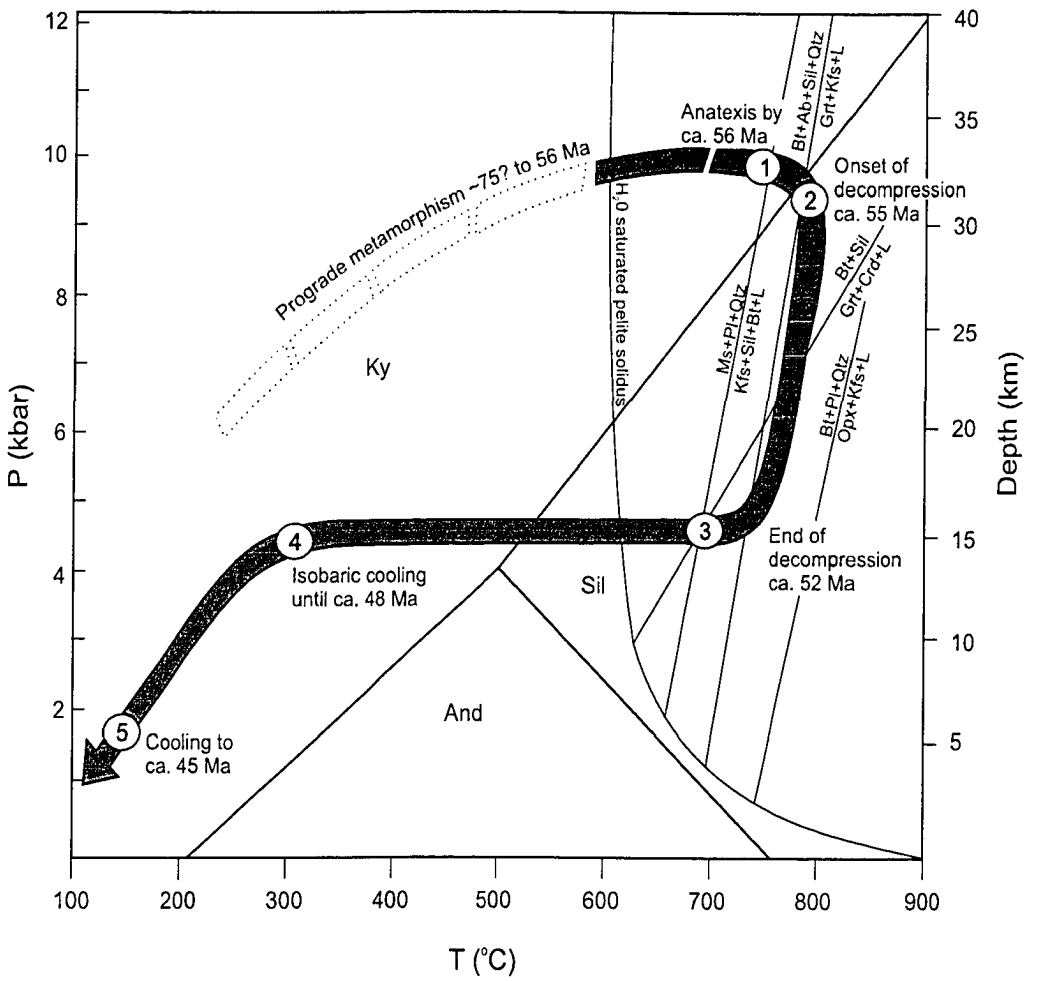


Events in the basement gneiss of Thor-Odin

① ca. 56 Ma - Culmination of peak metamorphism and onset of anatexis

② ca. 55 Ma - Onset of isothermal decompression and continued anatexis

③ ca. 52 Ma - End of decompression and anatexis

④ ca. 48 Ma - Isobaric cooling

⑤ ca. 45 Ma - Continued cooling and decompression

**Figure 5-4.** Pressure-Temperature-time path proposed for the basement gneiss of Thor-Odin dome, with approximate timing constraints for known parts of the path. Timing and geothermobarometric constraints provided by this study and the previous studies of Reesor and Moore (1971); Duncan (1982); Vanderhaeghe et al. (1999); Norlander et al. (2001); Lorencak et al., (2001) and Vanderhaeghe et al. (2003).

a)

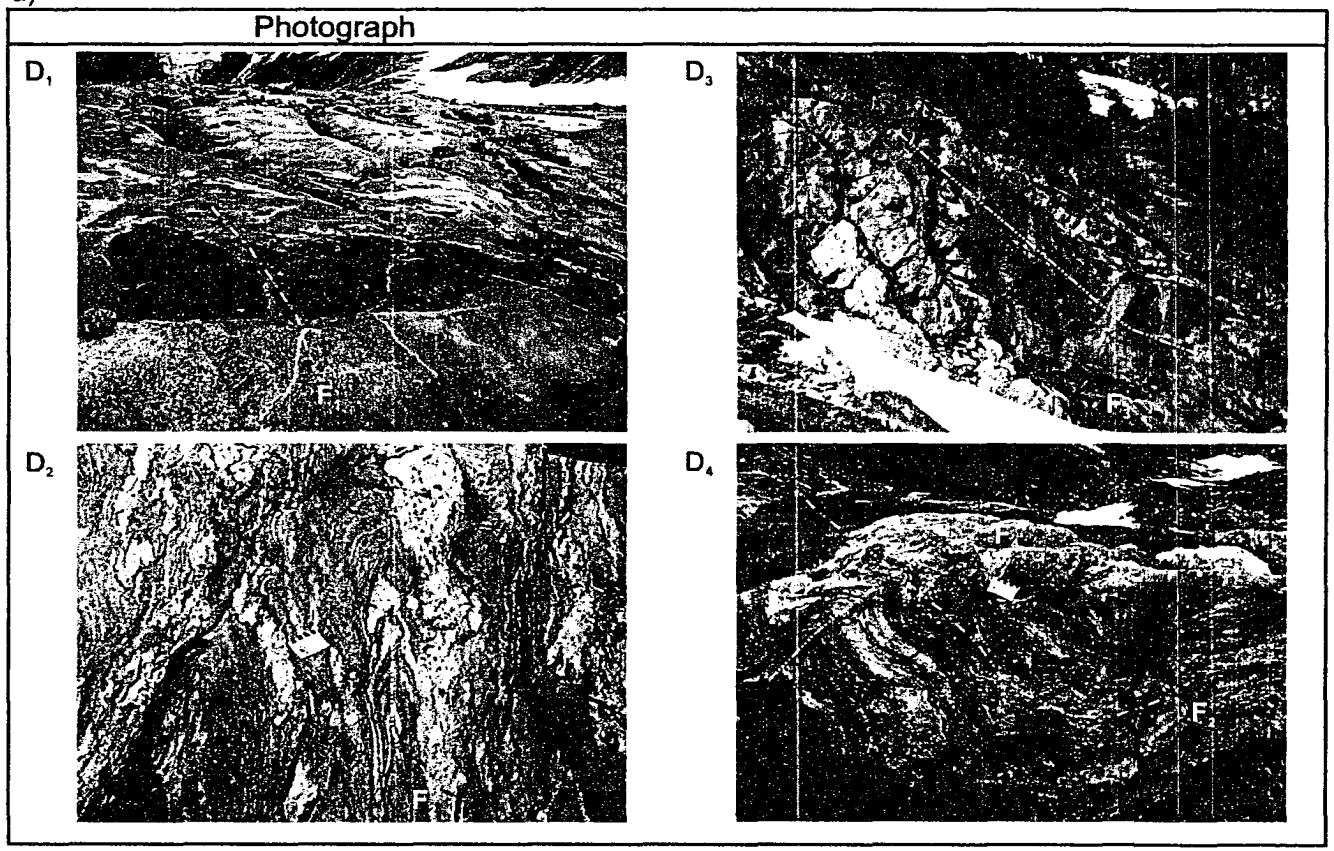

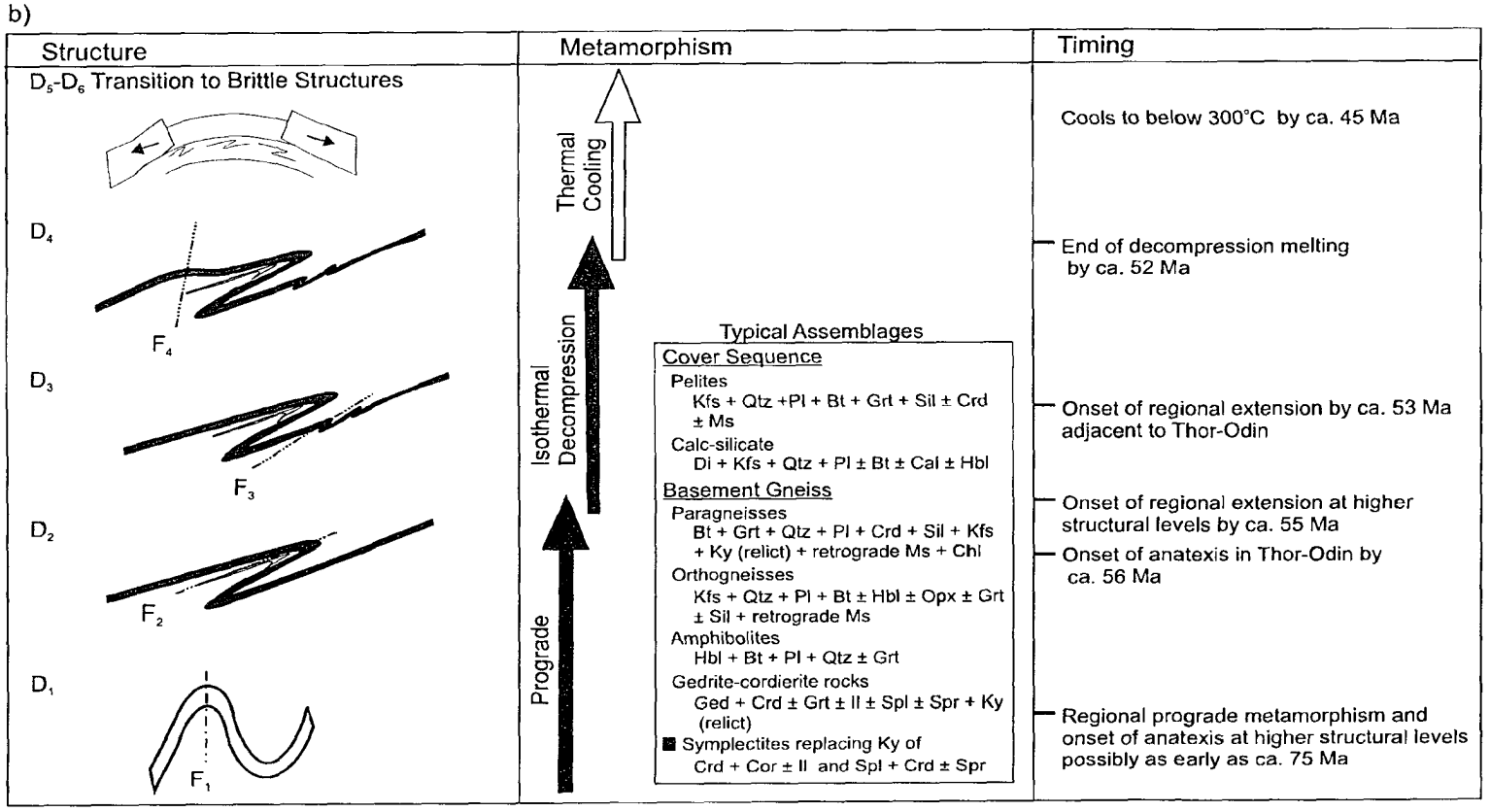


**Figure 5-5.** Summary diagram for Thor-Odin dome, Monashee complex. A) Shows the field photographs of each phase of folding preserved in Thor-Odin dome. B) Shows the style and timing of structures and metamorphism in the basement gneiss of the dome.

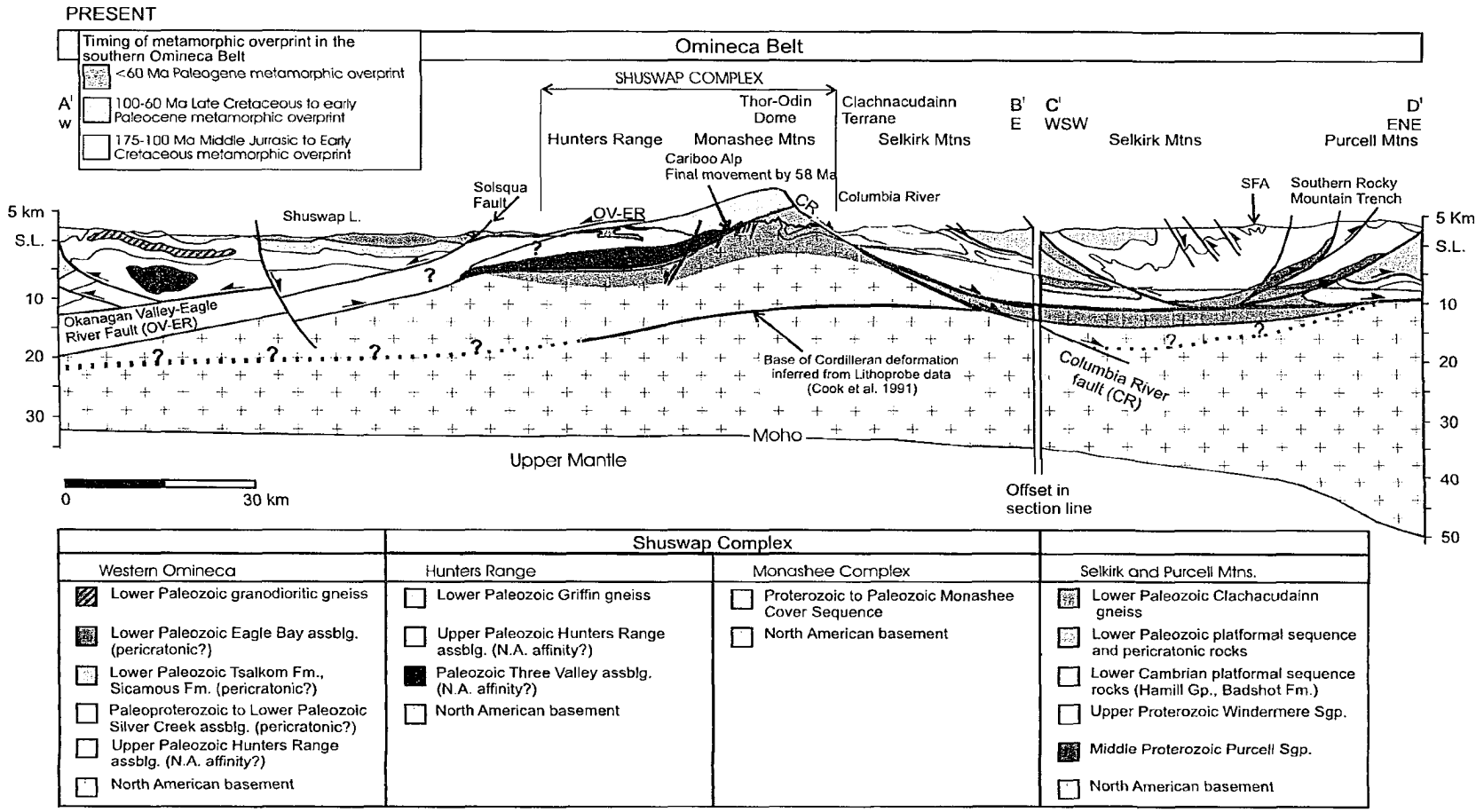


**Figure 5-6.** Cross section through the Omineca Belt, in the vicinity of the Monashee complex. Modified after Okulitch, 1979; Sears, 1979; Monger et al. 1985; Cook et al., 1992; Brown et al., 1992; Johson, 1994; Johnson and Brown, 1996; Kruse et al., 2003; Williams and Jiang, 2004; Cook and Van der Velden (unpublished geophysical cross section). Fields for different ages of deformation and/or metamorphism (Jurassic, Cretaceous and Tertiary) are shown and are interpreted from Figure 5-2. Cretaceous fields are modified after Gibson, 2003; Brown and Gibson, in review. The cross section lines are located in Figure 5-2. NA = North America.

# CHAPTER 6

## Summary of Conclusions

Thor-Odin dome of the Monashee complex, in the southeastern Canadian Cordillera, is part of the deepest exposed structural levels in the Omineca belt. The dome comprises > 1.8 Ga, North American basement ortho- and paragneisses that are unconformably overlain by Paleoproterozoic to Paleozoic supracrustal rocks of the Monashee cover sequence. Basement orthogneiss are dominated by migmatitic, hornblende-biotite-quartzo feldspathic gneiss with a lesser volume of quartz monzonite gneiss. The basement paragneiss comprise: a) heterogeneous, migmatitic garnet-sillimanite-quartzo feldspathic gneiss that are locally rich in cordierite, b) migmatitic cordierite-biotite-quartzo feldspathic gneiss, and c) calc-silicates, marbles, and quartzites, and are associated with minor cordierite-gedrite rocks and amphibolites. The rocks of Thor-Odin dome experienced polydeformation, high-grade metamorphism and anatexis during Late Cretaceous to Eocene Cordilleran orogenesis. Pervasive Paleocene - Eocene deformation transposed and overprinted Precambrian relationships and structures. The timing of onset of Cordilleran events in Thor-Odin dome is uncertain; however, deformation and prograde metamorphism were ongoing in the Late Cretaceous in the immediately overlying rocks and likely in Thor-Odin rocks as well. Peak P-T conditions of ~800 °C and 8-10 kb constrain the depth of burial of the basement rocks to 26 to 33 km.

### Chapter 1:

Basement ortho- and paragneiss of Thor-Odin dome contain ubiquitous stromatic leucosome as well as discrete phenocrystic and pegmatitic vein-type leucosome, which are all interpreted to have formed as a result of *in situ* melting in the Paleocene - Eocene. The stromatic leucosome is infolded with the country rock ($F_2$), contains a weak foliation,

and has a biotite rich melanosome. The phenocrystic and pegmatitic vein-type leucosome crosscut the stromatic leucosome, as well as the transposition foliation ($S_2$). Zircons in the folded and crosscutting leucosome were dated by Sensitive High Resolution Ion Microprobe (SHRIMP) to constrain the timing of anatexis and folding in the basement gneiss of Thor-Odin dome.

1) Folded stromatic, crosscutting phenocrystic and crosscutting pegmatitic vein-type leucosome in the basement paragneiss of Thor-Odin dome have SHRIMP $^{206}Pb/^{238}U$ zircon ages that range from ca. 56 to 52 Ma.
2) The onset of anatexis at ca. 56 Ma, a result of regional prograde metamorphism and dehydration melting, was coincident, at least in part, with the formation of the penetrative $S_2$ transposition foliation and large recumbent $F_2$ tight to isoclinal folds that infold basement and cover. Anatexis continued during $F_3$, and $F_4$ folding and decompression melting continued to ca. 52 Ma, and was concomitant with $D_5$ extensional deformation.
3) The Precambrian metamorphic and deformation history, if present, has been thoroughly overprinted by a pervasive penetrative Late Cretaceous to Eocene Cordilleran metamorphism and deformation.
4) Evidence that supports the interpretation that the leucosome in the basement are igneous and formed via *in situ* anatexis of the basement paragneiss include: A) the leucosome contains igneous textures such as euhedral phenocrysts of plagioclase and potassium feldspar with primary albite and carlsbad twinning and cumulate textures, myrmekitic intergrowths; there is no evidence of alteration of minerals. B) The major and trace element chemistry of the leucosome types is typical of S-type granites generated by partial melting of the continental crust. C) The Sr and Nd isotopic composition of the leucosome and host gneiss are similar to each other, which is consistent with production of leucosome by melting of gneiss in the region. D) The sharply faceted crystal shapes, internal fine-scale oscillatory

zoning and low Th/U ratios of zircon from the leucosome support an igneous source and are typical of zircons that grew in a partial melting environment.

5) In Thor-Odin dome, located in the hinterland of the southeastern Canadian Cordillera, high-grade metamorphism, anatexis, penetrative deformation and large scale folding are Paleocene - Eocene in age (ca. 56 to 52 Ma).

**Chapter 2:**

The 62-52 Ma Ladybird granite suite (LBG) is a peraluminous, leucocratic, S-type, leucoquartz monzonitic to granitic suite that occurs as batholiths, stocks, dikes, sills and pegmatite veins in the Middle Crustal Zone of the Shuswap complex, southeastern British Columbia. The emplacement of the LBG was synchronous with the production of abundant migmatites at deeper structural levels within Thor-Odin dome, an exposure of North American basement. Thor-Odin dome contains abundant leucosome hosted in ortho- and paragneiss basement migmatites that were exhumed by Eocene extensional faults from depths of ca. 26-33 km. The genesis of leucogranite, particularly of the South Fosthall pluton that immediately overlies Thor Odin dome, and leucosome from the Thor-Odin basement gneiss were studied to further investigate the strong spatial and temporal linkages between them. A comparison utilized major and trace element geochemistry, Rb-Sr and Sm-Nd isotope geochemistry, petrography and field data.

1) The Thor-Odin dome leucosome and Ladybird leucogranite samples have similar major and trace element chemistry, and are both characterized by zircons with inherited Precambrian cores. Samples from both the granites and leucosome are classified in the peraluminous granitic fields on discrimination diagrams. The leucosome samples have lower high field strength element (HFSE) concentrations, such as Zr, Ti, and Nb; as well as positive Eu anomalies, while the LBG samples have higher HFSE concentrations and negative Eu anomalies. The distribution of trace elements suggests that the leucosome and LBG are related in that most of the leucosome samples are cumulates, and the LBG samples represent residual

melts.

2) Whole rock initial Nd isotope compositions for the Ladybird granite suite overlap with those of the leucosome samples. Both groups had a range in initial $\varepsilon Nd_{(55Ma)}$ values; -5.0 to –17.2 for the granites and –9.5 to –23.6 for the leucosome samples. The similarity of initial isotopic ratios supports a genetic link between the two.
3) Whole rock initial Sr isotope compositions for both the peraluminous granites and leucosome samples show a large range in values. The initial $^{87}Sr/^{86}Sr$ isotope ratios for the granite suite (0.70603 to 0.73688) are lower than those of the leucosome samples (0.74256 to 0.76593). This isotopic heterogeneity suggests either: a) isotopic disequilibrium during partial melting in the mid to lower crust where the leucosome formed, b) the distribution of Sr during partial melting was controlled by different melt reactions, and/or c) isotopic heterogeneity in the source rocks.
4) At least part of the Ladybird granite suite likely formed via mid-crustal melting of North American basement rocks. The abundant leucosome in the exhumed basement gneiss of the Thor-Odin dome, in addition to the geochemical, isotopic, and U-Pb data, supports this hypothesis. The preservation of extensive melt leucosome may mark the melt migration paths for the overlying Ladybird granites. The metasedimentary supracrustal rocks that structurally overly Thor-Odin may have also contributed regionally to the formation of parts of the suite.

**Chapter 3:**

The Precambrian history of the Thor-Odin dome area is poorly constrained due to the pervasive overprinting of high-grade metamorphism, deformation, and anatexis associated with Cretaceous-Tertiary events during the Cordilleran orogeny. The occurrence of cordierite-gedrite rocks and associated garnet amphibolites in the North American basement rocks of Thor-Odin dome were the focus of major and trace element geochemical, Rb-Sr and Sm-Nd isotopic, petrographic and field studies to constrain the

origin of the cordierite-gedrite rocks and of the garnet amphibolites, and from these data constrain the Precambrian evolution of the basement gneisses.

Cordierite-orthoamphibole, dominantly gedrite-bearing, rocks are primarily preserved on the limbs of $F_2$ folds in the basement paragneiss from the southwestern area of the Thor-Odin dome. This unit appears to define a discontinuous marker horizon within the Paleoproterozoic North American basement paragneiss. The cordierite-gedrite rocks occur as discontinuous lenses, 15 to 50 meters thick and up to 500 meters long, and parallel the pervasive $S_2$ transposition foliation. The cordierite-gedrite rocks are interlayered with lenses of garnet amphibolites.

Garnet amphibolites occur throughout basement ortho- and paragneiss of Thor-Odin dome, are generally concordant with the pervasive $S_2$ transposition foliation and are commonly boudinaged. In the study area of Bearpaw Lake, the garnet amphibolite dykes are 10-20 meters thick and up to 400 meters long.

1) The cordierite-gedrite rocks have unique bulk rock chemistry which is characterized by depletions in the alkalies, notably CaO, and enrichments in $Al_2O_3$, MgO and $Fe_2O_3$. They have flat rare earth element (REE) patterns, depletions in most low field strength elements, such as Cs, Rb, Ba, and Sr and enrichments in high field strength elements, such as Zr, Hf, and Nb. The $^{87}Sr/^{86}Sr$ ratios for these rocks vary from 0.74923 to 0.85962 and the $\varepsilon Nd_{(today)}$ vary from –15.3 to –20.6.
2) The cordierite-gedrite rocks are interpreted as Paleoproterozoic lenses of mafic volcanics that are part of the North America basement paragneiss of Thor-Odin dome. Their unique chemical signature is interpreted to have resulted from hydrothermal alteration, likely by sea water.
3) The garnet amphibolites have a chemical signature typical of mafic volcanic rocks, with high MgO and $TiO_2$ values and depletions in the alkalies. The amphibolites have flat REE patterns, similar depletions in most low field strength

elements and enrichments in high field strength elements when compared to the cordierite-gedrite samples. The garnet amphibolites have $^{87}Sr/^{86}Sr$ ratios varying from 0.70953 to 0.74319 and $\varepsilon Nd_{(today)}$ from -0.8 to –7.3.

4) The garnet amphibolites are interpreted as metamorphosed mafic volcanics (or dykes) that likely formed during the Precambrian and they either post-date the formation of the protolith of the cordierite-gedrite rocks or escaped the hydrothermal alteration.

5) Due to overlapping signatures of major elements, trace elements and Nd isotopic ratios, neither the garnet amphibolites nor cordierite-gedrite rocks could be correlated regionally with similar mafic suites that are known to have intruded the rocks of North American basement and platformal sequences, such as lithologically similar candidates of the Moyie sills of the Belt-Purcell Supergroup; volcanics of the Horsethief creek group of the Windermere Supergroup; or, the Eocene lamprophyre dykes.

**Chapter 4:**

Basement gneiss of Thor-Odin dome preserve sillimanite-potassium feldspar-melt assemblages, were likely buried to depths 26-33 km, and were completely transposed and migmatized during Late Cretaceous to Eocene Cordilleran orogenesis. To constrain the timing of metamorphism in the basement rocks, monazite from cordierite-gedrite rocks and interlayered quartzite from the basement paragneiss were dated by U-Pb Sensitive High Resolution Ion Microprobe (SHRIMP) method. The cordierite-gedrite rocks and interlayered quartzite are preserved on the limbs of $F_2$ folds in the southwestern portion of Thor-Odin dome. Monazites were chemically X-ray mapped on the electron microprobe prior to analysis, to identify potential age domains within single monazite crystals.

1) Chemical maps of Y, Ca, U, and Th were created for grains from each sample and the maps were used to select SHRIMP analytical sites. Most monazite grains show a range of chemical patterns, including sector zoning, concentric zoning,

discontinuous or irregular patches with embayments, and cores varying in composition relative to the rims.

2) All three samples had monazite grains that overlapped in age, with mean $^{206}Pb/^{238}U$ ages that ranged from ca. 56 to 52 Ma.
3) The distinct chemical domains in the monazite grains did not appear to correspond to discernable age domains. Monazite growth or recrystallization occurred over a few million years and thus the complex internal chemical patterns are likely as a result of changing compositions during formation of monazite grains synchronous with high-grade metamorphism and anatexis.
4) Peak metamorphism in the basement gneiss of Thor-Odin dome occurred by ca. 56 Ma, but the timing of the onset of prograde metamorphism is uncertain. The basement underwent subsequent isothermal decompression which ended by ca. 52 Ma. Decompression is attributed to erosion and extensional faulting within the Shuswap complex.

**Chapter 5:**

The Monashee complex contains two structural culminations, Frenchman Cap and Thor-Odin domes that consist of high-grade Paleoproterozoic basement rocks and overlying cover sequence. The domes appear to have experienced different tectono-thermal histories during the Late Cretaceous to Eocene stage of the Cordilleran orogeny. Thor-Odin dome comprises supracrustal and > 1.8 Ga North American basement rocks that experienced polydeformation, high-grade metamorphism and anatexis during Late Cretaceous to Eocene Cordilleran orogenesis. Pervasive Paleocene - Eocene deformation transposed and overprinted Precambrian relationships and structures.

1) The timing of onset of Cordilleran events in Thor-Odin dome is uncertain; however, deformation and prograde metamorphism were likely ongoing in the Late Cretaceous (ca. 75 Ma) on the basis of the age of events in structurally overlying rocks.

2) The basement gneiss of Thor-Odin dome preserve sillimanite-potassium feldspar-melt assemblages and experienced peak Paleogene P-T conditions of ~800 °C and 8-10 kb which constrain the depth of burial of the basement rocks to ~26 to 33 km.

3) The onset of anatexis, a result of regional prograde metamorphism and dehydration melting, occurred in the Late Cretaceous to Paleocene and was ongoing by ca. 56 Ma. Large $F_2$ isoclinal folds and part of the $S_2$ transposition foliation were forming at ca. 56 Ma, based on the zircons from folded leucosome. This young deformation and metamorphism in the hinterland was synchronous with the final stages of compression in the Foothills.

4) Anatexis in Thor-Odin dome continued until ca. 52 Ma during isothermal decompression, and continued dehydration of the basement gneisses, as the dome underwent exhumation during regional extension.

5) Thor-Odin dome is part of a panel of strained rocks that developed during progressive loading, thickening and heating of the crust. Structural level above Thor-Odin dome, to the south, west and north of the dome, is referred to as the Middle Crustal Zone and include Joss Mountain, Three Valley Gap, and upper structural level of Cariboo Alp. The rocks of Cariboo Alp are located at the boundary between Thor-Odin dome and Middle Crustal Zone rocks, on the southwest portion of the dome. In rocks of Cariboo Alp, the end of deformation, metamorphism, and anatexis occurred ca. 58 Ma, while in the rocks of the Middle Crustal Zone the end of deformation, metamorphism, and anatexis occurred prior to ca. 70 Ma.

6) In Frenchman Cap dome, the base of Late Cretaceous – Eocene deformation and thermal events have been have been delineated, below which >1.8 Ga Proterozoic events are preserved. In contrast, Thor-Odin dome experienced pervasive Late-Cretaceous to Paleocene high temperature metamorphism, anatexis and

deformation, which penetratively overprinted Precambrian deformation and metamorphism. In the Paleocene, Thor-Odin dome was deeper and hotter than adjacent rocks of the Frenchman Cap dome, indicating that there are two different structural panels within the complex that were juxtaposed late in the tectonic evolution.

7) The most probable tectonic model invokes a ductile shear zone(s) to explain the diachronous timing of the end of deformation, metamorphism and anatexis in the Middle Crustal Zone and Thor-Odin dome. This model includes, either: a) two distinct ductile shear zones, one in the Late Cretaceous affecting the Middle Crustal zone followed by a localized zone of Paleocene-Eocene of high strain affecting the lower structural panel of Thor-Odin dome; or, b) one diachronous strain zone that either migrated progressively downward and/or forward or a zone of strain where deformation at lower structural levels of Thor-Odin dome outlasted that of higher structural levels of the Middle Crustal Zone.

# REFERENCES

Adams, M.G., Lentz, D.R., Shaw, C.S.J., Williams, P.F., Archibald, D.A., and Cousens, B. 2005. Eocene shoshonitic mafic dykes intruding the Monashee Complex, British Columbia: a petrogenetic relationship with the Kamloops Group volcanic sequence? Canadian Journal of Earth Sciences, 42: 11-24.

Anderson, H.E., and Goodfellow, W.D. 2000. Geochemistry and isotope chemistry of the Moyie sills: implications for early tectonic setting of the Mesoproterozoic Purcell basin. *In* The Geological Environment of the Sullivan Pb-Zn-Ag Deposit. *Edited by* Lydon, J.W., Höy, T, Slack, J.F. and Knapp, M.E. Mineral deposits division of the Geological Association of Canada, Special Publication No. 1, 302-321.

Andronicos, C.L., Chardon, D.H., Hollister, L.S., Gehrels, G.E., and Woodsworth, G.J. 2003. Strain partitioning in an obliquely convergent orogen, plutonism, and synorogenic collapse: Coast Mountains Batholith, British Columbia, Canada, Tectonics, 22: 1-7.

Archibald, D.A., Glover, J.K., Price, R.A., Farrar, E., and Carmicheal, D.M. 1983. Geochronology and tectonic implications of magmatism and metamorphism, southern Kootney arc and neighboring regions, southeastern British Columbia. Part I: Jurassic to mid-Cretaceous. Canadian Journal of Earth Sciences, 20: 1891-1913.

Armstrong, R.L. 1972. Cordilleran metamorphic core complexes, from Arizona to southern Canada. Annual Review of Earth and Planetary Sciences, 10: 129-154.

Armstrong, R.L. 1988. Mesozoic and early Cenozoic magmatic evolution of the Canadian Cordillera. Geological Society of America, Special Paper, 218: 55-91.

Armstrong, R.L. Parrish, R.R., van der Hyden, P., Scott, K., Runkle, D., and Brown, R.L. 1991. Early Proterozoic basement exposures in the southern Canadian Cordillera: core gneiss of Frenchman Cap, Unit 1 of the Grandforks Gneiss and Vaseaux Formation. Canadian Journal of Earth Sciences, 28: 1169-1201.

Ashworth, J.R. 1985. Migmatites. Blackie and Sons Limited, 715 pp.

Ashworth, J.R., and McLellan, E.L. 1985. Textures. *In* Migmatites. *Edited by* J.R. Ashworth. Blackie and Son Limited, 180-203.

Barbarin, B. 1996. Genesis of the two main types of peraluminous granitoids. Geology, 24: 295-298.

Barbey, P., Macaudiere, J., and Nzenti, J. P. 1990. High-pressure dehydration melting of metapelites; evidence from the migmatites of Yaounde (Cameroon). Journal of Petrology, 31: 401-427.

Bardoux, M. 1993. The Okanagan Valley normal fault from Penticton to Enderby South-central British Columbia. Ph.D. Thesis, Carleton University, 291 pp.

Beaumont, C., Jamieson, R.A., Nguyen, M.H., and Lee, B. 2001. Himalayan tectonic explained by extrusion of a low-viscosity crustal channel coupled to focused surface denudation. Nature, 414: 738-742.

Bickle, M.J., Wickham, S.M., Chapman, H.J., and Taylor, H.P. Jr. 1988. A strontium, neodymium and oxygen isotope study of hydrothermal metamorphism and crustal anatexis in the Trois Seigneurs Massif, Pyrenees, France. Contributions to Mineralogy and Petrology, 100: 399-417.

Brown, M., and D'Lemos, R.S. 1991. The Cadomian granites of Mancellia, Northeast Armorican Massif of France; relationship to the St. Malo migmatite belt, petrogenesis and tectonic setting. Precambrian Research, 51: 393-427.

Brown, M., Averkin, Y.A., and McLellan, E.L. 1995. Melt segregation in migmatites. Journal of Geophysical Research, B, Solid Earth and Planets, 100: 15 655-15 679.

Brown, R.L. 1980. Frenchman Cap Dome, Shuswap Complex, British Columbia: a progress report. *In* Current Research, part A. Geological Survey of Canada, Paper 80-1A, 47-51.

Brown R.L. 2003. Thrust-belt accretion and hinterland underplating of orogenic wedges-an example from the Canadian Cordillera. *In* Thrust tectonics and hydrocarbon

systems: AAPG Memoir 82, 1-14.

Brown, R.L., and Read, P.B. 1983. Shuswap terrane of British Columbia: a Mesozoic "core complex". Geology, 11: 164-168.

Brown, R.L., and Journeay, J.M. 1987. Tectonic denudation of the Shuswap metamorphic terrane of southeastern British Columbia. Geology, 15: 142-146.

Brown, R.L., and Carr, S.D. 1990. Lithospheric thickening and orogenic collapse within the Canadian Cordillera. Australian Institute of Mining and Metallurgy, 1990; Pacific Rim Proceedings, v II: 1-10.

Brown, R.L., and Gibson, H.D. In press. An argument for channel flow in the southern Canadian Cordillera and comparison with Himalayan tectonics. Submitted to Geological Society of London, Symposium volume Channel flow, ductile extrusion and exhumation of lower-mid-crust in continental collision zones.

Brown, R.L., Journey, J.M., Lane, L.S., Murphy, D.C., and Rees, C.J. 1986. Obduction, backfolding and piggyback thrusting in the metamorphic hinterland of the southeastern Canadian Cordillera. Journal of Structural Geology, 8: 225-268.

Brown, R.L., Carr, S.D., Johnson, B.J., Coleman, V.J., Cook, F.A., and Varsek, J.L. 1992. The Monashee décollement of the southern Canadian Cordillera; a crustal-scale shear zone linking the Rocky Mountain foreland belt to lower crust beneath accreted terranes. *In* Thrust Tectonics. *Edited by* K.R. McClay. Chapman and Hall, London, 357-364.

Brown, R.L., Beaumont, C., and Willett, S.D. 1993. Comparison of the Selkirk fan structure with mechanical models; implications for interpretation of the southern Canadian Cordillera. Geology, 21: 1015-1018.

Burwash, R.A., and Wagner, P.A. 1989. Sm/Nd geochronology of the Moyie Intrusions, Moyie Lake map area, British Columbia (82G/5). *In* Geological fieldwork 1988; a summary of field activities and current research. British Columbia Ministry of Energy, Mines and Petroleum Resources, Paper 1989-1, 45-48.

Burwash, R.A., Cavell, P.A., and Burwash, E.J. 1988. Source terranes for Proterozoic sedimentary rocks in southern British Columbia; Nd isotopic and petrographic evidence. Canadian Journal of Earth Sciences, 25: 824-832.

Carr, S.D. 1990. Late Cretaceous-early Tertiary tectonic evolution of the southern Omineca Belt, Canadian Cordillera. Ph. D. Thesis, Carleton University, 223 pp.

Carr, S.D. 1991.Three crustal zones in the Thor-Odin-Pinnacles area, southern Omineca Belt, British Columbia. Canadian Journal of Earth Sciences, 28: 2003-2023.

Carr, S.D. 1992. Tectonic setting and U-Pb geochronology of the early Tertiary Ladybird Leucogranite suite, Thor-Odin – Pinnacles area, southern Omineca belt, British Columbia. Tectonics, 11: 258-278.

Carr, S.D. 1995. The southern Omineca belt, British Columbia: new perspectives from the Lithoprobe Geoscience Program. Canadian Journal of Earth Sciences, 32: 1720-1739.

Carr, S.D., and Simony, P.S. In review. Evolution of a thick ductile shear zone at the base of a crystalline thrust sheet; evidence against channel flow in the southeastern Canadian Cordillera. Submitted to Geological Society of London, Symposium volume Channel flow, ductile extrusion and exhumation of lower-mid-crust in continental collision zones.

Carr, S.D., Parrish, R.R., and Brown, R.L. 1987. Eocene structural development of the Valhalla Complex, southeastern British Columbia. Tectonics, 6: 175-196.

Chappell, B.W., and White, A.J.R. 1992. I- and S-type granites in the Lachlan Fold Belt. Transactions of the Royal Society of Edinburgh: Earth Sciences, 86: 1-26.

Chappell, B.W., and White, A.J.R. 2001. Two contrasting granite types; 25 years later. Australian Journal of Earth Sciences, 48: 489-499.

Chavagnac, V.N., Nägler, T.F., and Kramers, J.D. 1999. Migmatization by metamorphic segregation at subsolidus conditions; implications for Nd-Pb isotope exchange. Lithos, 46: 275-298.

Clemens, J.D. 1990. The granulite-granite connection. *In* Granulites and Crustal Evolution. Edited by Vielseuf, D. and Vidal, P, Dordrecht, 25-36.

Clowes, R.M., Zelt, C.A., Armor, J.R., and Ellis, R.M. 1995. Lithospheric structure in the southern Canadian Cordillera from a network of seismic refraction lines. Canadian Journal of Earth Sciences, 32: 1485-1513.

Coleman, V.J. 1990. The Monashee décollement at Cariboo Alp and regional kinematic indicators, southeastern British Columbia. M.Sc. Thesis. Carleton University, 112 pp.

Colpron, M., Price, R.A., Archibald, D.A., and Carmicheal, D.M. 1996. Middle Jurassic exhumation along the western flank of the Selkirk fan structure; thermobarometric and thermochronometric constraints from the Illecillewaet Synclinorium, southeastern British Columbia. Geological Society of America Bulletin, 108: 1372-1392.

Coney, P.J. 1980. Cordilleran metamorphic core complexes: an overview. *In* Cordilleran metamorphic core complexes. *Edited by* M.D. Crittenden, P.J. Coney, and G.H. Davis. Geological Society of America, Memoir 153, 7-31.

Coney, P.J., and Harms, T.A. 1984. Cordilleran metamorphic core complexes; Cenozoic extensional relics of Mesozoic compression. Geology, 12:.550-554.

Cook, F.A., and Van der Velden, A.J. 1995. Three-dimensional crustal structure of the Purcell Anticlinorium in the Cordillera of southwestern Canada. Geological Society of America Bulletin, 107: 642-664.

Cook, F.A., Varsek, J.L., Clowes, R.M., Kanasewich, E.R., Spencer, C.S., Parrish, R.R., Brown, R.L., Carr, S.D., Johnson, B.J., and Price, R.A. 1992. Lithoprobe crustal reflection cross section of the southern Canadian Cordillera; 1, Foreland thrust and fold belt to Fraser River Fault. Tectonics, 11: 12-35.

Corfu, F., Hanchar, J.M., Hoskin, P.W.O., and Kinny, P.D. 2003. Atlas of zircon textures. Reviews in Mineralogy and Geochemistry, 53: 469-500.

Cornell, D.H., Thomas, R.J., Hoskin, P. Armstrong, R.A., and Whitehouse, M. 1999. Characterizing and dating the effects of metamorphism on zircon. Terra Abstracts, 11: 710.

Crowley, J.L. 1997. U-Pb geochronological constraints on the cover sequence of the Monashee complex, Canadian Cordillera: Paleoproterozoic deposition on basement. Canadian Journal of Earth Sciences, 34: 1008-1022.

Crowley, J.L. 1999. U-Pb geochronological constraints on Paleozoic tectonism in the Monashee complex, Canadian Cordillera: elucidating an overprinted geologic history. Geological Society of America Bulletin 111, 560-577.

Crowley, J.L., and Brown, R.L. 1994. Tectonic links between the Clachnacudainn Terrane and Selkirk Allochthon, southern Omineca Belt, Canadian Cordillera. Tectonics,.13: 1035-1051.

Crowley, J.L., and Parrish, R.R. 1999. U-Pb isotopic constraints on diachronous metamorphism in the northern Monashee Complex, southern Canadian Cordillera. Journal of Metamorphic Geology, 17: 483-502.

Crowley, J.L., Brown, R.L., and Parrish, R.R. 2001. Diachronous deformation and a strain gradient beneath the Selkirk allochthon, northern Monashee complex, southeastern Canadian Cordillera. Journal of Structural Geology, 23: 1103-1121.

Crowley, J.L., Ghent, E.D., Carr, S.D., Simony, P.S., and Hamilton, M.A. 2003. Multiple thermotectonic events in a continuous metamorphic sequence, Mica Creek area, southeastern Canadian Cordillera. Geological Materials Research, 2: 1-45.

Crowley, J.L., Brown, R.L., Gibson, H.D., and Turbrett, M. 2005. Weakly deformed ~1.85 Ga granites in the Monashee complex, British Columbia: evidence for a rigid basement during Tertiary orogenesis in the hinterland of the Canadian Cordillera. 2005 Cordilleran Tectonics Workshop, Whitehorse Yukon, Abstract Volume

Cumming, G.L., and Richards, J.R. 1975. Ore lead in a continuously changing Earth. Earth and Planetary Science Letters, 28, 155-171.

Degenhardt, H. 1957. Untersuchungen zur geochemischen Verteilung des Zirkoniums in der Lithosphaere. Geochimica et Cosmochimica Acta, 11: 279-309.

Deniel, C., Vidal, P., Fernandez, A., Le Fort, P., and Peucat, J.J. 1987. Isotopic study of the Manaslu granite (Himalaya, Nepal); inference on the age and source of Himalayan leucogranites. Contributions to Mineralogy and Petrology: 96: 78-92.

DePaolo, D.J. 1988. Neodymium Isotope Chemistry: an Introduction. Springer-Verlag, 187 pp.

Devlin, W.J., Bond, G.C., and Brueckner, H.K. 1985. An assessment of the age and tectonic setting of volcanics near the base of the Windermere Supergroup in northeastern Washington; implications for latest Proterozoic-earliest Cambrian continental separation. Canadian Journal of Earth Sciences, 22: 829-837.

Devlin, W.J., Brueckner, H.K., and Bond, G.C. 1988. New isotopic data and a preliminary age for volcanics near the base of the Windermere Supergroup, northeastern Washington, U.S.A. Canadian Journal of Earth Sciences, 25: 1906-1911.

Digel, S.G., Ghent, E.D., Carr, S.D., and Simony, P.S. 1998. Early Cretaceous kyanite-sillimanite metamorphism and Paleocene sillimanite overprint near Mount Cheadle, southeastern British Columbia; geometry, geochronology, and metamorphic implications. Canadian Journal of Earth Sciences, 35: 1070-1087.

Duncan, I.J. 1982. The evolution of the Thor-Odin gneiss dome and related geochronological studies. Ph.D. Thesis. University of British Columbia, 86 pp.

Duncan, I.J. 1984. Structural evolution of the Thor-Odin gneiss dome. Tectonophysics, 101: 87-130.

Ellis, D.J., and Obata, M. 1992. Migmatite and melt segregation at Cooma, New South Wales. Transactions of the Royal Society of Edinburgh: Earth Sciences, 83: 95-106.

Eskola, P. 1914. On the petrology of the Orijavi regional in southwestern Finland. Bulletin de la Commission Geologique de Finlande, 40: 1-279.

Evanchick, C.A., Parrish, R.R., and Gabrielse, H. 1984. Precambrian gneiss and late Proterozoic sedimentation in north-central British Columbia. Geology, 12: 233-237.

Ewing, T.E. 1981. Paleogene tectonic evolution of the Pacific Northwest. Journal of Geology, 25: 894-928.

Fayon, A.K., Whitney, D.L., and Teyssier, C. 2004. Exhumation of orogenic crust; diapiric ascent versus low-angle normal faulting. Special Paper - Geological Society of America, 380: 129-139.

Foster, G., Gibson, H. D., Parrish, R.R, Horstwood, M., Fraser, J., and Tindle, A. 2002. Textural, chemical and isotopic insights into the nature and behaviour of metamorphic monazite. Chemical Geology, 191: 183-207.

Foster, G., Parrish, R.R., Horstwood, M.S.A., Chenery, S., Pyle, J., and Gibson, H.D. 2004. The generation of prograde P-T-t points and paths; a textural, compositional, and chronological study of metamorphic monazite Earth and Planetary Science Letters, 228: 125-142.

Friedman, R.M., Mahoney, J.B., and Cui, Y. 1995. Magmatic evolution of the southern Coast Belt; constraints from Nd-Sr isotopic systematics and geochronology of the southern Coast plutonic complex. Canadian Journal of Earth Sciences, 32: 1681-1698.

Frost, C.D., and Burwash, R.A. 1986. Nd evidence for extensive Archean basement in the western Churchill Province, Canada. Canadian Journal of Earth Sciences, 23: 1433-1437.

Frost, C.D., and O'Nions, R.K. 1984. Nd evidence for Proterozoic crustal development in the Belt-Purcell Supergroup. Nature (London), 312: 53-56.

Frost, C.D., and Winston, D. 1987. Nd isotope systematics of coarse- and fine-grained sediments; examples from the middle Proterozoic Belt-Purcell Supergroup. Journal of Geology, 95: 309-327.

Gable, D.J., and Sims, P.K. 1969. Geology and regional metamorphism of some high-grade cordierite gneisses, Front Range, Colorado. Special Paper - Geological Society of America, 128: 87.

Gabrielse, H., and Campbell, R.B. 1991. Upper Proterozoic assemblages, Chapter 6. *In*: Geology of the Cordilleran Orogen in Canada. *Edited by*: H. Gabrielse, H and C.J. Yorath. Geology of Canada. Geological Survey of Canada, No. 4: 125-150.

George, M.T., and Bartlett, J.M. 1996. Rejuvenation of Rb-Sr mica ages during shearing on the northwestern margin of the Nanga Parbat-Haramosh Massif. Tectonophysics, 260: 167-185.

Gerasimoff, M.D. 1988. The Hobson Lake Pluton, Cariboo Mountains, British Columbia, and its significance to Mesozoic and early Cenozoic Cordilleran tectonics. M.Sc. Thesis, Queen's University, 196 pp.

Gervais, F., Brown, R.L., and Crowley, J.L. 2005. Proterozoic strain in the core of the Frenchman Cap dome, Monashee complex; tectonic implications of a strong basement. 2005 Cordilleran Tectonics Workshop, Whitehorse Yukon, Abstract Volume.

Ghosh, D.K. 1995. Nd-Sr isotopic constraints on the interactions of the Intermontane Superterrane with the western edge of North America in the southern Canadian Cordillera Canadian Journal of Earth Sciences, 32: 1740-1758.

Gibson, H.D. 1997. Thermotectonic evolution of the northern Monashee Complex, southern Omineca Belt, southeastern British Columbia. M.Sc. Thesis, Carleton University, 111 pp.

Gibson, H.D. 2003. Structural and thermal evolution of the Northern Selkirk Mountains, southeastern Canadian Cordillera: tectonic development of a regional-scale composite fan. Ph.D. Thesis, Carleton University, 298 pp.

Gibson, H.D., Brown, R.L., and Parrish, R.R. 1999. Deformation-induced inverted metamorphic field gradients; an example from the southeastern Canadian Cordillera. Journal of Structural Geology, 21: 751-767.

Gibson, H.D., Carr, S.D., Brown, R.L., and Hamilton, M.A. 2004. Correlations between chemical and age domains in monazite, and metamorphic reactions involving major pelitic phases: an integration of ID-TIMS and SHRIMP geochronology with Y-Th-U X-ray mapping. Chemical Geology, 211: 237-260.

Govindaraju, K. 1989. 1989 compilation of working values and sample description for 272 geostandards. Geostandards Newsletter, 13: 1-113.

Grant, J.A. 1968. Partial melting of common rocks as a possible source of cordierite-anthophyllite bearing assemblages. American Journal of Science, 266: 908-931.

Greenwood, H.J., Woodsworth, G.J., Read, P.B., Ghent, E.D., and Evenchick, C.A. 1991. Metamorphism, Chapter 16. *Edited by* H. Gabrielse, H and C.J. Yorath. *In* Geology of the Cordilleran Orogen in Canada. Geological Survey of Canada, Geology of Canada, 4: 535-572.

Hammouda, T., Pichavant, M., and Chaussidon, M. 1994. Mechanisms of isotopic equilibration during partial melting; an experimental test of the behaviour of Sr. Mineralogical Magazine, 58A: 368-369.

Harris, L.B., Koyi, H.A., and Fossen, H. 2002. Mechanisms for folding of high-grade rocks in extensional tectonic settings. Earth Science Reviews, 59: 163-210.

Hinchey, A.M., and Carr, S.D. 2003. Geochemical test for linkages in migmatitic basement rocks and the Ladybird granite suite; Thor-Odin dome, southeastern British Columbia. *In*: GAC-MAC 2003 Abstract Volume 28.

Hinchey, A.M., Carr, S.D., and Rayner, N. 2004. Timing constraints on mid-crustal events in the Thor-Odin dome, Monashee Complex: evidence for Paleocene-Eocene and penetrative deformation during the final stages of shortening in the southern Canadian Cordillera. In: Geoscience Africa 2004, University of Witwatersrand, Abstract Volume.

Hoffer, E., and Grant, J.A. 1980. Experimental investigation of the formation of cordierite-orthopyroxene paragneisses in pelitic rocks. Contributions to Mineralogy and Petrology, 73: 15-22.

Höy, T., and Brown, R.L. 1980. Geology of the Eastern Margin of the Shuswap complex, Frenchman Cap area. British Columbia Ministry of Energy, Mines and Petroleum resources Bulletin 80, 99 pp.

Inger, A., and Harris, N., 1993. Geochemical constraints on leucogranites magmatism in the Langtang Valley, Nepal Himalaya. Journal of Petrology, 34: 345-368.

Irving, A.J., and Ashley, P.M. 1976. Amphibole-olivine-spinel, cordierite-anthophyllite and related hornfelse associated with metamorphosed serpentinites in the Goobarragandra District, near Tumut, New South Wales. Journal of the Geological Society of Australia, 23: 19-43.

James, R.S., Grieve, R.A.F., and Pauk, L. 1978. The petrology of cordierite-anthophyllite gneisses and associated mafic and pelitic gneisses at Manitouwadge, Ontario. American Journal of Science, 278: 41-63.

Jenner, G.A. 1996. Trace element geochemistry of igneous rocks; geochemical nomenclature and analytical geochemistry. *In* Trace element geochemistry of volcanic rocks; applications for massive sulphide exploration. *Edited by* D.A Wyman. Short Course Notes - Geological Association of Canada, 12: 51-77.

Johannes, W., and Holtz, F. 1990. Formation and composition of H2O undersaturated granitic melts. *In* high temperature metamorphism and crustal anatexis. *Edited by* J.R. Ashworth and M. Brown. Unwin Hyman, 87-101.

Johannes, W., Holtz, F., and Moeller, P. 1995. REE distribution in some layered migmatites; constraints on their petrogenesis. Lithos, 35: 139-152.

Johannes, W., Ehlers, C., Kriegsman, L.M., and Mengel, K. 2003. The link between migmatites and S-type granites in the Turku area, southern Finland. Lithos, 68: 69-90.

Johnson, B.J. 1994. Structure and tectonic setting of the Okanagan Valley fault system in the Shuswap Lake area, southern British Columbia. Ph.D. Thesis, Carleton University, 266 pp.

Johnson, B.J., and Brown, R.L. 1996. Crustal structure and early Tertiary extensional tectonics on the Omineca belt at 51°N latitude, southern Canadian Cordillera. Canadian Journal of Earth Sciences, 33: 1596-1611.

Johnston, D.H. 1997. Structural and thermal evolution of Northwest Thor-Odin Dome, Monashee Complex, Southeast British Columbia. Ph.D. Thesis. University of New Brunswick. 321 pp.

Johnston, D.H., Williams, P.F., Brown, R.L., Crowley, J.L., and Carr, S.D. 2000. Northeastward extrusion and extensional exhumation of crystalline rocks from the Monashee complex, southeastern Canadian Cordillera. Journal of Structural Geology, 22: 603-625.

Journeay, J.M. 1986. Stratigraphy, internal strain, and thermotectonic evolution of the northern Frenchman Cap dome, an exhumed basement duplex structure, Omineca hinterland, southeastern Canadian Cordillera. Ph.D. Thesis. Queen's University. 399 pp.

Jung, S., Hoernes, S., Masberg, P., and Hoffer, E. 1999. The Petrogenesis of Some Migmatites and Granites (Central Damara Orogen, Namibia): Evidence for Disequilibrium Melting, Wall-Rock Contamination and Crystal Fractionation. Journal of Petrology, 40: 1241-1269.

Jung, S., Hoernes, S., and Mezger, K. 2000. Geochronology and petrology of migmatites from the Proterozoic Damara Belt; importance of episodic fluid-present disequilibrium melting and consequences for granite petrology. Lithos, 51: 153-179.

Kalsbeek, F., Jespen, H.F., and Nutman, A.P. 2001. From source migmatites to plutons; tracking the origin of ca. 435 Ma S-type granites in the East Greenland Caledonian Orogen. Lithos, 57: 1-21.

Kohn, M.J., and Malloy, M.A. 2004. Formation of monazite via prograde metamorphic reactions among common silicates: implication for age determinations. Geochimica et Cosmochimica Acta, 68: 101-113.

Knesel, K.M., and Davidson, J.P. 2002. Insights into collisional magmatism from isotopic fingerprints of melting reactions. Science, 296: 2206-2208.

Kriegsman, L.M. 2001. Partial melting, partial melt extraction and partial back reaction in anatectic migmatites. Lithos, 56: 75-96.

Kretz, R. 1983. Symbols for rock-forming minerals. American Mineralogist, 68: 77-279.

Kruse, S., and Williams, P.F. 2004. Structural evolution of the northeastern Thor-Odin culminations: why the dome? *In* From Forelands to Core Zones: Deformation and Tectonic Evolution of Orogenic Belts. Abstract Volume.

Kruse, S., McNeill, P., and Williams, P.F. 2003. A new compilation map of the Thor-Odin culmination, Monashee complex, B.C. *In*: GAC-MAC 2003 Abstract Volume 28.

Kruse, S., McNeill, P., and Williams, P.F. 2004. A geological map of the Thor-Odin dome, Monashee complex, B.C., http://www.unb.ca/fredericton/science/geology/monashee/

Kuiper, Y. 2003. Isotopic constraints on timing of deformation and metamorphism in the Thor–Odin dome, Monashee Complex, southeastern British Columbia. Ph.D. Thesis. University of New Brunswick. 290 pp.

Lane, L.S. 1984. Brittle deformation in the Columbia River fault zone near Revelstoke, southeastern British Columbia. Canadian Journal of Earth Sciences, 21: 584-598.

Le Maitre, R.W. 1976. Some problems of the projection of chemical data into mineralogical classifications. Contributions to Mineralogy and Petrology, 56: 181-189.

Le Maitre, R.W. (editor). 1989. A classification of Igneous Rocks and Glossary of Terms, Blackwell, Oxford, 193 pp.

Lonsdale, P.F. 1988. Paleogene history of the Kula Plate; offshore evidence and onshore implications. Geological Society of America Bulletin, 100: 733-754.

Lorencak, M., Seward, D., Vanderhaeghe, O., Teyssier, C., and Burg, J.P. 2001. Low-temperature cooling history of the Shuswap metamorphic core complex, British Columbia: Constraints from apatite and zircon fission-track ages. Canadian Journal of Earth Sciences, 38: 1615-1625.

Ludwig, K.R. 2001. User's manual for Isoplot/Ex rev. 2.49: a Geochronological Toolkit for Microsoft Excel. Special Publication, 1a, Berkeley Geochronology Center, Berkeley, 55 pp.

Maniar, P.D., and Piccoli, P.M. 1989. Tectonic discrimination of granitoids. Geological Society of America Bulletin, 101: 635-643.

McMillan, W.J. 1973. Petrology and structure of the west flank, Frenchman's Cap dome, near Revelstoke, British Columbia. Geological Survey of Canada Paper 71-29, 88 pp.

McNeill, P.D., and Williams, P.F. 2002. Structural evolution of migmatites of the Thor-Odin area of the Monashee Complex, southern British Columbia, Canada. *In* Abstracts with Programs - Geological Society of America, 34: 333.

McNeill, P.D., and Williams, P.F. 2003. Structural evolution of migmatites of the Thor-Odin area of the Monashee complex, southern British Columbia. *In* Cordilleran Tectonics Workshop 2003, Abstract Volume.

McNeill, P.D., and Williams, P.F. 2004. A structural approach to the study and mapping of partially melted terranes with emphasis on fabric/melting/timing relationships: an example from the Monashee complex of southeastern British Columbia. *In* GAC-MAC 2004 Abstract Volume 29.

McNeill, P.D., and Williams, P.F. 2005. The relationship between partial melting and deformation, and its significance to orogen scale shear zones of the middle to lower crust. *In* GAC-MAC 2005 Abstract Volume 30.

McNicoll, V.J., and Brown, R.L. 1995. The Monashee décollement at Cariboo Alp, southern flank of the Monashee complex, southern British Columbia, Canada. Journal of Structural Geology, 17: 17-30.

Mehnert, K.R. 1968. Migmatites and the origin of granitic rocks. Elsevier Publishing Company, 405 pp.

Misch, P. 1968. Plagioclase compositions and non-anatectic origin of migmatitic gneisses in Northern Cascade Mountains of Washington State. Contributions to Mineralogy and Petrology, 17: 1-70.

Monger, J.W.H. 1989. Overview of Cordilleran geology. *In* Western Canada sedimentary basin; a case history. *Edited by* B.D. Ricketts. Canadian Society of Petroleum Geologists, 9-32.

Monger, J.W.H., and Price, R.A. 2000. A transect of the southern Canadian Cordillera from Vancouver to Calgary, Open File 3902, 170 pp.

Monger, J.W.H., Price, R.A., and Tempelman-Kluit, D.J. 1982. Tectonic accretion and the origin of the two major metamorphic and plutonic welts in the Canadian Cordillera, Geology, 10: 70-75.

Monger, J.W.H., Clowes, R.M., Price, R.A., Simony, P.S., Riddihough, R.P., and Woodsworth, G.J. 1985. Centennial Continent/Ocean Transect #7, B-2 Juan de Fuca Plate to Alberta Plains. *Edited by* R. Speed. *In* Decade of North American Geology Continent/Ocean Transects. Geological Society of America, 2 sheets and 21.

Montel, J.M., Marignac, C., Barbey, P., and Pichavant, M. 1992. Thermobarometry and granite genesis: the Hercynian low-P, high-T Velay anatectic dome (French Massif Central). Journal of Metamorphic Geology, 10: 1-15.

Moore, J.M., and Waters, D.J. 1990. Geochemistry and origin of cordierite-orthoamphibole/orthopyroxene-phlogopite rocks from Namaqualand, South Africa. Chemical Geology, 85: 77-100.

Mortensen, J.K., Montgomery, J.R., and Fillipone, J. 1987. U-Pb zircon, monazite, and sphene ages for granitic orthogneiss of the Barkerville Terrane, east-central British Columbia. Canadian Journal of Earth Sciences, 24: 1261-1266.

Murphy, D.C. 1987. Suprastructure/infrastructure transition, east-central Cariboo Mountains, British Columbia; geometry, kinematics and tectonic implications. Journal of Structural Geology, 9: 13-29.

Murphy, D.C., van der Heyden, P., Parrish, R.R., Klepacki, D.W., McMillan, W., Struik, L.C., and Gabites, J. 1995. New geochronological constraints on Jurassic deformation of the western edge of North America, southeastern Canadian Cordillera. Special Paper - Geological Society of America, 299:159-171.

Norlander, B.H., Whitney, D.L., Teyssier, C., and Vanderhaeghe, O. 2002. Partial melting and decompression of the Thor-Odin Dome, Shuswap metamorphic core complex, Canadian Cordillera. Lithos, 61: 163-125.

Obata, M., Yoshimura, Y., Nagakawa, K., Odawara, S., and Osanai, Y. 1994. Crustal anatexis and melt migrations in the Higo metamorphic terrane, west-central Kyushu, Kumamoto, Japan. Lithos, 32: 135-147.

Oliver, N.H.S., Bodorkos, S., Nemchin, A.A., Kinny, P.D., and Watt, G.R. 1999. Relationships between zircon U-Pb SHRIMP ages and leucosome type in migmatites of the Halls Creek Orogen, western Australia. Journal of Petrology, 40: 1553-1575.

Olsen, S.N. 1984. Mass-balance and mass-transfer in migmatites from the Colorado Front Range. Contributions to Mineralogy and Petrology, 85: 30-44.

Olsen, S.N. 1985. Mass balance in migmatites. *In* Migmatites. *Edited by* J.R. Ashworth. Blackie and Son Limited, 145-179.

Okulitch, A.V. 1979. Lithology, stratigraphy, structure and mineral occurrences of the Thompson-Shuswap-Okanagan area, British Columbia. Geological Survey of Canada, Open File 637.

Okulitch, A.V. 1984. The role of the Shuswap metamorphic complex in Cordilleran tectonism; a review. Canadian Journal of Earth Sciences, 21: 1171-1193.

Paulsson, O., and Austrheim, H. 2003. A geochronological and geochemical study of rocks from Gjelsveifjella, Dronning Maud Land, Antarctica – implications for Mesoproterozoic correlation and assembly of Gondwana. Precambrian Research, 125: 113-138.

Parkinson, D.L. 1991. Age and isotopic character of Early Proterozoic basement gneisses in the southern Monashee Complex, southeastern British Columbia. Canadian Journal of Earth Sciences, 28: 1159-1168.

Parkinson, D.L. 1992. Age and tectonic evolution of the southern Monashee Complex, southeastern British Columbia; a window into the deep crust. PhD Thesis. University of California. 186 pp.

Parrish, R.R. 1985. Metamorphic core complexes of southern B.C.; distinctions between extensional or compressional origins. Abstracts with Programs - Geological Society of America, 17.

Parrish, R.R. 1995. Thermal evolution of the southeastern Canadian Cordillera. Canadian Journal of Earth Sciences, 32: 1618-1642.

Parrish, R.R., and Wheeler, J.O. 1983. A U-Pb zircon age from the Kuskanax Batholith, southeastern British Columbia. Canadian Journal of Earth Sciences, 20: 1751-1756.

Parrish, R R., and Armstrong, R L. 1987. The ca. 162 Ma Galena Bay Stock and its relationship to the Columbia River fault zone, Southeast British Columbia. Paper - Geological Survey of Canada, 87-2: 25-32.

Parrish, R.R., Carr, S.D., and Parkinson, D.L. 1988. Eocene extensional tectonics and geochronology of the southern Omineca Belt, British Columbia and Washington. Tectonics, 7: 181-212.

Patino Douce, A.E., Johnston, A.D., and Humphreys, E.D. 1990. Closed system Anatexis Closed system anatexis in the Cordilleran Interior; the importance of initial lithologic structure. Eos, Transactions American Geophysical Union, 71: 298-299.

Pattison, D.R.M., and Harte, B. 1988. Evolution of structurally contrasting anatectic migmatites in the 3-kbar Ballachulish aureole, Scotland. Journal of Metamorphic Geology, 6: 475-494.

Pidgeon, R.T., and Compston, W. 1992. A SHRIMP ion microprobe study of inherited and magmatic zircons from four Scottish Caledonian granites. Transactions from the Royal Society of Edinburgh: Earth Sciences, 83: 473-484.

Pidgeon, R.T., Bosch, D., and Bruguier, O. 1996. Inherited zircon and titanite U-Pb systems in an Archean syenite from southwestern Australian: implications for U-Pb stability of titanite. Earth and Planetary Science Letters, 141: 187-198.

Pigage, L.C. 1977. Rb-Sr dates for granodiorite intrusions on the northeast margin of the Shuswap metamorphic complex, Cariboo Mountains, British Columbia. Canadian Journal of Earth Sciences, 14: 1690-1695.

Poitrasson, F., Hanchar, J.M., and Schaltegger, U. 2002. The current state and future of accessory mineral research. Chemical Geology, 191: 3-24.

Price, R.A. 1986. The southeastern Canadian Cordillera: thrusting, tectonic wedging, and delamination of the lithosphere. Journal of Structural Geology, 8: 239-254.

Price, R.A., and Mountjoy, E.W. 1970. Geologic structure of the Canadian Rocky Mountains between Bow and Athabasca rivers; a progress report. *In*: Structure of the southern Canadian Cordillera. *Edited by*: J.O. Wheeler. Geological Association of Canada Special Paper, 6: 7-25.

Pyle, J.M., and Spear, F.S. 1999. Yttrium zoning in garnet; coupling of major and accessory phases during metamorphic reactions. Geological Materials Research, 1: 1-49.

Pyle, J.M., and Spear, F.S. 2003. Four generations of accessory-phase growth in low-pressure migmatites from SW New Hampshire. American Mineralogist, 88: 338-351.

Pyle, J.M., Spear, F.S, Rudnick, R.L., and McDonough, W.F. 2001. Monazite-xenotime-garnet equilibrium in metapelites and a new monazite-garnet thermometer. Journal of Petrology, 42: 2083-2107.

Read, P.B. 1979. Relationship between the Shuswap metamorphic complex and Kootenay Arc, Vernon east-half, southern British Columbia. Geological Survey of Canada, Paper, 79-1A, 37-40.

Read, P.B. 1980. Stratigraphy and structure: Thor-Odin to Frenchman Cap domes, Vernon east-half map areas, southeastern Canadian Cordillera. *In* Current research, part A. Geological Survey of Canada, Paper 80-1A, 19-25.

Read, P.B., and Wheeler, J.O. 1976. Geology of Lardeau W/2 (82k W/2): Geological Survey of Canada, Open File Map 432, scale 1:25 000.

Read, P.B., and Brown, R.L. 1981. Columbia River fault zone: southeastern margin of the Shuswap core complex, southeastern Canadian Cordillera. Canadian Journal

of Earth Sciences, 18: 1127-1145.

Read, P.B., Woodsworth, G.J., Greenwood, H.J., Ghent, E.D., and Evanchick, C.A. 1991. Metamorphic Map of the Canadian Cordillera, Geological Survey of Canada, Map 1714A, scale 1:2 000 000.

Reesor, J.E. 1970. Some aspects of structural evolution and regional setting in part of the Shuswap Metamorphic Complex. *In* Geology of the Cordilleran Orogen Canada. *Edited by* J.O. Wheeler. Geological Association of Canada, Special Paper 6, 73-86.

Reesor J.E., and Moore Jr., J.M. 1971. Petrology and structure of Thor-Odin gneiss dome, Shuswap metamorphic complex, British Columbia. Geological Survey of Canada, Paper 195: 149 pp.

Reid, L.F. 2003. Stratigraphy, structure, petrology, geochronology and geochemistry of the Hobson Lake area (Cariboo Mountains, British Columbia) in relation to the tectonic evolution of the southern Canadian Cordillera. Ph.D. Thesis. University of Calgary. 299 pp.

Robin, P.-Y.F. 1979. Theory of metamorphic segregation and related processes. Geochimica et Cosmochimica Acta, 43: 1587-1600.

Rollinson, H.R. 1993. Using Geochemical Data: evaluation, presentation, interpretation. Longman Scientific and Technical, John Wiley and Sons, 352 pp.

Ross, G.M., Villeneuve, M.E., Parrish, R.R., and Thériault, R.J. 1993. Tectonic assembly of crystalline basement, Alberta Basin; implications for mantle evolution and ancestry of Canada's Pacific margin. Lithoprobe Report, 31: 134-143.

Sanders, A.D., Tarney, J., Marsh, N.G., and Wood, D.A. 1980. Ophiolites as ocean crust or marginal basin crust: a geochemical approach. *Edited by* A. Panayiotou. *In* Ophiolites: proceedings of the International ophiolite symposium, Nicosia, Cyprus 1979, Ministry of Agriculture and Natural Resources, Geological Survey Department, Cyprus, 171-180.

Sawyer, E.W. 1987. The role of partial melting and fractional crystallization determining discordant migmatite leucosome compositions. Journal of Petrology, 28: 445-473.

Sawyer, E.W. 1998. Formation and Evolution of Granite Magmas during crustal Reworking: the Significance of diatexites. Journal of Petrology, 39: 1147-1167.

Scammell, R.J. 1987. Stratigraphy, structure and metamorphism of the north flank of the Monashee Complex, southeastern British Columbia; a record of Proterozoic extension and Phanerozoic crustal thickening. M.Sc. Thesis. Carleton University. 205 pp.

Scammell, R.J. 1993. Mid-Cretaceous to Tertiary thermotectonic history of former mid-crustal rocks, southern Omineca Belt, Canadian Cordillera. PhD thesis, Queen's University, 576 pp.

Scammell, R.J., and Brown, R.L. 1990. Cover gneisses of the Monashee Terrane: a record of synsedimentary rifting in the North American Cordillera. Canadian Journal of Earth Sciences, 27: 712-726.

Scammell, R.J., and Parrish, R.R. 1993. U-Pb zircon chronometry from a metamorphosed felsic volcaniclastic rock in cover gneisses, Monashee Terrane, southeastern British Columbia. Program with Abstracts - Geological Association of Canada; Mineralogical Association of Canada; Canadian Geophysical Union, Joint Annual Meeting, 1993: 93.

Schaubs, P.M., Carr, S.D., and Berman, R.G. 2002. Structural and metamorphic constraints on ca. 70 Ma deformation of the northern Valhalla Complex, British Columbia; implications for the tectonic evolution of the southern Omineca Belt. Journal of Structural Geology, 24: 1195-1214.

Schumacher, J.C. 1988. Stratigraphy and geochemistry of the Ammonoosuc Volcanics, central Massachusetts and southwestern New Hampshire. American Journal of Science, 288: 619-663.

Sears, J.W. 1979. Tectonic constrasts between infrastructure and suprastructure of the Columbian orogen, Albert Peak area, western Selkirk Mountains, British Columbia. Ph.D. thesis, Queen's University, 154 pp.

Sears, J.W., and Price, R.A. 2000. Early Cambrian separation of the Siberian craton from western Laurentia; implications for Cordilleran pericratonic terranes. Abstracts with Programs - Geological Society of America, 32: 67-68.

Sederholm, J.J. 1934. On migmatites and associated pre-Cambrian rocks of southwestern Finland. Bulletin of the Commission Geologique de Finlande, 23: 1-110.

Sevigny, J.H. 1988. Geochemistry of Late Proterozoic amphibolites and ultramafic rocks, southeastern Canadian Cordillera. Canadian Journal of Earth Sciences, 25: 1323-1337.

Sevigny, J.H., and Thériault, R.J. 2003. Geochemistry and Sr-Nd isotopic composition of Eocene lamprophyre dykes, southeastern British Columbia. Canadian Journal of Earth Sciences, 40: 853-864.

Sevigny, J.H., Parrish, R.R., and Ghent, E.D. 1989. Petrogenesis of peraluminous granites, Monashee Mountains, southeastern Canadian Cordillera. Journal of Petrology, 30: 557-581.

Sevigny, J.H., Parrish, R.R., Donelick, R.A., and Ghent, E.D. 1990. Northern Monashee Mountains, Omineca crystalline belt, British Columbia; timing of metamorphism, anatexis, and tectonic denudation. Geology, 18: 103-106.

Sinha, K.A., Wayne, D.M., and Hewitt, D.A. 1992. The hydrothermal stability of zircon: preliminary experimental and isotopic studies. Geochimica and Cosmochimica Acta, 56: 3551-3560.

Smith, M.S., Dymek, R.F., and Schneiderman, J.S. 1992. Implications of trace element geochemistry for the origin of cordierite-orthoamphibole rocks from Orijarvi, SW Finland. Journal of Geology, 100: 545-559.

Spark, R.N. 2001. Crustal thickening and tectonic denudation within the Thor-Odin culmination, Monashee complex, southern Canadian Cordillera. PhD Thesis, University of New Brunswick, 302 pp.

Spark, R.N., and Williams, P.F. 1996. Digital terrain models and the visualization of structural geology. Computer Methods in the Geosciences, 15: 421-446.

Spear, F.S. 1993. Metamorphic phase equilibria and pressure-temperature-time paths. Mineralogical Society of America, 799 pp.

Spear, F.S. 2004. Fast cooling and exhumation of the Valhalla metamorphic core complex, southeastern British Columbia. International Geology Review, 46: 193-209.

Spear, F.S., and Schumacher, J.C. 1982. Chapter 1, Phase relations of metamorphic amphiboles; natural occurrence and theory; Orthoamphibole and cummingtonite amphibolites; origin of cordierite-anthophyllite rocks. *In* Amphiboles; petrology and experimental phase relations. *Edited by* D.R. Veblen and P.H. Ribbe. Reviews in Mineralogy, 9B, 160-163.

Spear, F.S., Kohn, M.J., and Cheney, J.T. 1999. P-T paths from anatectic pelites. Contribution to Mineralogy and Petrology, 134: 17-32.

Stern, R.A. 1997. The GSC Sensitive High Resolution Ion Microprobe (SHRIMP): analytical techniques of zircon U-Th-Pb age determinations and performance evaluation: *In* Radiogenic Age and Isotopic Studies, Report 10, Geological Survey of Canada, Current Research 1997-F, 1-31.

Stern, R.A. 1999. In situ zircon trace element analysis by high mass-resolution SIMS. Ninth Annual V.M. Goldschmidt Conference, 284-285.

Stern, R.A., and Amelin, Y. 2003. Assessment of errors in SIMS zircon U-Pb geochronology using a natural zircon standard and NIST SRM 610 glass; Chemical Geology, 197: 111-146.

Stern, R.A., and Berman, R.G. 2000. Monazite U-Pb and Th-Pb geochronology by ion microprobe, with application to in situ dating of an Archean metasedimentary rock. Chemical Geology, 172: 113-130.

Stern, R.A., and Sanborn, N. 1998. Monazite U-Pb and Th-Ph geochronology by high-resolution secondary ion mass spectrometry. Radiogenic age and isotopic studies: Report 11. Geological Survey of Canada, Current Research Report, 1998-F: 1-18.

Struik, L.C. 1993. Intersecting intracontinental Tertiary transform fault systems in the North American Cordillera. Canadian Journal of Earth Sciences, 30: 1262-1274.

Solar, G.S., and Brown, M. 2001. Petrogenesis of migmatites in Maine, USA; possible source of peraluminous leucogranite in plutons? Journal of Petrology, 42: 789-823.

Souther, J.G. 1991. Volcanic regimes, Chapter 14. *Edited by* H. Gabrielse and C.J. Yorath. *In* Geology of the Cordilleran Orogen in Canada, no. 4, 457-490.

Sun, S.-S., and McDonough, W.F. 1989. Chemical and isotopic systematics of oceanic basalts: implications for mantle composition and processes. *In* Magmatism in ocean basins *Edited by*: Saunders A.D. and Norry M.J. Geological Society of London Special Publication, 42: 313-345.

Sun, M., Armstrong, R.L., and Maxwell, R.J. 1991. Proterozoic mantle under Quesnellia; variably reset Rb-Sr mineral isochrons in ultramafic nodules carried up in Cenozoic volcanic vents of the southern Omineca Belt. Canadian Journal of Earth Sciences, 28: 1239-1253.

Sylvester, P.J. 1998. Post-collisional strongly peraluminous granites. Lithos, 45: 29-44.

Taylor, S.R., and McLennan, S.M. 1985. The Continental Crust: Its Composition and Evolution. Oxford, Blackwell Scientific, 312 pp.

Taylor, S.R., and McLennan, S.M. 1995. The geochemical evolution of the continental crust. Reviews of Geophysics, 33: 241-265.

Tempelman-Kluit, D., and Parkinson, D. 1986. Extension across Eocene Okanagan crustal shear in southern British Columbia. Geology, 14: 318-321.

Tera, F., and Wasserburg, G.J. 1972. U-Th-Pb systematics in three Apollo 14 basalts and the problem of initial Pb in lunar rocks. Earth and Planetary Science Letters, 14: 281-283.

Teyssier, C., Ferré, E., Whitney, D.L., Norlander, B., Vanderhaeghe, O., and Parkinson, D. In review. Flow of partially molten crust and origin of detachments during collapse of the Cordilleran orogen. Submitted to Geological Society of London, Symposium volume Channel flow, ductile extrusion and exhumation of lower-mid-crust in continental collision zones.

Vallence, T.G. 1967. Mafic rock alteration and isochemical development of some cordierite-anthophyllite rocks. Journal of Petrology, 8: 84-96.

Vanderhaeghe, O., Ledru, P., Thieblemont, D., Egal, E., Cocherie, A., Tegyey, M., and Milesi, J-P. 1998. Contrasting mechanism of crustal growth; geodynamic evolution of the Paleoproterozoic granite-greenstone belts of French Guiana. Precambrian Research, 92: 165-194.

Vanderhaeghe, O., Teyssier, C., and Wysoczanski, R. 1999. Structural and geochronological constraints on the role of partial melting during the formation of the Shuswap metamorphic core complex at the latitude of the Thor-Odin dome, British Columbia. Canadian Journal of Earth Sciences, 36: 917-943.

Vanderhaeghe, O., Teyssier, C., McDougall, I., and Dunlap, D.W. 2003. Cooling and exhumation of the Shuswap metamorphic core complex constrained by $^{40}Ar/^{39}Ar$ thermochronology. Geological Society of America Bulletin, 115: 200-216.

van der Pluijm, B.A., Hall, C.M. Vrolijk, P.J., Pevear, D.R., and Covey, M.C. 2001a. The dating of shallow faults in the Earth's crust. Nature, .412: 172-175.

van der Pluijm, B.A., Hall, C.M., Vrolijk, P., and Pevear, D. 2001b. Ar dating of faults in the southern Canadian Rockies; the Rundle and McConnell thrust systems.

Abstracts with Programs - Geological Society of America, 33: 25.

Vernon, R.H. and Collins, W.J. 1988. Igneous microstructures in migmatites. Geology, 16: 1126-1129.

Villaseca, C., Barbero, L., and Rogers, G. 1988. Crustal origin of Hercynian peraluminous granitic batholiths of central Spain; petrological, geochemical and isotopic (Sr, Nd) constraints. Lithos, 43: 55-79.

Watson, E.B. 1996. Dissolution, growth and survival of zircons during crustal fusion: kinetic principles, geological models and implications for isotopic inheritance. Transactions of the Royal Society of Edinburgh, 87: 43-56.

Watt, G.R., Burns, I. M., and Graham, G. A. 1996. Chemical characteristics of migmatites: accessory phase distribution and evidence for fast melt segregation rates. Contributions to Mineralogy and Petrology, 125: 100-111.

Weber, C., and Barbey, P. 1986. The role of water, mixing processes and metamorphic fabric in the genesis of the Baume Migmatites (Ardeche, France). Contributions to Mineralogy and Petrology, 92: 481-491.

Wheeler, J.O. 1965. Big Bend map area, British Columbia. Geological Survey of Canada, Paper 64-32: 1-37.

Wheeler, J.O., and McFeely, P. 1991. Tectonic assemblage map of the Canadian Cordillera and adjacent parts of the United States of America: geological Survey of Canada, Map 17121, scale 1:2 000 000.

White, A.J.R., and Chappell, B.W. 1990. Per migma ad magma downunder. Geological Journal, 25: 221-225.

Whitney, D.L., Teyssier, C., and Vanderhaeghe, O. 2004. Gneiss domes and crustal flow. Special Paper - Geological Society of America, 380: 15-33.

Williams, M.L., Jercinovic, M.J., and Terry, M.P. 1999. Age mapping and dating of monazite on the electron microprobe; deconvoluting multistage tectonic histories. Geology, 27: 1023-1026.

Williams, P.F. 1999. Interpretation of thrust-like structures in middle and lower crustal rocks. *In* Tectonic and Magmatic processes in Crustal Growth: a Pan-Lithoprobe Perspective. Lithoprobe report 75, 67-68.

Williams, P.F., and Jiang, D. In press. An investigation of lower crustal deformation: evidence for channel flow and it's implications for tectonics and structural studies. Submitted to Journal of Structural Geology, May 2004.

Yorath, C.J. 1991. Upper Jurassic to Paleogene Assemblages, Chapter 9. *Edited by* H. Gabrielse and C.J. Yorath. *In* Geology of the Cordilleran Orogen in Canada, no. 4, 329-371.

Young, G.M. 1973. Tillites and aluminous quartzites as possible time markers for middle Precambrian (Aphebian) rocks of North America. Special Paper - Geological Association of Canada, 12: 97-127.

Xue, X., Baadsgaard, H., Irving, A.J., and Scarfe, C.M. 1990. Geochemical and isotopic characteristics of lithospheric mantle beneath West Kettle River, British Columbia; evidence from ultramafic xenoliths. Journal of Geophysical Research, B, 95: 15 879-15 891.

Zeng, L., Saleeby, J.B., and Asimow, P. 2005. Nd isotope disequilibrium during crustal anatexis; a record from the Goat Ranch migmatite complex, southern Sierra Nevada Batholith, California. Geology, 33: 53-56.

# APPENDIX I

Analytical Methods

## Whole rock major and trace element geochemistry analytical methods

Major elements and some trace elements (Cr, Ni, Cu, Zn, Ga, Y, Zr, Nb, Ba) were analyzed by X-Ray Fluorescence (XRF) on fused disks using a Philips PW 2400X-ray fluorescence spectrometer at the University of Ottawa. XRF precision is based on six replicate runs and was 0.71% for $SiO_2$, 0.27% for $Al_2O_3$, 0.74% for $K_2O$, 6.4% for Zn. The accuracy was monitored using international references DR-N and SY-2 and was within 0.6% for $SiO_2$, 0.3% for $Al_2O_3$, 0.8% for $K_2O$, 1.6% for Zn, and better than 1% and 10% for other major and trace elements, respectively. The REE and other trace elements were analyzed at Geoscience Laboratories in Sudbury, Ontario and at ACME analytical laboratories in Vancouver, British Columbia by Inductively Coupled Plasma Mass Spectrometry (ICP-MS) using a HP 4500plus quadrupole instrument following a $HNO_3$-$HClO_4$-HF-HCl digestion. This acid digestion technique was selected because of lower detection limits for many elements and the large number of elements analyzed. The precision of the REE analyses is based on seven replicates and was mostly better than 10%, but samples with concentrations close to detection limits had precision of only 20%. The accuracy of REE analyses was monitored by international references SY-4, BIR-1 and GSR-2, was better than 10% for materials with high concentrations of REE. As some trace element rich accessory phases are resistant to acid digestion, several samples were analyzed in duplicates using more rigorous combination of fusion and acid digestion. A comparison of 6 samples had precision for the REE mostly better than 10%, and therefore concerns about the effects of incomplete acid digestion are minimal.

## Whole rock isotope geochemistry analytical methods

Rubidium-strontium and samarium-neodymium isotopic analyses were carried at the Carleton University. Powdered samples were each dissolved with 1 ml of doubly distilled $HNO_3$ and HF for 2 to 7 days. The samples were loaded onto columns with Dowex

50WX8 resin for Sr and initial REE-group separation. The Sm-Nd isotopic concentration and isotope dilution fractions were pipetted into Teflon columns using 2x 0.15N HCl to separate these elements from the rest of the REE. The Nd was removed for using 2x 0.17N HCl.

The Sr and Sm-Nd fractions were loaded separately on outgassed single Ta filaments and double Re filaments for analysis on a Finnegan MAT 261 thermal ionization mass spectrometer. The isotopic composition fractions were measured using the Faraday multicollector routine, which collects 15 blocks of 10 scans, with on line drift and mass fractionation correction and statistical analysis. The $^{87}Sr/^{86}Sr$ and $^{143}Nd/^{144}Nd$ errors are reported to $2\sigma$ (95%) confidence intervals and were directly measured from the mass spectrometer. The $^{87}Rb/^{86}Sr$ and the $^{147}Sm/^{144}Nd$ ratio were calculated based on the measured Rb and Sr concentrations from the whole rock ICP-MS values. The estimated uncertainties, at the $2\sigma$ level, equate to a precision of 1% for the $^{147}Sm/^{144}Nd$ and $^{87}Sr/^{86}Sr$ ratios and the concentrations are reproducible to 0.5%. Based on numerous runs from September 1992 to October 2004 the La Jolla standard gave an average $^{143}Nd/^{144}Nd$ value of $0.511876 \pm 0.00018$ and the Sr standard NBS-987 gave an average $^{87}Sr/^{86}Sr$ value of $0.71025 \pm 0.00003$.

**U-Pb zircon and monazite SHRIMP analytical methods**

Ion microprobe analysis of zircon and monazite was performed using the SHRIMP II at the Geological Survey of Canada, following the procedure described by Stern (1997), with standards and U-Pb calibration methods following Stern and Amelin (2003). Grains were cast in 2.5 cm diameter epoxy mounts (GSC #283) along with fragments of the GSC laboratory standard zircon (z6266), which has a $^{206}Pb/^{238}U$ age of 559 Ma, and standard monazite (3345), which has a $^{206}Pb/^{238}U$ age of 1821 Ma. Internal sections of the grains were exposed by grinding and polishing using 9, 6, and 1 μm diamond compound. The internal features of the monazite and zircon grains (such as zoning, internal domains and alteration) were characterized with cathodoluminescence (CL) and backscattered

electron (BSE) imaging utilizing a Cambridge Instruments scanning electron microscope. Grain-mount surfaces were evaporatively coated with 10 nm Au of high purity. SHRIMP analyses were conducted using an $^{16}O^-$ primary beam, projected onto the zircons at 10 kV. The sputtered area used for analysis was ca. 35 μm in diameter with a beam current of ca. 13 nA. For the zircon analyses, the count rates of ten isotopes of $Zr^+$, $U^+$, $Th^+$, and $Pb^+$ in zircon were sequentially measured over 5 scans with a single electron multiplier and a pulse counting system that has a deadtime of 35 ns. For the monazite analyses, the count rates of nine isotopes of $CePO^+$, $Zr^+$, $U^+$, $Th^+$, and $Pb^+$ in monazite were sequentially measured over 6 scans with a single electron multiplier and a pulse counting system that has a deadtime of 35 ns. Off-line data processing was accomplished using customized in-house software. A 1σ external error for $^{206}Pb/^{238}U$ ratios reported in the data tables incorporate a ±1.1% error in calibrating the standard zircon (see Stern and Amelin, 2003). No fractionation correction was applied to the Pb-isotope data. The common Pb correction utilized the measured $^{204}Pb/^{206}Pb$ ratios and compositions modeled after Cumming and Richards (1975). Isoplot v. 2.49 (Ludwig, 2001) was used to calculate weighted means.

**Chemical mapping of monazite analytical methods**

Chemical maps of Y, Ca, Th, and U of selected monazites from each sample dated by U-Pb SHRIMP analysis were made using a Cameca SX-50 electron microprobe at the University of Massachusetts according to procedures outlined by Williams et al. (1999). High resolution X-ray maps of Y, Ca, Th, and U were created using a high sample current (>200 nA), a small step size (~ 0.5 μm), and rastering the electron beam. These chemical maps were obtained prior to the SHRIMP analysis and provided guidance for target location on the selected monazite grains.

# APPENDIX II

## Sample Details amd Locations

| Sample | Easting | Northing | Sample Description[a] | Location | Geochro-nology[be] | Geochem-istry[ce] | Isotopic Geochemistry[de] |
|---|---|---|---|---|---|---|---|
| AH-02-001 | 5600579 | 423386 | Amphibolite with leucosome | Frigg Glacier | | s | |
| AH-02-002 | 5600597 | 423416 | Bt granodiorite gneiss | Frigg Glacier | | s | |
| AH-02-003 | 5600049 | 423426 | Folded Grt amphibolite | Frigg Glacier | s | * | |
| AH-02-004 | 5600302 | 423299 | Folded Grt amphibolite | Frigg Glacier | s | * | |
| AH-02-005 | 5600302 | 423299 | Stromatic Bt granitic leucosome | Frigg Glacier | s | * | * |
| AH-02-006 | 5600302 | 423299 | Folded stromatic Ms-Bt granitic leucosome | Frigg Glacier | s | * | * |
| AH-02-007 | 5600318 | 423313 | Kfs augen granodiorite gneiss | Frigg Glacier | s | * | * |
| AH-02-008 | 5600311 | 423307 | Folded stromatic Bt granitic leucosome | Frigg Glacier | s | * | * |
| AH-02-009 | 5600301 | 423239 | Crosscutting phenocrystic Bt granitic leucosome | Frigg Glacier | s | * | * |
| AH-02-010 | 5600336 | 423270 | Sheared, stromatic Bt granititc leucosome | Frigg Glacier | s | * | * |
| AH-02-011 | 5600689 | 423291 | Sheared, stromatic Bt granititc leucosome | Frigg Glacier | s | * | * |
| AH-02-012 | 5600669 | 423299 | Bt granodiorite gneiss | Frigg Glacier | s | * | * |
| AH-02-013 | 5600386 | 423453 | Crosscutting phenocrystic Bt granitic leucosome | Frigg Glacier | s | * | * |
| AH-02-014 | 5604866 | 423934 | Sil-Grt-Ms-Bt Schist | Mt. Thor | s | s | * |
| AH-02-015 | 5604866 | 423934 | Stromatic Bt granitic leucosome | Mt. Thor | s | s | |
| AH-02-016 | 5604836 | 423897 | Crosscutting Grt-Tur-Bt Pegmatitic Dyke | Mt. Thor | s | * | |
| AH-02-017 | 5605001 | 423837 | Di calc-silicate (locally rich grt) | Mt. Thor | | s | |
| AH-02-018 | 5605058 | 423582 | Sil-Grt-Ms-Bt Schist layered felsic schist | Mt. Thor | | s | |
| AH-02-019 | 5604913 | 423274 | Crosscutting Grt-Tur-Bt Pegmatitic Dyke | Mt. Thor | s | * | |
| AH-02-020 | 5605100 | 423382 | Quarzite | Mt. Thor | s | s | |
| AH-02-021 | 5605078 | 423605 | Sil-Grt-Ms-Bt Schist | Mt. Thor | s | s | |
| AH-02-022 | 5605064 | 423568 | Sil-Grt-Ms-Bt Schist (more felsic zone) | Mt. Thor | | s | |
| AH-02-023 | 5605208 | 423517 | Quartzite | Mt. Thor | | s | |
| AH-02-024 | 5605181 | 423381 | Quarzite (basal) | Mt. Thor | s | * | |
| AH-02-025 | 5604712 | 423935 | Marble | Mt. Thor | s | s | |
| AH-02-026 | 5602040 | 417252 | Folded stromatic Bt granitic leucosome | Saturday Glacier | s | * | * |
| AH-02-027 | 5602034 | 417245 | Phenocrystic Ms-Bt granitic leucosome | Saturday Glacier | s | * | * |
| AH-02-028 | 5602033 | 417260 | Bt-Qtz-Kfs paragneiss | Saturday Glacier | s | * | * |
| AH-02-029 | 5602034 | 417252 | Crosscutting pegmatitic Ms-Bt granitic leucosome | Saturday Glacier | s | * | |

[a]Mineral abbreviations after Kretz (1983). [b]Geochonology = U-Pb zircon and monazite samples. [c]Geochemistry = whole rock XRF and ICP-MS. [d]Isotopic geochemistry = whole rock Rb/Sr and Sm/Nd TIMS. [e] * Indicates samples was analyzed, s indicates that a sample was taken but not analyzed.

| Sample | Easting | Northing | Sample Description[a] | Location | Geochronology[be] | Geochemistry[ce] | Isotopic Geochemistry[de] |
|---|---|---|---|---|---|---|---|
| AH-02-030 | 5602028 | 417243 | Grt-Sil-Qtz-Kfs-Pl paragneiss | Saturday Glacier | s | * | |
| AH-02-031 | 5601694 | 417513 | Felsic layer within Grt-Sil-Qtz-Kfs-Pl paragneiss | Saturday Glacier | | s | |
| AH-02-032 | 5601895 | 417407 | Ms-Sil-Grt-Di paragneiss | Saturday Glacier | | s | |
| AH-02-033 | 5602012 | 417150 | Crosscutting phenocrystic Bt granitic leucosome | Saturday Glacier | s | s | |
| LB-01-01 | 5513350 | 466600 | Ladybird Bt leucogranite | Slocan Lake | | * | * |
| LB-01-02 | 5513560 | 466550 | Ladybird Bt leucogranite | Slocan Lake | | * | * |
| LB-01-03 | 5513220 | 466700 | Ladybird Bt leucogranite | Slocan Lake | | * | * |
| AH-03-001 | 5518582 | 467217 | Cataclastic Ladybird Ms-Bt leucogranite | Slocan Lake | | s | |
| AH-03-002 | 5518580 | 466811 | Foliated Ladybird Ms-Bt leucogranite | Slocan Lake | | s | |
| AH-03-003 | 5518257 | 466661 | Foliated Ladybird Bt leucogranite | Slocan Lake | | * | * |
| AH-03-004 | 5518055 | 466611 | Foliated Ladybird Ms-Bt leucogranite | Slocan Lake | | s | |
| AH-03-005 | 5517365 | 466410 | Foliated Ladybird Ms-Bt leucogranite | Slocan Lake | | * | |
| AH-03-006 | 5587489 | 391283 | Foliated Ladybird Ms-Bt granite | Sugar Lake | | * | * |
| AH-03-007 | 5589929 | 393055 | Ladybird Bt granite | Sugar Lake | | * | * |
| AH-03-008 | 5589953 | 393059 | Pegmatitic Ladybird Ms-Bt granite | Sugar Lake | | s | |
| AH-03-009 | 5590126 | 393365 | Magma mingling Bt granite and Bt leucogranite | Sugar Lake | | | |
| AH-03-010 | 5579769 | 392429 | Phyllite | Sugar Lake | | | |
| AH-03-011 | 5587739 | 394881 | Pegmatitic Ladybird Ms-Bt granite | Sugar Lake | | s | |
| AH-03-012 | 5588528 | 396224 | Pegmatitic Ladybird Ms-Bt granite | Sugar Lake | s | * | * |
| AH-03-013 | 5588765 | 401342 | Ladybird Ms-Bt granite | Sugar Lake | | * | * |
| AH-03-014 | 5598701 | 418667 | Grt-Crd-Ged rock | Bearpaw Lake | * | * | * |
| AH-03-015 | 5598934 | 418472 | Sil-Crd-Grt-Ged rock | Bearpaw Lake | s | * | |
| AH-03-016 | 5599096 | 418563 | Sil-Crd-Grt-Ged rock | Bearpaw Lake | | * | |
| AH-03-017 | 5598756 | 419010 | Crosscutting pegmatitic Ms-Bt granitic leucosome | Bearpaw Lake | | * | |
| AH-03-018 | 5598744 | 419009 | Bt-Qtz-Kfs-Pl paragneiss | Bearpaw Lake | | * | * |
| AH-03-019 | 5598825 | 418966 | Folded stromatic Ms-Bt granitic leucosome | Bearpaw Lake | | * | |
| AH-03-020 | 5598801 | 419176 | Crosscutting phenocrystic Ms-Bt granitic leucosome | Bearpaw Lake | | * | * |
| AH-03-021 | 5598790 | 419186 | Hbl-Qtz-Kfs-Pl paragneiss | Bearpaw Lake | | * | |

[a]Mineral abbreviations after Kretz (1983). [b]Geochonology = U-Pb zircon and monazite samples. [c]Geochemistry = whole rock XRF and ICP-MS. [d]Isotopic geochemistry = whole rock Rb/Sr and Sm/Nd TIMS. [e] * Indicates samples was analyzed, s indicates that a sample was taken but not analyzed.

| Sample | Easting | Northing | Sample Description[a] | Location | Geochronology[be] | Geochemistry[ce] | Isotopic Geochemistry[de] |
|---|---|---|---|---|---|---|---|
| AH-03-022 | 5598883 | 419149 | Crosscutting pegmatitic Ms-Bt granitic leucosome | Bearpaw Lake | | * | |
| AH-03-023 | 5599189 | 419192 | Crd-Ged rock | Bearpaw Lake | | * | |
| AH-03-024 | 5598068 | 418812 | Grt amphibolite | Bearpaw Lake | s | * | * |
| AH-03-025 | 5598004 | 418836 | Grt-Crd-Ged rock | Bearpaw Lake | | * | * |
| AH-03-026 | 5598418 | 418513 | Sil-Grt-Crd-Ged rock | Bearpaw Lake | * | * | * |
| AH-03-027 | 5598391 | 418513 | Quartzite | Bearpaw Lake | * | * | |
| AH-03-028 | 5598704 | 418642 | Sil-Grt-Crd-Ged rock | Bearpaw Lake | s | | |
| AH-03-029 | 5598511 | 418497 | Grt amphibolite | Bearpaw Lake | s | * | * |
| AH-03-030 | 5586175 | 415498 | Ladybird Ms Kfs-phenocrystic granite | Mt Baldur | | * | * |
| AH-03-031 | 5586216 | 416123 | Ladybird Bt granite | Mt Baldur | s | * | * |
| AH-03-032 | 5586113 | 416111 | Ladybird Grt-Ms-Bt granite | Mt Baldur | | * | * |
| AH-03-033 | 5585582 | 415822 | Ladybird Ms granite | Mt Baldur | | * | * |
| AH-03-034 | 5585952 | 416348 | Ladybird Ms Kfs-phenocrystic granite | Mt Baldur | s | * | * |
| AH-03-035 | 5578737 | 424173 | Foliated Ladybird Ms-Bt granite | Arrow Park | | * | |
| AH-03-036 | 5579930 | 422451 | Foliated Ladybird Ms-Bt granite | Arrow Park | | s | |
| AH-03-037 | 5579663 | 421983 | Ladybird Bt granite | Arrow Park | | * | * |
| AH-03-038 | 5581968 | 423497 | Ladybird Bt granite | Arrow Park | | * | |

[a]Mineral abbreviations after Kretz (1983). [b]Geochonology = U-Pb zircon and monazite samples. [c]Geochemistry = whole rock XRF and ICP-MS. [d]Isotopic geochemistry = whole rock Rb/Sr and Sm/Nd TIMS. [e] * Indicates samples was analyzed, s indicates that a sample was taken but not analyzed.

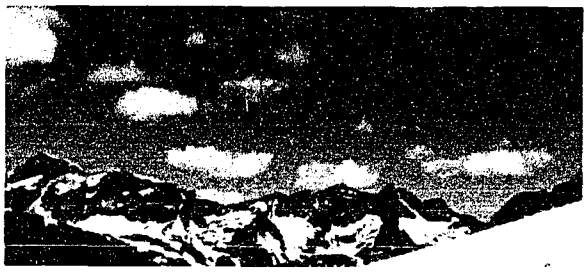


# Map 1. Cross

PRESENT

| Intermontane | Omineca Belt |
|---|---|

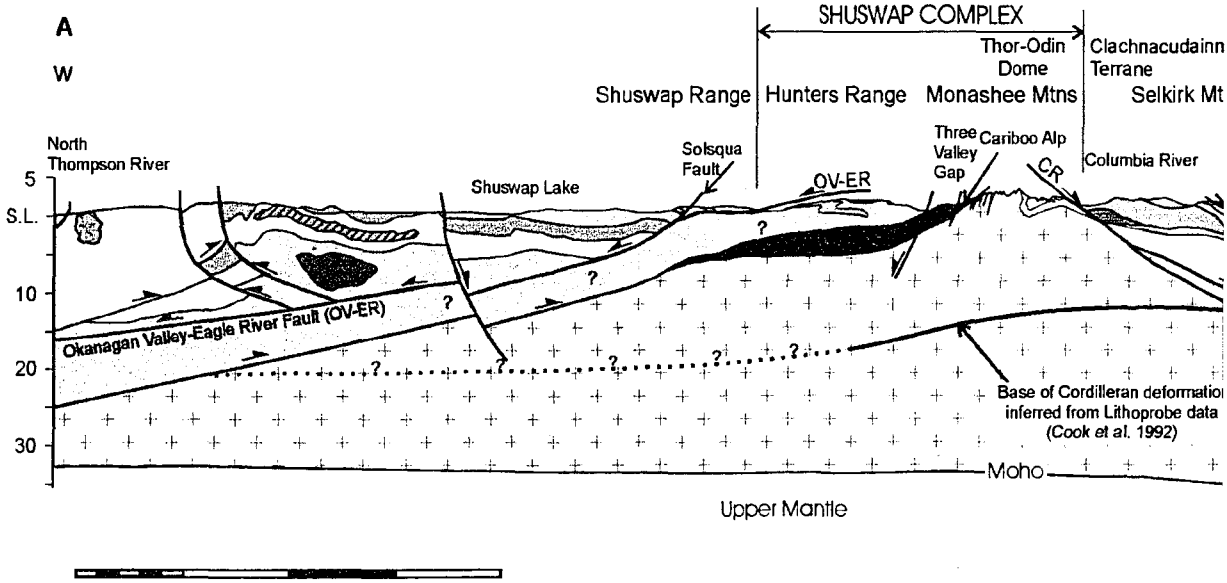


| Intermontane Belt | Western Omineca | Hunters Range |
|---|---|---|
| Cretaceous granite and qtz monzonite | Lower Paleozoic granodioritic gneiss | Lower Paleozoic Griffin |
| Triassic granite and syenite | Lower Paleozoic Eagle Bay assblg. (pericratonic?) | Upper Paleozoic Hunter assblg. (N.A. affinity?) |
| Devonian to Triassic Quesnel Terrane | Lower Paleozoic Tsalkom Fm., Sicamous Fm. (pericratonic?) | Paleozoic Three Valley (N.A. affinity?) |
| North American basement | Paleoproterozoic to Lower Paleozoic Silver Creek assblg. (pericratonic?) | North American baseme |
| | Upper Paleozoic Hunters Range assblg. (N.A. affinity?) | |
| | North American basement | |

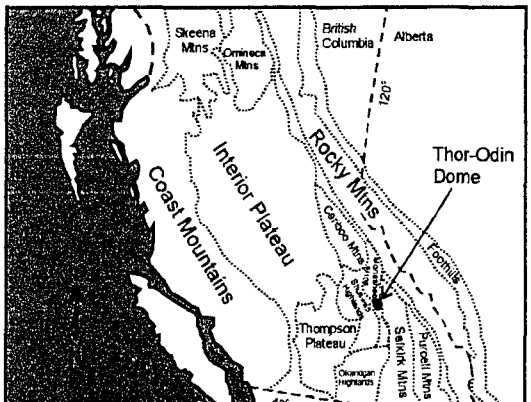



**References**

**Intermontane**

Monger, J.W.H. 1989. Overview of Cordilleran geology. In Western Canada sedimenta Canadian Society of Petroleum Geologists, 9-32.

**Western Omenica belt**

Okulitch, A.V. 1979. Lithology, stratigraphy, structure and mineral occurrences of the T Geological Survey of Canada, Open File 637.

Johnson, B.J. 1994. Structure and tectonic setting of the Okanagan Valley fault syste Columbia. Ph.D. Thesis, Carleton University, 266 pp.

**Monashee Complex**

Kruse, S., McNeill, P., and Williams, P.F. 2003. A new compilation map of the Thor-Od GAC-MAC 2003 Abstract Volume 28.

Williams P.F., and Jiang, D. in press. An investigation of lower crustal deformation: ev tectonics and structural studies. Submitted to Journal of Structural Geology,

**Selkirk Mtns**

Sears, J.W. 1979. Tectonic constrasts between infrastructure and suprastructure of th Selkirk Mountains, British Columbia. Ph.D. thesis, Queen's University, 154 pp.

Monger, J.W.H., Clowes, R.M., Price, R.A., Simony, P.S., Riddihough, R.P., and Wood Continent/Ocean Transect #7, B-2 Juan de Fuca Plate to Alberta Plains. Edited by R. Geology Continent/Ocean Transects. Geological Society of America, 2 sheets and 21.

# Map 1. Cross Section of the southeastern Canadian Cordillera

Ottawa-Carleton
Geoscience Centre

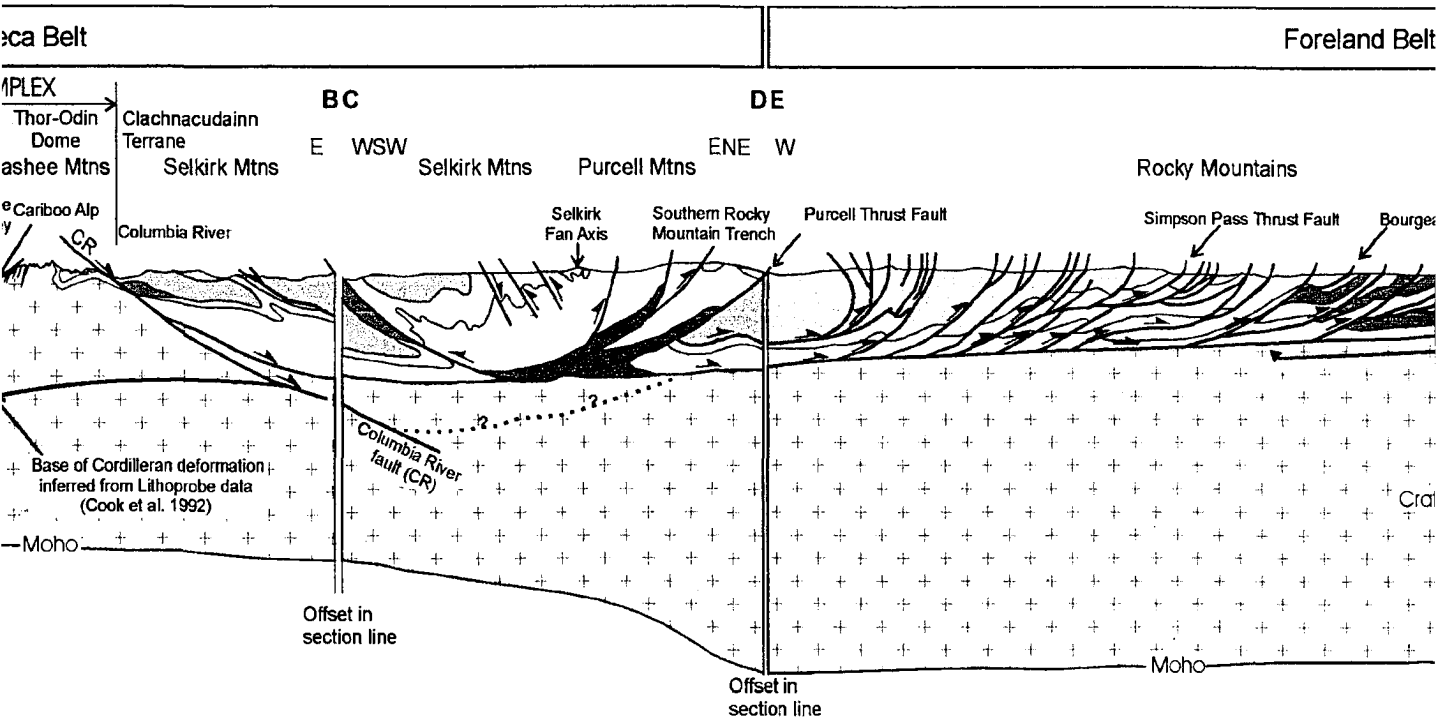


## Shuswap Complex

### Hunters Range

- Lower Paleozoic Griffin gneiss
- Upper Paleozoic Hunters Range assblg. (N.A. affinity?)
- Paleozoic Three Valley assblg. (N.A. affinity?)
- North American basement

### Monashee Complex

- Proterozoic to Paleozoic Monashee cover sequence
- North American basement

### Selkirk and Purcell Mtns.

- Lower Paleozoic Clachacudainn gneiss
- Lower Paleozoic platformal sequence and pericratonic rocks
- Lower Cambrian platformal sequence rocks (Hamill Gp., Badshot Fm.)
- Upper Proterozoic Windermere Sgp.
- Middle Proterozoic Purcell Sgp.
- North American basement

### Rocky Mou

- Cenozoic
- Mesozoic and Rocki
- Upper Pali rocks
- Lower Pal rocks
- Upper Pro
- North Amé


ology. In Western Canada sedimentary basin; a case history. Edited by B.D. Ricketts.

ure and mineral occurrences of the Thompson-Shuswap-Okanagan area, British Columbia.

g of the Okanagan Valley fault system in the Shuswap Lake area, southern British
pp.

new compilation map of the Thor-Odin culmination, Monashee complex, B.C. In:

tion of lower crustal deformation: evidence for channel flow and it's implications for
rnal of Structural Geology,

frastructure and suprastructure of the Columbian orogen, Albert Peak area, western
, Queen's University, 154 pp.
ny, P.S., Riddihough, R.P., and Woodsworth, G.J. 1985. Centennial
Plate to Alberta Plains. Edited by R. Speed. In Decade of North American
Society of America, 2 sheets and 21.

Brown, R.L., Beaumont, C., and Willett, S.D. 1993. Comparison of the Selkirk fan structure with mechanical n
interpretation of the southern Canadian Cordillera. Geology, 21: 1015-1018.
Crowley, J.L., and Brown, R.L. 1994. Tectonic links between the Clachnacudainn Terrane and Selkirk Allochth
Belt, Canadian Cordillera. Tectonics,.13: 1035-1051.

**Foreland**

Monger, J.W.H., Clowes, R.M., Price, R.A., Simony, P.S., Riddihough, R.P., and Woodsworth, G.J. 1985. Cen
Transect #7, B-2 Juan de Fuca Plate to Alberta Plains. Edited by R. Speed. In Decade of North American Ge
Transects. Geological Society of America, 2 sheets and 21.
Price, R.A., and Mountjoy, E.W. 1970. Geologic structure of the Canadian Rocky Mountains between Bow an
report. In: Structure of the southern Canadian Cordillera. Edited by: J.O. Wheeler. Geological Association of C

**Subsurface**

Cook F.A., Varsek, J.L., Clowes, R.M., Kanasewich, E.R., Spencer, C.S., Parrish, R.R., Brown, R.L., Carr, S.D
Price, R.A. 1992. Lithoprobe crustal reflection cross section of the southern Canadian Cordillera; 1, Foreland
Fraser River Fault. Tectonics, 11: 12-35.
Brown, R.L., Carr, S.D., Johnson, B.J., Coleman, V.J., Cook, F.A., and Varsek, J.L. 1992. The Monashee déc
Canadian Cordillera; a crustal-scale shear zone linking the Rocky Mountain foreland belt to lower crust benea
Thrust Tectonics. Edited by K.R. McClay. Chapman and Hall, London, 357-364.
Cook F.A.,and Van der Velden, A.J. (Unpublished). Unpublished seismic re-interpreted of lines 6 to 10, south

# nadian Cordillera

Ottawa-Carleton Geoscience Centre

Foreland Belt | Interior Plains

F

E

Rocky Mountains | Foothills

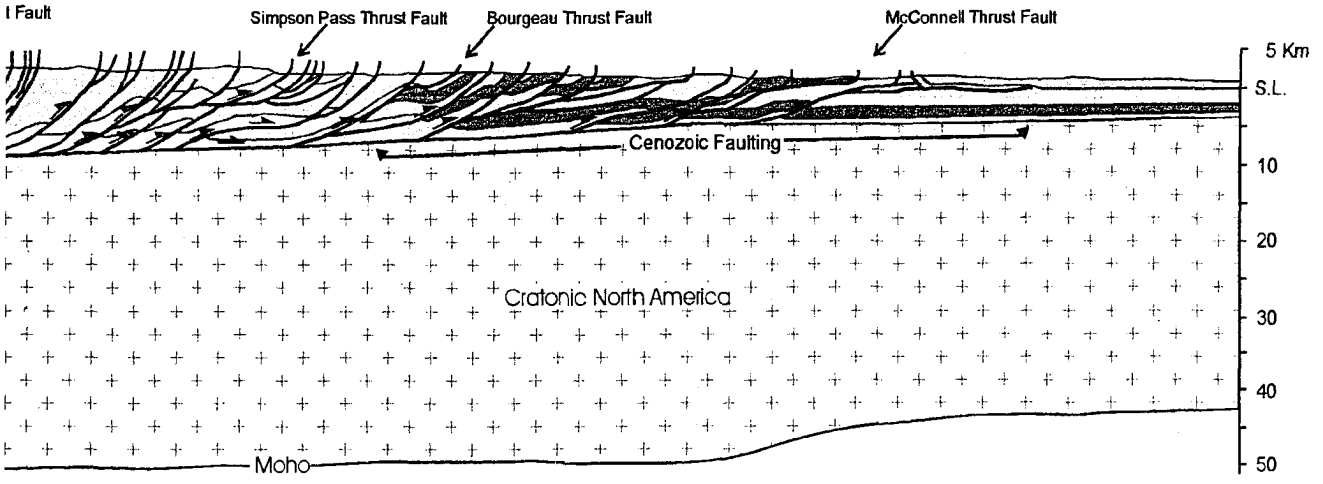


| elkirk and Purcell Mtns. | Rocky Mountains and Foothills |
|---|---|
| Lower Paleozoic Clachacudainn gneiss | Cenozoic clastic rocks of the Foothills |
| Lower Paleozoic platformal sequence and pericratonic rocks | Mesozoic clastic rocks of the Foothills and Rockies |
| Lower Cambrian platformal sequence rocks (Hamill Gp., Badshot Fm.) | Upper Paleozoic platformal sequence rocks |
| Upper Proterozoic Windermere Sgp. | Lower Paleozoic platformal sequence rocks |
| Middle Proterozoic Purcell Sgp. | Upper Proterozoic Windermere Sgp. |
| North American basement | North American basement |

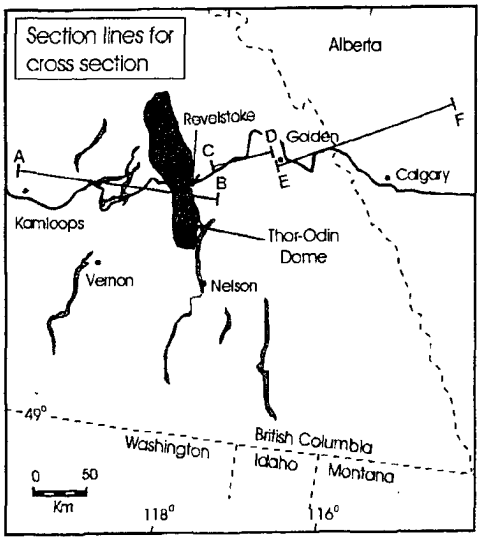



Willett, S.D. 1993. Comparison of the Selkirk fan structure with mechanical models; implications for ıadian Cordillera. Geology, 21: 1015-1018.

94. Tectonic links between the Clachnacudainn Terrane and Selkirk Allochthon, southern Omineca ics,.13: 1035-1051.

rice, R.A., Simony, P.S., Riddihough, R.P., and Woodsworth, G.J. 1985. Centennial Continent/Ocean late to Alberta Plains. Edited by R. Speed. In Decade of North American Geology Continent/Ocean America, 2 sheets and 21.

970. Geologic structure of the Canadian Rocky Mountains between Bow and Athabasca rivers; a progress rn Canadian Cordillera. Edited by: J.O. Wheeler. Geological Association of Canada Special Paper, 6. 7-25.

R.M., Kanasewich, E.R., Spencer, C.S., Parrish, R.R., Brown, R.L., Carr, S.D., Johnson, B.J., and tal reflection cross section of the southern Canadian Cordillera; 1, Foreland thrust and fold belt to 12-35.

B.J., Coleman, V.J., Cook, F.A., and Varsek, J.L. 1992. The Monashee décollement of the southern ale shear zone linking the Rocky Mountain foreland belt to lower crust beneath accreted terranes. In McClay. Chapman and Hall, London, 357-364.

J. (Unpublished). Unpublished seismic re-interpreted of lines 6 to 10, southeastern Omineca belt.


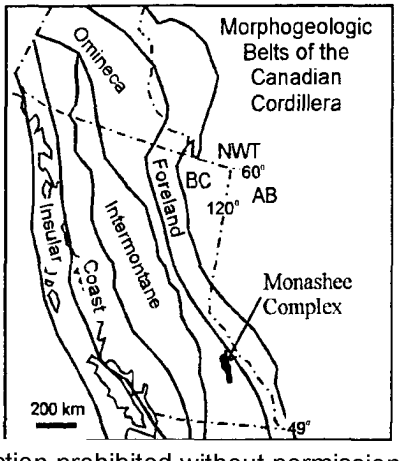

# Saturday Glacier Area, Thor-Odin Dom

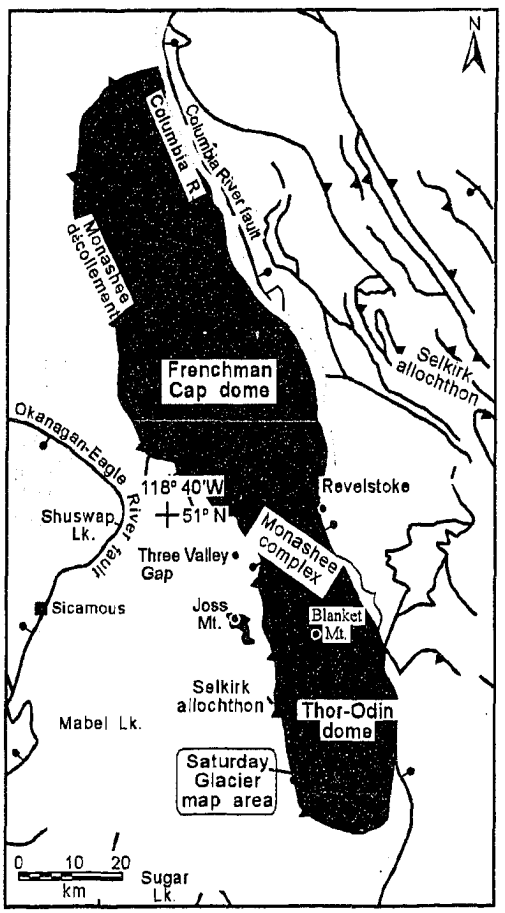


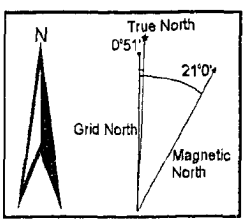


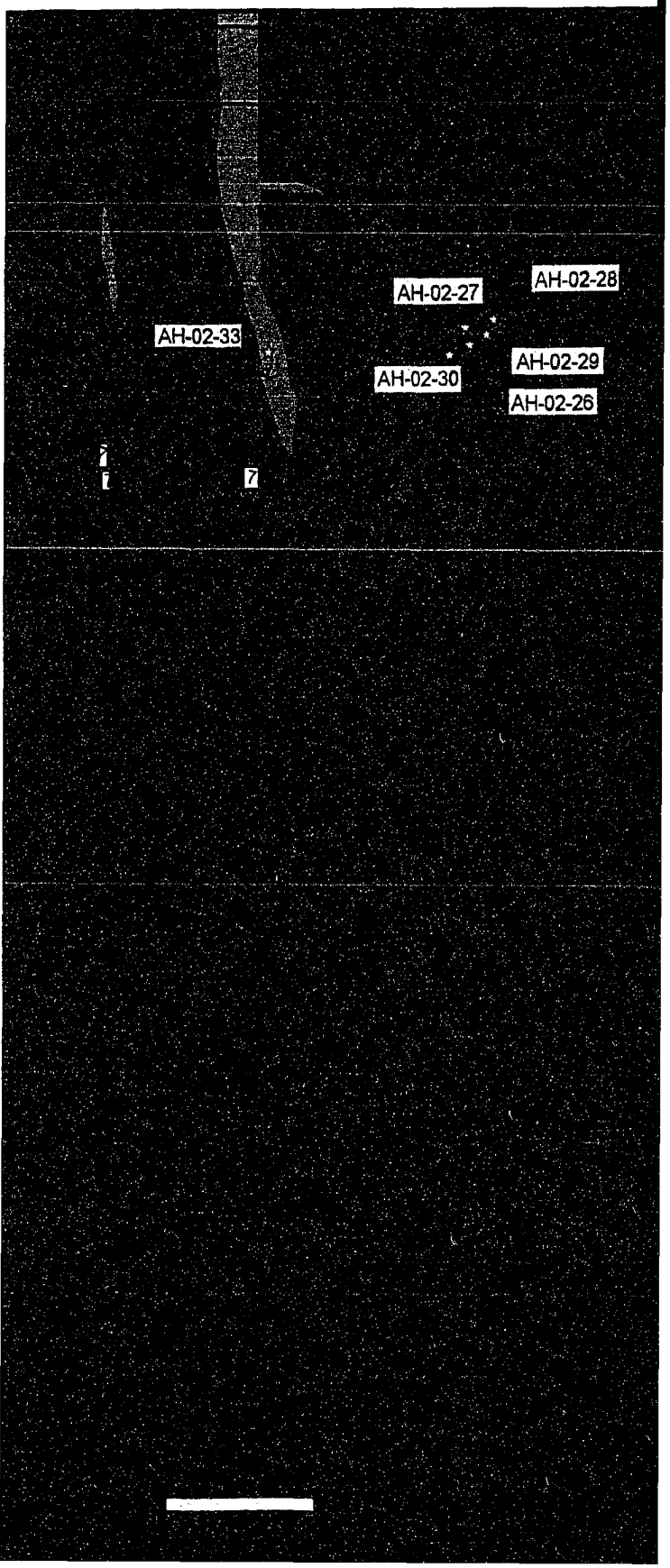


## Map 2.
## Geology map of the Saturday Glacier area, Thor-Odin dome, southeastern British Columbia.

Mapping by A.M. Hinchey, 2002

Scale 1:5 000

# aturday Glacier Area, Thor-Odin Dome, Monashee Complex

Ottawa-Carleton Geoscience Centre

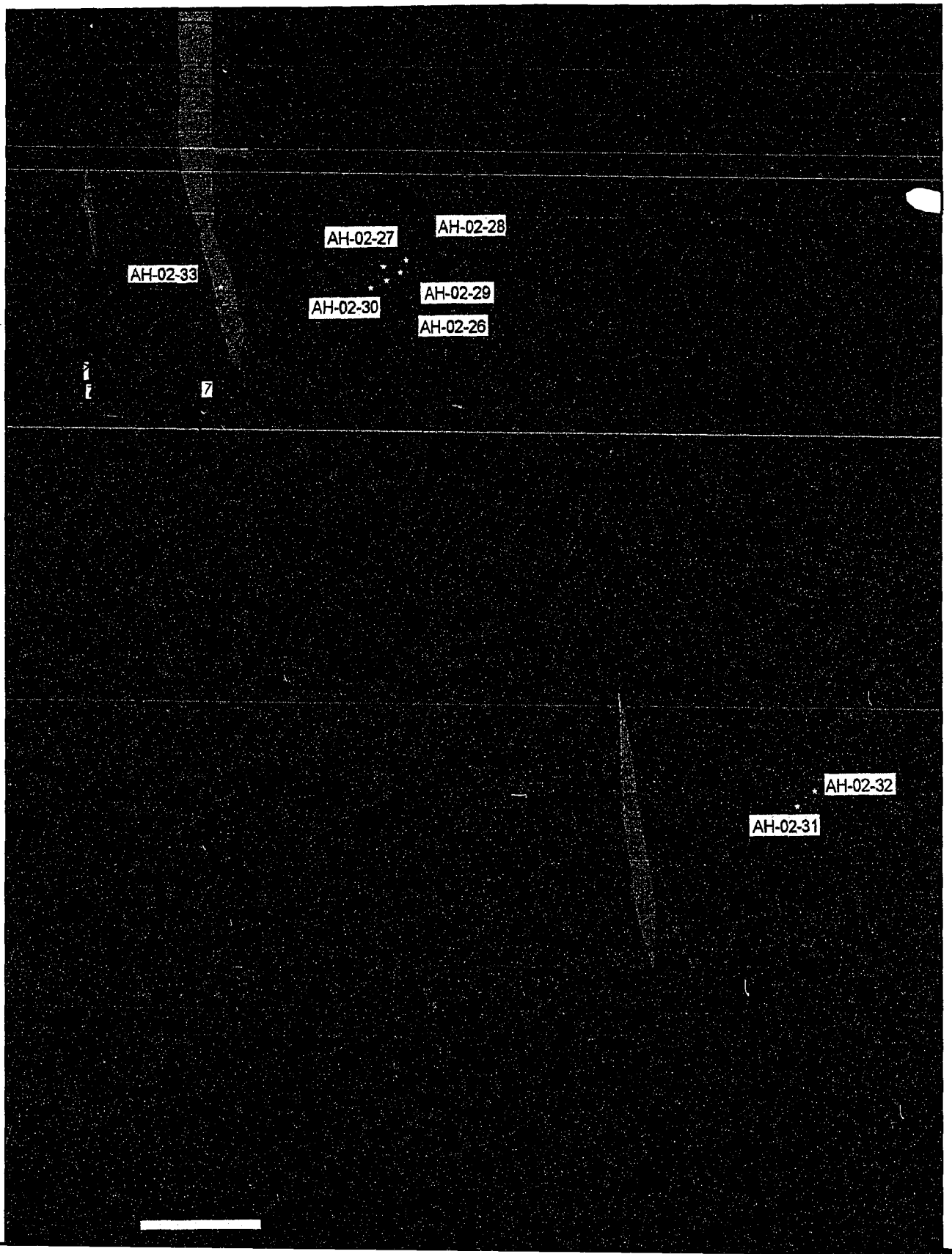

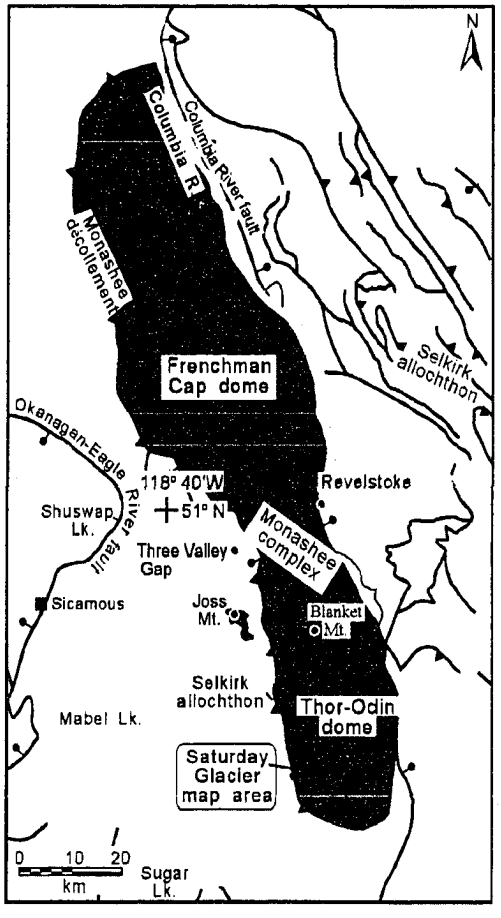


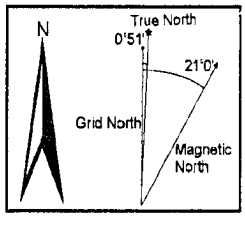


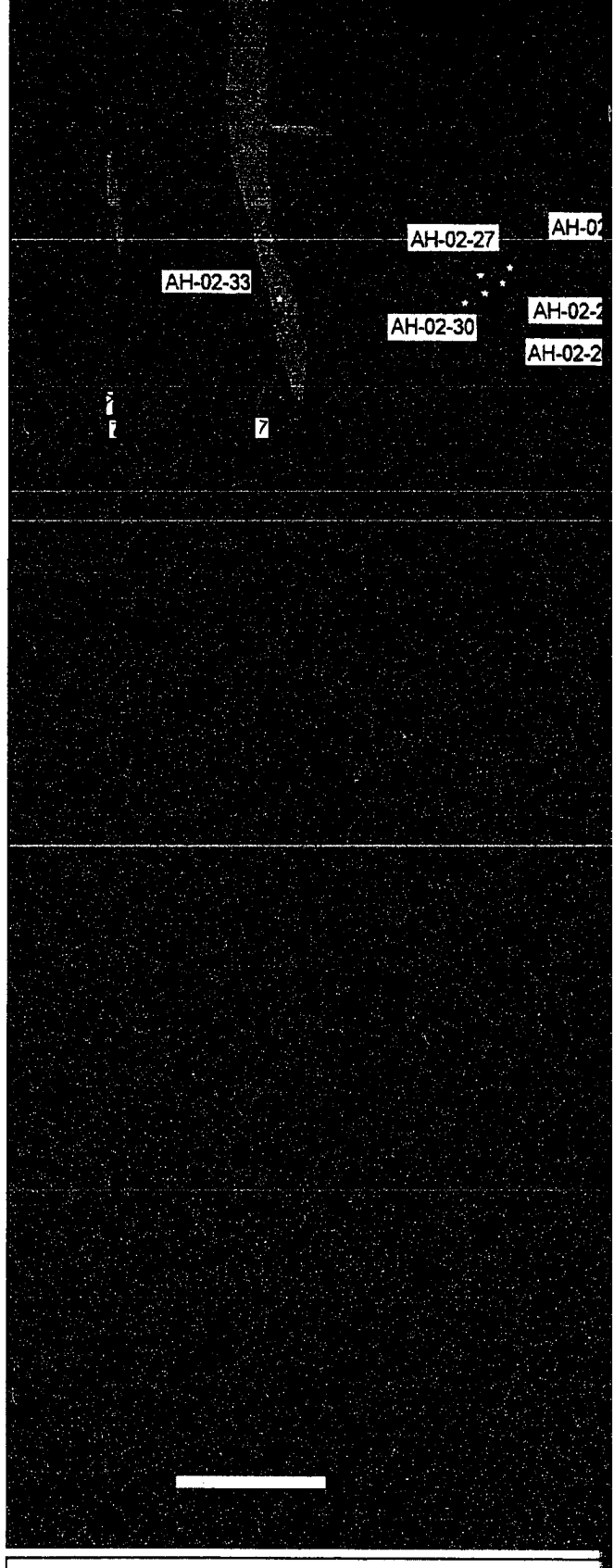


**Map 2.**
**Geology map of the Saturday Glacier area, Thor-Odin dome, southeastern British Columbia.**

Mapping by A.M. Hinchey, 2002

Scale 1:5 000
Contour interval 20 meters

Topography from digital TRIM maps provided by the Province of British Columbia Ministry of Environments and Parks: 82L.060

North American Datum - NAD 83
UTM Zone 11

Legend

- Tourmaline-garnet granite pegmatite dyke
- Amphibolite boudin
- Cordierite-biotite-quartzo feldspathic migmatite paragneiss with accessory garnet + sillimanite, and 30-50% leucosome
- Garnett-sillimanite-cordierite-quartzo feldspathic migmatite paragneiss with 15-20% leucosome

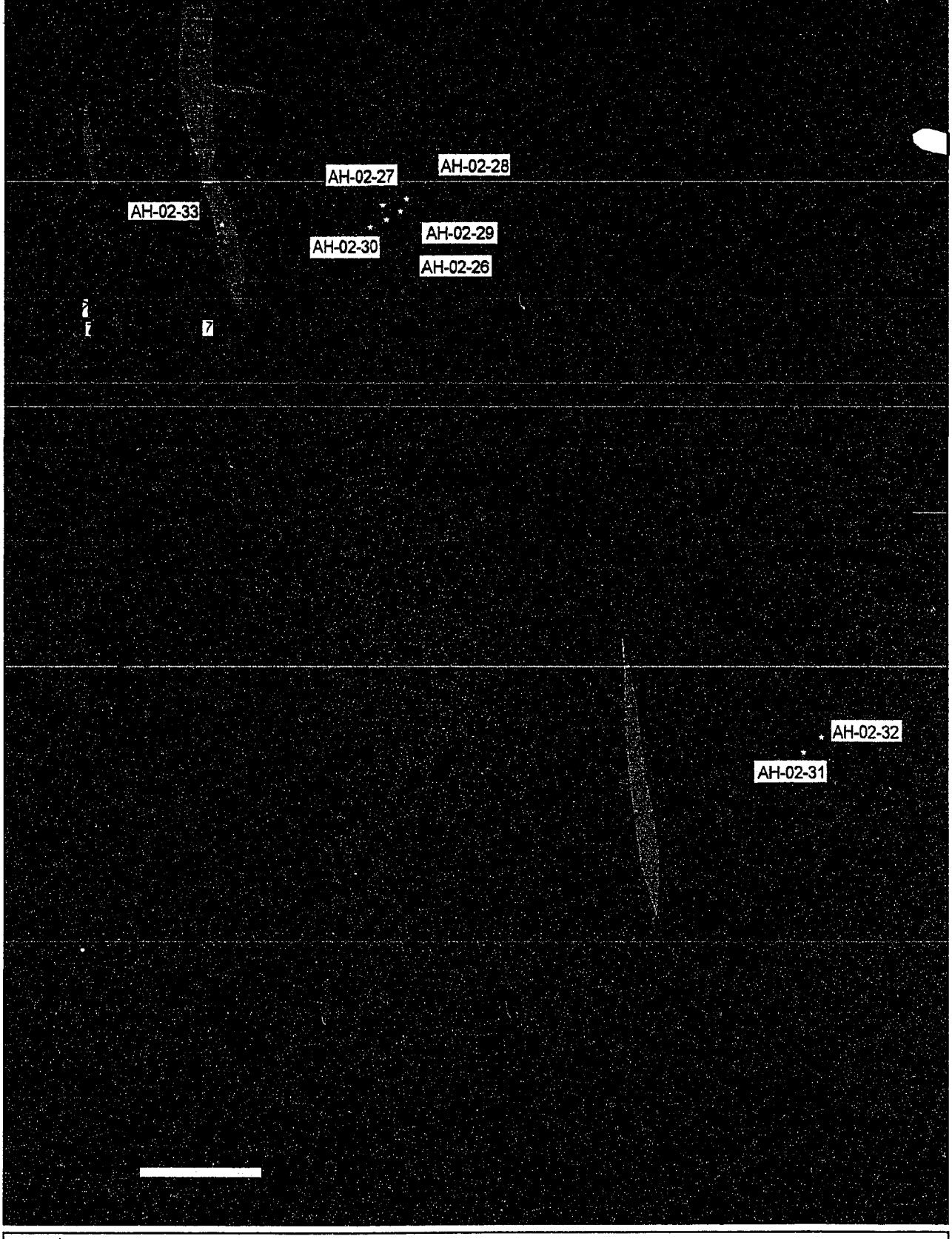


Legend

- Tourmaline-garnet granite pegmatite dyke
- Amphibolite boudin
- Cordierite-biotite-quartzo feldspathic migmatite paragneiss with accessory garnet + sillimanite, and 30-50% leucosome
- Garnett-sillimanite-cordierite-quartzo feldspathic migmatite paragneiss with 15-20% leucosome

Symbols

- Defined contact
- Approximate contact
- Strike and dip of $S_2$ foliation
- Trend and plunge of $L_2$ mineral lineation
- Sample location
- Glacier boundary

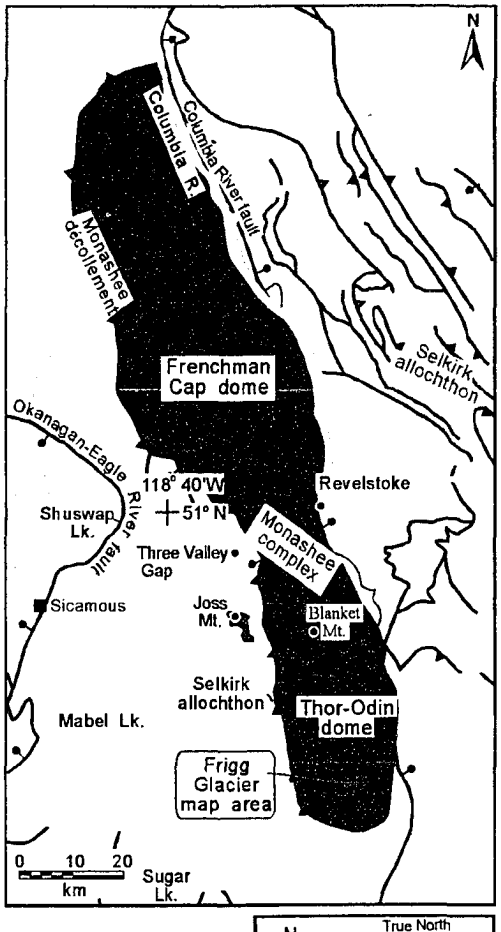


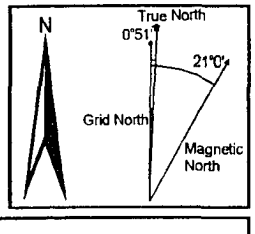


# Frigg Glacier Area, Thor-Odin Dome,

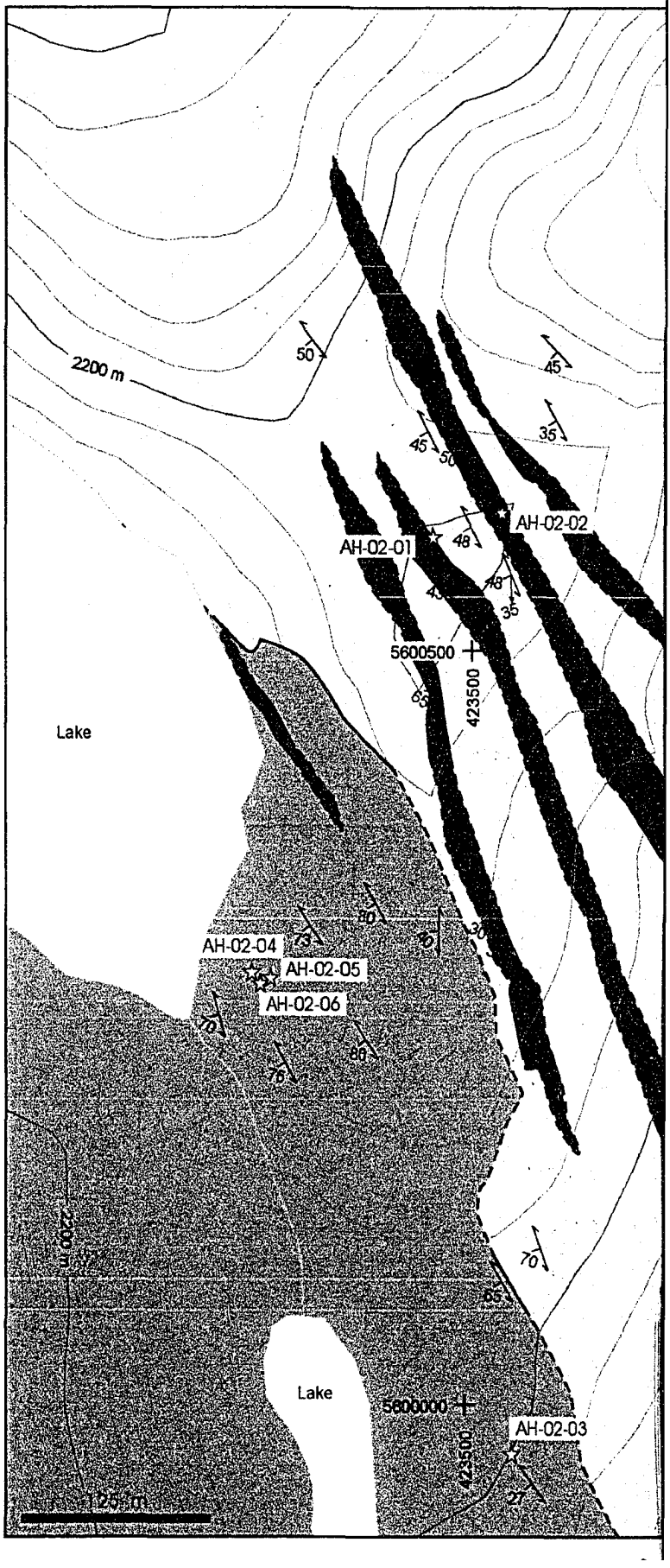


## Map 3.
## Geology map of the Frigg Glacier area, Thor-Odin dome, southeastern British Columbia

Mapping by A.M. Hinchey, 2002

Scale 1:5 000
Contour interval 20 meters

# Frigg Glacier Area, Thor-Odin Dome, Monashee Complex

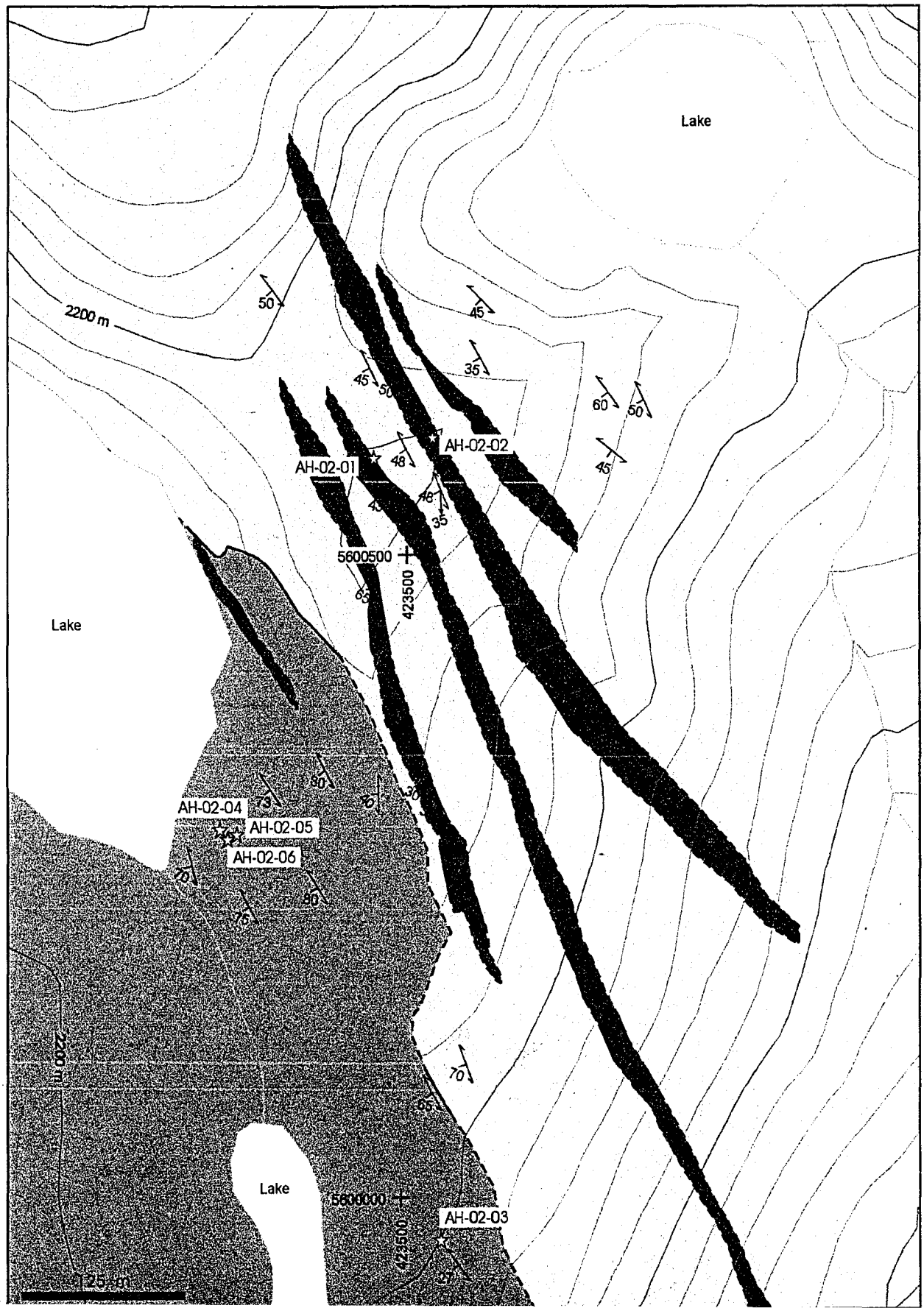

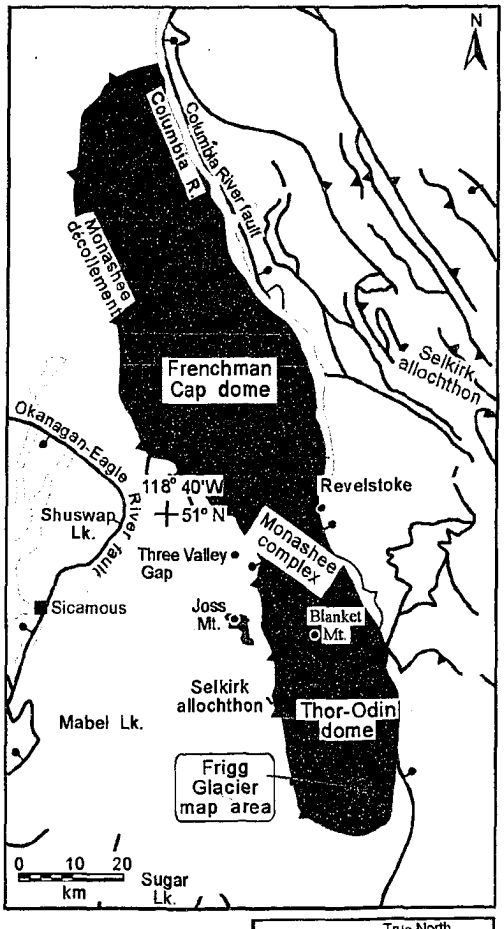


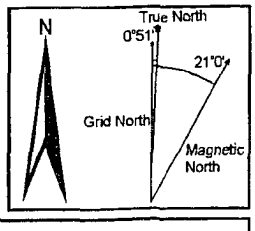


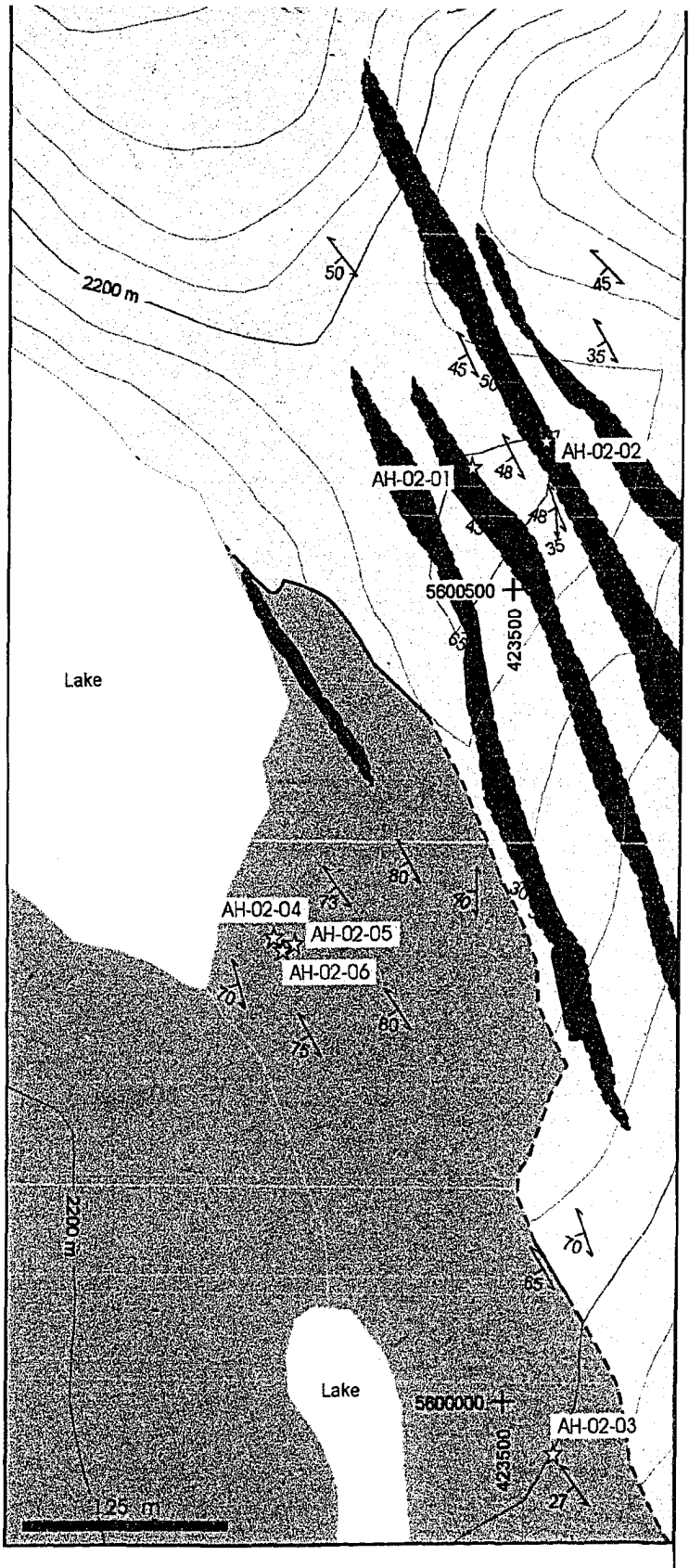


# Map 3.
# Geology map of the Frigg Glacier area, Thor-Odin dome, southeastern British Columbia

Mapping by A.M. Hinchey, 2002

Scale 1:5 000
Contour interval 20 meters

Topography from digital TRIM maps provided by the Province of British Columbia Ministry of Environments and Parks: 82L.060

North American Datum - NAD 83
UTM Zone 11

Legend

Amphibolite boudin

Hornblende-biotite granodiorite migmatitic orthogneiss, 15-30% leucosome

Augen potassium feldspar, hornblende-biotite granodiorite migmatitic orthogneiss, 10-25% leucosome

Symbo

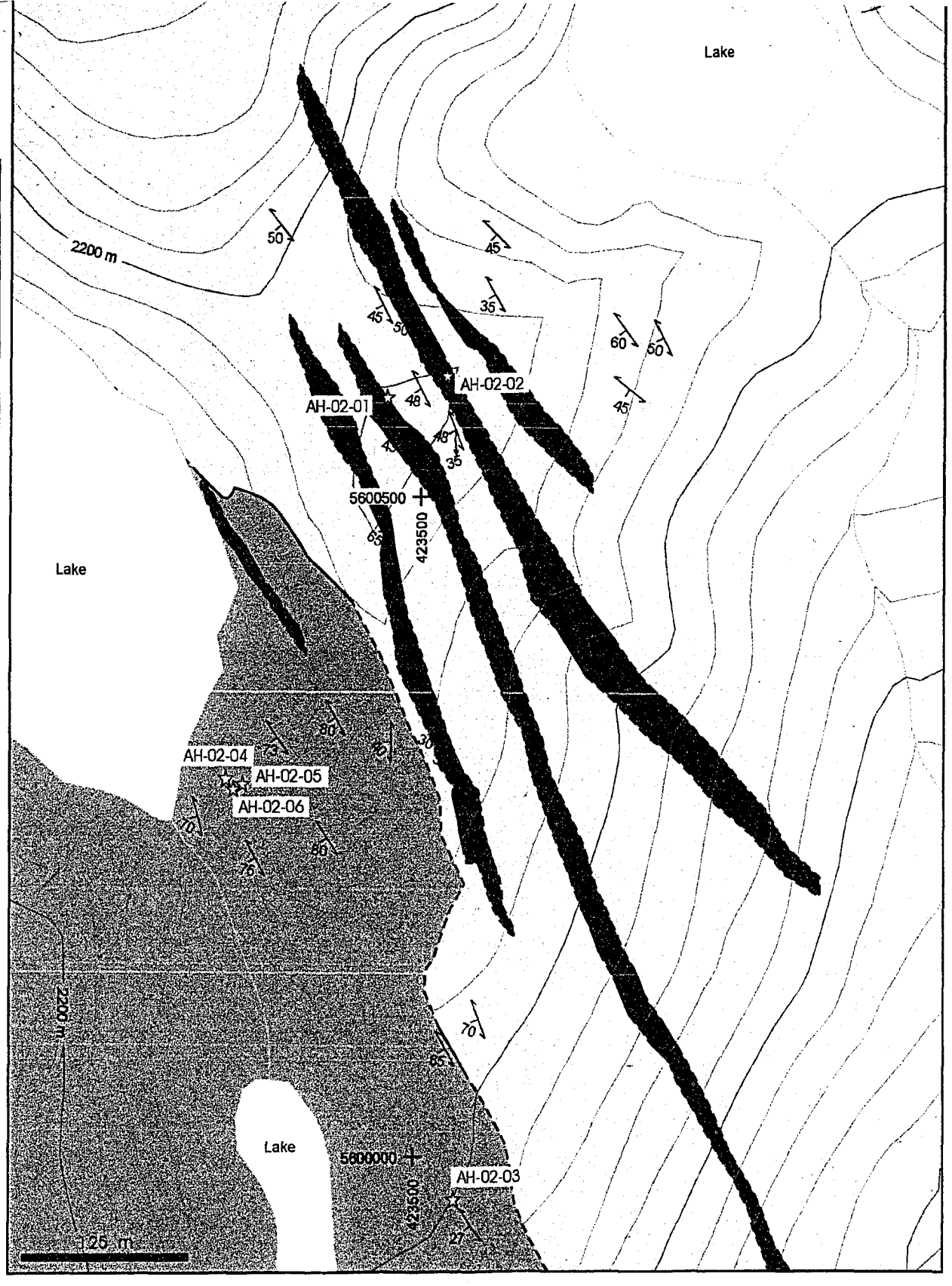


Legend

- Amphibolite boudin
- Hornblende-biotite granodiorite migmatitic orthogneiss, 15-30% leucosome
- Augen potassium feldspar, hornblende-biotite granodiorite migmatitic orthogneiss, 10-25% leucosome

Symbols

- Strike and dip of contact between units
- Strike and dip of $S_2$ foliation
- Trend and plunge of $L_2$ mineral lineation
- Contact (defined, approximate, assumed)
- Sample location

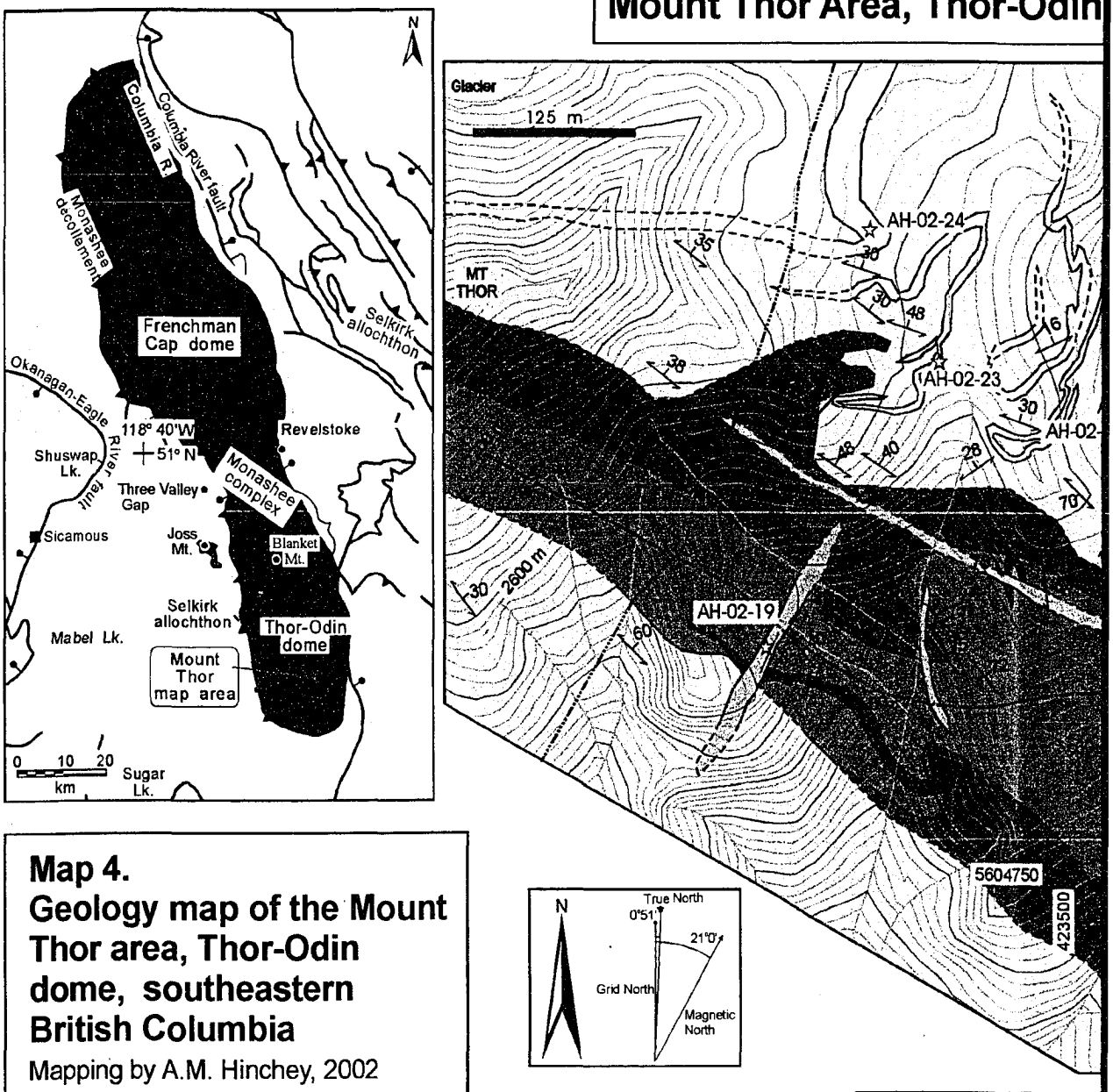


## Map 4.
## Geology map of the Mount Thor area, Thor-Odin dome, southeastern British Columbia

Mapping by A.M. Hinchey, 2002

Scale 1:5 000
Contour interval 20 meters

Fold generation interpretation is from P. McNeill, unpublished maps

Topography from digital TRIM maps provided by the Province of British Columbia Ministry of Environments and Parks: 82L.060

North American Datum - NAD 83
UTM Zone 11

# Area, Thor-Odin Dome, Monashee Complex

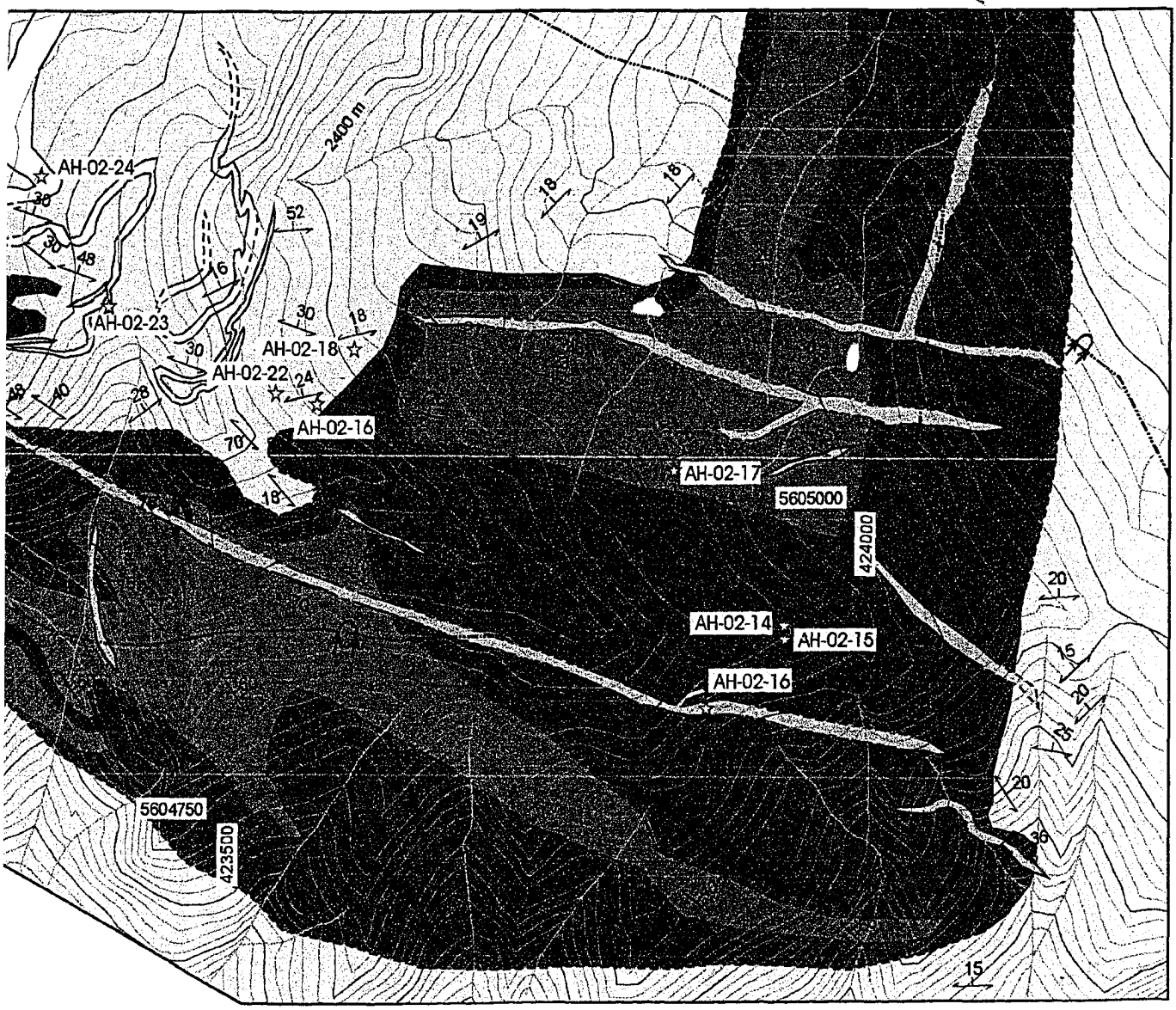


## Legend

- Tourmaline-garnet granite pegmatite dyke
- Quartzite, varying amounts of feldspar
- Silimanite-garnet-biotite pelitic schist, with local retrograde muscovite
- Marble
- *Interlayered calc-silicate with silimanite-garnet-biotite schist*
- Diopside calc-silicate gneiss
- Hornblende-biotite granodiorite migmatitic orthogneiss

## Symbols

- Strike and dip of contact between units
- Strike and dip of $S_2$ foliation
- Trend and plunge of $L_2$ mineral lineation
- Contact (defined, approximate, assumed)
- ☆ Sample location

Axial surface fold trace

anticline syncline

$F_2$

$F_3$

$F_4$

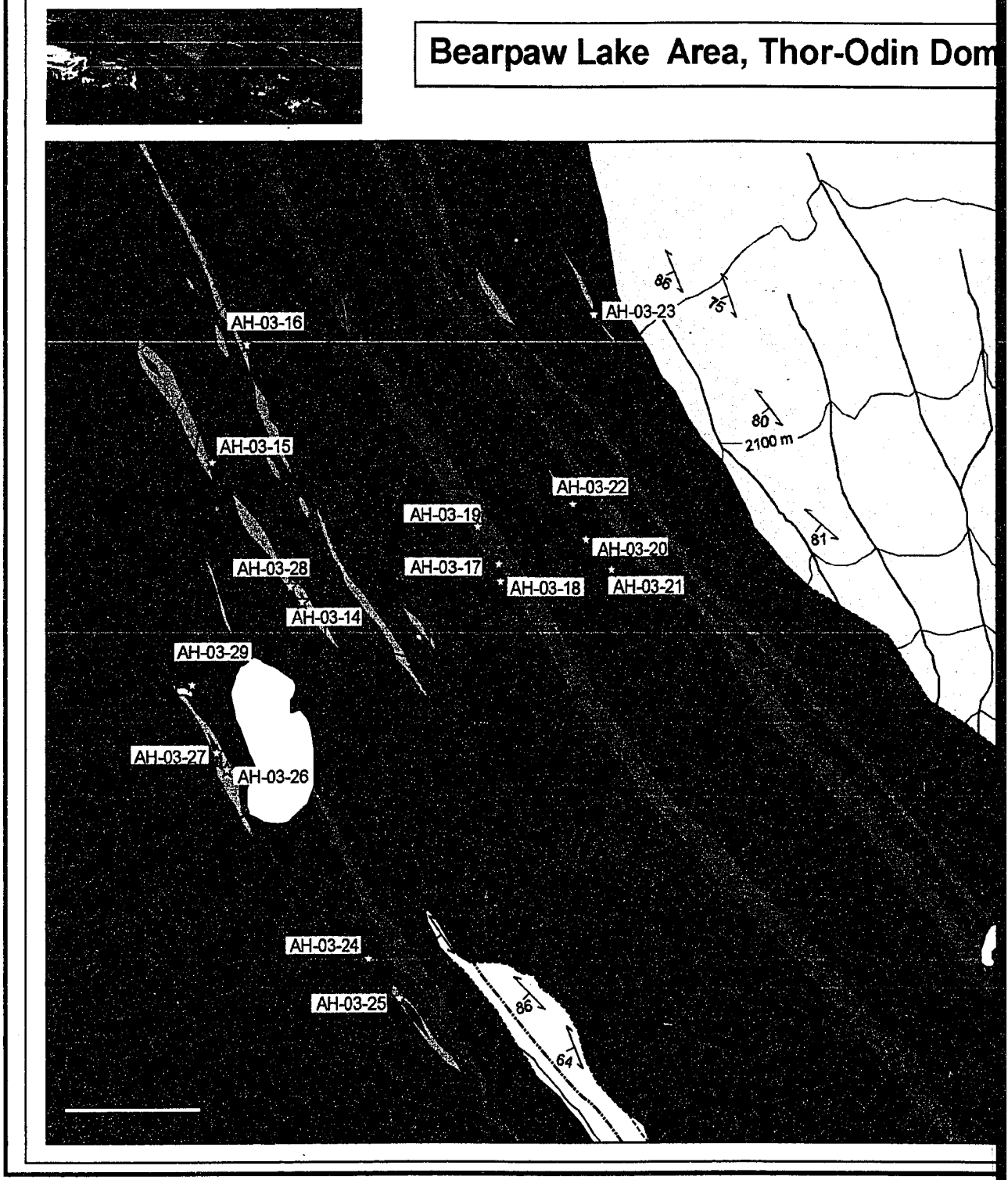

# ıor-Odin Dome, Monashee Complex

Ottawa-Carleton Geoscience Centre

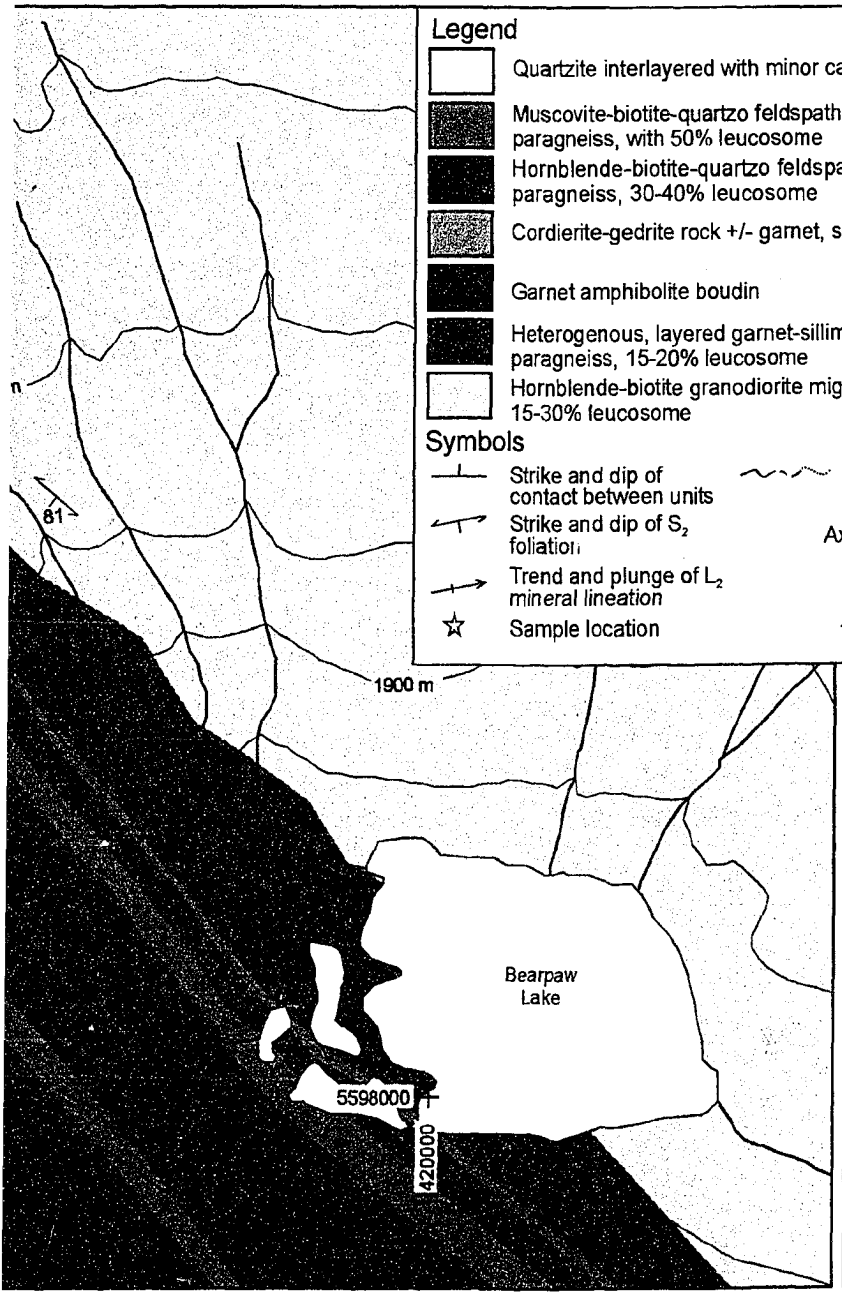


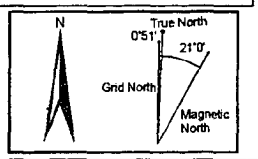


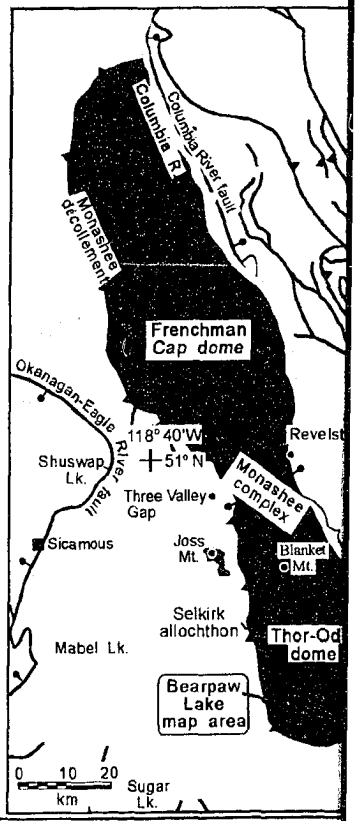


## Map 5.

## Geology map of the Bearpaw La area, Thor-Odin dome, southeas British Columbia

Mapping by A.M. Hinchey, 2003
Scale 1:10 000
Contour interval 100 meters
Topography from digital TRIM maps provided Province of British Columbia Ministry of Enviro and Parks: 82L.060
North American Datum - NAD 83
UTM Zone 11

# ıe, Monashee Complex

Ottawa-Carleton Geoscience Centre

## Legend

- Quartzite interlayered with minor calc-silicate
- Muscovite-biotite-quartzo feldspathic diatexite paragneiss, with 50% leucosome
- Hornblende-biotite-quartzo feldspathic migmatitic paragneiss, 30-40% leucosome
- Cordierite-gedrite rock +/- garnet, sillimanite, kyanite
- Garnet amphibolite boudin
- Heterogenous, layered garnet-sillimanite-quartzo feldspathic paragneiss, 15-20% leucosome
- Hornblende-biotite granodiorite migmatitic orthogneiss, 15-30% leucosome

## Symbols

- Strike and dip of contact between units
- Strike and dip of $S_2$ foliation
- Trend and plunge of $L_2$ mineral lineation
- Sample location
- Contact (defined, approximate, assumed)
- Axial surface fold trace ($F_2$) overturned
- anticline
- syncline

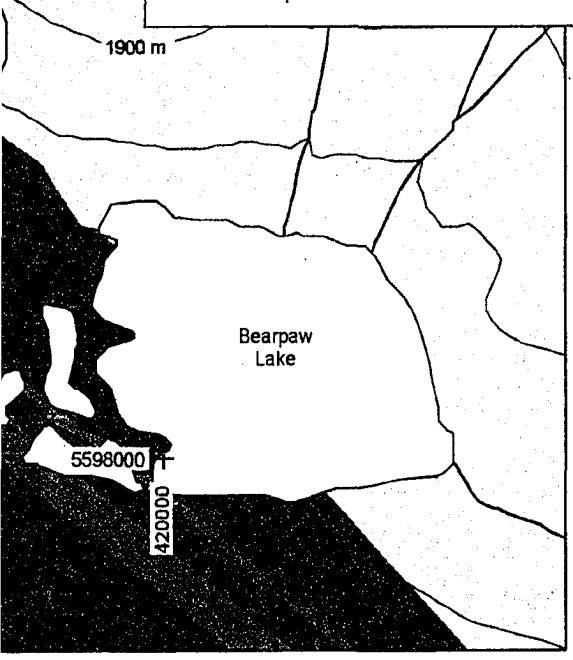


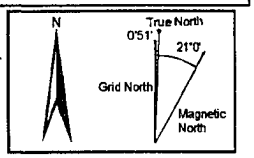


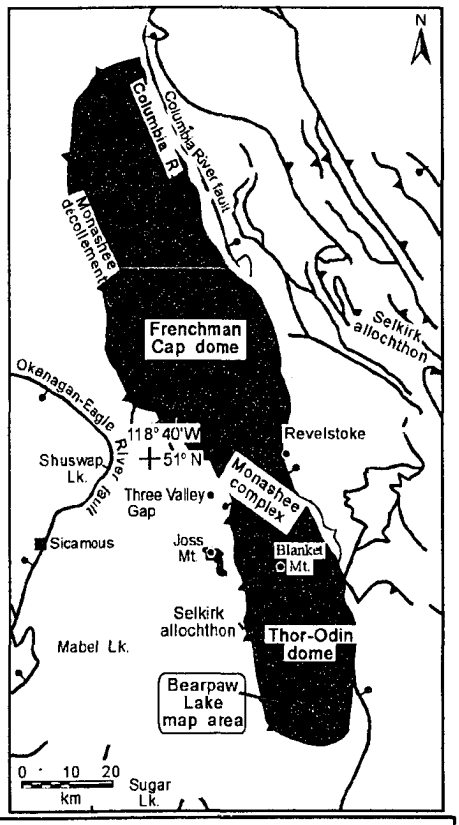


## Map 5.
## Geology map of the Bearpaw Lake area, Thor-Odin dome, southeastern British Columbia

Mapping by A.M. Hinchey, 2003
Scale 1:10 000
Contour interval 100 meters
Topography from digital TRIM maps provided by the Province of British Columbia Ministry of Environments and Parks: 82L.060
North American Datum - NAD 83
UTM Zone 11

# Mount Baldur Area, Thor-Odin - Pin

AH-03-30
AH-03-31
AH-03-32
AH-03-33
AH-03-34
Mount Baldur
2300 m
2200 m
2100 m
5586000
5585500
416000
416500
0

## Legend

- Paleocene to Eocene biotite leucogranite (Ladybird Granite Suite)
- Muscovite phyllite
- Quartzite interlayered with minor calc-silicate
- Garnet bearing amphibolite dykes
- Heterogenous, layered biotite-muscovite-quartzo feldspathic paragneiss

## Symbols

- Strike and dip of igneous layering
- Strike and dip of foliation
- Trend and plunge of mineral lineation
- Sample location
- Defined
- Approxi
- Assume

# Area, Thor-Odin - Pinnacles

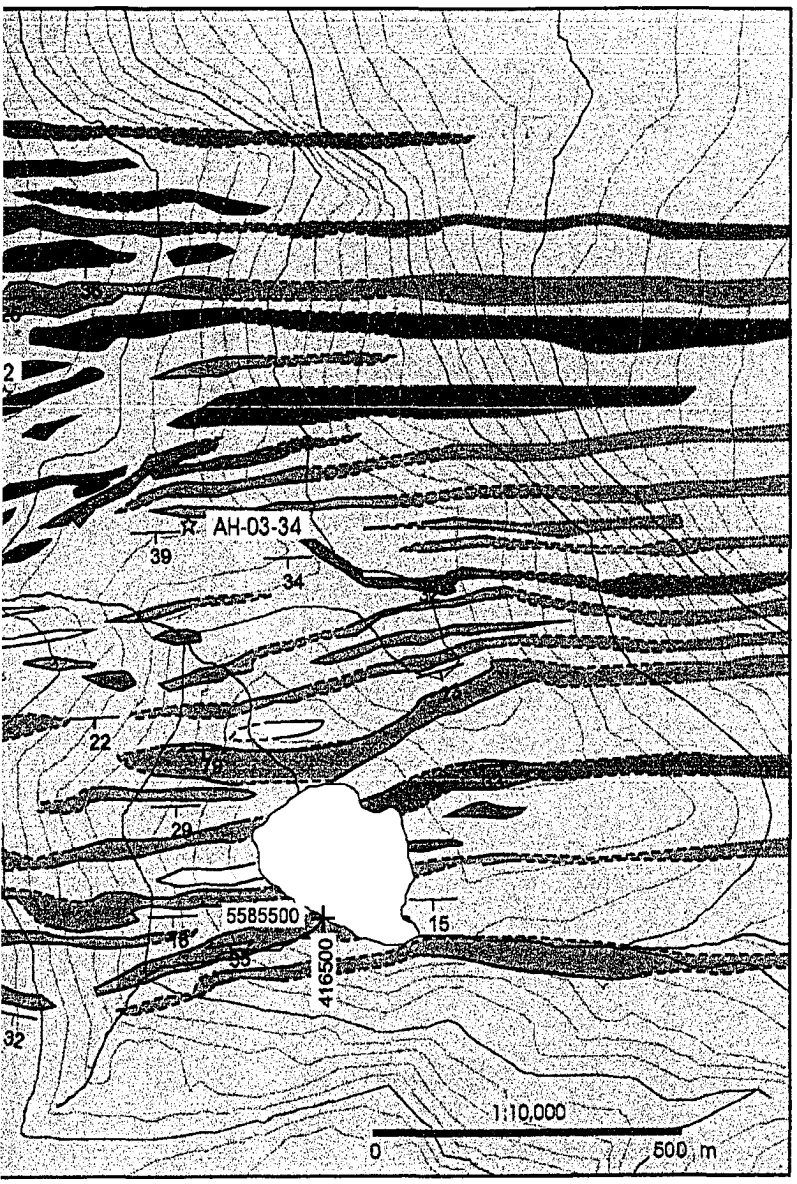


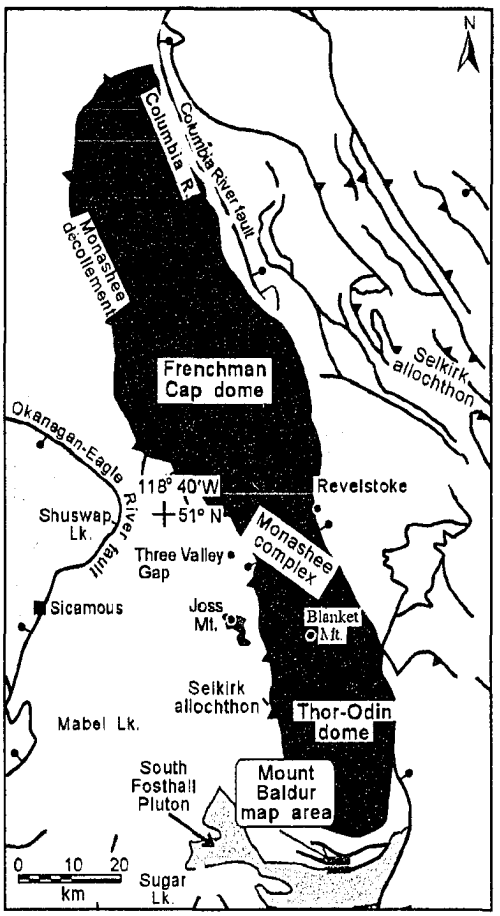


## Map 6.
## Geology map of the Mount Baldur area, southeastern British Columbia

Mapping by A.M. Hinchey, 2003

Scale 1:10 000
Contour interval 20 meters

Topography from digital TRIM maps provided by the Province of British Columbia Ministry of Environments and Parks: 82L.050

North American Datum - NAD 83
UTM Zone 11

Symbols

- Strike and dip of igneous layering
- Strike and dip of foliation
- Trend and plunge of mineral lineation
- Sample location
- Defined contact
- Approximate contact
- Assumed contact

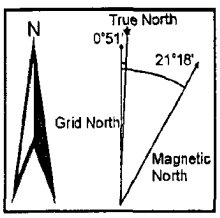

# South Fosthall Area, Thor-Odin

1700 m

1500 m

1300 m

28

12

23

5582000

423000

AH-03-37

## Legend

- Paleocene to Eocene biotite leucogranite (Ladybird Granite Suite)
- Cataclastic leucogranite interlayered with ~30% paragneiss xenoliths
- Quartzite interlayered with minor calc-silicate gneiss
- Marble with minor quartzite
- Garnet bearing amphibolite dykes
- Biotite rich psammite interlayered with minor phyllite

## Symbols

- Strike and dip of igneous layering
- Strike and dip of gneissic foliation
- Trend and plunge of mineral lineation
- Sample location

# all Area, Thor-Odin - Pinnacles

Ottawa-Carleton Geoscience Centre

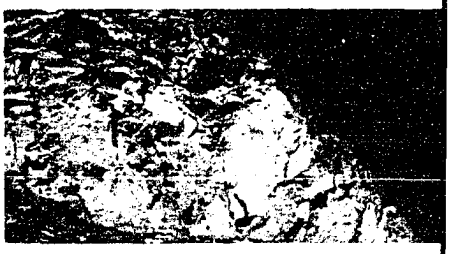

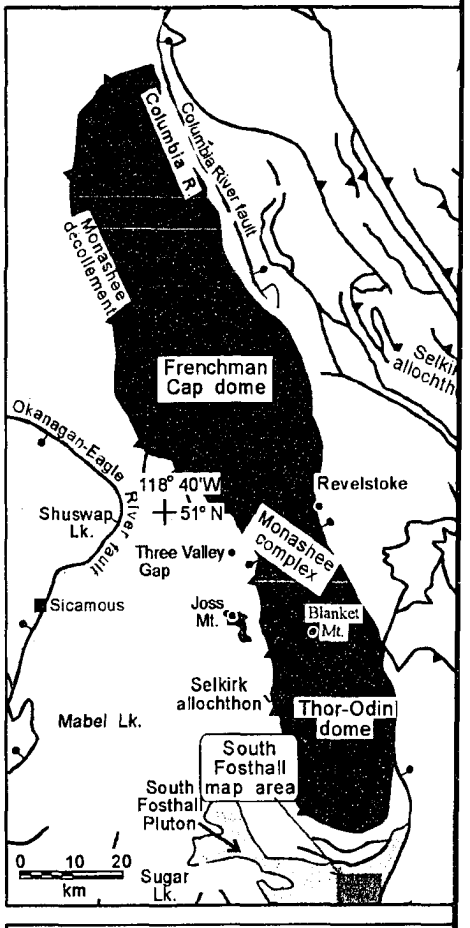


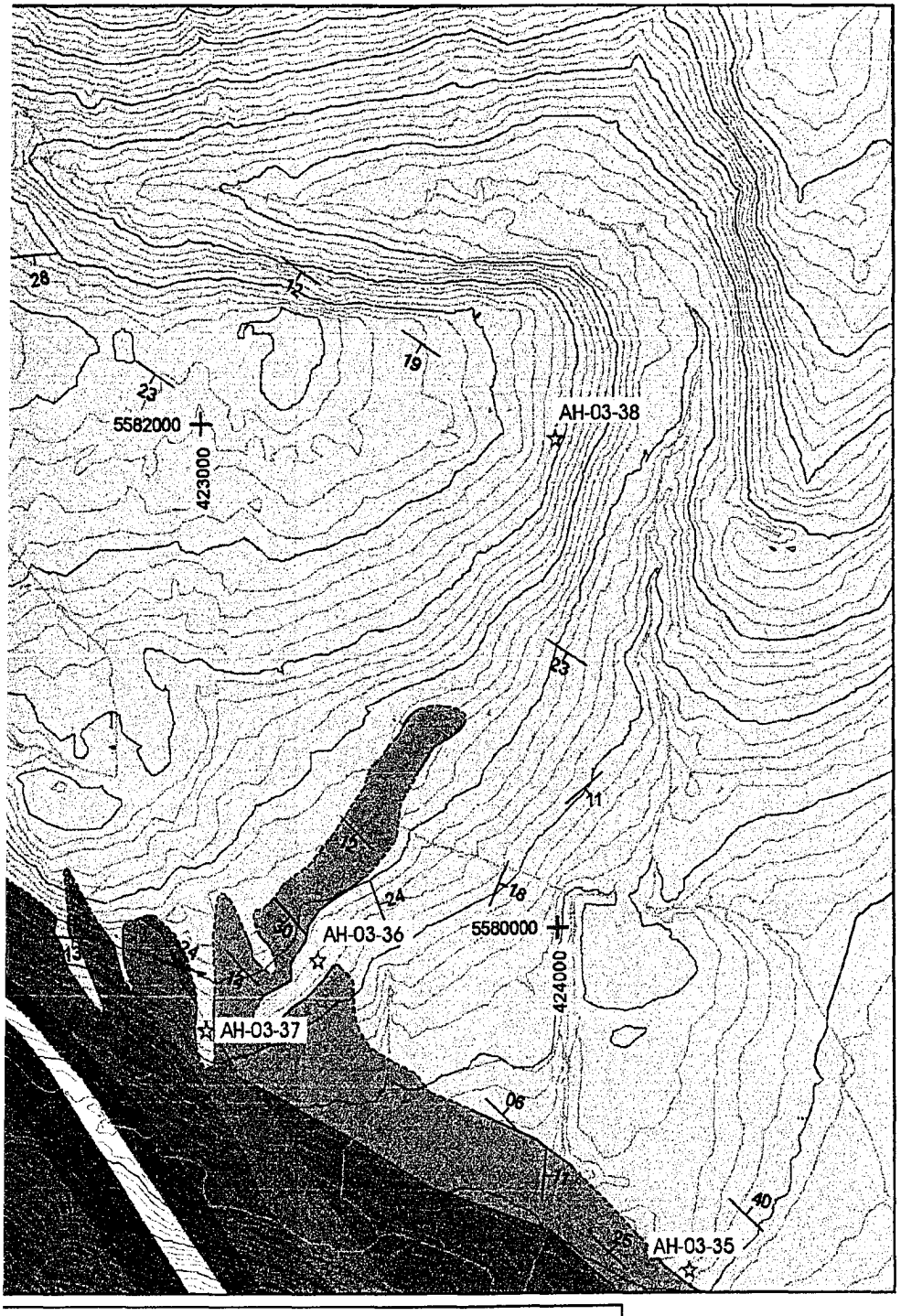


## Map 7.
## Geology map of the South Fosthall area, southeastern British Columbia

Mapping by A.M. Hinchey, 2003

Scale 1:10 000
Contour interval 20 meters

Topography from digital TRIM ma provided by the Province of British Columbia Ministry of Environment and Parks: 82L.040 and 82K.031

North American Datum - NAD 83
UTM Zone 11

Symbols

- Strike and dip of igneous layering
- Strike and dip of gneissic foliation
- Trend and plunge of mineral lineation
- Sample location
- Defined contact
- Approximate contact
- Assumed contact

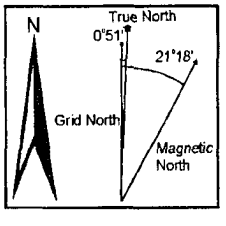

# r-Odin - Pinnacles

Ottawa-Carleton Geoscience Centre

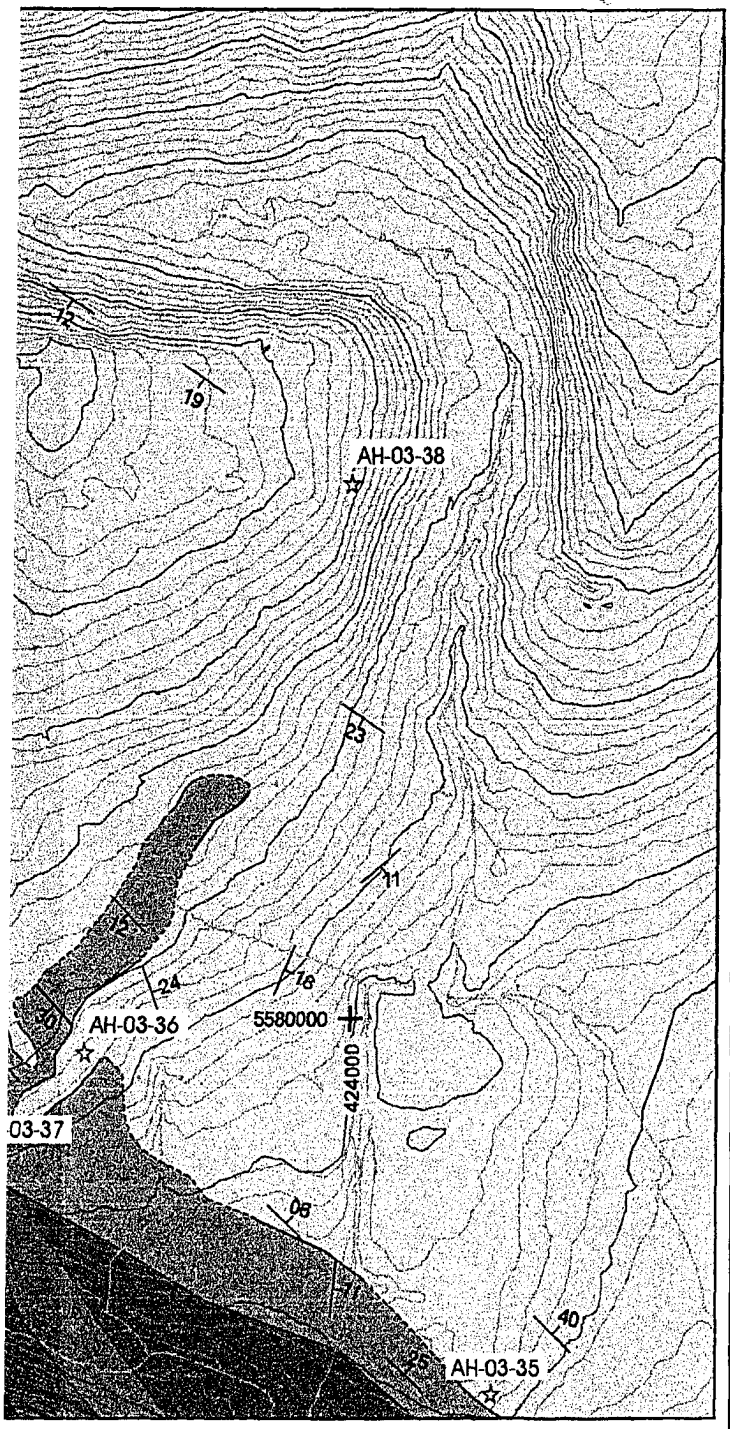


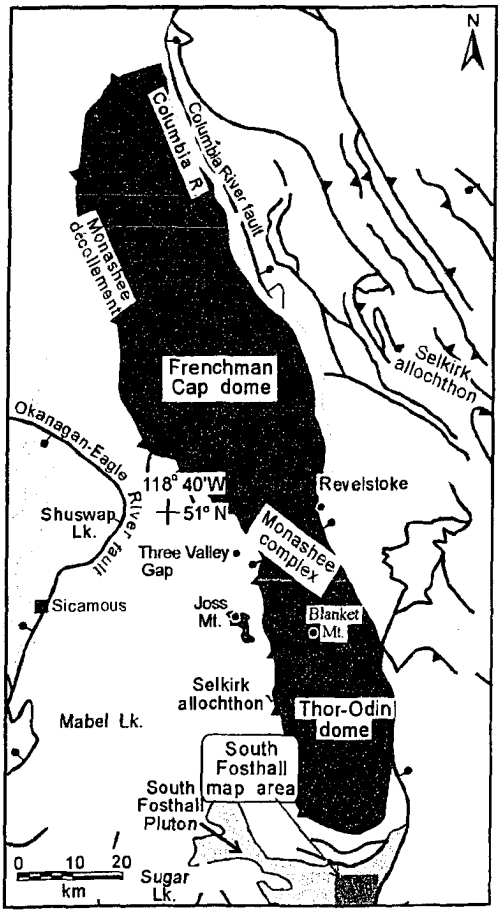


## Map 7.
## Geology map of the South Fosthall area, southeastern British Columbia

Mapping by A.M. Hinchey, 2003

Scale 1:10 000
Contour interval 20 meters

Topography from digital TRIM maps provided by the Province of British Columbia Ministry of Environments and Parks: 82L.040 and 82K.031

North American Datum - NAD 83
UTM Zone 11

neous — Defined contact

Approximate contact

of — Assumed contact